~~Author~~
" Jeathe
" Kingsbury

Return to Vase
Assign Technical
Report Number

TECHNICAL INFORMATION SERIES

Title Page

AUTHOR	SUBJECT CLASSIFICATION	NO.
J. Fehlmann J M Fehlmann	1. L. A. - Line Station and H.V. 2. L. A. - Testing 3. Insulators	59PT157
		DATE 12/9/59

TITLE

CONTAMINATION TEST ON LIGHTNING ARRESTER HOUSINGS

RECEIVED
RECEIVED
FEB 1 1960
1960
H. A. EREY
H. A. FREY

FOR USE OF G-E EMPLOYEES ONLY

GENERAL ELECTRIC

TRANSFORMER AND ALLIED PRODUCTS DIVISION

[redacted]

FOR USE OF G-E EMPLOYEES ONLY

GENERAL ELECTRIC

TECHNICAL INFORMATION SERIES

Title Page

AUTHOR	SUBJECT CLASSIFICATION	NO.
H. Fehlmann H Fehlmann	1. L.A.-Line Station and H.V. 2. L.A. - Testing 3. Insulators	59PT157
		DATE 12/9/59

TITLE

CONTAMINATION TEST ON LIGHTNING ARRESTER HOUSINGS

ABSTRACT

Sixty-cycle flashover tests were made on L.A. housings with three variations of both housing diameter and number of petticoats. In addition to fog tests with 0%, 3%, and 10% salt solutions, standard dry and wet tests were made. Also tested were a 79 kv Ohio Brass L.A. housing and 7785 pin type insulators.

G.E. CLASS	REPRODUCIBLE COPY FILED	NO. PAGES
IV	TECHNICAL DOCUMENTS	
GOV. CLASS		
None	Pittsfield, Mass.	54

CONCLUSION

1. Under contaminated conditions the withstand voltage increased and the leakage current decreased with the number of petticoats.

2. The Ohio Brass housing and the 7785 insulator supports had significantly higher withstand values under salt spray contamination than the G.E. housings. This appears to be the result of both increased creepage length and different design.

More detailed conclusions are given at the end of the report.

By cutting out this rectangle and folding on the center line, the above information can be fitted into a standard card file.

For list of contents-drawings, photos, etc. and for distribution see reverse side.

INFORMATION PREPARED FOR Lightning Arrester/W.J. Rudge

TESTS MADE BY JS Bozyczko, JE Eulian, HR Fehlmann Tests Completed: 9-24-59

COUNTERSIGNED F.J. Turner F J Turner SECTION High Voltage Laboratory

BUILDING and ROOM No. #9 - Rm. 102 LOCATION Pittsfield, Mass.

/hrq

2. Sixty-cycle withstand and flashover tests as well as leakage current measurements were performed while the units were subjected to a fog spray. Water solutions with 0%, 3% and 10% salt were used.

B. Dry and Wet Flashover and Withstand Tests

In order to get the same ground configurations for all the test series, the units were mounted on a stationary turn-table as shown in Fig. 33. In order not to influence the electric field across the units, a rod antenna was mounted on top of the units and the sixty-cycle voltage was applied to that rod. The 500 kva, 350 kv test transformer in Area 4 was used as the voltage supply. The transformer was fed by a 500 kva, sixty-cycle induction generator.

For each type of arrester housing, three different units were tested. For the Ohio Brass and the 7785 insulators, only one unit of each type was tested.

1. Dry Test

Each unit was subjected to five flashovers with rapid rising voltage. The average values were calculated from these.

For the sixty second dry withstand test, the starting point was a voltage of 90% of the average flashover value, with increases in 5% steps.

The results of dry tests are summarized in Table II. Reported are the average flashover and withstand voltages and the highest and lowest flashover and withstand values. In all cases the withstand voltages were at least 90% of the average flashover values.

In Fig. 1 the average withstand voltages for all the tested units are plotted against the creepage length. This curve shows, as expected, that the dry withstand voltages are independent of the creepage length as well as of the housing diameter. The dry flashover voltage is mainly a function of the arc string length.

The Ohio Brass unit had an average flashover voltage of 294 kv-rms, but a one minute withstand voltage of only 261 kv-rms. The higher flashover voltage for this unit can be expected, considering its arc string length of 32 inches, compared with 29-1/2 inches for the 12K-066, 12 petticoat units.

The withstand and flashover values for the 7785 unit are comparable with those obtained for the 3K, 1H and 2H units.

No damage to the arrester housings or porcelain seals could be observed due to this test series.

2. Rain Test

The NEMA standard rain test equipment was used for these tests.

For each unit, five flashovers with rapid rising voltage were performed, and the average flashover value was computed.

For the 10 sec. wet withstand tests, 80% of the average flashover value was chosen as the starting voltage and the voltage was increased in 5% steps.

The results for this test series are summarized in Table II. Shown are the average flashover and withstand voltages and the highest and lowest flashover and withstand values.

Fig. 1 shows that the withstand voltage increases with the creepage length (or number of petticoats), whereas the diameter has no influence. For the Ohio Brass and the 7785 units, according to their creepage lengths, the wet withstand voltages should be higher than those of the 3K, 1H and 2H units. Design may also be a factor. All the GE units have equally shaped petticoats whereas the petticoats for the Ohio Brass and the 7785 units are not of the same outside diameters and have undercut skirts.

During the wet flashover, and mainly the 10 second wet withstand tests on the 3K, 1H and 2H units, the cement seal started to melt and dripped along the surface of the units. At the same time a typical sulphur smell was noted. With decreasing amount of petticoats (increasing leakage current), the burnt marks were larger and the melting of the cement more severe.

This melting of the seal could decrease the flashover voltage and increase the spread of results. To evaluate this, a new series of wet flashover and withstand tests were performed with hipot wire wrapped around the top and the bottom seal of each unit and connected to the line metal.

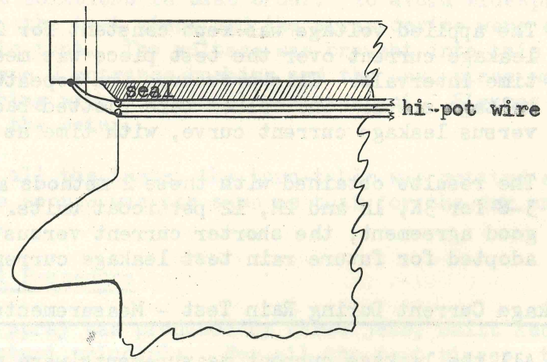

The wire guards prevented the burning of the cement, but it also reduced the flashover voltage by 10 to 20%, without helping to reduce the spread of results. Since this test series was performed after the withstand tests without the protecting hipot wire, the housing surface may have already been contaminated enough to cause inconsistencies. The results for the flashover and withstand voltages obtained for the units tested with and without hipot wire are given in Table III.

The withstand voltages obtained for the case with hipot wire wrapped around the cement seals show more regularity than those without protected seal. In Fig. 2, the minimum required creepage length for a withstand voltage of 1 kv-rms is plotted against the diameter of the housings, measured over the petticoats. The values obtained with the protected seal show evidence that the creepage path has to be increased with diameter. This is not the case for those withstand values obtained with the unprotected cement seal, which do not seem to follow any trend as shown in Fig. 2.

Later in the test, it was felt that this burning of the seal is a reality which must be faced while the units are in service. Therefore, all future testing was done without hipot wire protecting the cement seal.

a. Leakage Current During Rain Tests - Method of Test:

All leakage current measurements for the rain tests were performed with hipot wire wrapped around the cement seal.

Measurements were made with a vacuum tube voltmeter across a shunt connected in the ground circuit.

Two test methods were used for this test:

1) The 50% 10 sec. wet withstand voltage was applied to the test piece and kept constant until the leakage current flowing for that voltage became stable. Then, the applied voltage was increased steadily and the leakage current was measured at 5% intervals.

2) The applied voltage was kept constant for 20 sec. and the leakage current over the test piece was measured at certain time intervals. This procedure was repeated for several voltage steps. The values were plotted back to the voltage versus leakage current curve, with time as the parameter.

The results obtained with these 2 methods are shown in Figures 3-8 for 3K, 1H and 2H, 12 petticoat units. Since there is good agreement, the shorter current versus voltage method was adopted for future rain test leakage current measurements.

b. Leakage Current During Rain Test - Measurements:

All the leakage current measurements were made on three units of each type of arrester housing and are reported as average values based on arithmetic means. The leakage current versus the applied voltage across the arrester housings is shown in Figures 9-11.

According to these curves for the same housing diameter the leakage current decreased with increasing number of petticoats. Fig. 9 shows the leakage currents for the 3K-066 housings, where values up to 110 ma crest were measured.

Fig. 10 shows the leakage currents for the 1H-065 units where the highest recorded average value is only 85 ma crest. The three-petticoat container, probably due to spread in results, has less leakage current than the six-petticoat units. The average leakage current flowing across a unit with no petticoats (with an applied voltage of 90 kv-rms) is approximately 70 ma crest. For a 12 petticoat unit (with an applied voltage of 210 kv-rms), the value is only 50 ma crest.

In Fig. 11, the average leakage current is plotted for 2H-064 units, with a maximum leakage current of 70 ma crest.

According to Figures 9-11, as well as Figures 12-14, the leakage current increased with container diameter. The inconsistencies shown in Fig. 12, where the measured leakage current for the 2H-064 unit was higher than for the 1H-065 units, is unexplainable at present.d of results.

The leakage current versus the applied voltage for the 3K-12 petticoat unit, the Ohio Brass and the 7785 units is plotted in Fig. 15. Although the 7785 unit has the lowest leakage current, it also has the lowest flashover voltage. The 3K-066 unit was tested with hipot wire protecting the cement seal electrically. This was not the case with the Ohio Brass or the 7785 units. Furthermore, the leakage current values for the 3K unit are the average values measured on three units. Only one unit was tested for the Ohio Brass and the 7785 insulators.

C. Fog Spray Test

For the salt fog test, the units were sprayed with 0%, 10% and 3% salt solutions in that order. To avoid widespread contamination, the test piece and the spray device were enclosed in a plastic tent. The voltage was brought into this tent with a 138 kv type U entrance bushing and the test piece was connected to the bushing with a spring loaded contact. Figures 34 and 35 illustrate the setup.

During all the tests, the turn-table was rotated at 11-1/2 RPM. The voltage source was the same as that for the dry and wet flashover tests.

1. General Procedure:

The spray was produced by three jets, built according to the Venturi principle. For all the test pieces, the distance between the top jet and the top petticoat was fixed at 30 inches. The test pieces were sprayed for 4 minutes (at 10 cu. in./min.) in such a way as to cover the total surface, including the parts under the petticoats.

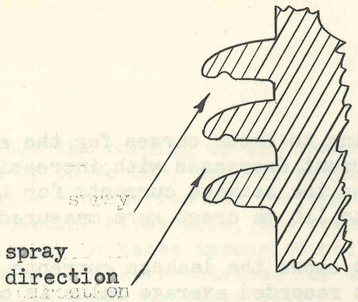

Each unit was tested by making runs at increasing levels of voltage until a flashover occurred. The procedure was to apply a given voltage to the test piece, spray for 4 minutes, turn off the spray, but continue holding voltage for 2 to 4 minutes depending on the magnitude of the leakage current.

The leakage current was recorded every 15 seconds. After flashover occurred, the same procedure was followed with decreasing voltage levels until a withstand level was obtained.

The temperature inside the plastic tent was measured with thermocouples during the 10% salt solution tests. An average temperature increase of about 5°F was noted, although in one special case, an increase of 11°F was measured right after flashover occurred.

2. Test Results:

a. 0% Salt Spray Test:

Only two units of each type were tested during this series, the results of which are summarized in Table IV. Withstand and flashover values are recorded for tests with both increasing and decreasing voltage levels.

1) Withstand Test

The withstand voltages for the different units are plotted versus the creepage length in Fig. 16. For this graph and those following, the withstand values shown were obtained by increasing the voltage.

Fig. 16 shows that, under fog spray conditions, the maximum withstand voltages increase with increasing creepage length (or number of petticoats). A comparison of these withstand values with those for the standard rain test indicate close agreement.

The increase in withstand voltage for the Ohio Brass unit compared with the 3K units is proportional to the increase in creepage length between these units. On the other hand, the withstand voltage for the 7785 unit is very low, considering its creepage length.

On a kv/inch creepage length base, the 7785 unit has the lowest values, followed by the 1H-0 petticoat units.

2) Leakage Current Measurements

During the 0% salt spray tests, severe melting of the cement seals on the housings was observed. For some units, the cement seal was burning with a blue flame even after the voltage was shut off. Where no melting of the seal was observed, the measured leakage currents were low. However, as soon as the seal started to melt and the dripping cement contaminated the housing surface, the leakage current increased sharply. In these cases the withstand voltage was found to be lower on the succeeding test.

Detailed results for the fog spray tests on the three-petticoat 3K-066 lightning arrester housing are given in Fig. 17. This is an example of the observations mentioned above. The numbers at the end of each run indicate, respectively, the applied voltage and the sequence. For each run, the spray was shut off after 240 sec. The voltage applied to the unit was 60, 80, 100, 120 and 140 kv. During all of these runs, the leakage current was below 10 ma crest and no melting of the cement seal was observed. However, at an applied voltage of 160 kv-rms, discharge streamers were observed originating from the top seal. At the same time, the leakage current was increasing and a flashover took place after about 200 seconds. For the next runs, with applied voltages of 140 and 120 kv (voltages which the test piece withstood previously), the leakage current increased sharply and led to flashovers. At an applied voltage of 100 kv, another withstand level was reached but the leakage current was higher than 100 ma crest. Similar observations were made on all the other units except the Ohio Brass, the 7785, and some 12-petticoat units where no melting or negligible melting of the cement seal was observed.

The electrical strength lost after a flashover could not be regained by letting the unit dry and cool off. As shown in Fig. 18, a 12-petticoat container (3K-066) which originally flashed over at 200 kv-rms later required a reduction to 160 kv to get another withstand value. After the unit was completely dry and cool, 180 kv was applied to the test piece. This time, the leakage current increased rapidly and led to a flashover.

The test indicated that the reduction of withstand voltage on successive runs was influenced more by contamination of the housing through the melting seal than by the accumulation of too much water on the surface or by increased housing temperature.

The influence of the housing diameter is shown in Fig. 19, a plot of the average leakage current versus time. For the 12- and the 6-petticoat housings, the leakage current had the highest values for the 3K-066 units. The difference in the leakage current between the 1H-065 and the 2H-064 units was very small and no conclusions can be drawn from the data. For the 3-petticoat units, the results for only one unit (instead of the average values) are reported for the 3K-066 and the 1H-065 unit. However, the average leakage current measured on two units is recorded for the 2H-064 units. Since the leakage currents for all these units is not over 6 ma crest, no valid conclusions can be drawn.

The leakage current before flashover occurs is reported in Table V. For the test series with 0% salt solution, these values may be more the result of the melting cement seal than due to the fog contamination.

Fig. 20 shows leakage current versus time for a complete run before a flashover occurred. Tested were: 3K, 12 petticoat unit I (180 kv-rms), the 3K, 12-petticoat unit II (200 kv), the 7785 unit (180 kv) and the Ohio Brass unit (240 kv). The leakage current for these units was low and within the limits of 5 and 7 ma crest. Only the 3K-066 unit I had a somewhat higher leakage current - in the order of 15 ma crest. Nevertheless, this value can be considered low and in line with the results obtained for the Ohio Brass, the 7785 and the 3K-066 unit II.

b. 10% Salt Spray Test

The results for this test series are given in Table IV and in Fig. 21 identified as number "10".

1) Withstand Test

The withstand voltages drop to values between 17-1/2 and 40 kv-rms and decrease with decreasing number of petticoats. Nothing can be predicted as far as influence of the housing diameters on the withstand voltages.

The Ohio Brass unit has a withstand voltage of 50 kv, the highest recorded, however this seems to be consistent with its greater creepage length.

2) Leakage Current Measurements

The measured leakage currents were extremely high and, because of difficulties in the measuring circuits, values could not always be recorded accurately. Therefore, no leakage current measurement results are reported for the 10% salt spray test.

c. 3% Salt Spray Test

As a result of the high leakage current measured during the 10% salt spray tests, additional tests were made with a 3% salt solution. One unit of each type was tested.

1) Withstand Test

The withstand and flashover voltages for this test series are summarized in Table IV. Fig. 16 shows the withstand voltages plotted against the creepage length for the different housings. Except for the 3K-066 housings, the creepage length had only a small influence on the withstand voltage.

In Fig. 21, the withstand voltages for the 10% and 3% salt solution are compared. There is only a slight increase for the 3K-066 units. For the 6-petticoat configuration, the withstand voltage measured for the 3% salt solution is even lower than for the 10% salt solution. However, there is an increase of 30 to 150% in withstand voltage for the 1H-065 and the 2H-064 units.

In Fig. 22, the minimum required creepage length to withstand 1 kv is plotted against the housing diameter. According to this (as well as the data in Fig. 21), the 1H-065 (medium diameter) units have the highest withstand values. They need the lowest creepage length to withstand 1 kv. The required creepage length is slightly higher for the 2H-064 units and considerably higher for the 3K-066 units. This suggests an optimum value for the housing diameter.

The Ohio Brass unit, with 55 kv, has a withstand voltage higher than any GE housings and, considering both housing diameter and creepage length, this unit is superior to the GE units. In addition, the Ohio Brass housing has the same strength before and after flashover while the other units dropped in withstand voltage about 15% after a flashover occurred. This drop probably is due to the melting of the seal, a process not observed in the Ohio Brass units.

With 70 kv withstand voltage, the 7785 unit has the highest value of all the units tested. At the same time, the creepage length is only 66 inches - 10 inches less than the Ohio Brass and 7-1/2 inches more than the 3K-066, 12-petticoat units. This indicates that the design of the petticoats has an importance influence on the flashover voltage.

The significant design feature common to both the Ohio Brass and the 7785 insulators is that the petticoats are undercut.

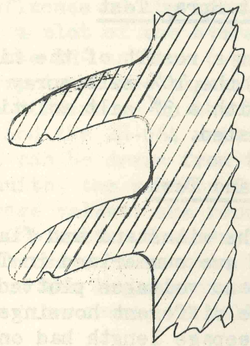

2) Leakage Current Measurements

Leakage current up to 1000 ma crest were measured during this test series.

Fig. 23 shows the leakage current as a function of time for a 3-petticoat container (2H-064) during the 3% salt spray test. The behavior of the leakage current for this unit is typical and was about the same for all other units during this test series. At the beginning, the leakage current is less than 1 ma crest. After 300 to 400 seconds of spray time, the leakage current increases rapidly, as shown by the curve for 45 kv-rms #2. In this case, a flashover did not occur as the spray was shut off at 240 seconds, shortly after the leakage current started to increase. However, at the next voltage level of 50 kv (series 3), the leakage current started high and increased rapidly, with a flashover at 60 seconds. For the next series of 45 and 40 kv (4 and 5 series), the leakage current was high and flashovers took place. On the other hand, with an applied voltage of 35 kv, leakage current reached magnitudes of over 300 ma crest without flashover. It was observed that for the Ohio Brass unit the leakage current increased steadily with voltage and spray time rather than taking erratic jumps like the G.E.

Figures 24 and 25 show the influence of housing diameter on the leakage current. Fig. 24 represents the 12-petticoat units and Fig. 25 the 6-petticoat units. For the same applied voltage, leakage current increases with increasing housing diameter.

Fig. 26 is a comparison of the leakage current for the 3K, 12-petticoat unit with an applied voltage of 35 kv, the Ohio Brass unit with an applied voltage of 35 kv and the 7785 unit with an applied voltage of 40 kv. The results for the 3K units are questionable since the unit was subjected to salt spray tests before that run. Despite washing and cleaning, some contamination was probably left on its surface and may have caused the high amount of leakage current.

Leakage currents which occurred before flashover are given in Table V. From this, the outstanding performance for the 7785 unit is apparent. With a flashover voltage of 80 kv-rms, the leakage current was only 17 ma crest before the first flashover occurred.

On runs made after a flashover occurred, leakage currents were higher than those reported, reaching maximums up to 1000 ma crest. Thus far in the test, it had been assumed that a flashover is inevitable as soon as the leakage current reaches a magnitude of several hundred ma. A possible explanation for the extra-ordinary behavior observed during this test series may be that a fairly uniform coating of salt spray over the whole insulator surface was obtained. The physics of the flashover for this type of contamination may be such that a flow of leakage current dries and heats up the path along the housing to such a degree that a thermal flashover can be formed. If this is the case, it should be possible to have fairly high leakage currents flow before a flashover occurs.

The flashovers over housings with dry spots along the surface can start because of local high voltage gradients at the boundaries between the contaminated and the nearly clean parts of the surface. If high enough, each gradient can lead to a partial flashover which, in turn, could initiate a complete flashover.

An important consideration during these tests was to prevent a drop of the testing voltage due to high pulses of leakage currents which may flow over the surface of the insulator before a total flashover occurred. In Fig. 27, the internal voltage drop of the power supply used for the test is plotted as a function of the leakage current. The voltage reduction, while a leakage current of 500 ma crest is flowing, is more than 5 kv-rms. This cannot be neglected for applied voltages of 15 to 50 kv-rms.

During each run, the leakage current fluctuates over a wide range, with many high spits. Because of the voltage source limitations, a sudden increase in leakage current may decrease the voltage across the test piece. Such a decrease will reduce the local voltage gradient at the boundary between contaminated and clean zones enough to prevent a flashover. Therefore, it is possible that the withstand values reported are too high. This is especially true for the Ohio Brass unit where, due to the shape of the petticoats a uniform coating is unlikely. It can also be true for the GE units (see Fig. 36). Measured withstand voltages are plotted versus resistivity of the sprayed solution in Fig. 28 for the 3K-066 units, Fig. 29 for the 1H-065 units, Fig. 30 for the 2H-064 units and in Fig. 31 for the Ohio Brass and the 7785 units. The measured points for each unit are connected by straight lines, with the full knowledge that this is not the actual case. The gap

in resistivity between the 3% and the 0% salt solution is too large to draw any reliable curves.

RECOMMENDATIONS AND IMPROVEMENTS FOR FUTURE SALT CONTAMINATION TESTS

A. A better control of the amount of contamination sprayed on the unit is required. To accomplish this the following measures are proposed.

1. Reduce the rate of spraying. No water drops should build up along the petticoats at any time during the spray test.

2. Wash unit with water after each run so that when a new voltage level is applied the unit will be clean of salt.

3. Test each unit with the same voltage sequence. Care has to be taken that the first applied voltage is low enough so that all the tested units of one group (same diameter and same number of petticoats) will withstand it.

B. A "stiffer" voltage source must be used for the salt spray tests. This may be obtained by connecting a capacitor in parallel with the test piece. This capacitor will act as a voltage stabilizer when the leakage current is fluctuating due to the large spits that occur.

C. A switch should be installed in the leakage current measurement circuit to change the shunt resistors while voltage is applied to the test piece.

D. The vacuum tube voltmeter which was used to measure the leakage current was not able to follow the fast pulses. A first improvement would be to substitute a recording milliammeter for the voltmeter, and observe the fast fluctuations in both the current and the applied voltage with an oscilloscope. To record the pulses in the leakage current, a counting device can be used which could count pulses exceeding a determined leakage current.

Conclusions:

A. Dry Withstand

1. No influence of the number of petticoats or the housing diameter was observed during this test series.

B. Rain Spray - Standard Test

1. The wet flashover value increased with the number of petticoats but was not affected by the housing diameter.

2. The leakage current decreased with the number of petticoats but increased with the housing diameter.

3. On several G.E. units, the insulator seal ignited and partially burned. The dripping of the melted seal along the insulator housing introduced an additional surface contamination which reduced dielectric strength.

C. Fog Test: 0% Salt Solution

1. The results for this test series agree, in general, with those of the rain test.

2. The Ohio Brass has a significantly higher withstand voltage compared to the GE 3K-066, 12 petticoat unit.

3. Burning of the insulator seal was noted in several GE units.

D. Fog Test: 10% Salt Solution

1. The withstand value fell to about 20% of the water fog values.

2. The withstand voltage increased with the number of petticoats.

3. The Ohio Brass unit had a 25% higher withstand voltage than the GE 3K-066, 12 petticoat unit.

E. Fog Test: 3% Salt Solution

1. The number of petticoats had only a minor influence on the flashover voltage, except for the unit with no petticoats.

2. The medium diameter housings (11-5/8" O.D. over petticoats) had the highest flashover values.

3. The Ohio Brass unit withstand voltage was about 10% higher than that of the 3K-066 units.

4. After flashover, the Ohio Brass unit had the same strength. The GE units fell about 15%.

5. The leakage current is increased with the housing diameter.

TABLE I

Description of Test Pieces

Name Class Size	# of Petticoats	Diameter over Petticoats	Creepage Length (inches)	Flashover Length (inches)	Height (inches)	Design Sketch of Petticoats
9LA3K066	12	15-3/8"	58-1/2	29-1/2	38	
9LA3K066	6		43-1/2	29-1/2	38	
9LA3K066	3		36	29-1/2	38	
9LA1H065	12	11-5/8"	58-1/2	29-1/8	33-3/4	
9LA1H065	6		42-1/4	29	33-3/4	
9LA1H065	3		35	29	33-3/4	
9LA1H071	0		28-1/2	29	33-3/4	
9LA2H064	12	9-1/16"	57-1/2	29-1/4	33-3/4	
9LA2H064	6		42-1/2	29-1/2	33-3/4	
9LA2H063	3		35-1/4	29	33-3/4	
Ohio Brass*	8 Large 7 Small	16"	76	32	37-1/2	
Pin Type 7785* 2 Units in Series	2X3	17"	66	29	29	

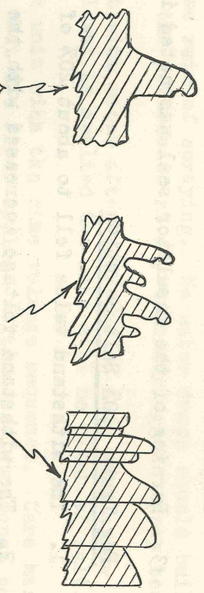

*1 unit only.

TABLE II

NEMA Standard Dry and Wet Withstand and Flashover Tests

Unit	Number of Petticoats	Dry Test						Wet Test					
		Flashover Test			Withstand Test			Flashover Test			Withstand Test		
		Highest* 1)	Lowest* 1)	Avg.* 2)	Highest* 1)	Lowest* 1)	Avg.* 2)	Highest* 1)	Lowest* 1)	Avg.* 2)	Highest* 1)	Lowest* 1)	Avg.* 2)
3K-066	12	261	257	260	247	246	247	249	210	236	238	204	217
	6	263	254	258	247	244	246	242	215	229	209	155	191
	3	264	259	263	249	252	250	195	154	177	141	133	136
1H-065	12	263	254	261	246	260	252	244	202	226	222	199	206
	6	280	265	273	247	255	250	234	210	233	184	169	178
	3	286	252	271	241	265	253	218	176	192	157	149	153
071	0	282	220	265	248	256	251	133	116	125	105	84	96
2H-064	12	285	258	274	233	256	242	258	218	245	224	215	220
	6	295	263	279	253	271	260	257	226	240	197	186	194
	3	274	269	275	248	254	252	192	169	178	153	138	146
Ohio Brass 3)	8 large 7 small	304	284	294			261	237	222	230			216
7785 3)	2X3	278	260	266			239	207	196	199			179

* Values corrected for RAD
1) Highest and lowest values measured on 3 units
2) Avg. out of 3 units
3) Only one unit tested

TABLE III

Sixty-Cycle Wet Flashover and Withstand Voltages for Differently Shaped Lightning Arrester Housing With and Without Cement Seal Protecting Hi-pot Wire Connected

Unit	Number of Petticoats	Without Hi-pot Wire		With Hi-pot Wire	
		F.O. kv rms	Withstand kv rms	F.O. kv rms	Withstand kv rms
3K	12	237	217	211	199
	6	229	191	202	162
	3	177	136	159	135
1H	12	226	206	227	224
	6	233	178	205	164
	3	192	153	175	146
	0	125	96	115	105
2H	12	245	220	245	216
	6	240	194	216	174
	3	178	146	174	152

All values corrected for RAD

TABLE IV

Contamination Test on L.A. Housings Fog Spray Test

Unit	Number of Petticoats	0% Salt Spray Test			3% Salt Spray Test			10% Salt Spray Test		
		1) WS Volt. in kv - rms		2) FO Volt. in kv - rms	2) WS Volt. in kv - rms		2) FO Volt. in kv - rms	1) WS Volt. in kv - rms		1) FO Volt. in kv - rms
		Inc. Volt.	Dec. Volt.	Inc. Volt.	Inc. Volt.	Dec. Volt.	Inc. Volt.	Inc. Volt.	Dec. Volt.	Inc. Volt.
3K-066	12	200	190	220	40	35	40	40	20	50
	6	160	115	180	27-1/2	30	35	27-1/2	20	32-1/2
	3	140	90	150	30	--	30	30	17-1/2	32-1/2
1H-065	12	210	210	230	40	40	55	40	30	55
	6	180	140	200	20	35	50	20	20	25
	3	140	120	150	20	50	55	20	20	25
	0	90	80	110	17-1/2	--	30	15	17-1/2	22-1/2
2H-064	12	220	220	240	35	45	50	25	25	40
	6	160	140	180	25	35	45	22-1/2	22-1/2	30
	3	120	80	140	20	40	50	20	20	25
Ohio Brass 7785 5)	8 large 7 small	3) 240	3) 240	3) 260	--	--	60	50	--	4) 50
	2X3	180	180	200	--	70	80	45	70	--
								--	--	--

1) Average out of 2 units
2) Highest and lowest value measured on 2 units
3) Tent was rolled up, fresh air could enter all the time
4) Repeat after long break
5) Only one unit tested

TABLE V

Contamination Test on LA Housings

Leakage Current Before Unit Flashed Over

Container	Petticoats	0% Salt Spray F.O. Voltage kv-rms	0% Salt Spray Leakage Current milliamp. crest	3% Salt Spray F.O. Voltage kv-rms	3% Salt Spray Leakage Cur milliamp. c
3K-066	12 I	200	97	40	255
	II	240	21		
	6 I	180	67	35	740
	II	180	>40		
	3 I	140	--	30	1040
	II	160	32		
1H-065	12 I	220	5	55	247
	II	240	5		
	6 I	200	25	50	305
	II	200	30		
	3 I	160	33	55	--
	II	140	30		
	0 I	120	67	30	72
	II	100	36		
2H-065	12 I	220	5	50	432
	II	240	11		
	6 I	180	28	45	340
	II	180	25		
	3 I	140	25	50	114
	II	140	35		
O.B.		260	10	60	430
7785		200	7	80	17

References:

1) A Review of The Surface Leakage Problem By A.D. Lantz,Jr., published by Ohio Brass Company, Mansfield, Ohio.

2) The Insulating Ability of High Tension Insulators under Various Surface Conditions By H. Von Cron; W. Estorff and H. Laepple; CIGRE 1954 #218.

3) Counter Measures Against Salt Pollution on Insulators used For Extra High Voltage Transmission System Located Near and Along Sea Coasts - CIGRE 1958 #412.

4) Der Rillenisolator mit Oberflaechenfremdschicht. H. Von Cron ETZ A Heft 3 - 1954. S. 65.

Figure 1

183HA737

Dry and Wet Withstand Voltages for LA Housings

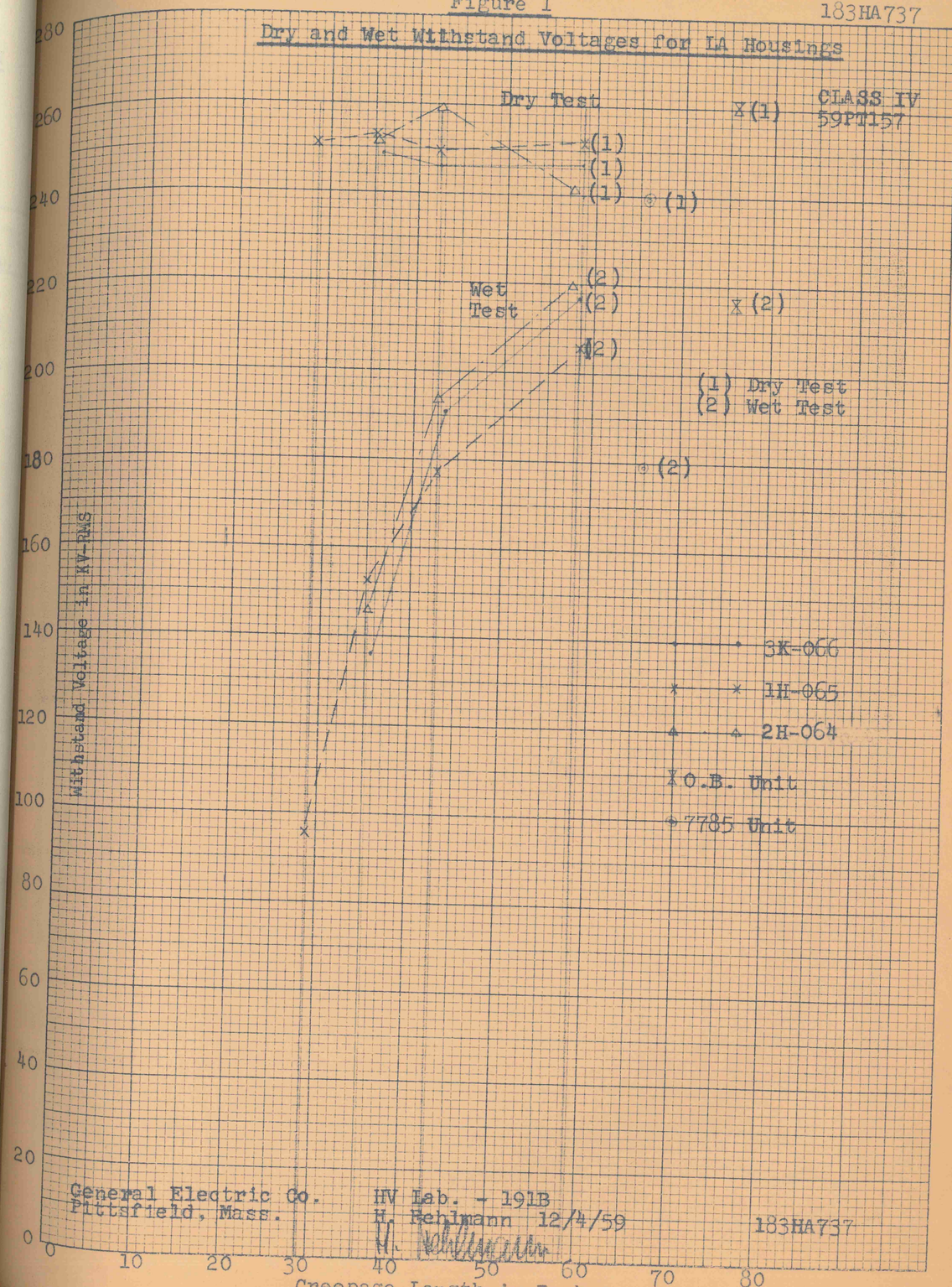

General Electric Co. HV Lab. - 191B
Pittsfield, Mass. H. Hehlmann 12/4/59

183HA737

Figure 2

183HA738
CLASS IV
59PT157

Required Creepage Length to Withstand
1 KV-RMS Rain Test

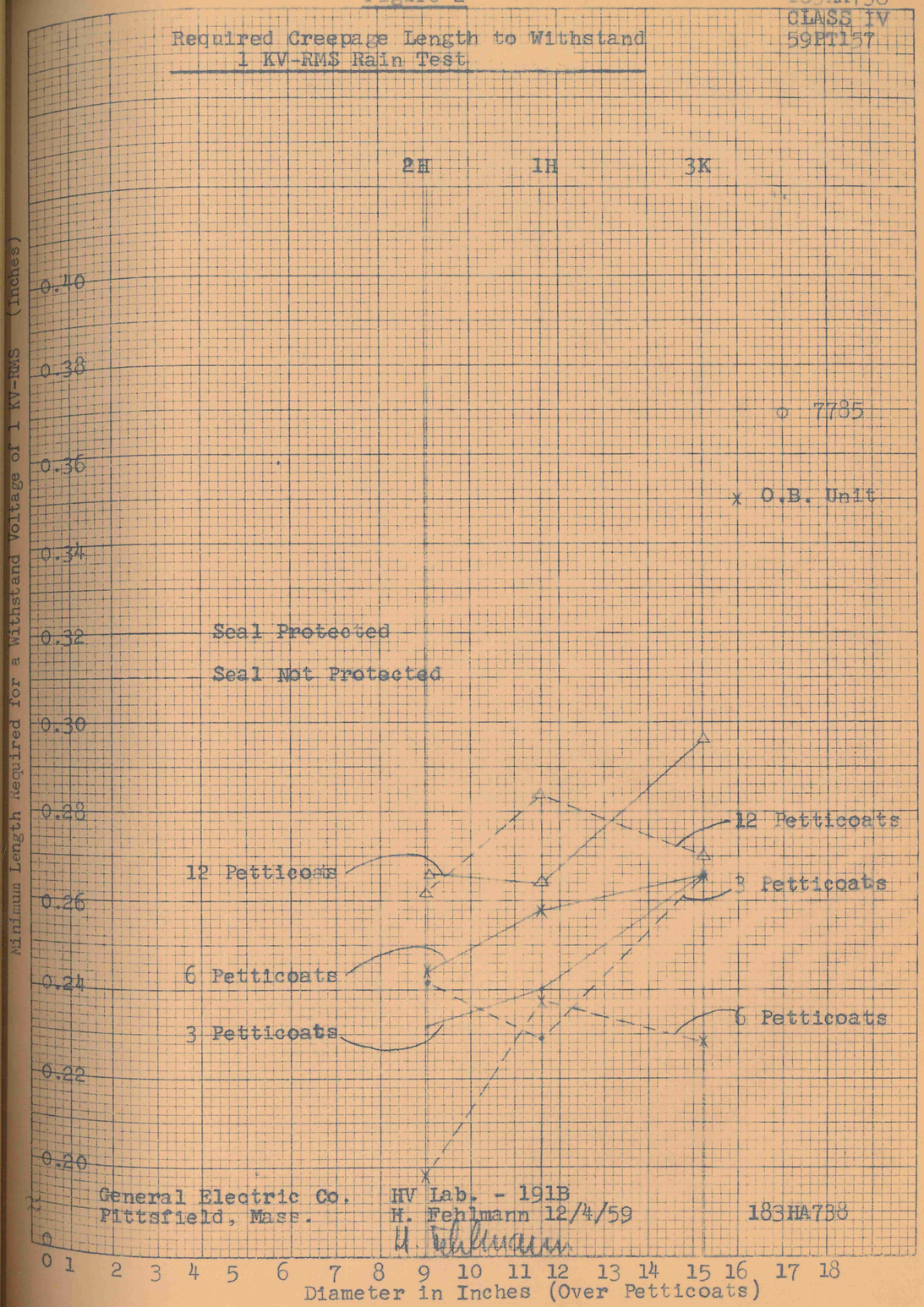

General Electric Co.
Pittsfield, Mass.

HV Lab. - 191B
H. Fehlmann 12/4/59

183HA738

Figure 3

183HA739

12 Petticoat Container 3K-066 II

CLASS IV
59PT157

Leakage Current vs. Applied Voltage
NEMA Standard Rain Test

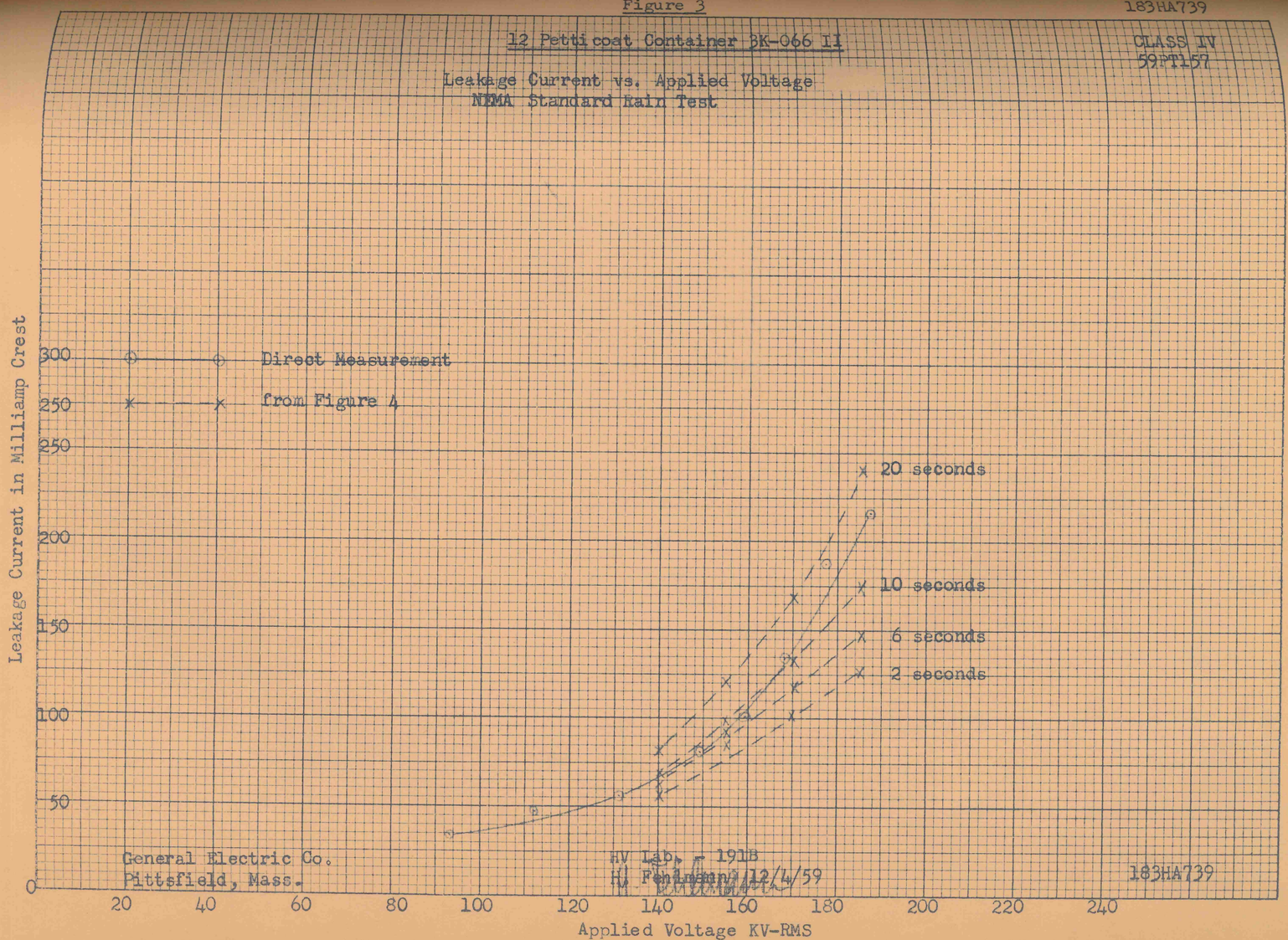

General Electric Co.
Pittsfield, Mass.

HV Lab. - 191B
H. Fenlason 12/4/59

183HA739

1-11-1960

Figure 4

183HA740
CLASS IV
59PT157

12 Petticoat Container 3K-066 IL

Leakage Current vs. time at constant Voltage

NEMA Standard Rain Test

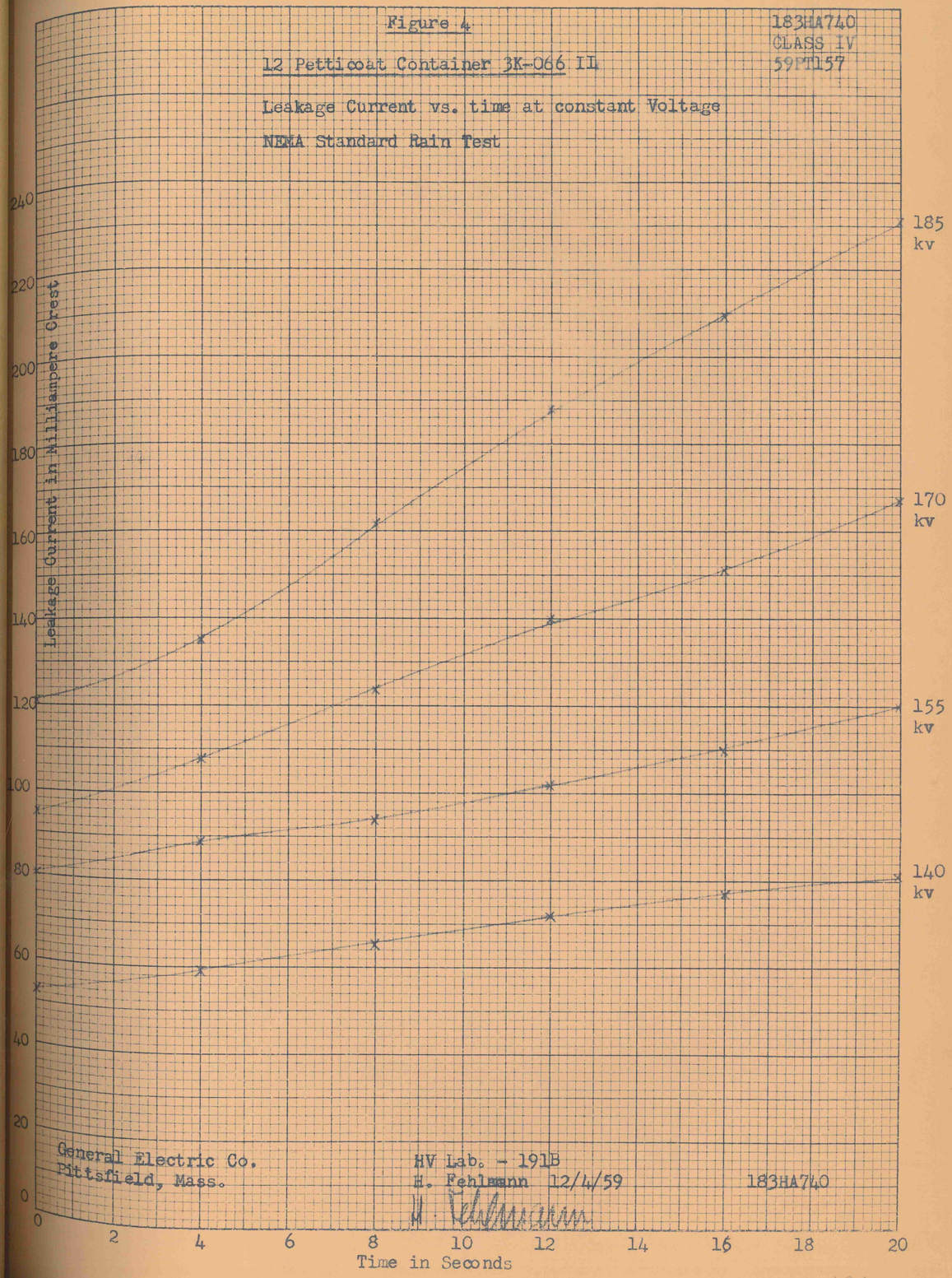

General Electric Co.
Pittsfield, Mass.

HV Lab. - 191B
H. Fehlmann 12/4/59

183HA740

H. Fehlmann

1-11-1960

Figure 5

183HA741
CLASS IV
59PT157

12 Petticoat Container 1H-065 II

Leakage Current vs. Applied Voltage
NEMA Standard Rain Test

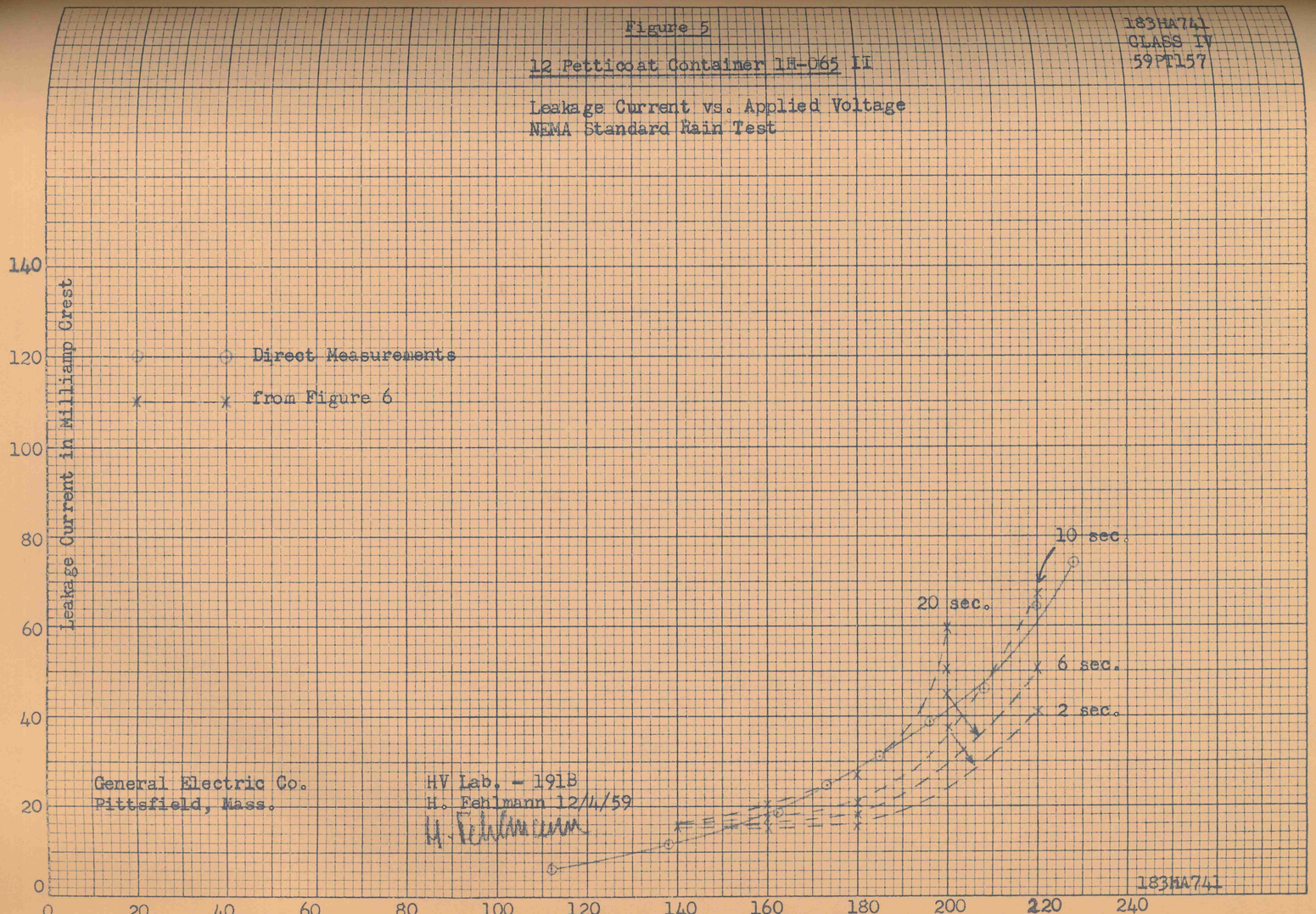

General Electric Co.
Pittsfield, Mass.

HV Lab. - 191B
H. Fehlmann 12/4/59

H. Fehlmann

INDEXED 1-11-1960

Figure 6

183HA742
CLASS IV
59PT157

12 Petticoat Container 1H-065 II

Leakage Current vs. Time at Constant Voltage
NEMA Standard Rain Test

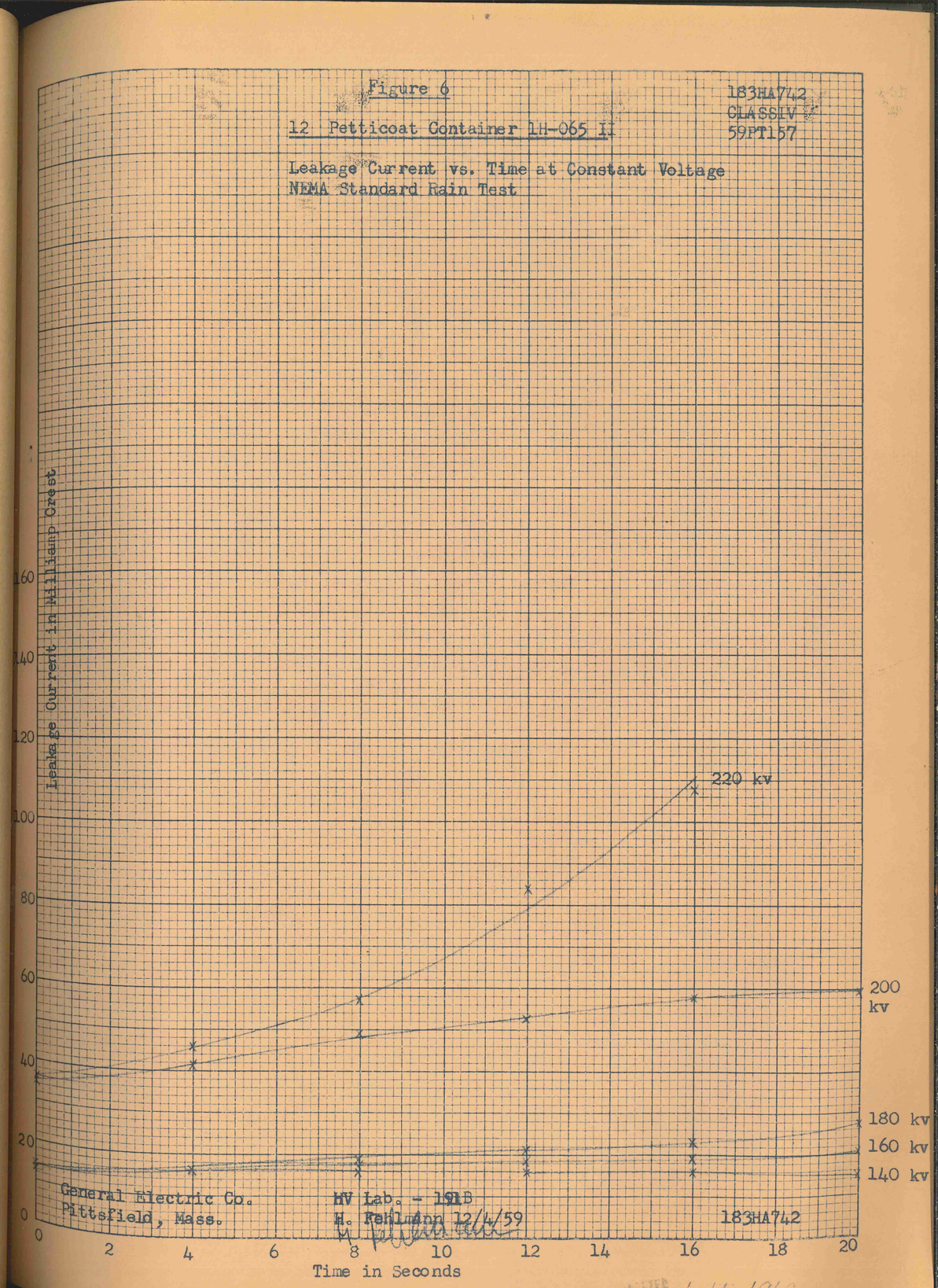

DELETED 1-11-1960

Figure 7

12 Petticoat Container 2H-064 III

Leakage Current Vs. Applied Voltage
NEMA Standard Rain Test

183HA743
CLASS IV
59PT157

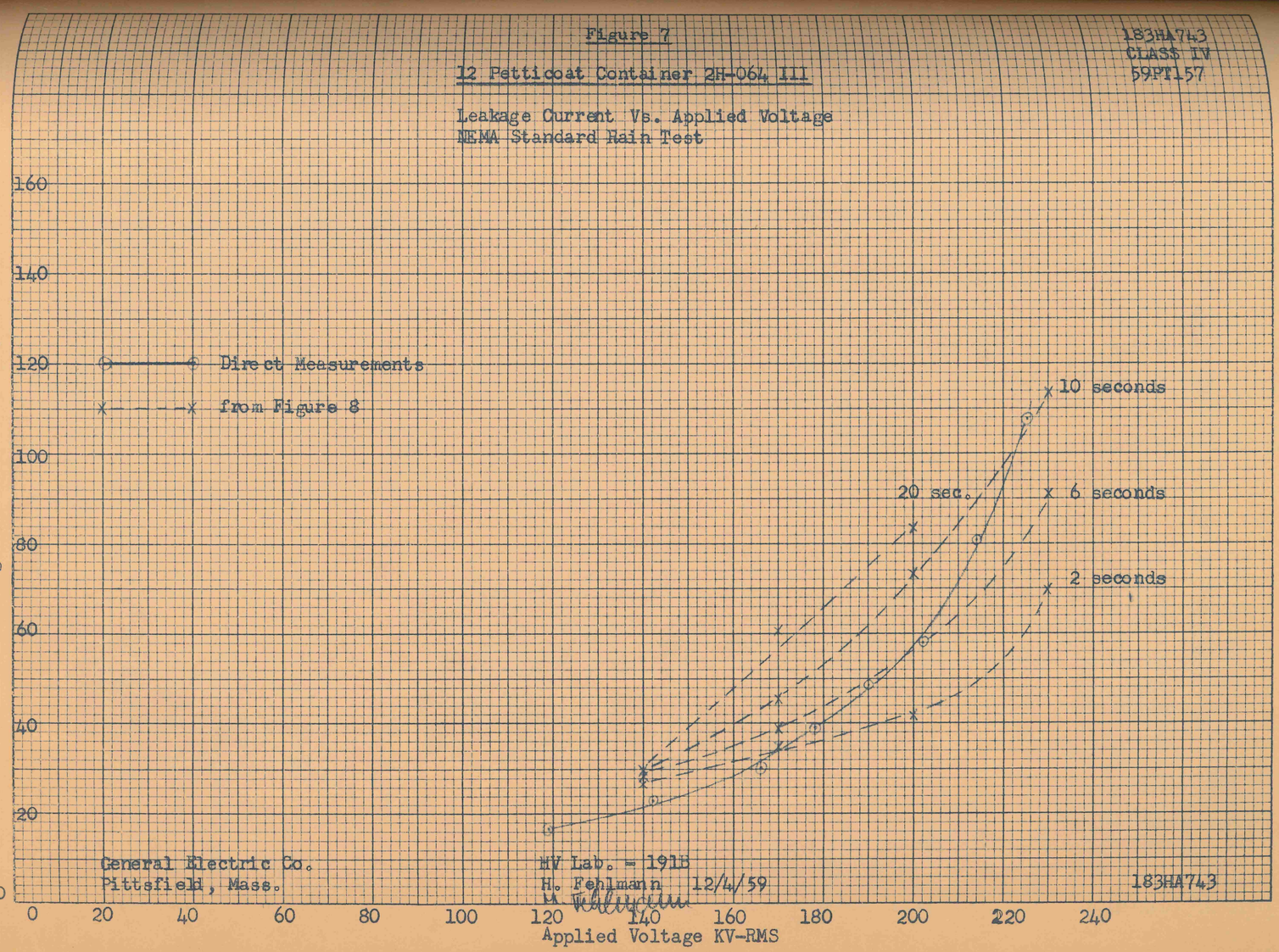

General Electric Co.
Pittsfield, Mass.

HV Lab. - 191B
H. Fehlmann 12/4/59
M. Wellington

183HA743

INDEXED 1-11-1960

Figure 8

183HA744
CLASS IV
59PT157

12 Petticoat Container 2H-064 III

Leakage Current vs. Time at Constant Voltage
NEMA Standard Rain Test

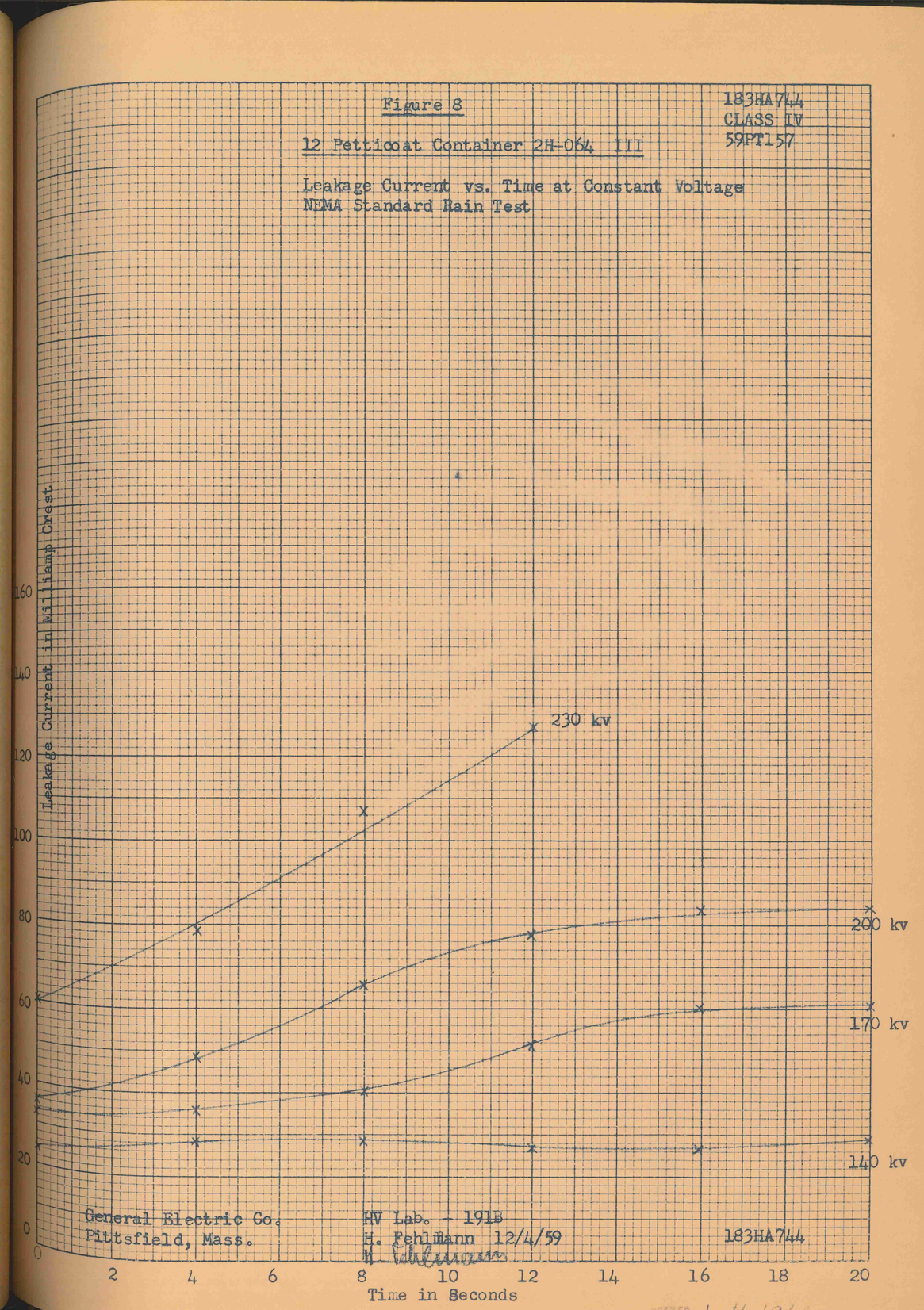

Figure 9

183HA745
CLASS IV
59PT157

Leakage Current vs. Applied Voltage

3K-066 Units
Rain Test

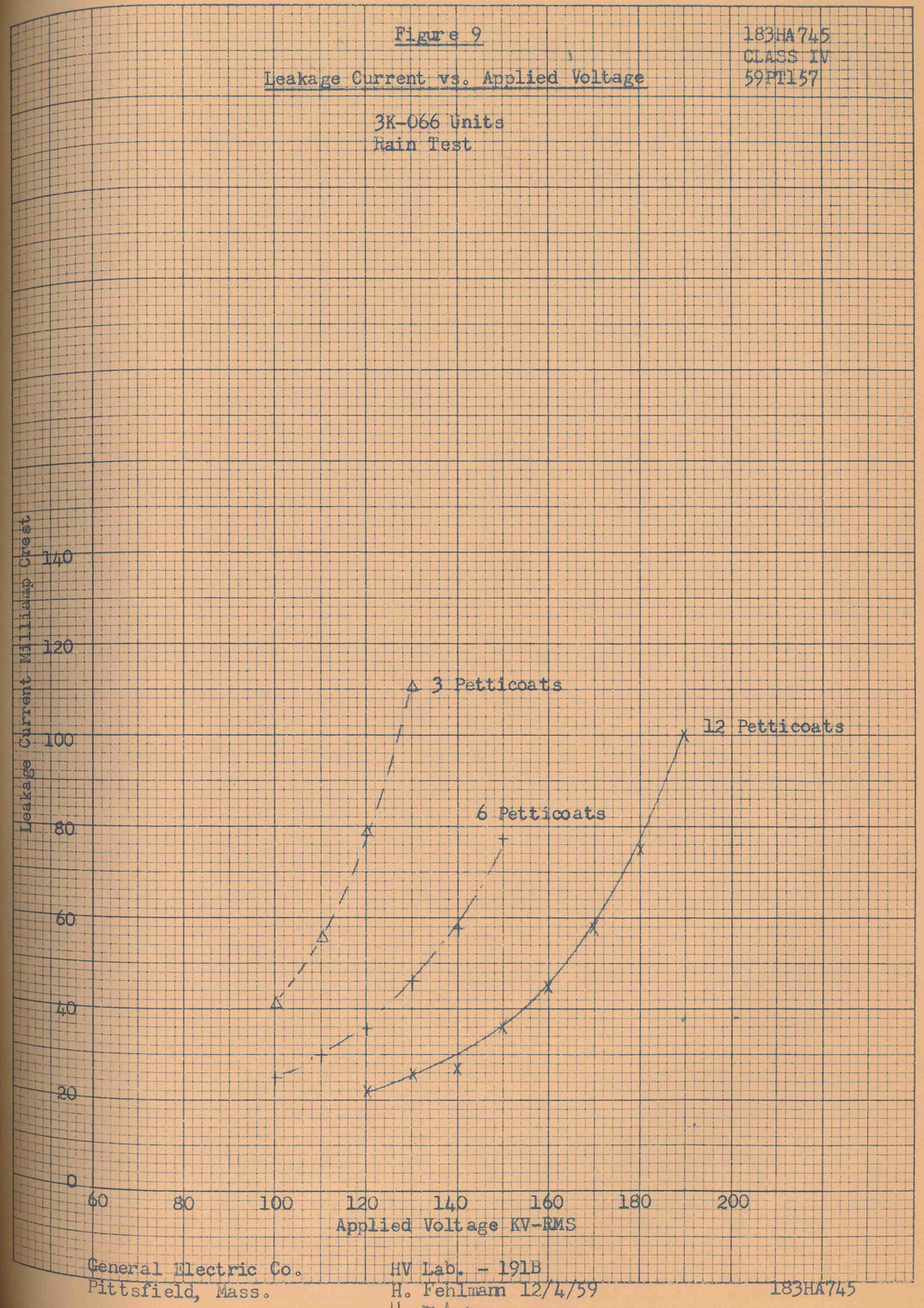

General Electric Co.
Pittsfield, Mass.

HV Lab. - 191B
H. Fehlmam 12/4/59

183HA745

H. Fehlmann

1-11-60

183HA746
CLASS IV
59PT157

Figure 10

Leakage Current vs. Applied Voltage

1H-065 Units
1H-071
Rain Test

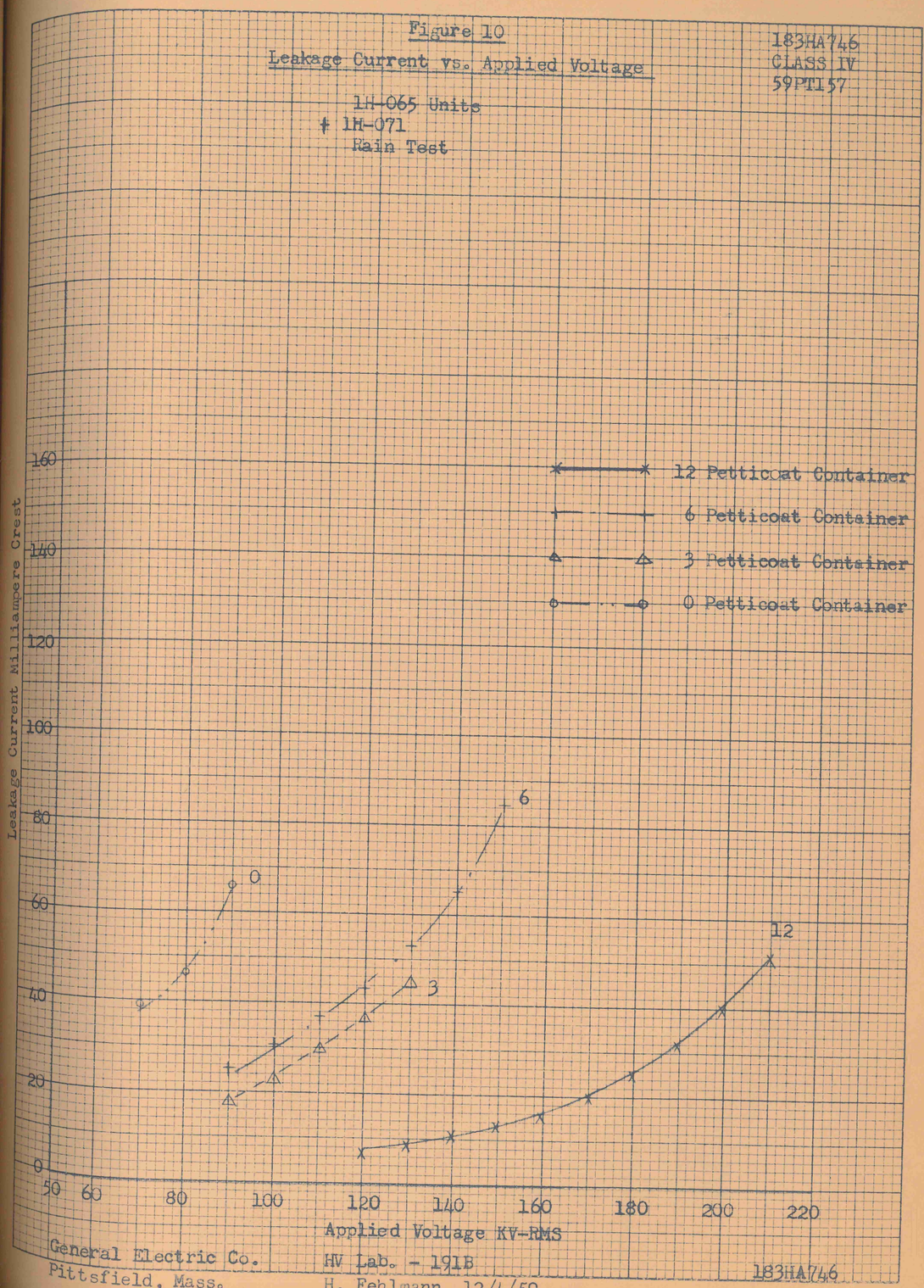

General Electric Co.
Pittsfield, Mass.

HV Lab. - 191B
H. Fehlmann 12/4/59

183HA746

Figure 11

183HA747
CLASS IV
59PT157

Leakage Current vs. Applied Voltage

2H-064 Units
Rain Test

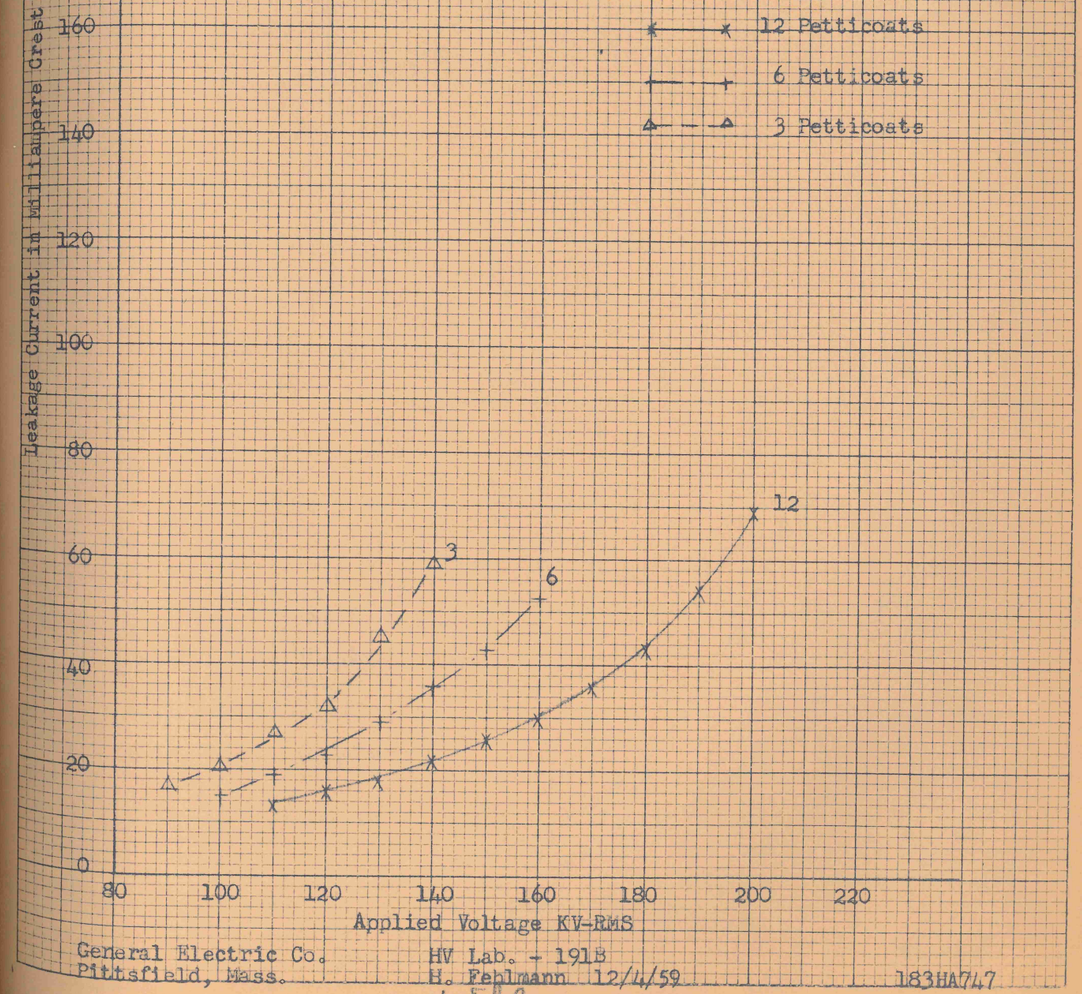

General Electric Co.
Pittsfield, Mass.

HV Lab. - 191B
H. Fehlmann 12/4/59

183HA747

H. Fehlmann

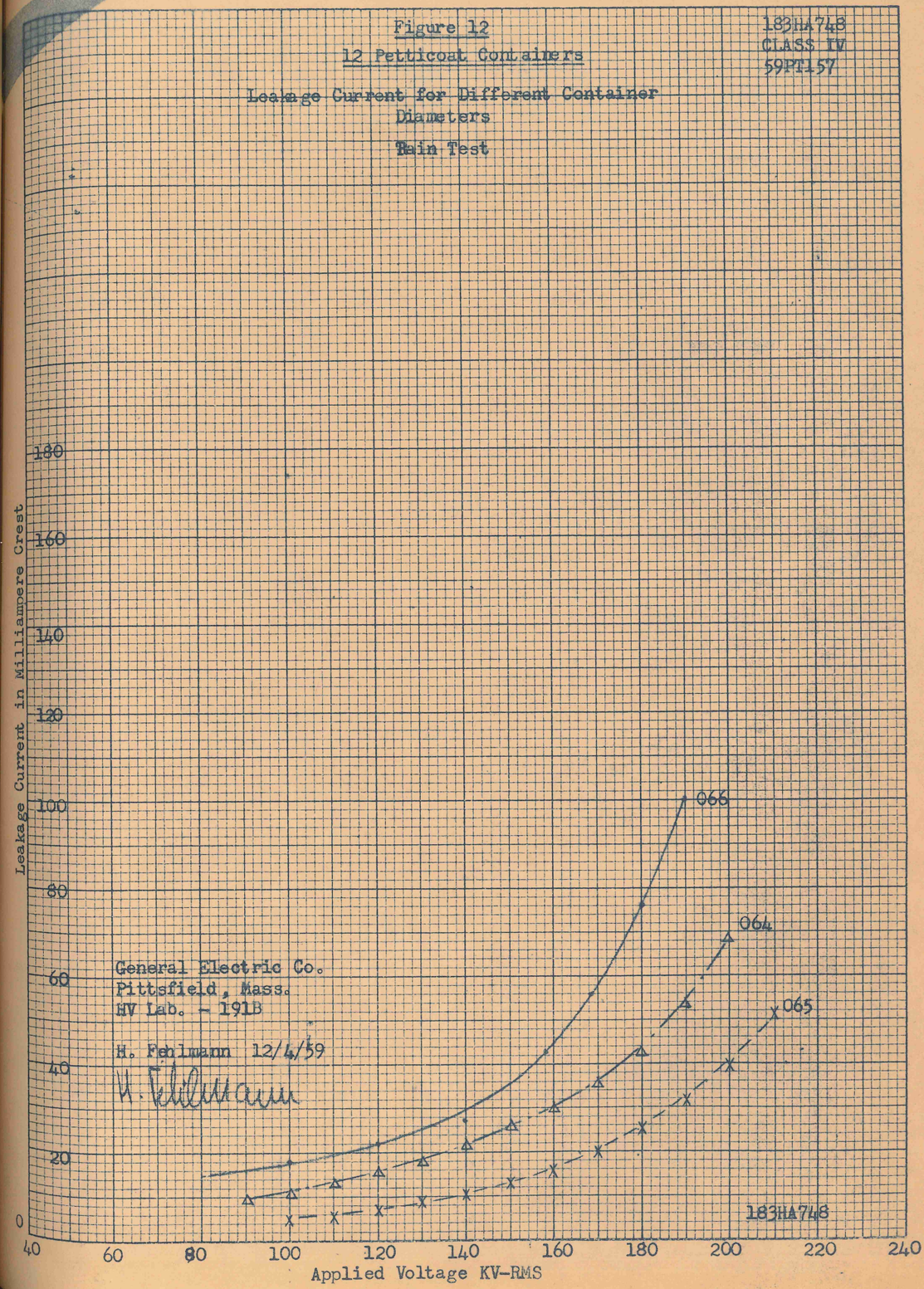

Figure 12
12 Petticoat Containers
Leakage Current for Different Container Diameters
Rain Test
183HA748
CLASS IV
59PT157
Leakage Current in Milliampere Crest
Applied Voltage KV-RMS
066
064
065
General Electric Co.
Pittsfield, Mass.
HV Lab. - 191B
H. Fehlmann 12/4/59
H. Fehlmann
183HA748

1-11-1960

183HA749
CLASS IV
59PT157

Figure 13

6 Petticoat Container

Leakage Current for Different Container Dalmeters

Rain Test

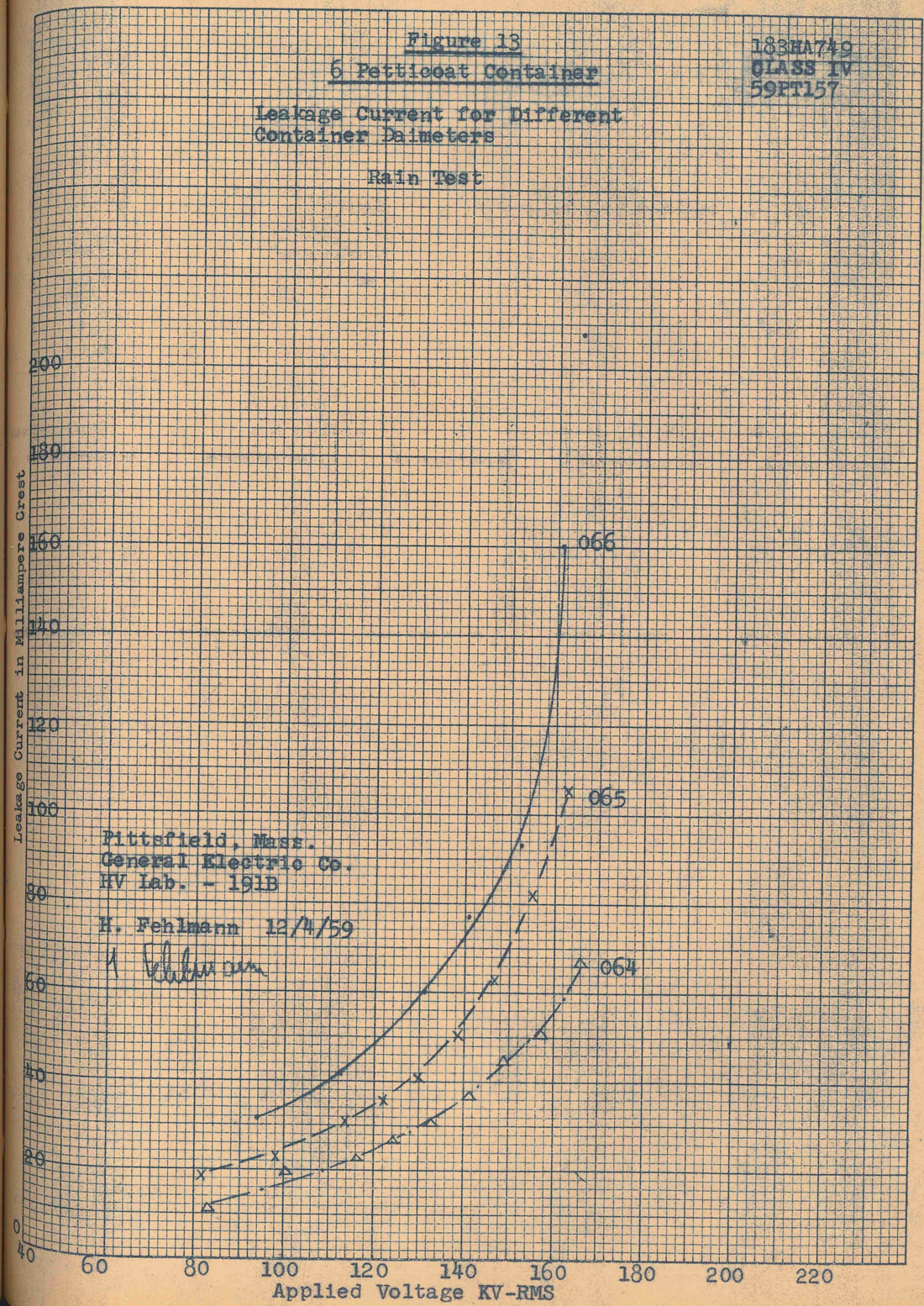

1-11-1960

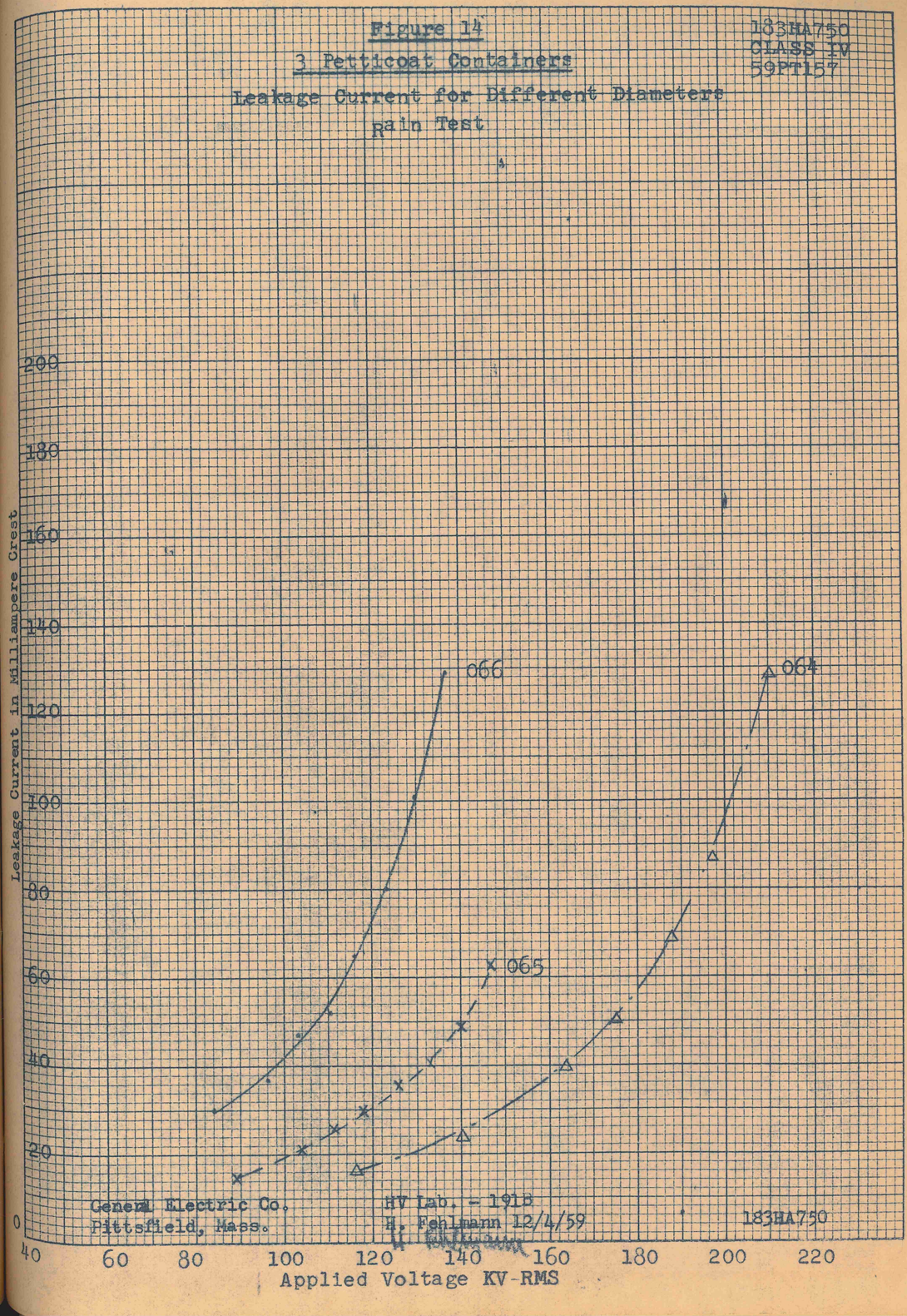
Figure 14
3 Petticoat Containers
Leakage Current for Different Diameters
Rain Test
183HA750
CLASS IV
59PT157
Leakage Current in Milliampere Crest
0
20
40
60
80
100
120
140
160
180
200
066
064
065
General Electric Co.
Pittsfield, Mass.
HV Lab. - 1918
H. Fehlmann 12/4/59
183HA750
40
60
80
100
120
140
160
180
200
220
Applied Voltage KV-RMS

1-11-1960

Figure 15

183HA751
CLASS IV
59PT157

Leakage Current vs. Applied Voltage for the 3K-12 Petticoat, the O.B., the 7785 Unit

Rain Test

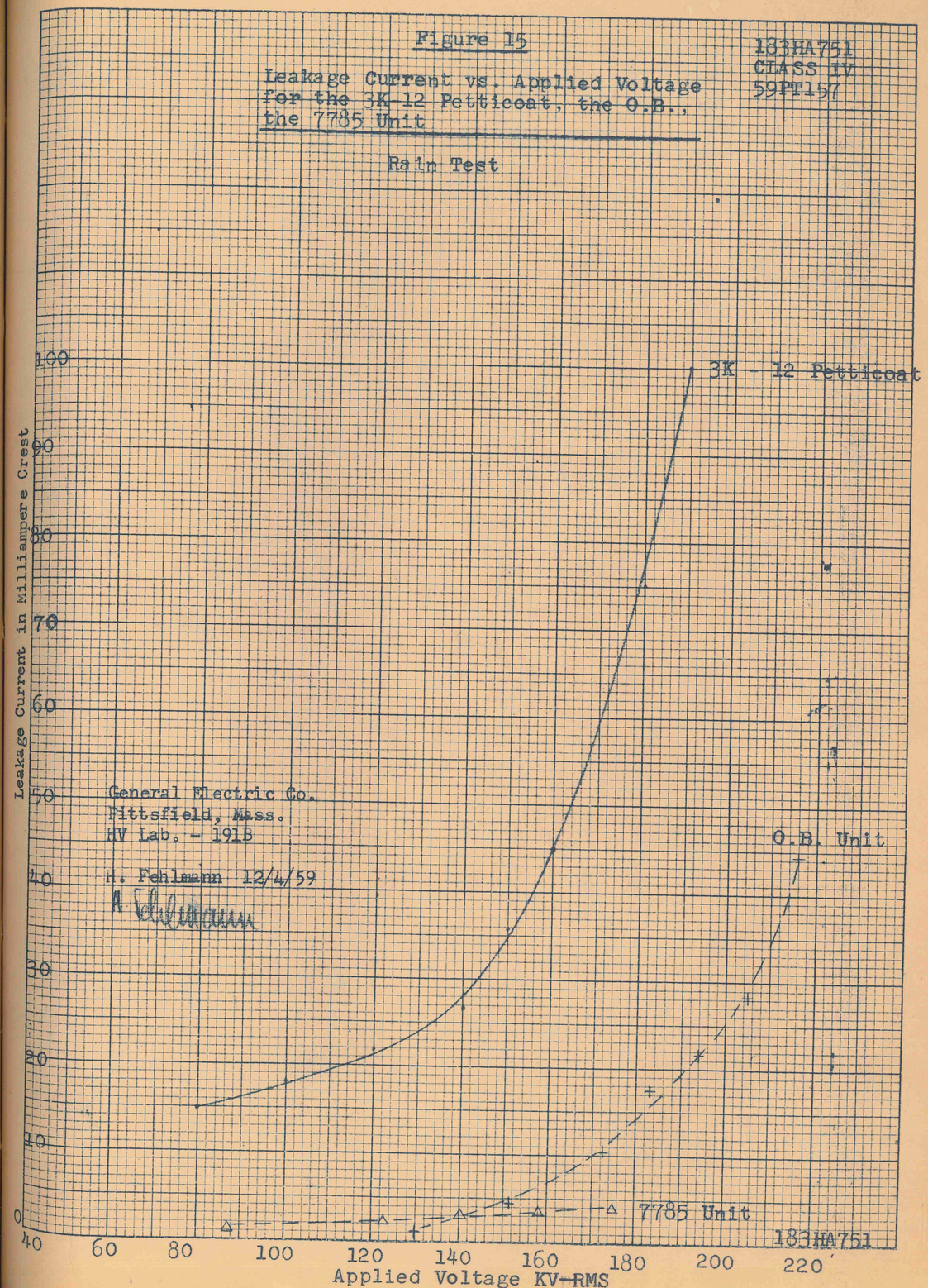

1-11-1960

Figure 16

Withstand Voltages for Spray Test

Contamination test on LA Housings

0% Salt Solution

183HA752
CLASS IV
59PT157

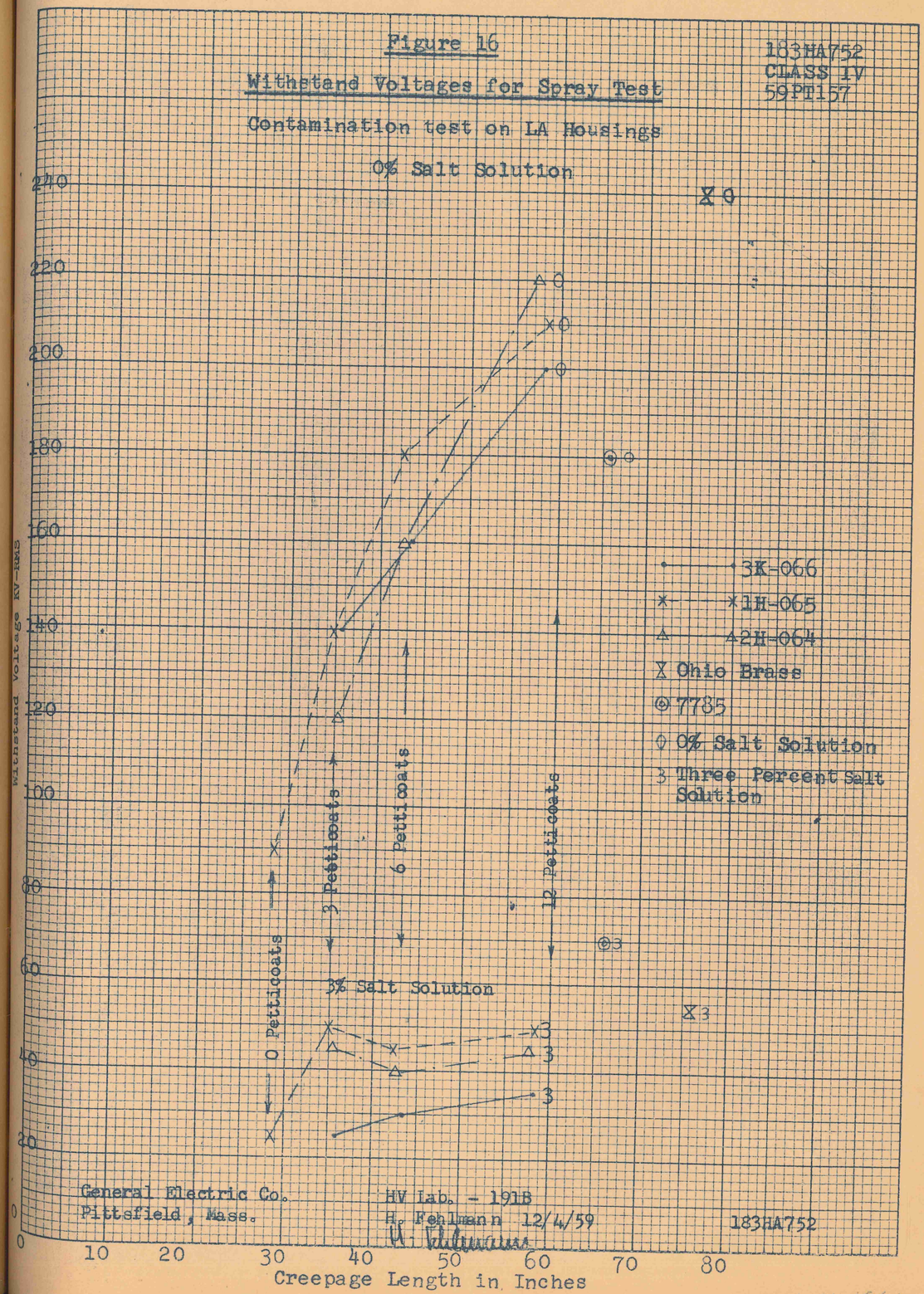

1-11-1960

Figure 17

Contamination Test on LA Housings

3 Petticoat housing 3K-066 LT.

0% Salt solution Spray

General Electric Co.
Pittsfield, Mass.

HV Lab. - 191B
H. Rehlmann 12/4/59

183A753
CLASS IV
59PT157

183A753

1-11-1960

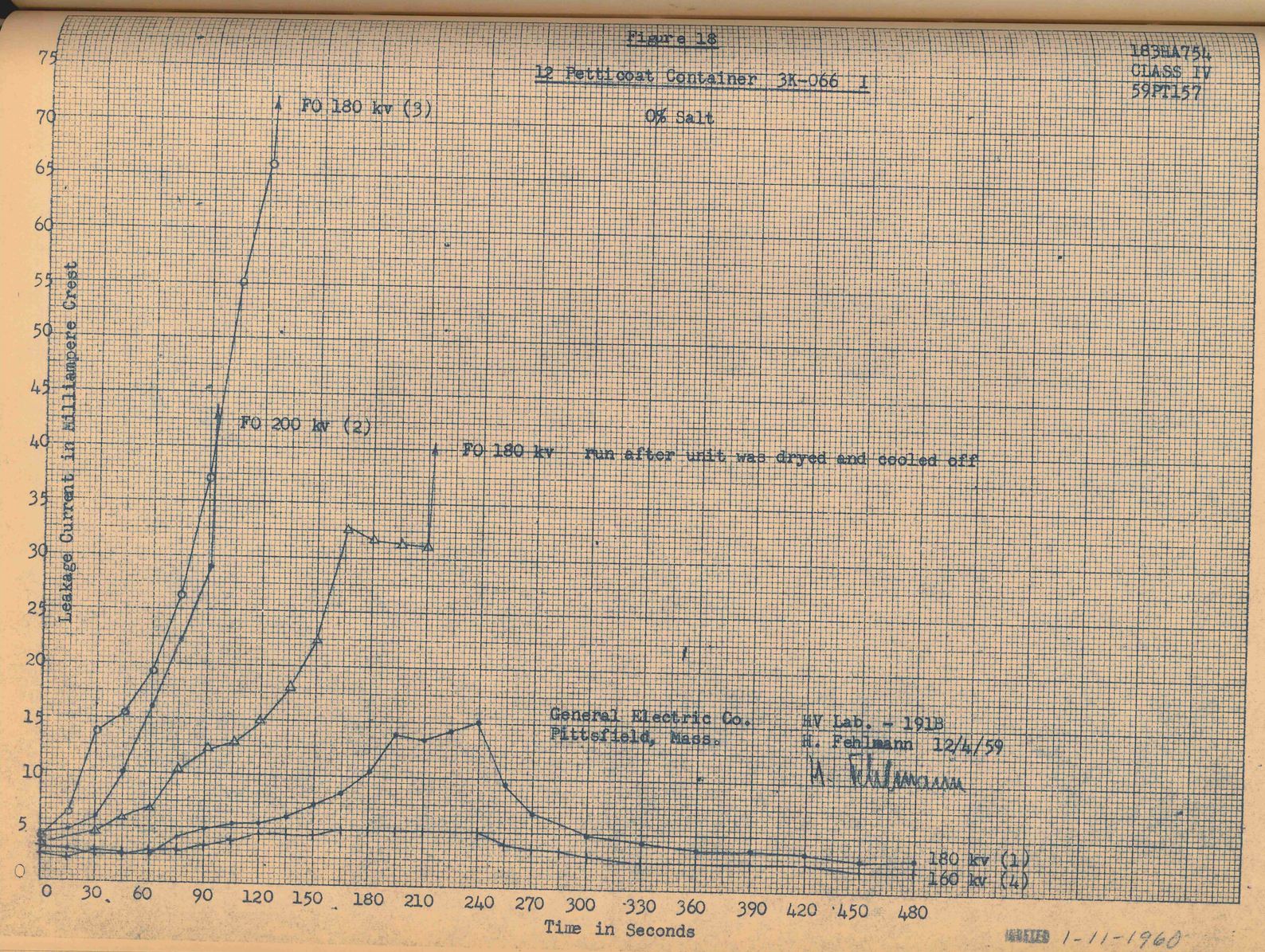
Figure 18
12 Petticoat Container 3K-066 I
0% Salt
183HA754
CLASS IV
59PT157
FO 180 kv (3)
FO 200 kv (2)
FO 180 kv run after unit was dryed and cooled off
General Electric Co.
Pittsfield, Mass.
HV Lab. - 191B
H. Fehlmann 12/4/59
H. Fehlmann
180 kv (1)
160 kv (4)
Leakage Current in Milliampere Crest
Time in Seconds
0
5
10
15
20
25
30
35
40
45
50
55
60
65
70
75
0
30
60
90
120
150
180
210
240
270
300
330
360
390
420
450
480

1-11-1960

Figure 19

183HA755
CLASS IV
59PT157

Influence of Housing Diameter on Leakage Current

0% Salt Spray

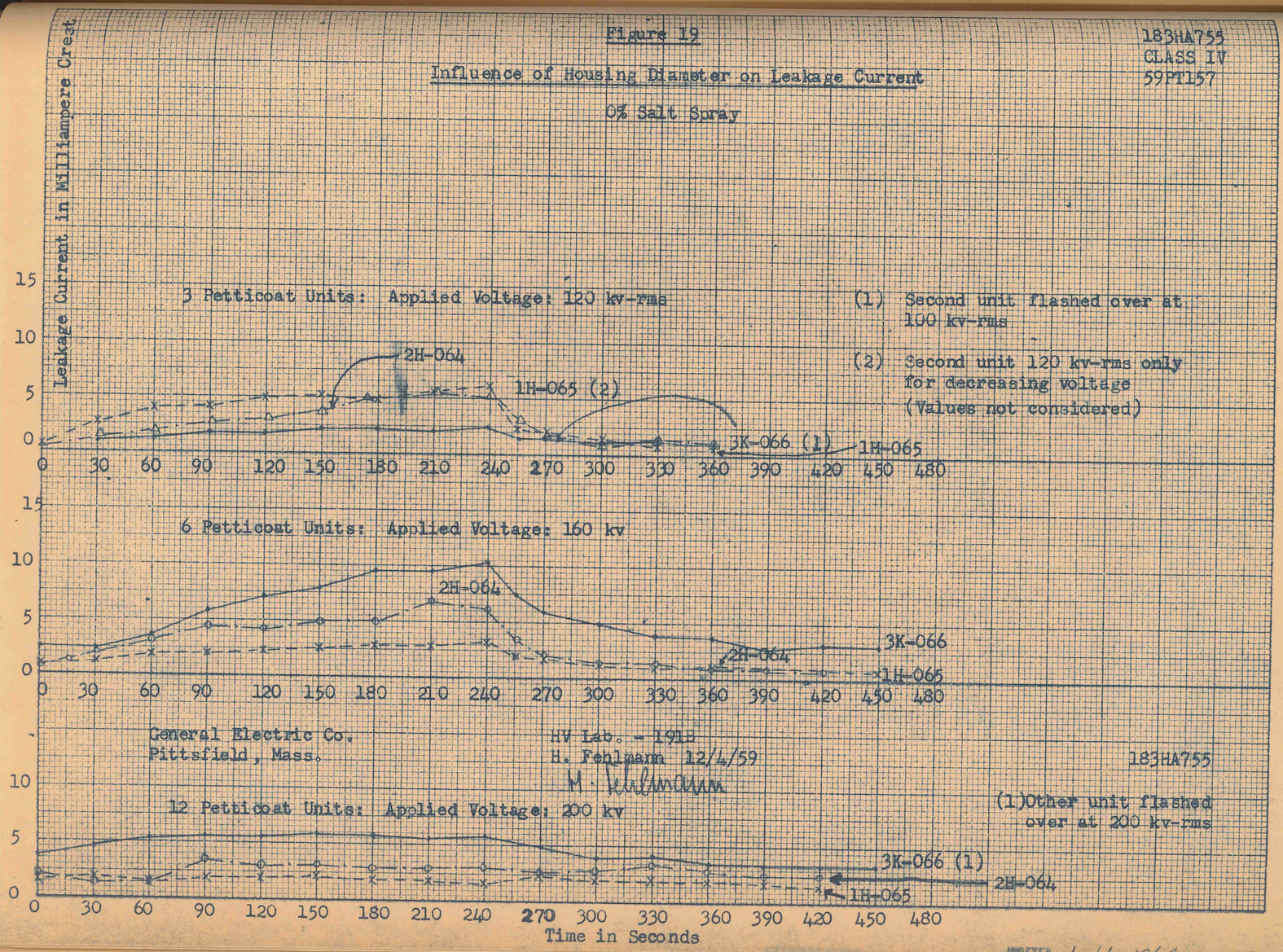

(1) Second unit flashed over at 100 kv-rms

(2) Second unit 120 kv-rms only for decreasing voltage (Values not considered)

(1) Other unit flashed over at 200 kv-rms

General Electric Co.
Pittsfield, Mass.

HV Lab. - 191B
H. Fehlmann 12/4/59
M. Fehlmann

183HA755

DRAWER 1-11-1960

Figure 20

183HA756
CLASS IV
59PT157

Leakage Current vs. Time for 3K - 12 Petticoats O.B. & 7785 Unit

0% Salt Spray

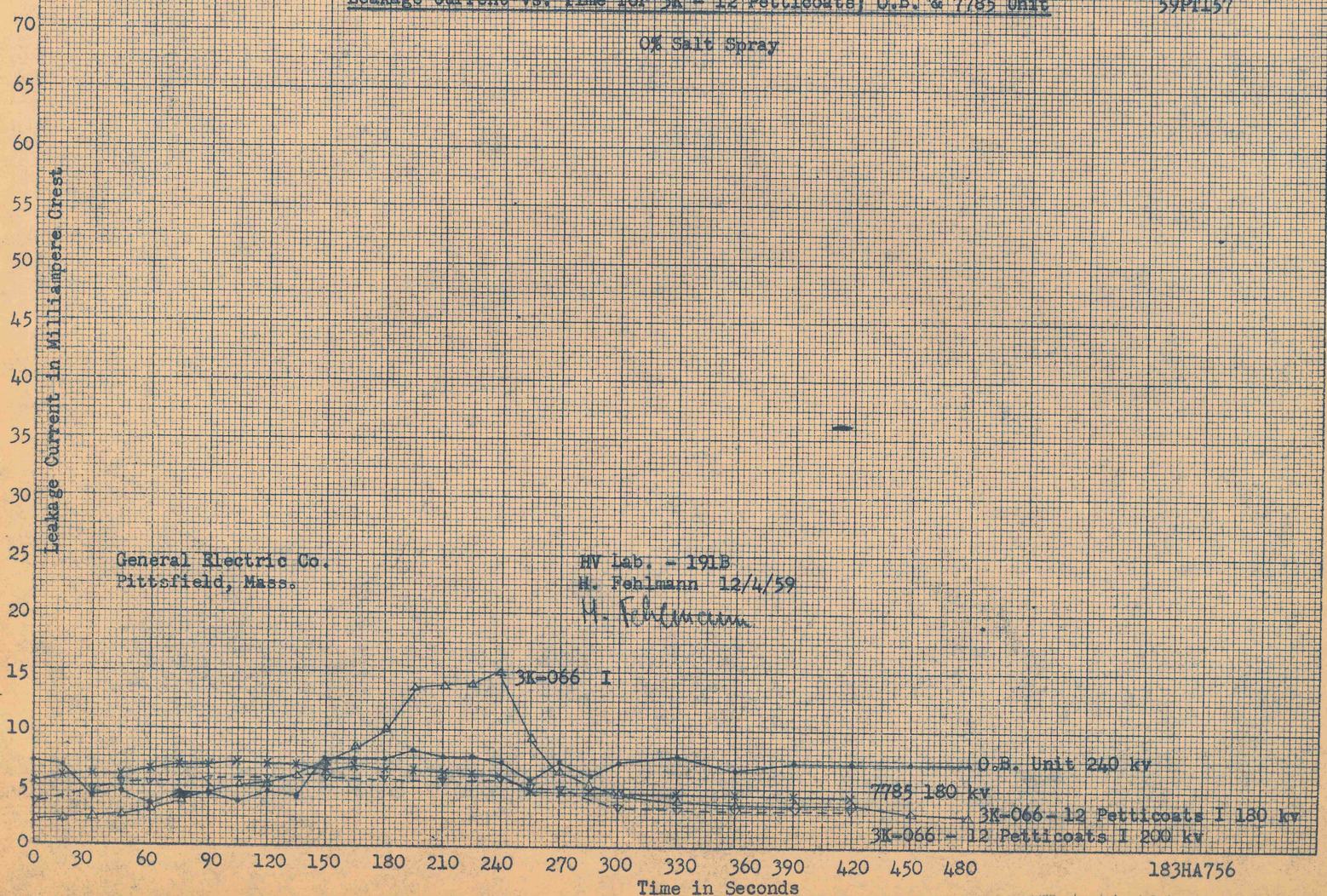

1-11-1960

183HA757
CLASS IV
59PT157

Figure 21

Withstand Voltages for Salt Spray Test

Contamination Test on LA Housings

3% and 10% Salt Solutions

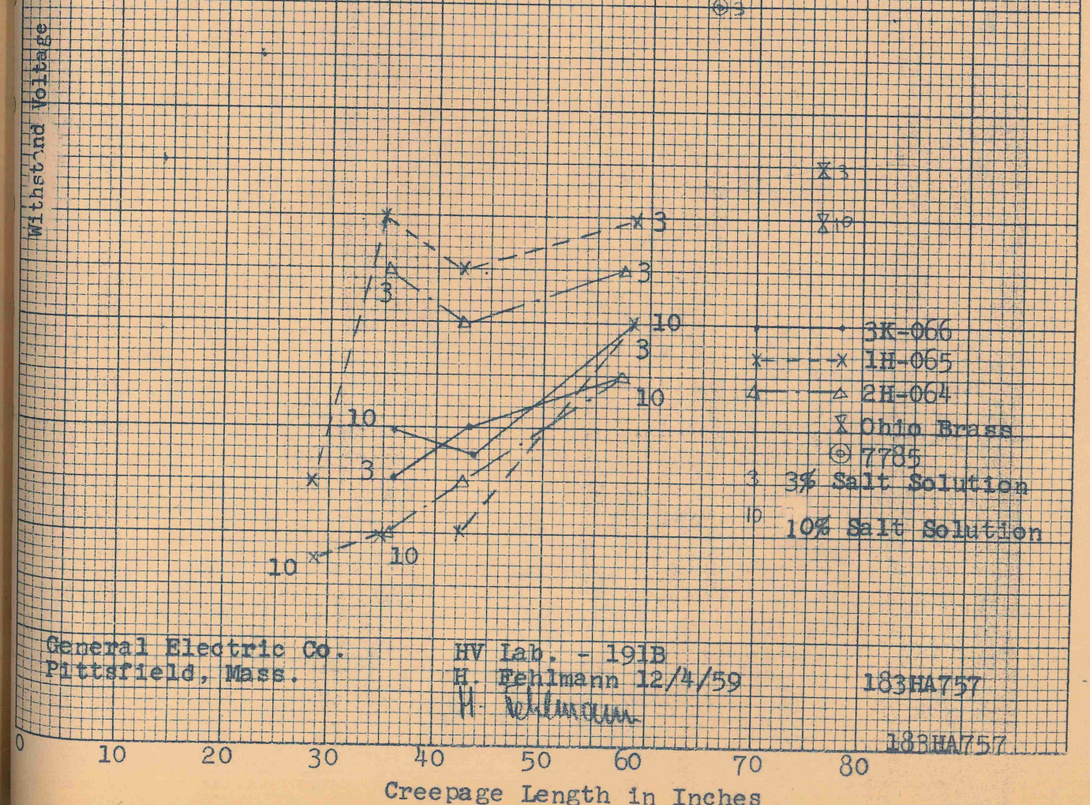

ENGR 1-11-1960

Figure 22

183HA758
CLASS IV
59PT157

Required Creepage Length to Withstand
1 KV-RMS for a 3% Salt Spray Test

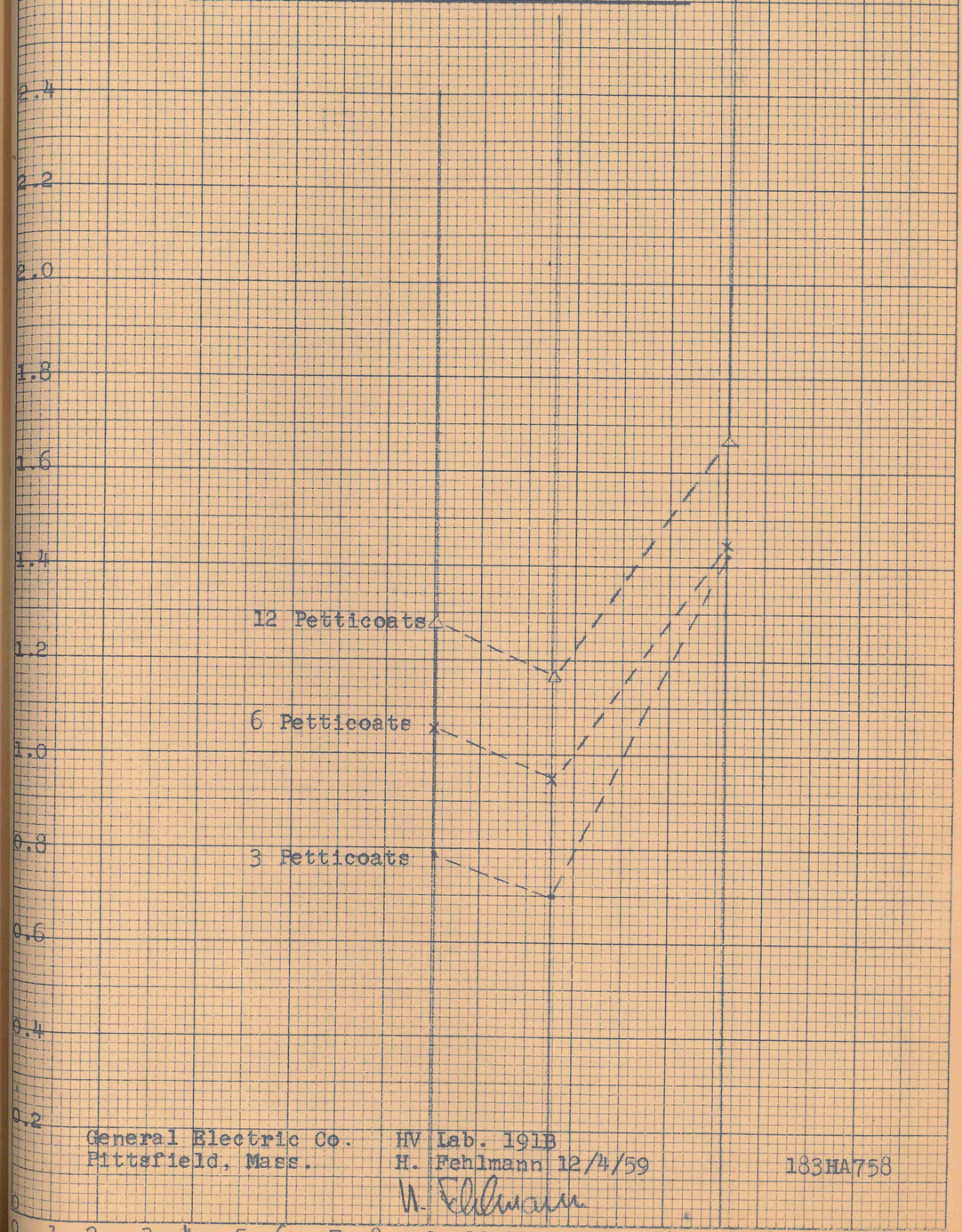

General Electric Co.
Pittsfield, Mass.

HV Lab. 191B
H. Fehlmann 12/4/59

183HA758

W. Fehlmann

1-11-196

Figure 23

183HA759
CLASS IV
59PT157

3 Petticoat Container 064 2H II

3% Salt Solution

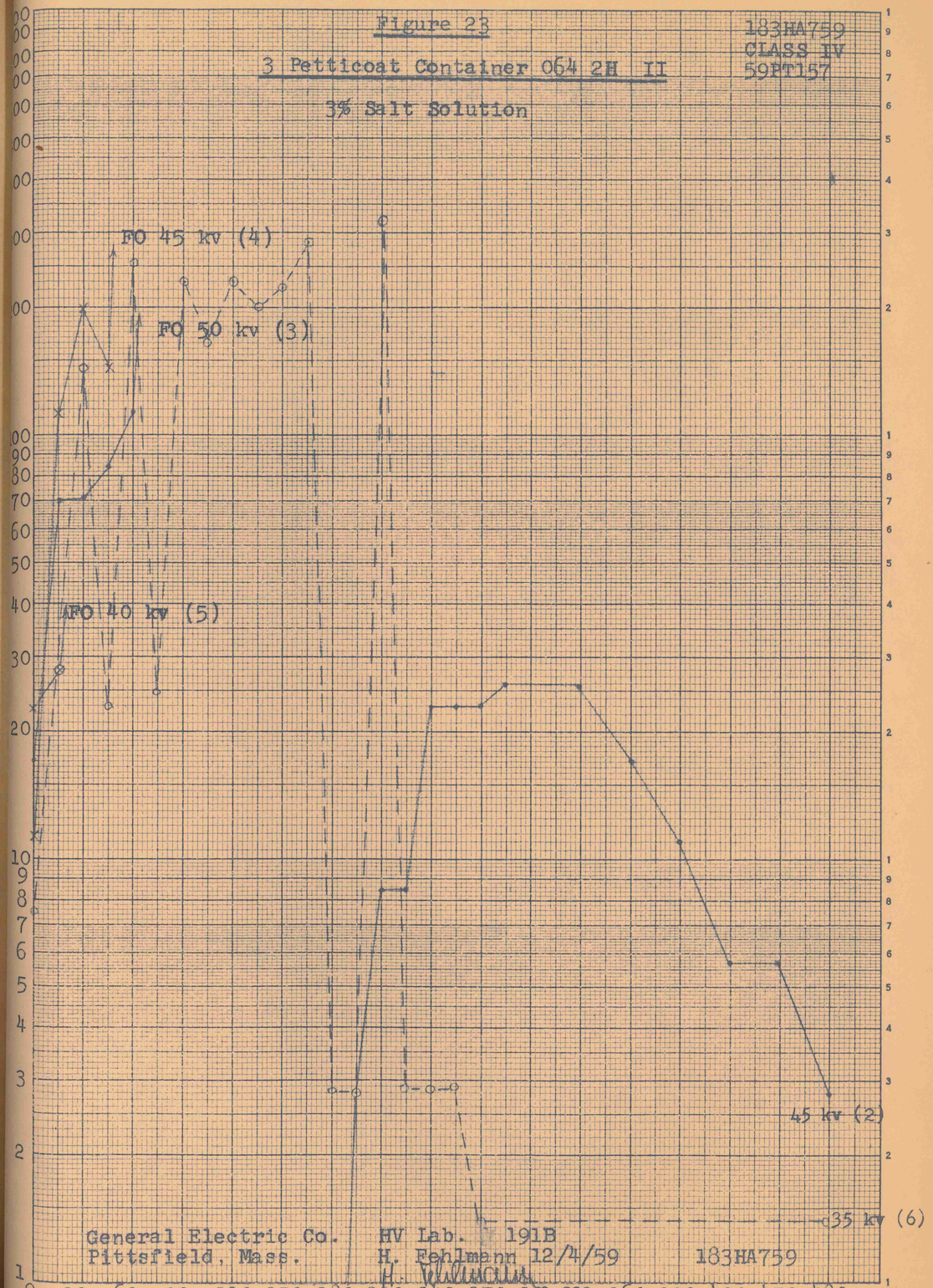

General Electric Co. HV Lab. 191B
Pittsfield, Mass. H. Fehlmann 12/4/59 183HA759
H. Fehlmann

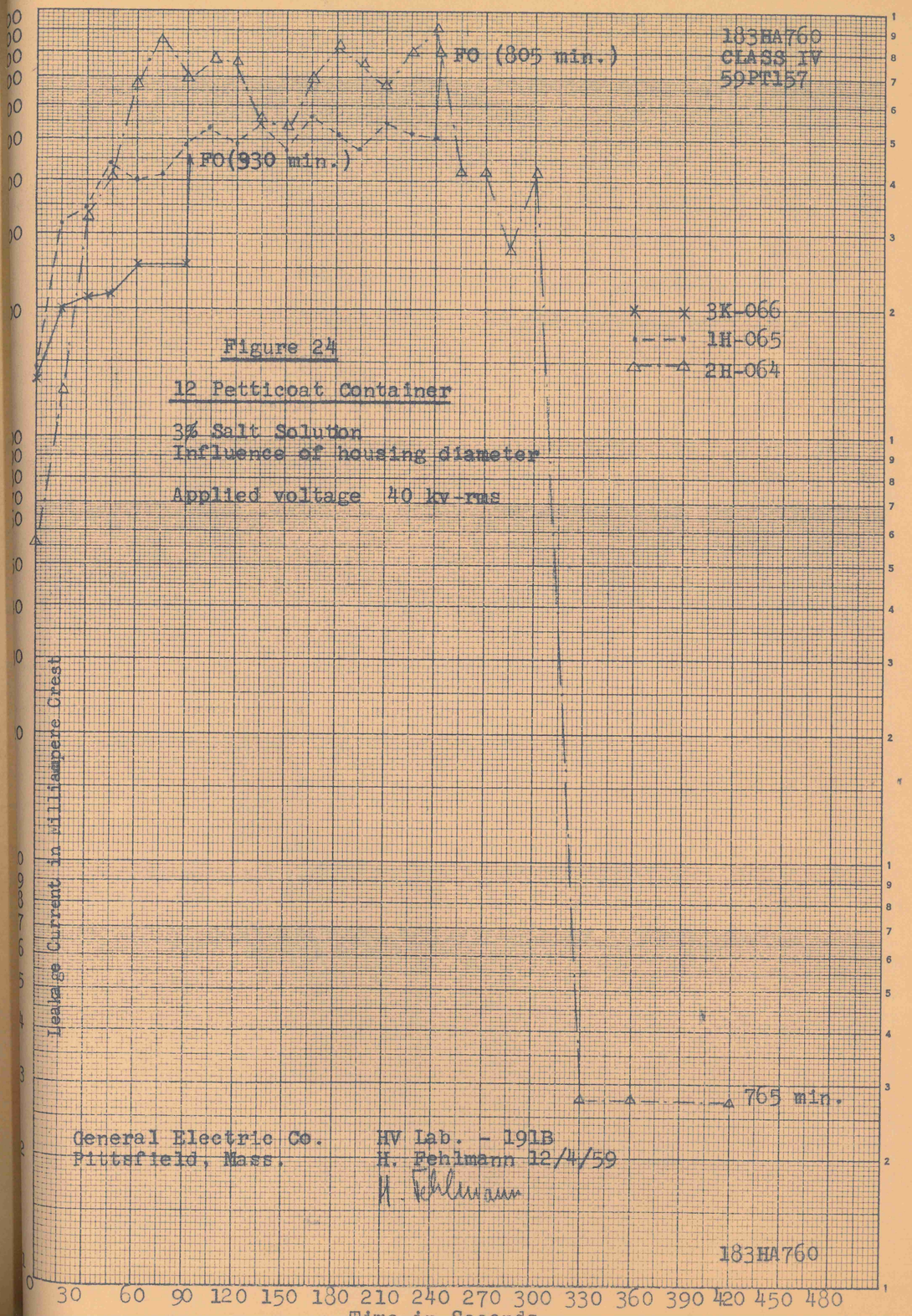

Figure 24

12 Petticoat Container

3% Salt Solution
Influence of housing diameter

Applied voltage 40 kv-rms

183HA761
CLASS IV
59PT157

FO 690 min.

Figure 25

6 Petticoat Container

3% Salt Solution

Influence of housing diameter

Applied voltage 30 kv-rms

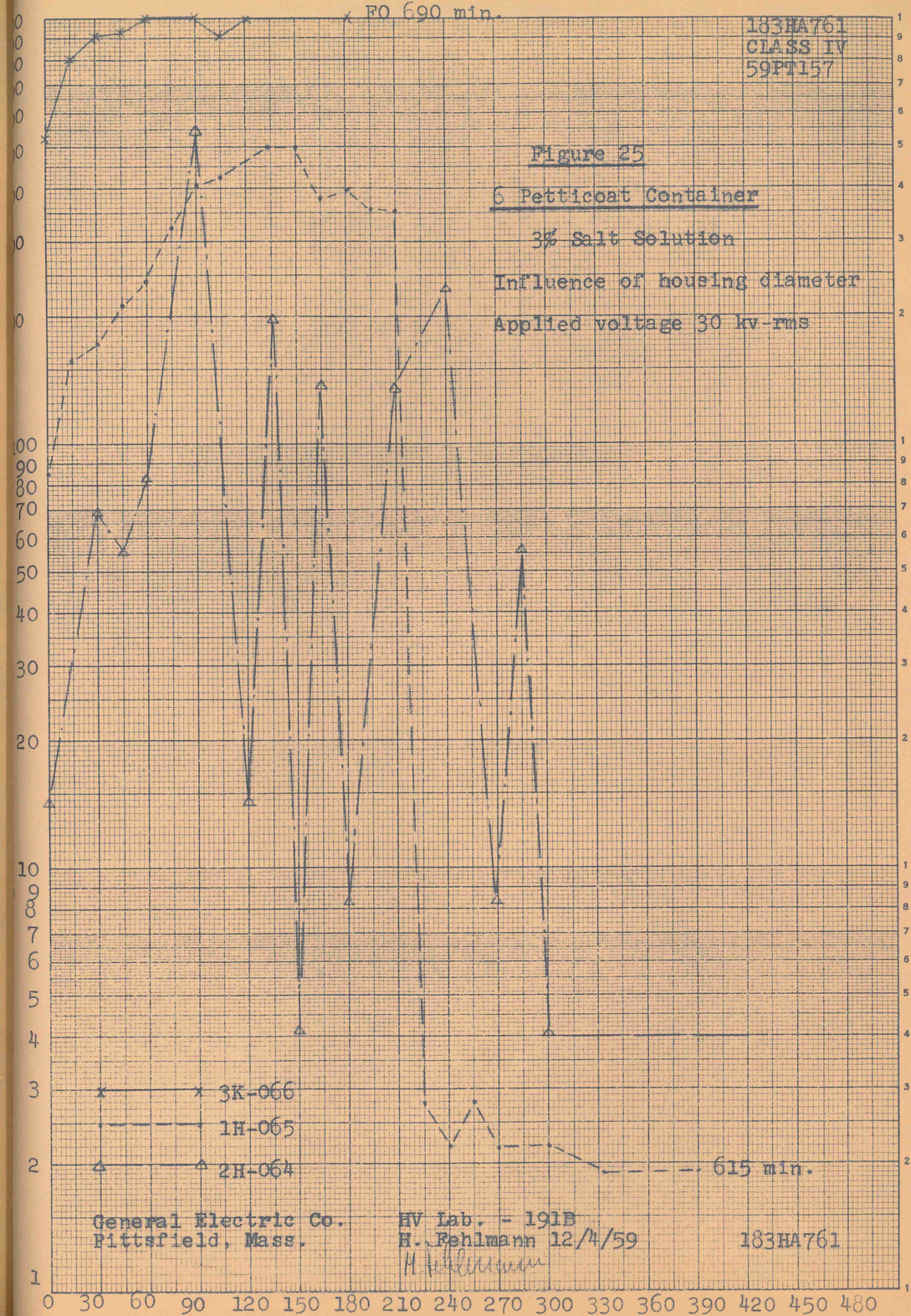

General Electric Co.
Pittsfield, Mass.

HV Lab. - 191B
H. Rehlmann 12/4/59

183HA761

Figure 26

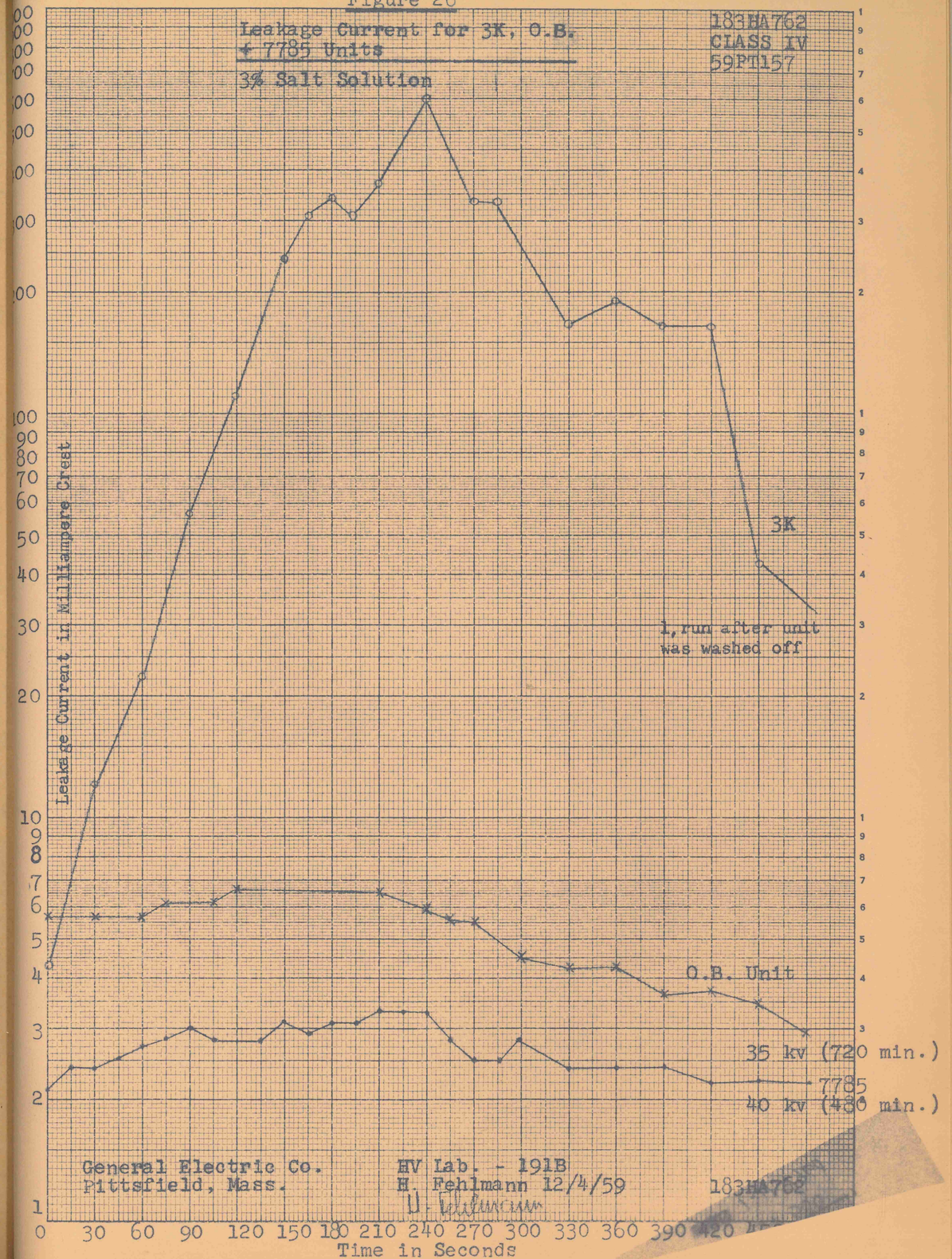
Leakage Current for 3K, O.B.
+ 7785 Units
3% Salt Solution
183HA762
CLASS IV
59PT157
Leakage Current in Milliampere Crest
Time in Seconds
3K
1 run after unit was washed off
O.B. Unit
35 kv (720 min.)
7785
40 kv (480 min.)
General Electric Co.
Pittsfield, Mass.
HV Lab. - 191B
H. Fehlmann 12/4/59
183HA762

Figure 27

183HA763
CLASS IV
59PT157

Voltage Drop of Source Due to Load

Generator 2G1

350 kv "World Fair" Transformer Turn Ratio = 76
Short circuit impedances transformer: 0.819 Ω * (51PT1851)
Generator : 1.2 Ω * 176HA566

* Values referred to primary side of transformer

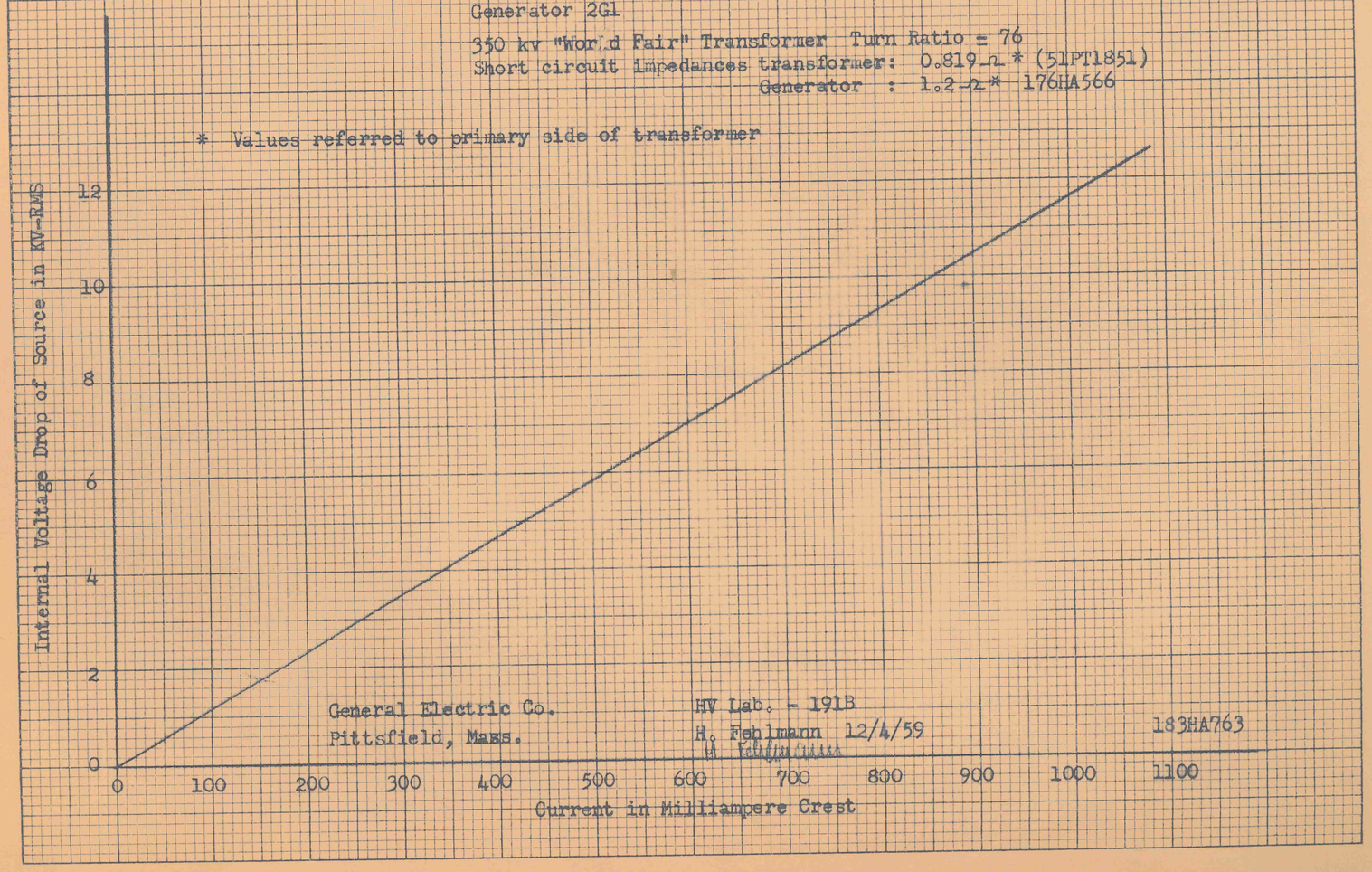

General Electric Co.
Pittsfield, Mass.

HV Lab. - 191B
H. Fehlmann 12/4/59

183HA763

REVISED 1-11-1960

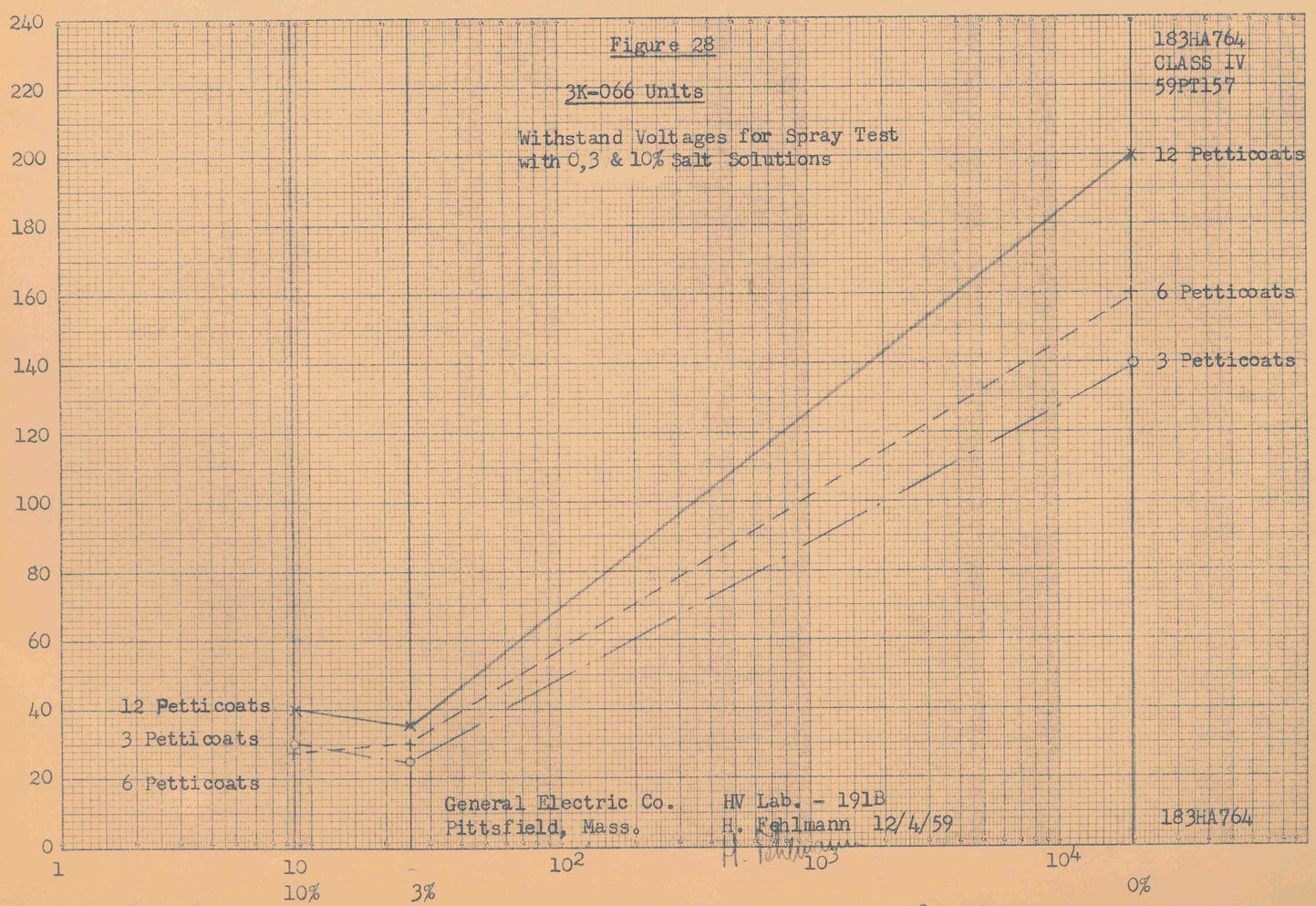
Figure 28
3K-066 Units
Withstand Voltages for Spray Test
with 0,3 & 10% Salt Solutions
183HA764
CLASS IV
59PT157
12 Petticoats
6 Petticoats
3 Petticoats
240
220
200
180
160
140
120
100
80
60
40
20
0
12 Petticoats
3 Petticoats
6 Petticoats
General Electric Co.
Pittsfield, Mass.
HV Lab. - 191B
H. Fehlmann 12/4/59
183HA764
1
10
10^2
10^3
10^4
10%
3%
0%
Resistivity of Salt Solution in Ohms x CM (Ω cm)

183HA765
CLASS IV
59PT157

Figure 29

1H-065 Units

Withstand Voltages for Spray Test
with 0, 3 & 10% Salt Solutions

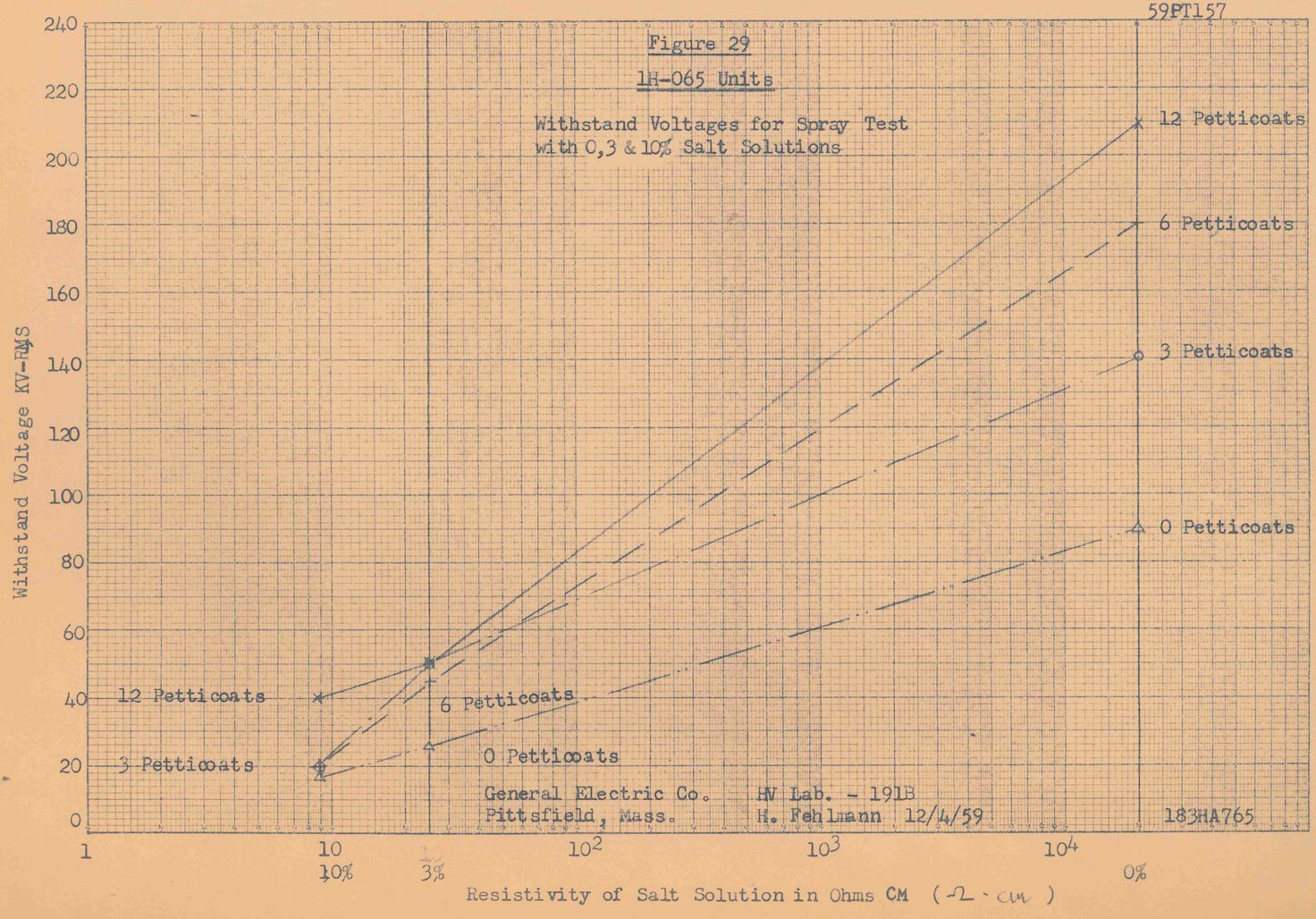

183HA766
CLASS IV
59PT157

Figure 30
2H - 064 Units

Withstand Voltages for 0,3 & 10% Spray Tests

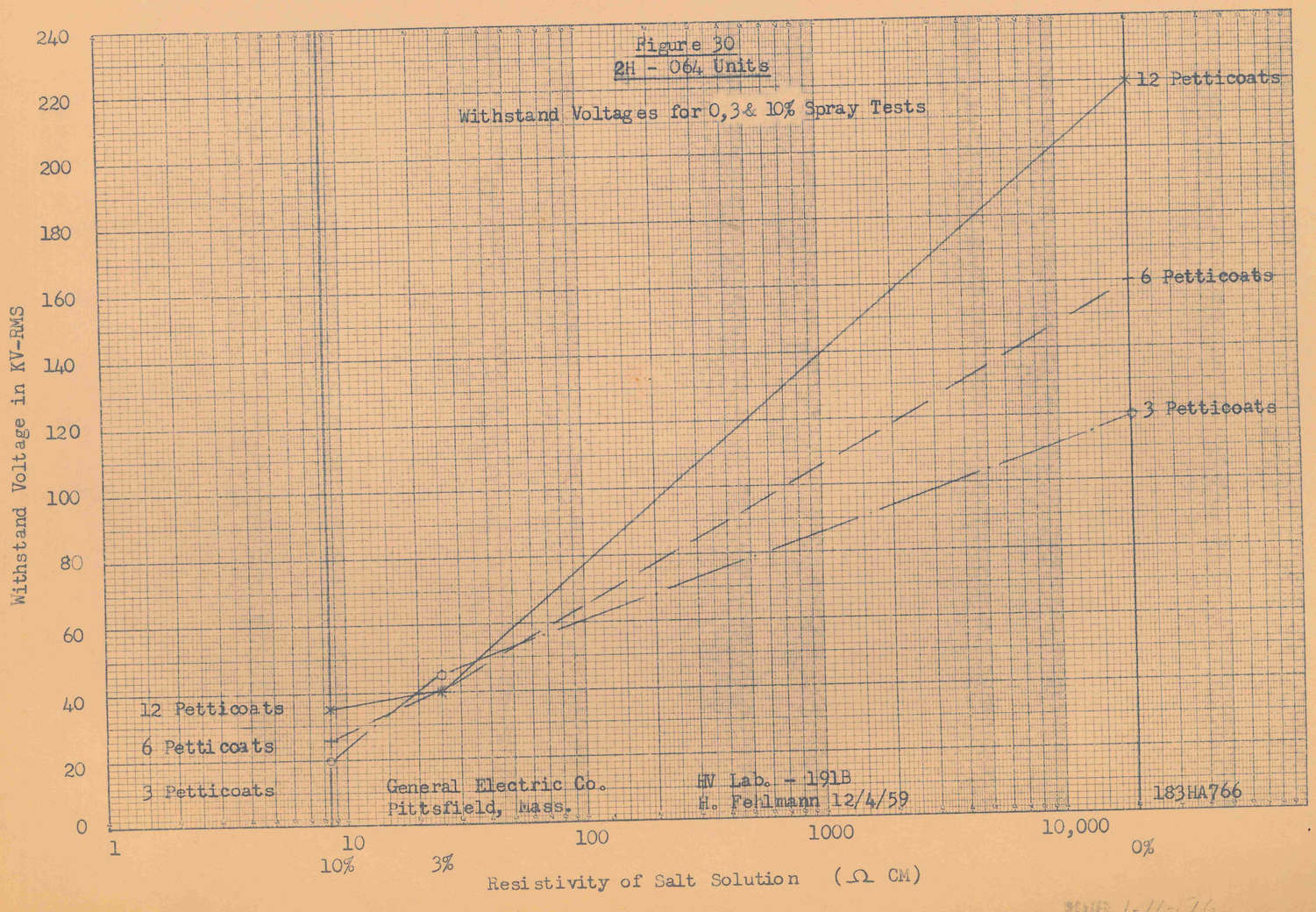

SCALE 1-11-176

183HA767
CLASS IV
59PT157

Figure 31

Ohio Brass and 7785 Unit

Withstand Voltages for Spray Test with
0,3 & 10% Salt Solutions

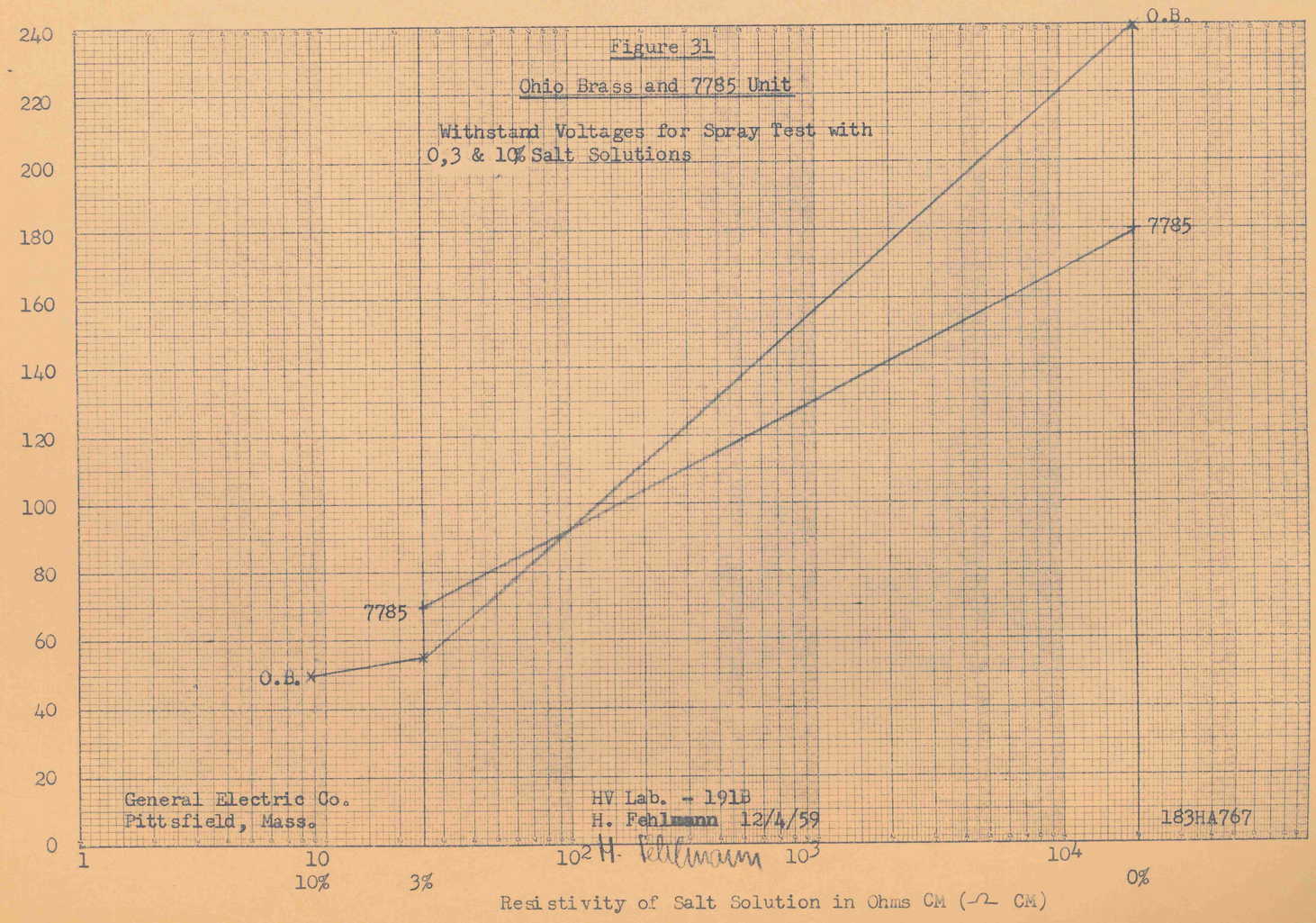

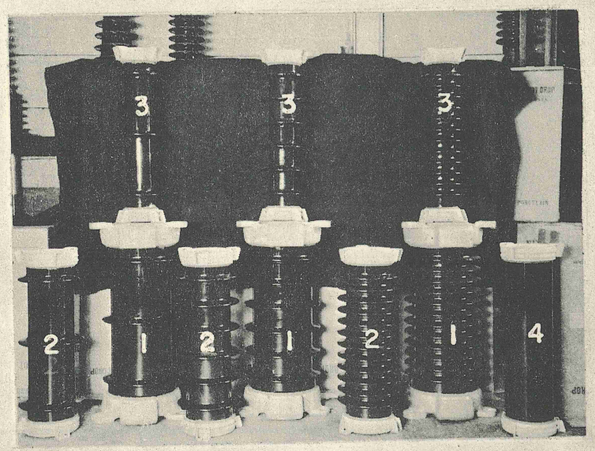

Figure 32

Lightning Arrester Housings

1	3K-060 units, OD over petticoats	15 3/8"
2	1H-065 units, OD over petticoats	11 5/8"
3	2H-064 units, OD over petticoats	9 1/16"
4	071 no petticoat unit	

59PT157
CLASS IV

PL-123886

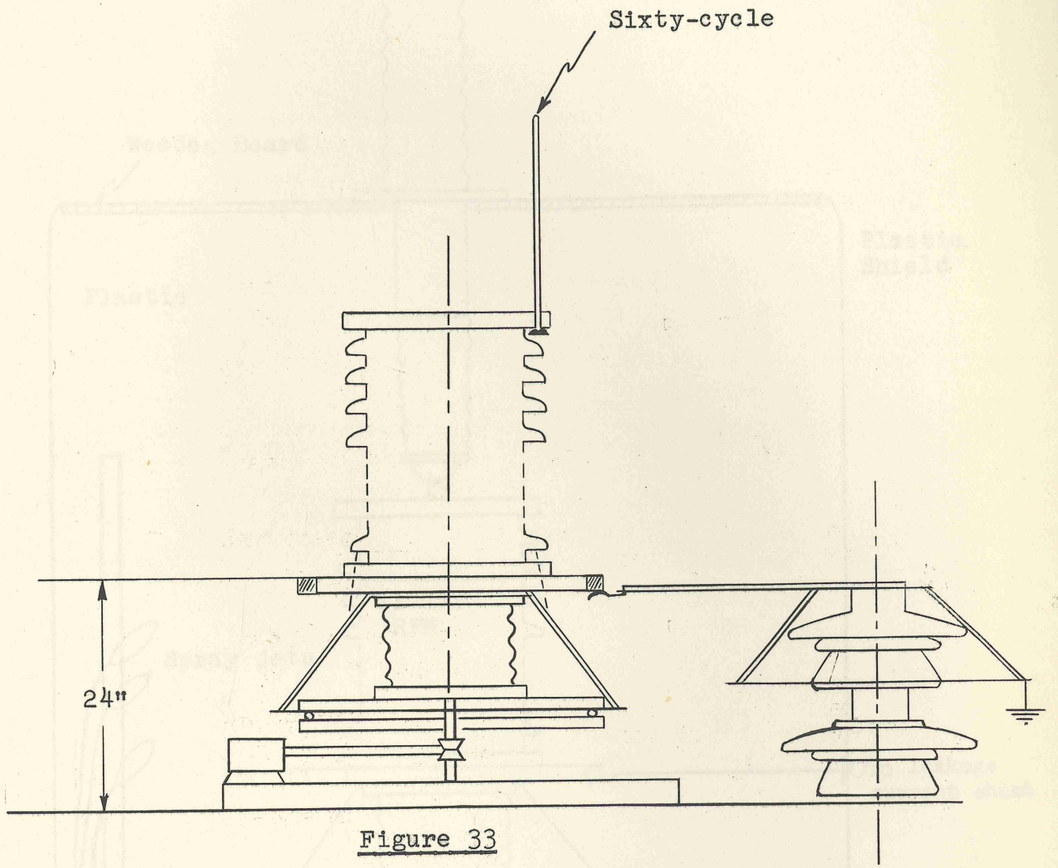

Figure 33

Lightning Arrester housing mounted on turn table.
Test setup for dry and wet NEMA Standard flashover and withstand tests.

No turn table movements.

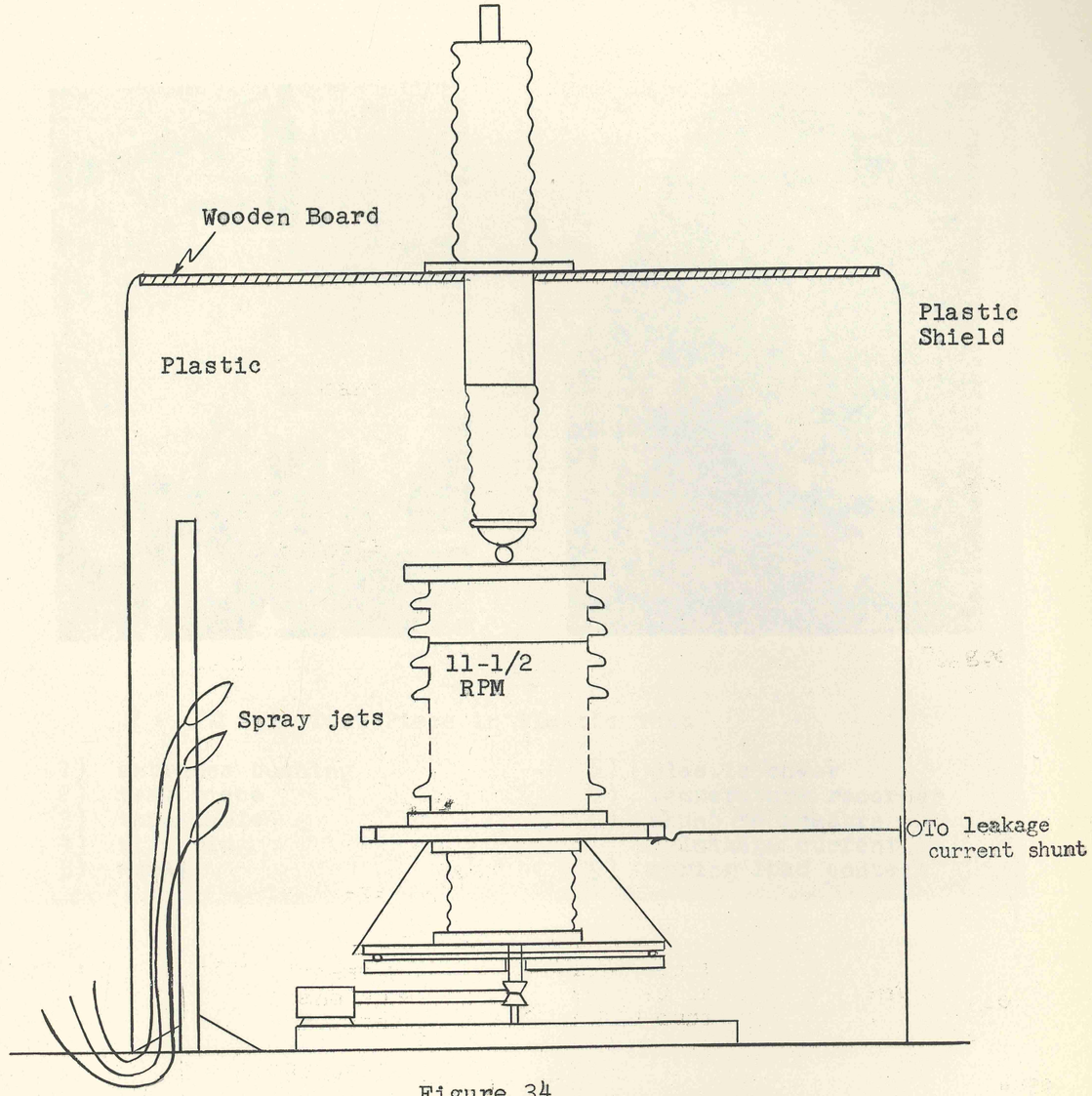

Figure 34

Lightning Arrester housing mounted on turn table.
Test piece and spray device enclosed in plastic tent.
Turn table rotated with 11-1/2 RPM during testing.

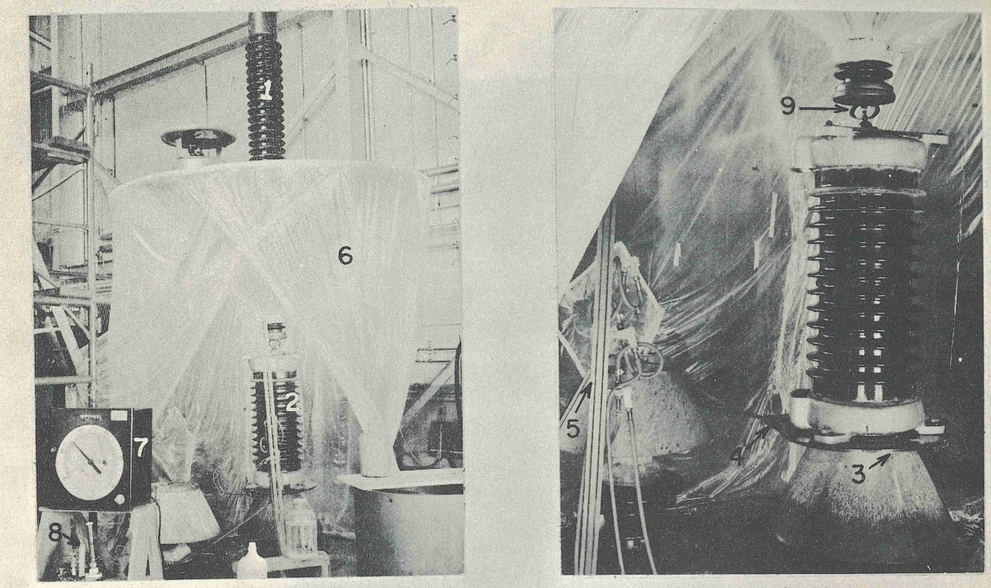

Figure 35

Test Piece in Plastic Tent

1) entrance bushing
2) test piece
3) turn table
4) slip ring
5) spray
6) plastic cover
7) temperature recorder
8) shunt to measure leakage current
9) spring load contact

59PT157
CLASS IV

PL-123887

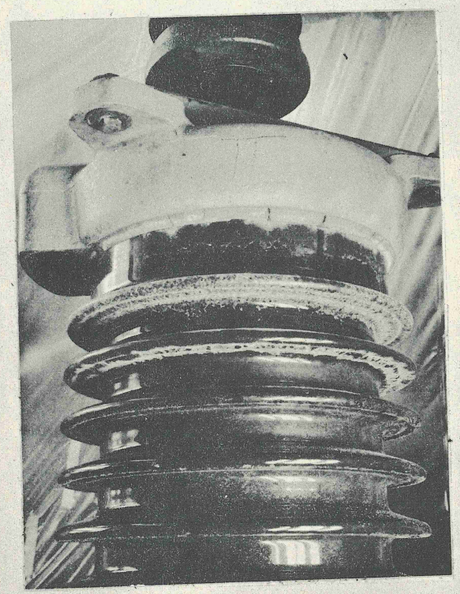

Figure 36

Salt Contaminated 3K-066
12 Petticoat Lightning
Arrester Housing

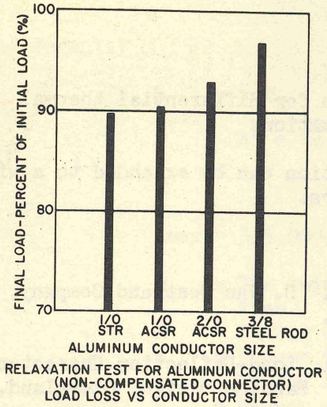

Fig. 1. Relaxation test for aluminum conductor (non-compensated connector)

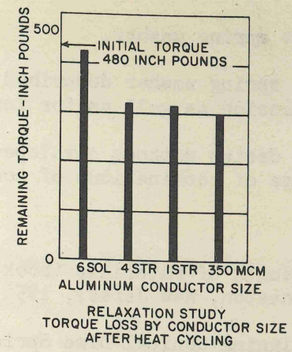

Fig. 2. Torque loss by conductor size after heat cycling

Fig. 3. Relaxation test for aluminum conductor (compensated connector)

Fig. 4. Relaxation compensating washer

Relaxation compensating

Fig. 6. Relaxation compensated connector

Mechanics
RECEIVED
AUG 15 1961
G. M. BOYD

Conference Paper

RECEIVED
AUG 8 1961
H. A. EREY

ALUMINUM COLD FLOW COMPENSATION IN BOLTED ELECTRICAL CONNECTIONS

G. L. Flynn
Nonmember AIEE

T. L. Rundlett
Member AIEE

Both of:
Anderson Electric Corp.
Birmingham, Ala.

A paper recommended by the AIEE Transmission and Distribution Committee for presentation at the AIEE Pacific General Meeting, Salt Lake City, Utah, August 23-25, 1961. Manuscript submitted May 25, 1961; made available for printing June 23, 1961.

Price: $ .50 To Members
$1.00 To Nonmembers

(5¢ per copy additional if first class mailing desired)

All Rights Reserved by the
American Institute of Electrical Engineers
33 West 39th Street, New York 18, N. Y.
Litho in USA

Paper No. CP
61-940

ALUMINUM COLD FLOW COMPENSATION IN BOLTED ELECTRICAL CONNECTIONS

G. L. Flynn T. L. Rundlett

The advent of aluminum conductor in the electric utility field for use in transmission and distribution systems brought with it many advantages, but also several problems. The problem most acute to the electrical connector manufacturer is the dimensional change, called relaxation, that occurs in all connections involving aluminum conductor. Specifically, it is caused by the uncontrolled cold flowing of the aluminum conductor when under the influence of connector pressure. Although this dimensional change is so minute as to be difficult to observe, it may be sufficient to cause the loss of good electrical contact areas, thereby causing high resistance points that shorten the life of the connection.

It is the purpose of this paper to present the results of an investigation conducted to determine ways and means to satisfactorily obviate the relaxation deterioration in bolted connections for aluminum conductors. As a result of the investigation, a new design principle evolved which can provide users who prefer bolted aluminum connectors a design which adjusts for relaxation and maintains satisfactory electrical contact for an indefinitely long service period.

DISCUSSION

For years the bolted aluminum cast connector was the primary clamping component for making aluminum to aluminum or aluminum to copper connection. The bolts used in these connectors were usually either steel or aluminum.

At first, aluminum hardware was preferred because of its anti-corrosion properties and because it had the same coefficient of thermal expansion as the cast connector. This latter factor purported to permit uniform expansion and contraction of the connection when it was subjected to thermal ratchetting during operation. However, the cost savings to be realized led to increasing adoption of galvanized steel bolts in the more common connector types, particularly for distribution line applications. In-service electrical performance at first seemed generally comparable to connectors with aluminum bolts.

The use of steel bolts probably aggravated the effects of thermal ratchetting. Since the modulus of elasticity of the steel is about three times that of aluminum, the steel bolt was stiffer. It did not elongate or creep under load as much, and, therefore, exerted greater pressure throughout the connection. Further, since the coefficient of thermal expansion of steel is much less than that of aluminum, additional pressure on the conductor was produced when the connection was thermally cycled.

The problem of relaxation in bolted aluminum distribution connections reached such a point several years ago that various Utility companies began looking for alternate connection methods. Some felt the answer was a compression connector, extruded from a ductile aluminum alloy. These connectors were very soft in comparison to their cast contemporaries. Being boltless, they were joined to conductors with special compression tools whose crimping dies deformed the connector material around the conductor.

There is less of a problem with relaxation with compression connectors because of the inherent physical properties of the connector material. Today almost all Utility companies have at least considered the use of compression fittings for secondary distribution use. Some companies use them exclusively while others have rejected them, still

preferring the advantages bolted connectors offer even with the relaxation problem.

In an attempt to provide those who prefer bolted aluminum connectors a design that would adjust for relaxation, and, therefore, maintain a good electrical contact, a research program was undertaken to determine the magnitude and mode of the relaxation of a connection. The data obtained was then used in the design and development of a cast aluminum connector that compensates for such relaxation as occurs within the connection.

RELAXATION INVESTIGATION AND RESULTS

Three indicators of relaxation in aluminum connections had been determined from field information and from experimental work in the laboratory. These were:

1. Torque loss from that originally applied.
2. Load loss with time. Loss of the load imposed on the connection assembly by the bolt. This may be measured either with Dynamometer apparatus or by relating measured torque to torque - tension curves.
3. Connector burnouts caused by a dimensional looseness in the connection between the connector components and the conductor.

It was felt that if the factors contributing to the above could be controlled by design, the relaxation problem would become non-existent.

Numerous electrical heat cycling tests revealed for example connectors with 3/8 inch steel bolts and lockwashers, serving in aluminum conductor test loops, experienced an average torque loss of 110 inch pounds from an original torque of 240 inch pounds. The desired torque loss average was 40 inch pounds, i.e. a deviation from the original torque of 17 %. To attain this, the approach of incorporating a spring washer was selected. Torque data after heat cycling on connectors with commercially available dished disc (Belleville) spring washers revealed an average torque loss of about 60 inch pounds. Unique designs of dished disc washers to provide the desired compensation were computed and considered. Costs of special materials and special manufacturing tolerances dictated consideration of new concepts, one of which will be described in detail.

Load loss versus time tests were conducted on all components making up a connection. A standard cast aluminum parallel groove connector was selected as the test specimen for relaxation evaluation. The connector had symmetrical grooves and a cable range from #8 solid copper to 2/0 ACSR. It employed a 3/8 inch round head, square shank, galvanized steel bolt. Torque tests run on a particular specification bolt of this size revealed load level capabilities of about 2,000 pounds dry and 4,300 pounds lubricated. It was within this load range that this investigation was centered.

The load loss of the connector components and the hardware was found to be insignificant. As was suspected, the conductor was the predominant source of the observed load loss. The load loss of several conductor sizes and the connector itself was measured (Figure 1). These tests were all conducted at ambient temperature. Readings were taken until the curve had definitely become asymptotic to the axis of abscissas.

The load loss (Figure 1) is seen to vary with the conductor type as well as size. The greatest load loss in this set of data occurred on the 1/0 stranded all aluminum conductor. The load loss was approximately 300 pounds. This verified the findings of a similar unpublished investigation at Auburn University, Auburn, Alabama.

The reason the 2/0 ACSR conductor suffered less load loss than the 1/0 stranded aluminum involves consideration of unit pressure. When the connector-conductor bearing area is less, as with smaller diameter conductors, the unit pressure corresponding to a given load is greater and, therefore, causes more deformation of the conductor strands.

As for solid conductor, absence of inter-strand deformation permits less conductor deformation under load. Although tests have shown that connections with #2 stranded and #2 solid aluminum conductors experience about the same amount of load loss, the difference in the diameters probably offsets the difference in geometries.

A different rationale applies to load loss when produced by heat cycling beyond that produced at constant temperature (Figure 2). The rise in temperature resulting from test current produces expansion stresses in the conductor and connector. The relative dimensions, co-efficients of expansion and moduli of elasticity combine to determine the effect on load loss of plastic flow of the conductor. The net result (Figure 2) was shown to produce greater load loss in larger conductors in the particular connector used for these tests. These data (Figure 1 and Figure 2) confirmed the necessity of using both load-time and heat cycle observations to determine the magnitude of the relaxation effect to be overcome, as well as the effectiveness of the compensation achieved.

The relation between connector burnouts and connection relaxation was established by examination of failed connections. Evidence of dimensional instability in a bolted connection was first observed upon microscopic examination of connectors that had failed. In these examples, areas of severe pitting were observed. Also, lava-like deposits created by arcing from the conductor to the connector groove surface could be seen. From this it was reasoned that initially a good electrical contact existed along the intermetallic conductor-connector junction. Enough pressure had initially been exerted on the connector and conductor contact surfaces to physically breach the aluminum oxide barriers separating the two. As time passed and the aluminum conductor underwent cold flow, the contact pressure along the intermetallic face was not maintained. Enough physical separation between the conductor strands and the connector groove wall occurred to permit the build up of aluminum oxide layers, reducing the area of low-resistance metallic contact. This action increased the current density in the remaining contact area. Continuation of this process led ultimately to the failure mechanism observed.

It was noticed that if after a few heat cycles a connection was re-torqued to the original value, the connection would proceed through the test without a marked build-up of either resistance or temperature while identical connectors not re-torqued increased in resistance and temperature. The re-torquing brought the conductor, which had already undergone cold flow one time, back into contact with the connector. The second time the bearing area between the two was greater due to the previous mating, and less additional cold flowing of the aluminum conductor took place, an insufficient amount to again cause a poor contact. This retorquing observation reinforced the belief that a dimensional change taking place after initial torquing caused the instances of poor performance.

Physical measurements of the connection after torquing also revealed a dimensional difference with time. Quantitative determination of the cold flow magnitude of a stranded or solid conductor was not practical. This had been previously attempted by a major research institute without conclusive results. Therefore, the dimensional variation of the entire connection system was analyzed. This information was considered sufficient to permit the development of a compensating mechanism that would permit a good electrical contact to be maintained.

The most satisfying experimental results with respect to this dimensional study were produced by heat cycling of connections. These were torqued to the recommended value and were then subjected to thermal cycling. A torque loss was always experienced after heat cycling. The angular rotation of the nut necessary to regain the original torque was recorded. By knowing this angular displacement and the pitch of the bolt threads, the gross nut advancement could be calculated. It was found that for the connector type investigated and its cable range, an advancement range from 0.006 inches

to 0.008 inches had to be compensated for. This conclusion was later proved valid by the successful tests of connector assemblies so compensated.

RELAXATION COMPENSATING SYSTEM DESIGN

The system selected to compensate for the relaxation in the connection was a flat spring washer. The design criteria adopted for this washer were: (a) remain elastic when deflected .018 inches, and (b) have no more than .002 inches permanent set after being repeatedly cycled through its full range of deflection.

A recessed circular fulcrum in the bottom connector component was provided for dishing the washer. Figure 5 shows a cross-sectional view of the washer-fulcrum combination. The washer is shown in its unloaded and loaded states. As the nut is advanced, the washer will proceed to dish around the fulcrum until it seats against the tapered seat shown. The seat serves to prevent the washer's being overstressed as a result of overtorquing the bolt in the field.

A question to be answered was whether non-uniformity of bolts would add to the load variations to be compensated. Enough bolt samples were tested to readily demonstrate that this was not a major source of concern. Bolts purchased to the same specification were found to deviate very little in tensile load when tightened to recommended torque value.

With the load and deflection requirements determined by experiment, a theoretical stress analysis was conducted, to determine preliminary washer dimensions for washer-fulcrum combinations, and to estimate the ultimate stress at full load on the washer.

Type 420 stainless steel was selected as the washer material. This is a heat treatable alloy with excellent anti-corrosion properties. With the proper heat treat, a yield strength of 215,000-225,000 psi can be obtained. The ultimate strength corresponding to this yield was about 265,000 psi. This strength was found sufficient for the intended application.

The final washer dimensions were determined empirically. The inner diameter of the washer was limited by the bolt size. Therefore, the washer's outer diameter and thickness were varied, along with the fulcrum diameter. A combination of the three was found which produced the desired relaxation compensating device.

COMPUTATIONS AND TESTS

The load-deflection characteristic of the final compensator washer design was measured. (Figure 3) Characteristic curves of designs for other connectors have similar shapes and slopes. The tapered seat angle is designed so that the washer seats fully at close to recommended initial torque load, or about 0.018 in deflection. Assuming the maximum dimensional change, (0.008 inches) the remaining washer deflection is about 0.010 inches which maintains the load previously determined necessary for satisfactory electrical contact.

Load-loss data at ambient temperature was taken on the assembled connection with compensating washer (Figure 4). The loss of load was comparable to the probable inaccuracy in field torquing and therefore insignificant.

After the washer's and the fulcrum's dimensions had been finalized another theoretical stress analysis was made to again review the maximum stress in the washer. Timoshenko presents an approach to a flat circular plate loaded such as this application.1

Using the formula:

$$S_{max} = \frac{6 M_t a}{h^2 c \ln \frac{d}{c}}$$

$$S_{max} = 335{,}000 \text{ psi}$$

Where: M_t = The twisting couple per unit length of the vertical centerline.
a = Radius of the vertical centerline.
h = Washer thickness.
c = Washer inner radius.
d = Washer outer radius.

This calculated value is higher by about 70,000 psi than the washer material's ultimate strength. The reason for this difference is complex. This case appears similar to the loading of a disc washer analyzed by Brickman. 2 He postulated that residual compressive stresses set up in the spring when it is formed cancel to a degree the high tensile stresses developed at the inner diameter when the washer is deflected. Also, as the inner diameter boundary reaches its stress yield point and goes beyond it, more load is assumed by the washer material outboard of the inner diameter. This stress adjusted continues until the load is fully accommodated. When the load is removed the washer returns to normal.

Torque tests were conducted on five spring washer connectors that were thermally cycled for ten cycles and then were re-torqued to the original value. (Table I).

Four relaxation compensated connectors were subjected to heat cycling test similar to that proposed as standard by a joint EEI-NEMA Committee. 3 The test was continued beyond the 500 cycles recommended as standard, and was discontinued at 892 cycles. There were no failures of the compensated connectors, although other non-compensated connectors in the same loop failed. At the conclusion of the test the connector temperatures gave no evidence of electrical instability (Figure 6).

CONCLUSIONS

1. There is a primary causal relationship between maintenance of connector pressure and maintenance of electrical performance in a bolted connection on aluminum conductor.

2. The dominant factor in the loss of connector pressure is deformation of the aluminum conductor by (a) compaction under connector pressure and (b) plastic cold flow (relaxation) under connector pressure and thermal stresses.

3. After initial deformation, sufficient contact pressure can be sustained by the conductor for maintenance of satisfactory electrical performance of the connection.

4. The amount of permanent deformation necessary before the conductor can sustain sufficient contact pressure can be determined for any combination of conductor and connector.

5. A device to compensate for the necessary initial deformation and to maintain the necessary contact pressure has been designed and tested in the form of a

flat spring washer.

6. The spring washer described provides compensation for differential thermal expansion as well as for initial conductor deformation.

7. The design methods developed from this investigation can be extended to a wide range of combinations of conductors and connectors.

REFERENCES

1. Strength of Materials (book), Stephen Timoshenko. D. Van Nostrand Company, Inc. Princeton, New Jersey, 1956, Part II, pp. 140-41.

2. Designing Conical-Disc Springs To Provide Specific Load-Deflection Characteristics With A Minimum Space, Arthur D. Brickman. Machine Design, Cleveland, Ohio, March 16, 1961, pp. 141-45.

3. Tentative Specifications For Connectors For Aluminum Conductors, A Joint Report of the Steering and Advisory Committees Aluminum Connector Research Project. Edison Electric Institute Publication No. 59-70, New York, New York, 1958.

TABLE I

TORQUE MAINTENANCE TEST - COMPENSATED CONNECTOR

SAMPLE NO.	ORIGINAL TORQUE (Inch Pounds)	FINAL TORQUE (Inch Pounds)
1	240	220
2	240	180
3	240	150
4	240	220
5	240	230
	Average	200 Inch Pounds

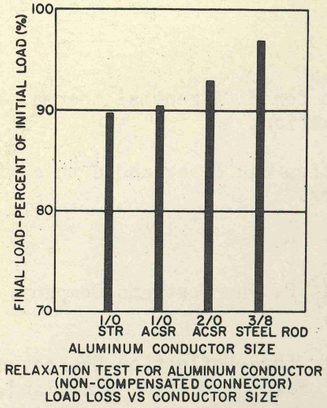

Fig. 1. Relaxation test for aluminum conductor (non-compensated connector)

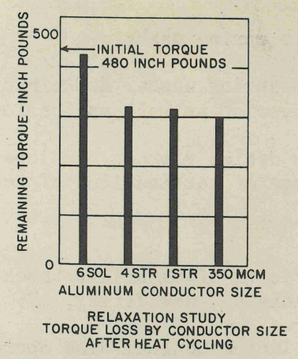

Fig. 2. Torque loss by conductor size after heat cycling

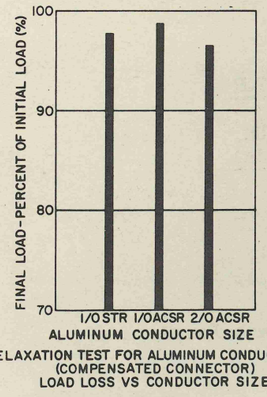

Fig. 3. Relaxation test for aluminum conductor (compensated connector)

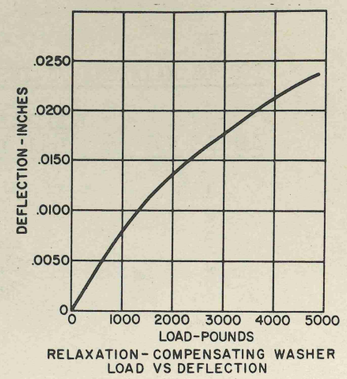

Fig. 4. Relaxation compensating washer

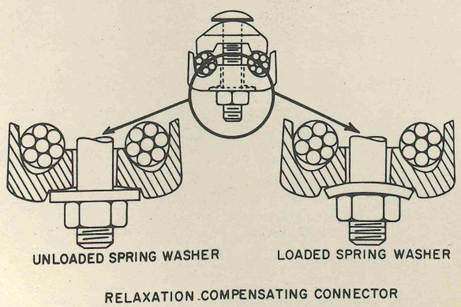

Fig. 5. Relaxation compensating connector

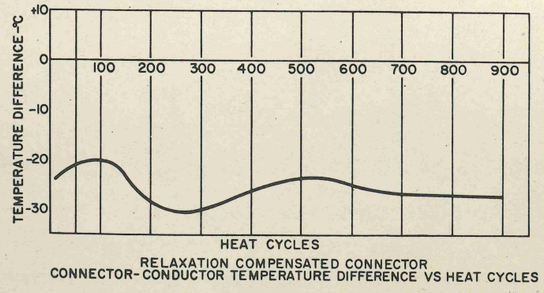

Fig. 6. Relaxation compensated connector

Mechanics

Mr. Boyd

Conference Paper

RECEIVED
AUG 15 1961
G. M. BOYD

ALUMINUM COLD FLOW COMPENSATION IN BOLTED ELECTRICAL CONNECTIONS

G. L. Flynn
Nonmember AIEE

T. L. Rundlett
Member AIEE

Both of:
Anderson Electric Corp.
Birmingham, Ala.

RECEIVED
AUG 8 1961
H. A. EREY

A paper recommended by the AIEE Transmission and Distribution Committee for presentation at the AIEE Pacific General Meeting, Salt Lake City, Utah, August 23-25, 1961. Manuscript submitted May 25, 1961; made available for printing June 23, 1961.

Price: $ .50 To Members
$1.00 To Nonmembers

(5¢ per copy additional if first class mailing desired)

All Rights Reserved by the
American Institute of Electrical Engineers
33 West 39th Street, New York 18, N. Y.
Litho in USA

Paper No. CP
61-940

TECHNICAL INFORMATION SERIES

Title Page

AUTHOR	SUBJECT CLASSIFICATION	NO.
J. P. Benedict JP Benedict	1. L.A.-Line Station and H.V. 2. L.A.-Testing 3. Insulators	60PT145 DATE 7/6/60

TITLE CONTAMINATION TEST ON SIX TYPES OF DEVELOPMENTAL LIGHTNING ARRESTER HOUSINGS. PHASE II

FOR USE OF G-E EMPLOYEES ONLY

GENERAL ELECTRIC

TRANSFORMER DIVISION

RECEIVED
JUL 18 1960
H. A. EREY

[redacted]

FOR USE OF G-E EMPLOYEES ONLY

GENERAL ELECTRIC

TECHNICAL INFORMATION SERIES

Title Page

AUTHOR	SUBJECT CLASSIFICATION	NO.
J.P. Benedict JP Benedict	1. L.A.-Line Station and H.V. 2. L.A.-Testing 3. Insulators	60PT145
		DATE 7/6/60

TITLE

CONTAMINATION TEST ON SIX TYPES OF DEVELOPMENTAL LIGHTNING ARRESTER HOUSINGS. PHASE II

ABSTRACT Sixty-cycle flashover tests were made on developmental L.A. housings having various hood configurations. In addition to fog tests with 0% and 3.8% salt solutions, standard dry and wet tests were made. Also tested were a 79 kv Ohio Brass L.A. housing, a 9LA3K066 housing and 7785 cap and pin type insulators.

G.E. CLASS	FILE COPY AVAILABLE IN THE WILLIAM STANLEY LIBRARY, PITTSFIELD	NO. PAGES
IV M		
GOV. CLASS		
None	Pittsfield Works	18

CONCLUSION

1. On the basis of these tests, two designs appear to be best suited for application in contaminated areas. They are:

   a. Lightning arrester housings having 14 hoods with the underside corrugated.

   b. Lightning arrester housings having 15 hoods with a 15 degree undercut.

2. The ability of these lightning arrester housings to withstand 10 cycles of 3.8 percent salt solution fog at 50 kv appeared to be a function of design profile rather than the total creepage length or the ratio of protected creepage length to the total creepage length.

By cutting out this rectangle and folding on the center line, the above information can be fitted into a standard card file.

For list of contents-drawings, photos, etc. and for distribution see reverse side.

INFORMATION PREPARED FOR Lightning Arrester / W.J. Rudge

TESTS MADE BY HR Fehlmann, JE Eulian, and JP Benedict Tests Completed: 6/13/60

COUNTERSIGNED AF Rohlfs A F Rohlfs SECTION High Voltage Laboratory

BUILDING and ROOM No. 9-102 LOCATION Pittsfield, Massachusetts

-mjb

CONTENTS OF REPORT

NO. PAGES TEXT 12

NO. CHARTS

DRAWING NOS.

184HA587
184HA588
184HA589
184HA590

PHOTO NOS.

References:

EL 4941, DB 990, pp. 1-100
DB 996, pp. 1-72

Report: 59PT157

DISTRIBUTION

Complete Reports

William Stanley Library - (6) copies
Technical Data Center, General Engineering Laboratory, Schenectady - (2) copies of Class I, II and III reports and (1) copy of Class IV reports

L. Wetherill/	1 copy	42-322
JR Meador/		9-204
AF Rohlfs		9-203
HV Laboratory		9-102
WH Eason		43-553
WJ Rudge		42-550
SR Smith		9-304
TJ Carpenter		9-304
GF Lincks		43-554
EC Sakshaug		43-550
HA Frey		Baltimore
B. Kingsbury		Baltimore
JH Hagenguth		9-201
DL Johnston		51-101
GF Milne		43-552
FJ Turner		9-102
JP Benedict		9-102

Title Sheets

William Stanley Library - (6) copies
Technical Data Center, General Engineering Laboratory, Schenectady - (6) copies

JW Albright	51-103
PA Abetti	9-202
JH Hagenguth	9-201
RB Ames	43-568
JR Meador	9-204
AF Rohlfs	9-203
VB Ross	Canadian G.E. Ghelph
ME Scoville	Hudson Falls
HC Stanley	16-200
JA Van Lund	51-103
TF Volkmer	Rome
TR Walters	9-314
L. Wetherill	42-322
FL Woods	43-382
HV Laboratory	9-102
FJ Turner	9-102

Additional copies, where needed, can be obtained from the William Stanley Library, Pittsfield.

CONTAMINATION TEST ON SIX TYPES OF DEVELOPMENTAL LIGHTNING ARRESTER HOUSINGS. PHASE II

INTRODUCTION:

In the first phase of the investigation, reported in 59PT157, it was found that under contaminated conditions the withstand voltage increased and the leakage current decreased with the number of hoods. For the Phase 1 tests, the maximum number of hoods on G.E. L.A. housings was 12; therefore some unit designs for the Phase 2 tests incorporated as many as 18 hoods.

It was also found that the Ohio Brass L.A. housing and the 7785 insulator supports had significantly higher withstand values under salt fog contamination than the G.E. housings. This appeared to be the result of increased creepage length and different design. From the designs submitted for investigation some of the most promising hood configurations were selected and units were constructed for the Phase 2 tests. The creepage length for these units varied between 74 and 95 inches.

OBJECT:

The test had two objects:

A. The general object was to obtain data leading to a better understanding of insulator design, especially the effects of contamination on arrester insulating housings.

B. The immediate objective was to evaluate the six developmental lightning arrester housings having different hood configurations.

DESCRIPTION OF TEST PIECE:

Eighteen developmental lightning arrester housings, having six different hood configurations, were tested. For each configuration, three units were constructed. Profiles of the various housings are shown in Figure 1 and pertinent descriptive data are given in Table I.

The type F porcelains were especially dimensioned to meet the basic requirements of a contamination proof porcelain based on conclusions from 25 year weathering tests by the Central Electricity Board of England which were:

1. Creepage distance should be three times the porcelain height.

2. Protected creepage distance should be 1/2 the total creepage distance.

Wire shields were installed on both top and bottom of all the developmental units to prevent the cap cement from melting.

In addition to the developmental housings, the OB arrester housing, 9LA3K066 arrester housing and the two 7785 cap and pin insulators in series (tested in Phase 1 investigation and results reported in 59PT157) were tested with Phase 2 procedures.

PROCEDURE:

Initially all of the 18 developmental units were subjected to sixty-cycle withstand and flashover tests for both wet and dry conditions using AIEE Standard methods. The test results are given in Table II. All units except the spiraled hood type had substantially the same electrical characteristics. The withstand and flashover values for the spiral hood units were approximately 15% higher than the average values for all the others. When the spiral hood unit was inverted for testing the results were approximately 5% higher than the average results for the others.

In addition to the Standard AIEE tests, leakage current measurements were made on all 18 developmental housings during rain spray condition. The data obtained and given in Table III does not appear to have any relation to the ratio of protected creepage distance to total creepage distance nor to the creepage length. The data does appear to indicate that the design of the hoods to keep some areas dry beneath the hoods results in lower leakage currents just prior to flashover. Units "C" (14-15° undercut hoods), "D" (9 large and 9 small diameter hoods), "E" inverted (with spiraled hood undercut down) and "F" (corrugated 15° undercut hoods) all had low leakage currents as compared to units A, B and E.

Fog Tests

For these tests the plastic sheet tent was used as described in 59PT157 and shown in Figures 34 and 35 of that report. An error in Figure 34 omits the plastic protective covering used to protect the bottom end of the entrance bushing. The covering was stretched from the bottom end of the bushing out to the outer diameter of

the wooden tent support. This plastic covering over the bushing can be seen in Figure 35.

In brief, the test procedure was to mount the unit on the turn table with the top fog nozzle 30 inches from the top hood. The unit was rotated at 11-1/2 revolutions per minute, and with the fog nozzles on, voltage was applied starting at 150 kv. The rest of the procedure was as follows:

a. Fog on for four minutes measuring leakage current every 30 seconds.

b. Fog off for four minutes measuring leakage current every 30 seconds.

c. Voltage off and evacuate tent for three minutes with vacuum cleaner.

d. Raise voltage in 20 kv steps to flashover repeating a, b and c at each level.

In order to save time, for this test and those that followed, only one unit was tested from each of the six developmental housing groups.

In addition to the developmental housings, the same G.E. 9LA3K066 and (2) 7785 cap and pin insulators tested in 1959 were included in this part of the investigation in an attempt to correlate the data obtained for the two separate tests. All test results for the fog tests are given in Table IV.

When comparing results in Table IV with data reported in 59PT157 for fog tests it was found that the 9LA3K066 unit showed approximately a 20 kv increase in flashover strength and the 7785 insulators were approximately 10 kv low in flashover voltage. The values for this test are the result of only two tests and the difference in flashover voltages could be accounted for by the normal spread in results had there been several tests made. Also there was no evidence of the cement burning on the 9LA3K066 during this test which may have resulted in higher flashover voltage for this unit.

The other units appear to have approximately equal flashover strengths except the E type unit with the spiral hoods which, in the inverted position, had the highest withstand value under fog condition.

Contamination Tests 3.8% Salt Solution Fog

In preparing the salt solution for this part of the investigation, it was found that during Phase 1 tests, the percentage was calculated as 3% by volume rather than weight. During the present tests the same percent of salt by volume was used, but in order to convert the percentage to a weight basis, the salt was weighed and the calculated percentage on a weight basis was found to be 3.8.

The test procedure was exactly the same as for the 0% fog except the starting voltage was 40 kv and the voltage was raised in 5 kv increments. After flashover the 40 kv level was repeated for each unit in order to determine, from the leakage current measurements, to what degree the unit was contaminated. These data are given in Table V.

After completion of the salt fog tests, the data was summarized and a meeting was held with persons involved in the investigation attending. From the test results obtained, four unit types were selected for further evaluation with altered test procedures. The eighteen hood type B unit was eliminated from further testing because its characteristics showed no improvement over the other types selected and it probably would be more expensive to manufacture. These unit types were A, C, D and F housings in addition to the Ohio Brass housing, 9LA3K066 housing and the 7785 cap and pin insulators. The test procedure for these tests was as follows:

a. Apply 50 kv to unit

b. With salt fog on four minutes, take leakage current measurements every 30 seconds.

c. With salt fog off four minutes, take leakage current measurements every 30 seconds.

d. Repeat b and c above for a total of 10 cycles holding 50 kv continuously.

e. Let unit dry in place, remove and test next unit.

f. After 24 hours drying period, apply 50 kv, spray with water fog continuously and measure leakage current every 30 seconds until it levels off.

g. When leakage current levels off, raise voltage to flashover.

The test voltages for the Ohio Brass unit was graded proportional to its creepage length in comparison with the developmental units tested. The creepage length was 10% greater than other units tested; therefore it was tested at 55 kv rather than 50 kv.

For part "f" of the above procedure, the setup inside the tent was altered in order to apply an even coat of fog on the unit. The fog nozzles were directed away from the unit towards a fan on the floor which was adjusted so its direction of circulation was upwards towards the under surfaces of the housing hoods.

All of the units used were previously contaminated and were washed prior to this test. Washing was done with cold tap water from a hose equipped with a pressure nozzle while scrubbing with a venetian blind brush having stiff bristles. Special attention was given to washing the cap and hardware on the top of the units.

The maximum leakage current measured during each of the 10 contamination cycles at 50 kv are given graphically in Figures 2 and 3. The maximum leakage current measurements during the water fog application after contamination are plotted versus time fog was on in Figures 4 and 5.

During the fog cycling test only the C and F housings and the 7785 cap and pin insulators withstood all 10 cycles without flashover at 50 kv. The Ohio Brass unit withstood eight cycles at 55 kv before flashover. Also, as can be seen by the graphs in Figures 4 and 5, the leakage current during water fog tests was lowest for the C and F units which appears to indicate that these two units are of the best design for operation in contaminated areas.

It is suggested that to further evaluate these two units, these tests should be repeated at elevated voltages.

These tests seem to indicate that the ability of the units to resist contamination depends upon the protected area under the hoods. It appears that if the degree of undercut were increased and the top surface of the hood conform to this angle then each hood would protect the top surface of the one underneath it. For example see sketch on Page 6. Of course the compatibility of such hoods with other requirements would need to be studied.

It is also suggested that units could be designed with complicated hood contours if they were manufactured with individual hoods cemented together.

TABLE I

Description of L.A. Housings and the 7785 Cap and Pin Insulator Tested (See Also Figure 1)

Group Ident.	Dwg. No.	No. of Hoods	Dist. between Hoods Inches	Diam. Over Hoods Inches	Creepage Length Inches		Meas. Flashover Length Inches	Nominal Dist. between Castings Inches	(2) Ratio Creep to Height	(3) Ratio Prot. Creep to Total Creep
					Nominal	Meas. (1)				
A	Y-R938-59A Figure 1	15	1-11/16	15-3/8	80	82.3	29-1/8	30	2.67	0.37
B	Y-R938-59A Figure 2	18	1-3/8	15-3/8	95	96.5	29	30	3.16	0.37
C	Y-R938-59A Figure 3	14	1-13/16	15-3/8	81	79.8	29-1/4	30	2.70	0.38
D	Y-R938-59B	9 LG 9 SM	1-1/4 to SM 1-1/2 to LG	15-3/8 13-7/8	80	81.3	29	30	2.67	0.34
E	Y-R938-59C	Cont. Spiral 13 Turns	2-1/8	15-3/8	74(4)	74.3	29-1/2	30	2.50	0.40
F	S60B009	14	1-13/16	15-3/8	94	95.5	29	30	3.10	0.49
GE	9LA3K066	12	---	15-3/8	---	58-1/2	29-1/2	30	---	---
OB	-------	8 LG 7 SM	---	16 14	---	76	32	---	---	---
7785	Cap & Pin Insul. 2 in Series	6	---	17	66	---	29	---	---	---

(1) Average of three units measured. Masking tape was applied over the creepage length, removed and measured.

(2) Ratio creepage to Height = $\frac{\text{Creep Length}}{\text{Dist. between Castings}}$

(3) Ratio protected creepage to total creepage = $\frac{\text{Sum of Protected Lengths under Hoods}}{\text{Creepage Length}}$

(4) Path along spiral of hood at 15-3/8 inch dia. equals approx. 444 inches

TABLE II

Sixty-Cycle Wet and Dry Withstand and Flashover Tests on Six Developmental Lightning Arrester Housings

Group Ident.	Unit No.	Dry FO * kv-rms	Wet FO ** kv-rms	10 Sec. Wet Withstand kv-rms	RAD	V.P.
A	1	241	215	215	0.986	0.32
	2	239	219	197	0.986	0.32
	3	240	234	199	0.986	0.32
	Avg.	240	223	204		
B	1	239	236	212	0.960	0.22
	2	233	226	203	0.990	0.26
	3	236	224	213	0.990	0.26
	Avg.	236	229	209		
C	1	237	216	194	0.990	0.23
	2	236	218	196	0.990	0.23
	3	238	234	222	0.990	0.23
	Avg.	237	223	204		
D	1	236	219	208	0.980	0.36
	2	237	227	204	0.990	0.23
	3	237	226	192	0.990	0.23
	Avg.	237	224	201		
E	1	245	251	238	0.990	0.26
	2	240	248	236	0.986	0.32
	3	247	255	242	0.986	0.32
	Avg.	244	251	239		
E Upside Down	1	253	238	214	0.974	0.45
	2	253	235	223	0.974	0.45
	3	---	238	214	0.974	0.45
	Avg.	253	237	217		
F	1	241	233	209	0.990	0.23
	2	239	213	181	0.960	0.22
	3	229	207	196	0.960	0.22
	Avg.	236	218	195		

* Average of three flashovers

** Average of five flashovers

TABLE III

Sixty-Cycle Leakage Current Measurements on Six Developmental Lightning Arrester Housings During Rain Spray Condition.

(Water Resistivity 16,800 to 30,000 Ohms/cc.)

Group Ident.	Unit No.	Max. 10 Sec. Wet W.S. kv-rms	Percent of Maximum 10 Second Withstand							
			50	60	70	80	85	90	95	100
			Leakage Current ma Crest							
A	1	215	3.0	3.5	4.0	5.0	7.0	9.2	10.2	12.3
	2	197	1.0	1.5	1.5	1.8	2.3	2.5	4.0	----
	3	199	2.3	3.0	3.8	4.0	3.0	6.1	7.1	8.1
B	1	212	5.1	6.1	9.2	10.2	11.2	13.3	14.3	16.3
	2	203	3.8	5.5	6.1	8.0	9.0	10.0	12.0	18.5
	3	213	4.1	5.1	6.1	7.1	9.2	11.2	14.3	17.3
C	1	194	0.5	0.7	0.9	1.0	1.1	1.2	1.4	1.5
	2	196	0.6	1.6	2.7	4.5	3.5	1.2	2.0	2.2
	3	222	2.5	3.2	3.7	6.0	5.0	4.1	7.5	---
D	1	208	1.0	1.4	1.5	1.6	1.6	1.7	---	2.5
	2	204	0.8	1.0	1.1	1.2	1.3	1.4	1.5	1.7
	3	192	0.7	0.8	1.0	1.2	1.3	1.3	1.5	1.7
E	1	238	2.8	3.5	4.5	4.1	5.1	6.1	7.2	8.2
	2	236	2.5	3.5	4.0	4.8	5.1	6.1	7.2	8.2
	3	242	1.8	2.7	3.5	3.8	4.0	4.3	5.1	6.1
E Upside Down	1	214	0.7	1.2	2.2	3.5	5.0	5.1	4.0	4.0
	2	223	0.6	0.8	1.0	1.2	1.3	1.4	1.5	1.7
	3	214	1.4	2.4	4.0	5.0	7.1	8.1	3.0	4.5
F	1	209 *	0.40	0.6	0.8	1.0	1.3	1.5	1.8	2.0
Repeat	1	209 *	0.50	0.6	0.8	1.0	1.1	1.2	1.7	4.3
	2	181	0.41	1.02	1.4	1.8	2.0	2.1	3.5	4.1
	3	196 **	1.5	2.3	2.8	4.5	6.	10.	12.2	14.3

* Percentages were calculated on a maximum withstand of 196 kv resulting in a 5% error in applied voltages while measuring the leakage currents.

** There is no explanation for this data being high.

TABLE IV

Sixty-Cycle Leakage Current Measurements and Flashover Tests on Six Developmental Lightning Arrester Housings During Water Fog Condition
(Water Resistivity = 21,900 - 25,000 Ohms/cc)

Group Ident.	Unit No.	Kilovolts rms Applied												Flashover Level Data			
		150		170		190		210		230		250		Leakage Current before F.O. MA Crest	Time before F.O. Min.	F.O. kv-rms	RAD
		Fog															
		On	Off	On	Off	On	Off	On	Off	On	Off	On	Off				
		Maximum Leakage Current MA Crest															
A	3	1.1	1.1	1.8	1.7	3.2	2.8	5.7	6.4	--	---	--	---	11.3	0'-32"	230	0.980
B	3	1.0	1.0	2.4	2.0	3.7	3.4	---	---	---	---	---	---	6.2	2'-20"	210	0.980
C	1	1.0	1.0	2.1	2.4	3.9	4.1	6.3	7.8	---	---	---	---	9.2	3'-25"	230	0.980
D	3	1.1	1.0	2.5	2.0	3.4	3.3	5.3	8.2	5.7	7.8	---	---	>35.	0'-10"	250	0.980
E	1	1.0	1.0	2.3	2.0	3.9	4.3	6.3	6.3	12.0	10.6	---	---	28.3	6'-40"	250	0.977
E Inverted	1	1.0	0.9	1.8	1.5	3.8	4.3	7.1	5.7	9.2	9.2	14.1	17.7	15.5	0'-20"	270	0.976
F	1	1.0	0.9	1.8	1.5	2.8	2.8	5.7	5.7	---	---	---	---	9.2	1'-40"	230	0.977
Retest Units Tested in 1959 and Reported in 59PT157																	
9LA3K066	II*	1.2	1.2	1.7	1.6	3.3	3.5	6.4	5.3	---	---	---	---	9.2	1'-5"	230	0.974
9LA3K066	III*	1.1	1.1	2.5	2.0	3.0	3.0	5.0	5.1	6.4	6.4	---	---	7.8	0'-45"	250	0.974
7785	Cap & Pin Insul.	3.1	3.1	4.5	4.4	---	---	---	---	---	---	---	---	5.9	0'-10"	190	0.974
		Wiped Dry and Retested															
	Two in Series	3.4	3.4	4.1	4.0	---	---	---	---	---	---	---	---	4.8	1'-0"	190	0.974

* Cement bond between cap and insulator, both top and bottom, shielded with a strand of hipot wire connected to caps.

RESTER

Group Ident.	Unit No.	Kilovel Data				Max. Leakage Cur. at 40 KV After Flashover	
		Fo me				Fog On	Fog Off
		On		fore **		MA Crest	
		Le		n.-Sec.	RMS		
A	3	.27		-10	70	141	212
B	3	.33		nd retested			
B	3	.56		-15	50	424	flashover
B	2	.32		-35	70	495	424
C	1	.32		-15	70	424	565
D	3	.29		-25	70	466	354
E	1	.78		-5	45	566	flashover
E - inverted	2	16		-35	60	212	197
F	3	.32		-5	70	170	127
9LA3K066	II	.60		nst.	55	636	423
7785	Cap. & Pin Insu-lators two in series	1.8		-55	60	21	4.3

*

d off and

TABLE V

SIXTY-CYCLE LEAKAGE CURRENT MEASUREMENTS AND FLASHOVER TESTS ON SIX DEVELOPMENTAL LIGHTNING ARRESTER HOUSINGS DURING 3.8% SALT FOG CONDITION
(Salt Solution Resistivity = 18.5 - 23.7 ohms/cc)

Group Ident.	Unit No.	Kilovolts RMS Applied: 40 Fog On	40 Off	40 Final	45 On	45 Off	45 Final	50 On	50 Off	50 Final	55 On	55 Off	55 Final	60 On	60 Off	60 Final	65 On	65 Off	65 Final	Flashover Level Data: Leak.Cur. Before F.O. MA Crest	Time Before FO ** Min.-Sec.	FO KV RMS	Max. Leakage Cur. at 40 KV After Flashover: Fog On MA Crest	Fog Off MA Crest
		Leakage Current MA Crest*																						
A	3	.27	.28	.28	.37	.38	.38	.49	.51	.51	1.8	1.1	.85	2.8	2.1	1.4	4.9	10.6	10.6	A 635	4-10	70	141	212
B	3	.33	.34	.34	.47	.48	.48	.67	.64	.62	.71	mechanical failure of test circuit - Washed unit and retested												
B	3	.56	.61	.61	1.8	2.0	1.3	-	-	-	-	-	-	-	-	-	-	-	-	B 566	6-15	50	424	flashover
		Apparently the unit was not washed clean. Tested another unit of same type.																						
B	2	.32	.32	.29	.57	.42	.35	.78	.78	.45	1.6	1.4	.57	3.2	2.8	.78	141	283	283	B 425	0-35	70	495	424
C	1	.32	.33	.33	.48	.51	.51	.67	.66	.66	1.8	1.4	.85	169	155	28	354	354	14	C 141	0-15	70	424	565
D	3	.29	.30	.30	.42	.43	.43	.54	.57	.57	.78	.85	.71	1.8	1.4	.78	3.5	2.8	1.1	D 566	4-25	70	466	354
E	1	.78	198	57	-	-	-	-	-	-	-	-	-	-	-	-	-	-	-	E 495	5-5	45	566	flashover
E - inverted	2	16	14	8.5	skipped		level	113	127	35	354	282	2.8	-	-	-	-	-	-	F 170	0-35	60	212	197
F	3	.32	.37	.37	3.2	1.1	1.1	85	57	35	212	170	2.8	212	212	85	283	170	71	F 354	4-5	70	170	127
9LA3K066	II	.60	.65	.65	1.8	1.8	1.5	423	280	71	-	-	-	-	-	-	-	-	-	3K No reading	Inst.	55	636	423
7785	Cap. & Pin Insulators two in series	1.8	1.9	1.9	3.3	3.0	2.7	31	34	17	85	5.7	2.8	-	-	-	-	-	-	7785 170	0-55	60	21	4.3

* Leakage currents reported are the maximums recorded for the 4 minute periods during fog spray on and off and the final leakage current at the completion of the 4 minute fog off cycle.

** For the first 4 minutes the fog spray was on. At time beyond 4 minutes the fog was off.

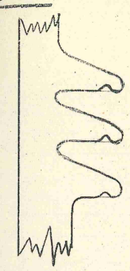

Unit A
Hoods - 15
Flashover Length - 29-1/8"
Leakage Length - 80"

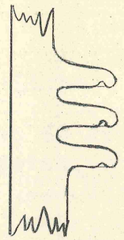

Unit B
Hoods - 18
Flashover Length - 29"
Leakage Length - 95"

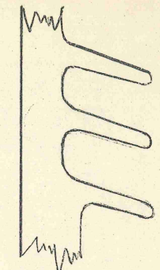

Unit C
Hoods - 14
Flashover Length - 29-1/4"
Leakage Length - 81"

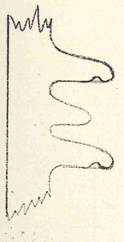

Unit D
Hoods - 9 Large
9 Small
Flashover Length - 29"
Leakage Length - 80"

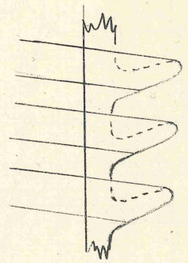

Unit E
Cont. Spiral 13 Turns

Flashover Length - 29-1/2"
Leakage Length - 74"

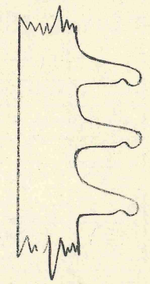

9LA3K066
Hoods - 12

Flashover Length - 29"
Leakage Length - 58-1/2"

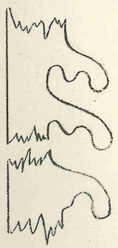

Unit F
Hoods - 14

Flashover Length - 29"
Leakage Length - 94"

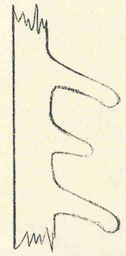

Ohio Brass
Hoods - 8 Large
7 Small
Flashover Lenghh - 32 1/8"
Leakage Length - 76"

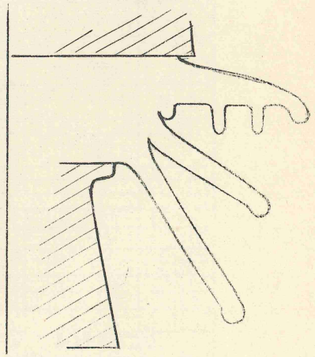

7785 Cap & Pin Insulator
Hoods - 3

Flashover Length - 14-1/2"
Leakage Length - 33"

Figure 1 - Profiles of Insulators Tested

Figure 2

184HA587
CLASS IV
60PT145

Leakage Current at 50 kv Versus Salt Fog Cycles

Units

7785 cap and pin Insuls —•
A-3 LA Housing —x
D-3 LA Housing —Φ
F-3 LA Housing —△

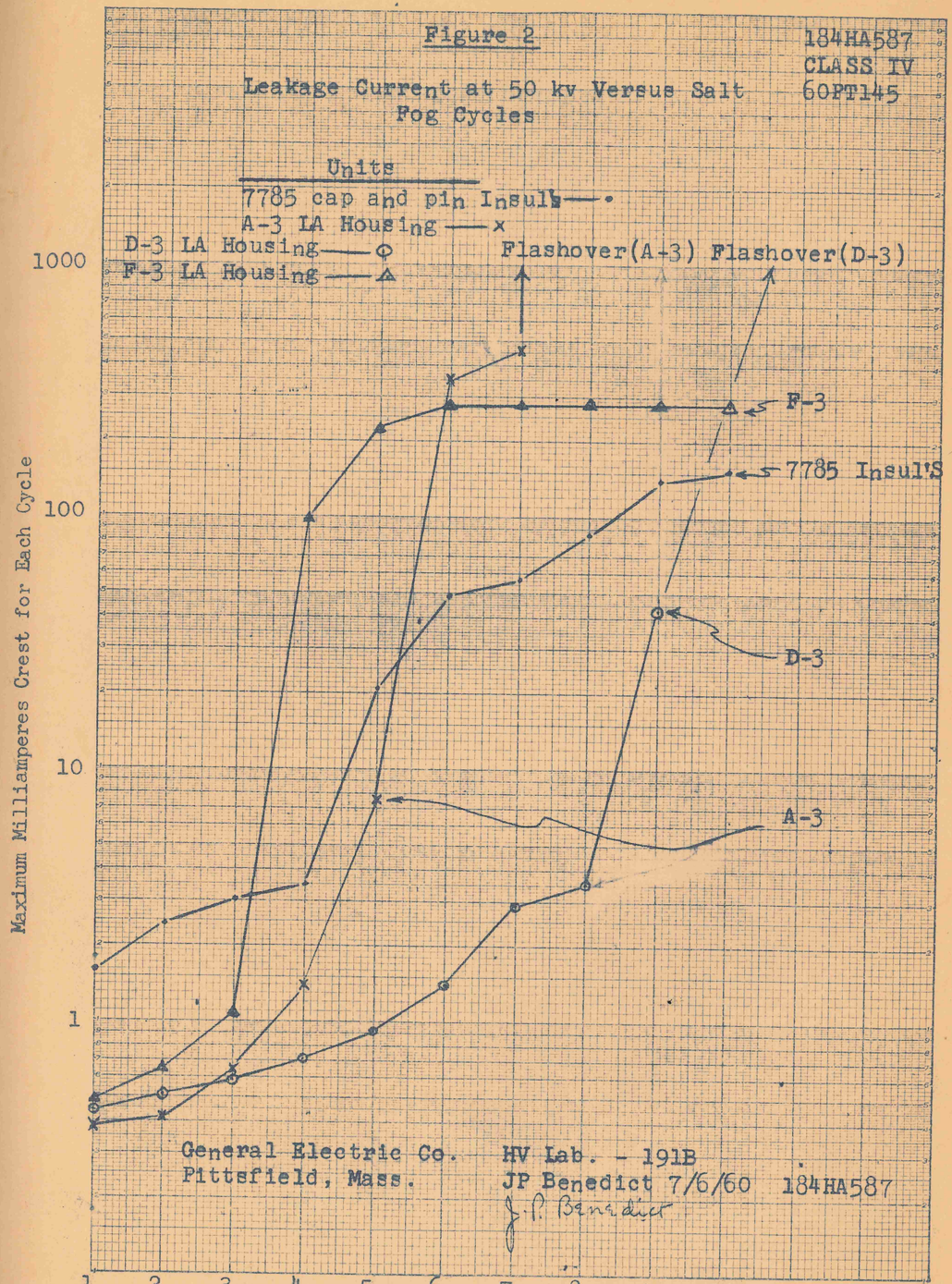

General Electric Co. Pittsfield, Mass.

HV Lab. - 191B
JP Benedict 7/6/60 184HA587
J.P. Benedict

Figure 3

184HA588
CLASS IV
60PT145

Leakage Current at 50 kv Versus Salt Fog Cycles

Note: The leakage current for the OB unit was measured at 55 kv.

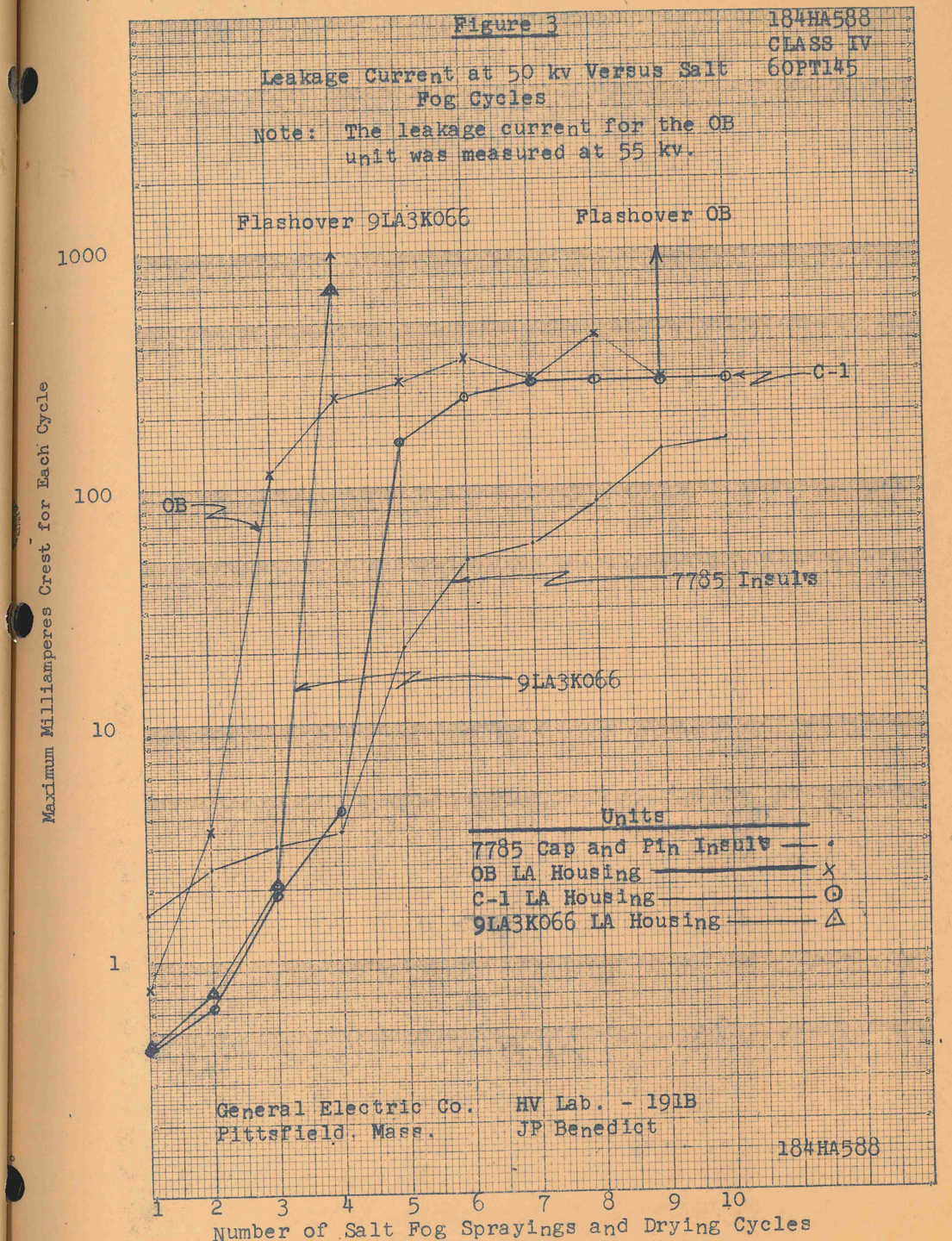

184HA589
CLASS IV
60PT145

Figure 4

Leakage Current at 50 kv for Contaminated Units under Fog Condition

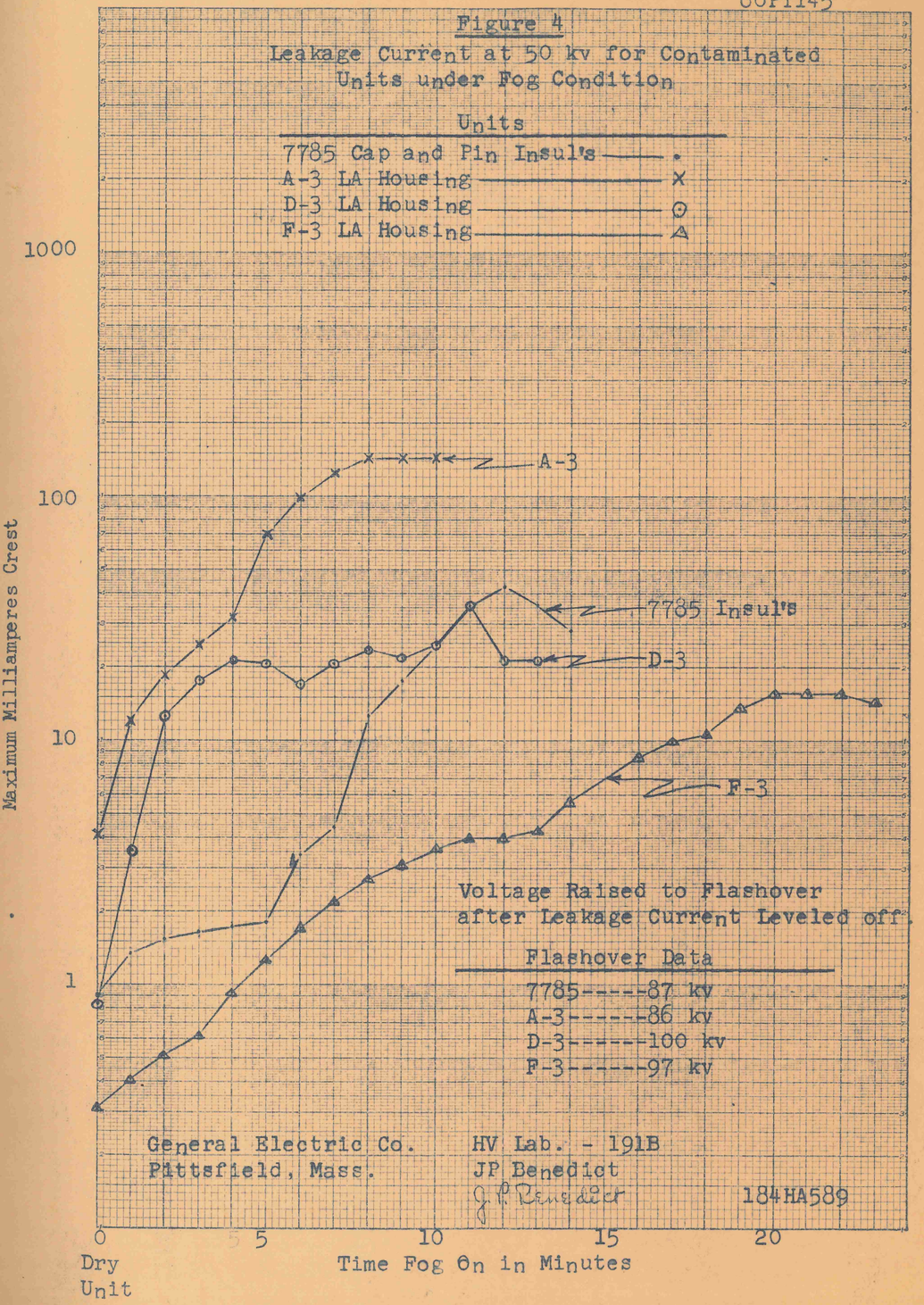

184HA590
CLASS IV
60PT145

Figure 5

Leakage Current at 50 kv for Contaminated Units under Fog Condition

Note: The leakage current for the OB unit was measured at 55 kv.

Units	
7785 Cap and Pin Insul's	•
OB LA Housing	X
C-1 LA Housing	⊙
9LA3K066 LA Housing	△

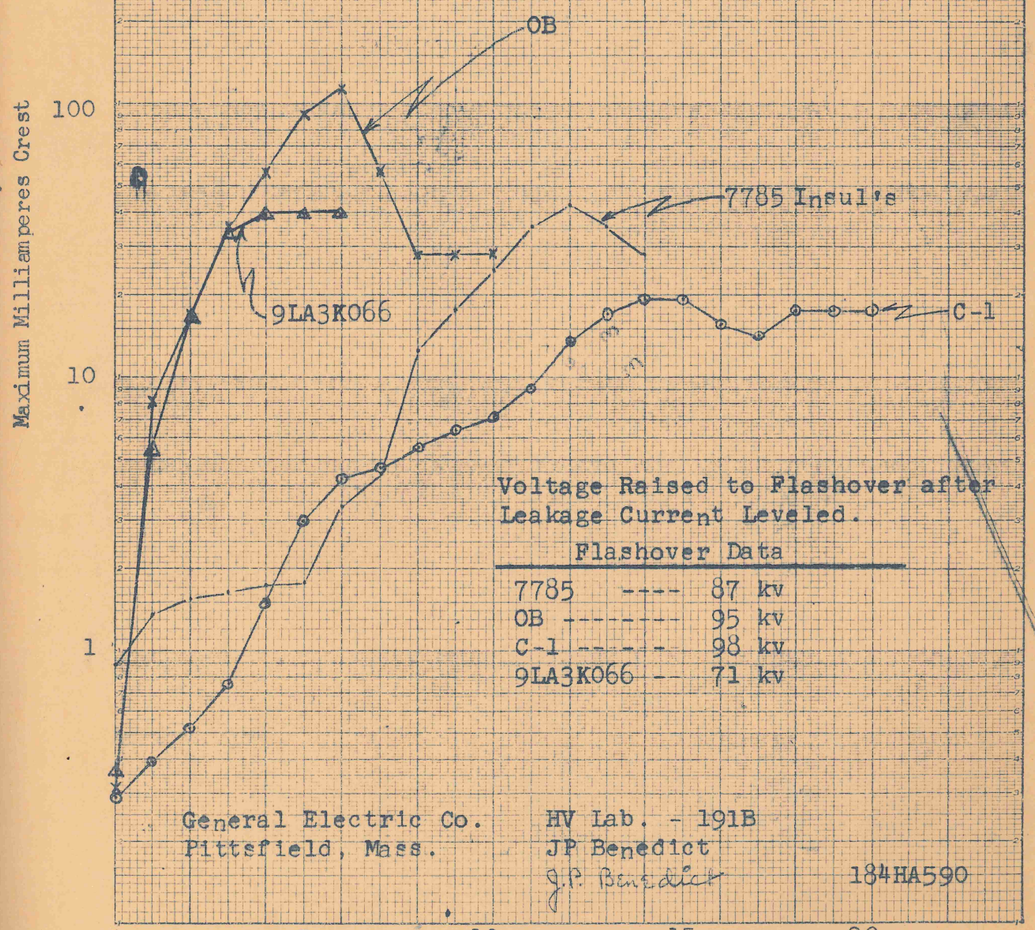

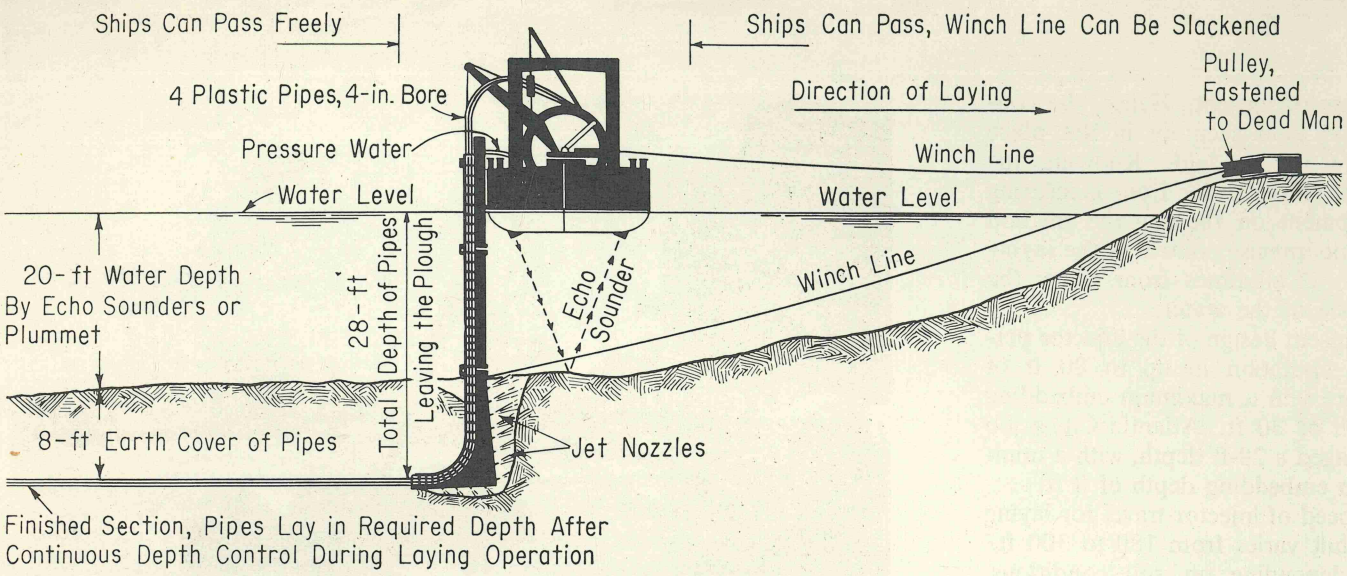

Conduits 'Hydro-Jet' Embedded for 750-Ft River Crossing

High density polyethylene conduit for 69-kv cable is currently being jet-embedded 8-ft below the bottom surface of Beach Thorofare waterway at Atlantic City Electric Co. A novel "hydro-jet" method of embedding the conduit is being employed for the job by the job-contractor, Harmstorf Corp, Larchmont, NY.

The project involves a distance of 750-ft at the point of waterway crossing. Four, 4-in. I.D. high density polyethylene conduits (0.45-in. wall thickness) have been jet-laid to date. Sixteen of them will eventually be installed in four separate cuts.

In contrast to conventional methods used in laying underwater conductor conduit or cable, the hydro-jet method does not require removal of soil with a dredge and its subsequent replacement, is not subject to "filling-in" (as in a dredged-trench) before the conduit or cable is laid: and, the method does not rely on the skill and physical stamina of divers. Furthermore, and of significance is the basic advantage of being able to efficiently and economically embed conduit under the river bottom.

The use of "buried" plastic conduits to house the cable permits the use of more flexible, less expensive unarmored cable. Also, spare conduits can be buried at the time of installation, so that additional cables can be pulled through the spare conduits at a later date when service is expanded. Idle investment in spare conduits is low. Removal of cable for repair or replacement is simple.

Cable embedding begins with the "hydro-jetter" equipment positioned just outside the "near-shore" sheet piling; with winch-control lines rigged from both the near and far shore; and, with the four-conduit lines threaded from its source coil around the outboard side of the tug and down through the injector housing and conduit guide section.

The essential part of equipment required for hydro-jetting is the injector. It includes a high-pressure water section and a conduit guide section. At the leading narrow edge of the injector, in the direction of travel, and at its bottom, water jets are provided.

As the injection jets are pressurized to about 170 psi, a narrow cut of controllable depth is made into the bottom of the body of water and the conduit is simultaneously laid along the bottom of the cut—the winch lines from the far shore move the "hydro-jetter" along its laying route.

This bottom "trench" is produced primarily by the action of high-power water jets. The soil loosened by the jets, temporarily in suspension in the surrounding water, settles rapidly and immediately starts to embed the conduit laid along the

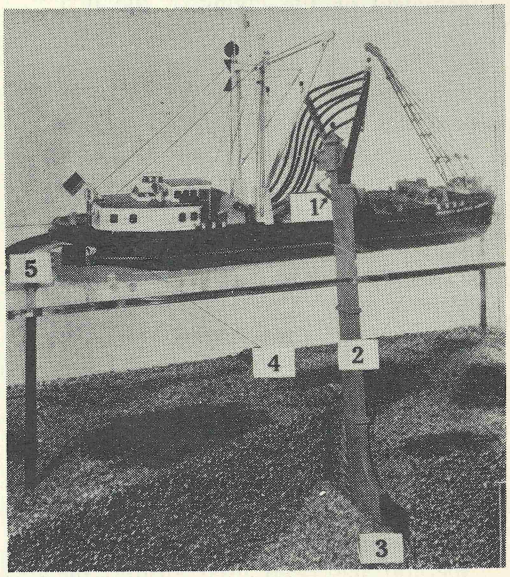

HYDRO-JETTER UNIT: 1-water-pressure hose; 2-injector; 3-plastic conduit to be embedded in river bottom; 4-winch line; 5-free-running conduit coils

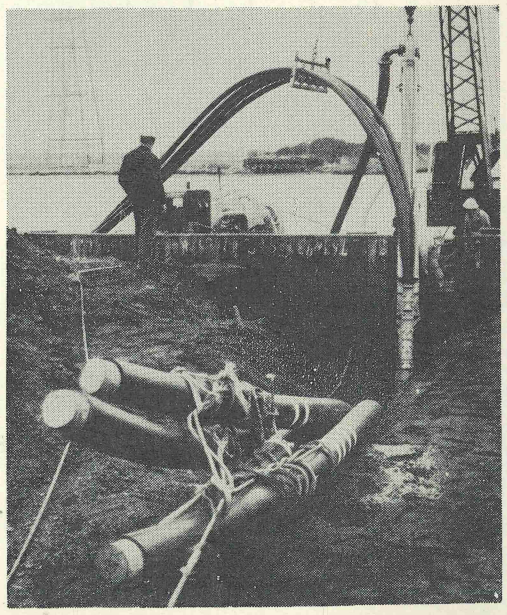

Reprinted from December 16, 1963 Issue of ELECTRICAL WORLD
© Copyright 1963, McGraw-Hill Publishing Co., Inc.
All Rights Reserved

bottom of the cut. Hence, the conduit is held securely in the place where it was laid. Knowing the depth of the water from measuring equipment on the tug the method permits precise control of the laying depth at all times from above the surface of the water.

Present design of the injector permits operation in up to 80 ft of water, with a maximum embedding depth of 30 ft. Atlantic City's job averaged a 28-ft depth, with a minimum embedding depth of 8 ft.

Speed of injector travel for laying conduit varies from 180 to 300 ft/hr, depending on soil conditions. An average rate of 200 ft/hr was achieved on the laying of the first four conduits at Atlantic City Elec.

The high density polyethylene conduit embedded for this job was manufactured and supplied by the Triangle Conduit & Cable Co, Inc, New Brunswick, NJ. Hercules Power Co, Willminton, Del, supplied Triangle with their Hi-Fax raw-polyethylene compound. The approximate 5-in. O.D. conduit, supplied in 750-ft lengths (11-ft, 4-in. I.D. 13-ft, 7-in. O.D. coils) was transported to the worksite on flat bed over-the-road trailers.

While the job at Atlantic City involves a 4-in. I.D. conduit and a crossing-length of 750 ft the Harmstorf hydro-jet cable burying method has been used around the world for distances up to 16 miles, and for water and gas pipelines, as well as electric cable.

To date about 260 miles of cable and about 100 miles of plastic conduit and pipelines have been hydro-jet embedded.

Rudolf Harmstorf G.M.B.H. of Hamburg, Germany, (founded in 1865) is the parent company of the recently organized Harmstorf Corp.

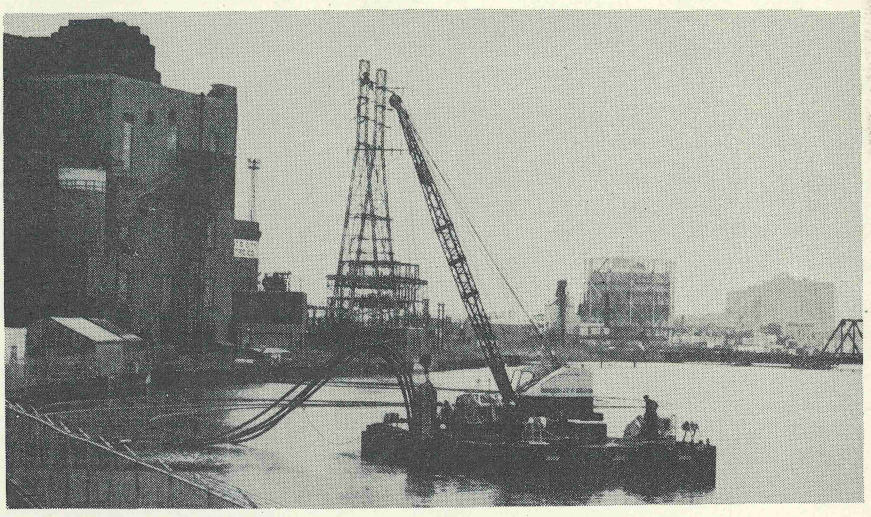

FOUR 4-IN. I.D. CONDUITS feed into the injector to be buried 8-ft under "bottom"

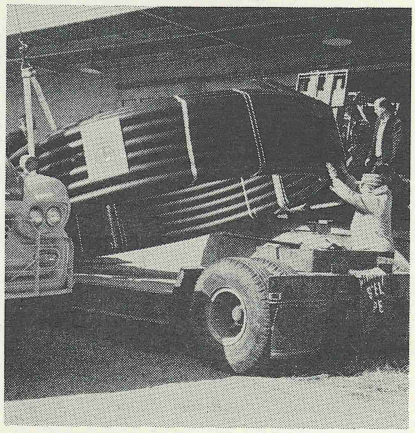

PLASTIC CONDUIT, in 750-ft lengths, is shipped to work-site in 14-ft OD coils on over-the-road flat-bed-trailers

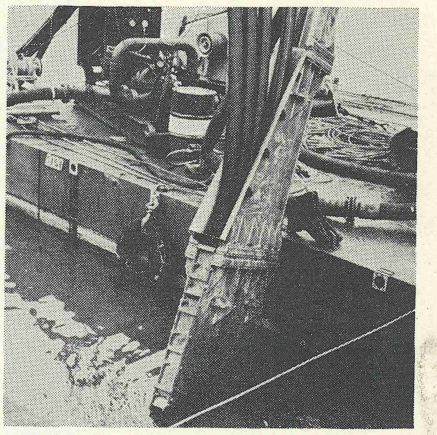

INJECTOR, including high-pressure water section, conduit guide section and jet nozzles, is depth-controlled

Please direct inquiries to:

HARMSTORF CORPORATION CABLE CONSULTANTS CORPORATION

7 Woodland Avenue

Larchmont, New York

Telephone: 914-834-6164

TWX: 914-835-1874

G. Raymond Hoffman
Texas Power & Co.

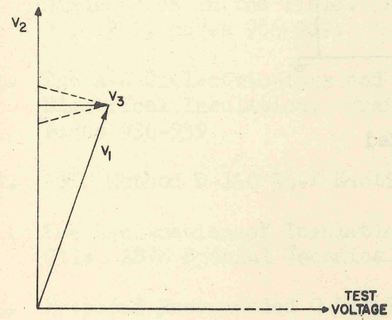

Figure 4. Phasor Diagram - Component Separation Method

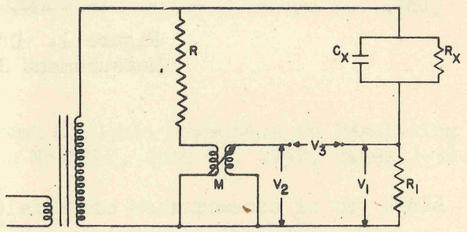

Figure 5. Component Separation Circuit with Mutual Inductor

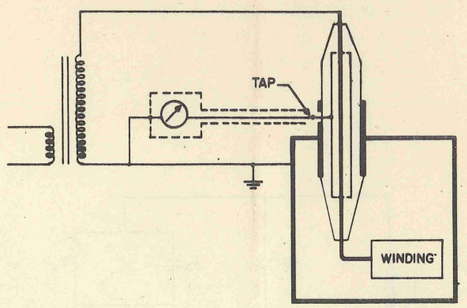

Figure 6. Simplified Circuit Diagram of Ungrounded Specimen Test on Transformer Bushing

Conference Paper

THE DEVELOPMENT OF POWER FACTOR MEASUREMENT OF INSULATION IN THE FIELD

E. H. Povey
Member AIEE
Doble Engineering Co.
Belmont, Mass.

A paper recommended by the AIEE Special Instruments and Auxiliary Apparatus Committee for the AIEE Winter General Meeting, New York, N. Y., February 2-7, 1958. Manuscript submitted October 14, 1957; made available for printing November 19, 1957.

Price: 40¢ To Members
80¢ To Nonmembers

(5¢ per copy additional if first class mailing desired)

All Rights Reserved by the
American Institute of Electrical Engineers
33 West 39th Street, New York 18, N. Y.
Litho in USA

Paper No. CP
58-49

THE DEVELOPMENT OF POWER FACTOR MEASUREMENT OF INSULATION IN THE FIELD

E. H. Povey

INTRODUCTION

The periodic measurement of the power factor of insulating units of large electric transmission systems has become, for a majority of such systems, an established practice in their maintenance procedures.[1] Equipment for making test measurements on insulation under field conditions has now been available for over twenty-five years, and measuring techniques have been developed and improved during this time. The original purpose of the test, which was to identify deteriorated terminal bushings before failures could cause system outages, has been greatly expanded. Interchange of information obtained from test results has been encouraged both among system operators and between them and equipment manufacturers, and insulation design has thereby been influenced. Some of the progress in test techniques and in insulation design over the past quarter century is herein described, with a brief review of earlier work.

SHIELDING

Insulation tests in a power system substation must usually be made in the presence of strong electric fields and with a permanent ground on one terminal of the unit under test. Stray currents induced in the measuring circuit by the electric fields, and leakage currents from the circuit to ground, made measurements practically useless until the development of the double shielding system shown in Figure 1. An inner shield prevents leakage from the circuit to ground and an outer shield protects the circuit from external electric fields. This development marked the start of successful insulation testing in the field.[2]

VOLTMETER - AMMETER - WATTMETER METHOD

Apart from the problem of shielding, the measurement of insulation power factor and dielectric loss at power frequency requires considerable care. The power factor of terminal bushing insulation is in the order of 1% and dielectric losses are in the order of 100 milliwatts at a test voltage of 10 kv. A measurement in this range would normally be made in the laboratory by a special bridge such as the Schering bridge. For field testing of insulation, however, it was decided that an adaptation of the voltmeter-ammeter-wattmeter method would offer the advantages of more rapid measurement and of greater familiarity to power system maintenance personnel. This method also provides current and loss values which are essential in some types of data analysis, and although power factor must be calculated, the calculation is simple.

Development of the voltmeter-ammeter-wattmeter method for insulation measurements continued during several years of use in the field. The wattmeter in particular was a problem on account of the low power factor requirement. By suspending the movement so that the pivots could be lifted from the jewels during transport, it was possible to obtain a 2.4 watt scale for a test voltage of 10 kv and a current of 10 milliamperes, or a maximum range power factor of 2.4%. This figure may be compared with a normal maximum range power factor of 50%, or the 20% range of special low power factor wattmeters. The wattmeter current coil was wound

for direct connection into the circuit to avoid phase-shift problems that would be introduced by current transformers.

For some years the wattmeter potential circuit was supplied from the primary of the step-up transformer that supplied the test voltage. This expedient, adopted as a concession to portability, required that the test results be corrected for losses in the transformer as well as for I^2R losses in the current coil of the wattmeter. The magnitude of these internal losses was small for the current of a single terminal bushing, but when winding insulation was tested, even that of a small instrument transformer, the internal losses were often large compared with the loss to be measured. To remedy this situation, the compensating circuit shown in Figure 2 was devised, in which a portion of the current flowing through the wattmeter current coil is directed through the potential coil in a direction to reduce the wattmeter reading. The magnitude of the reduction depends on the square of the current and the design of the apportioning network. The network may therefore be designed to reduce the wattmeter reading by I^2R, where R is the equivalent resistance of the transformer plus the resistance of the wattmeter current coil. The compensating circuit worked well but was eventually abandoned when the wattmeter potential circuit was redesigned to be supplied directly from the secondary of the step-up transformer through a resistance multiplier of 500,000 ohms.

COMPONENT SEPARATION METHOD

The voltmeter-ammeter-wattmeter method, while still in use today, is gradually being superseded by the component separation method. This method utilizes a partially balanced network and combines to some extent the advantage of the direct-reading wattmeter with the accuracy of bridge methods.[3] A circuit illustrating the component separation method in simplified form is shown in Figure 3. The test specimen is represented by the parallel circuit Cx and Rx, while C_2 is a capacitor having no appreciable loss. Resistors R_1 and R_2 are chosen such that V_1 is smaller than V_2 and both are insignificant fractions of the test voltage. In the test procedure a vacuum-tube voltmeter (VTVM) is first used to measure V_1. The current through the test specimen may be calculated as V_1/R_1, or may be read directly by providing the VTVM with a scale calibrated in current for the selected value of R_1. The voltmeter is next connected to measure V_3, and the slider on R_2 is adjusted to include that portion of V_2 which results in a minimum value for V_3. The minimum reading represents to a high degree of accuracy the voltage drop across R_1 due to the resistive or in-phase component of the specimen current; the voltage drop across R_1 due to the capacitive or quadrature component of the speciman current is balanced out by a portion of the quadrature voltage drop across R_2 due to the capacitive current of C_2. If the VTVM has been provided with a current scale as explained above, the minimum reading as read on this scale is the resistive on in-phase component of the specimen current. The loss in the specimen is the product of the in-phase current and the test voltage. Here again calculation can be avoided by providing the VTVM with a watts scale for a selected value of R_1 and a selected test voltage.

The phasor diagram in Figure 4 indicates how the minimum reading identifies the in-phase component. The minimum value of V_3 occurs when V_3 makes a right angle with V_2 or is in phase with the test voltage, as shown. The dotted lines show the greater values of V_3 if its angle with V_2 is acute or obtuse.

A modification has been made to the circuit of Figure 3 to obviate the difficulty of finding a capacitor for C_2 which will withstand test potentials up to 10 KV, be small in size for portability, and yet have no significant loss. In the modification (Figure 5) the capacitor is replaced by a high-grade resistor R, and the resistor R_2 is replaced by a variable mutual inductor M. The primary impedance of the inductor is insignificant compared with R, so that the current passing through the primary is substantially in phase with the test voltage and develops a quadrature voltage V_2 across the secondary terminals of the inductor. In the test procedure for finding the minimum value of V_3, the magnitude of V_2 is varied by changing the coupling between the windings of the inductor. The modification has proven to be quite stable with time and offers an infinitely smooth adjustment.

The component separation method not only approaches the accuracy of bridge methods but also retains their flexibility in regard to ranges and test voltages. For example, one type of instrument using the component separation method has full scale current ranges from 1 milliampere to 10 amperes, while another is designed to measure at any test voltage from 2 kv to 50 kv. Other instruments are designed for 100 volt test work, and still others are made to read directly in power factor with a low range full scale deflection for 1% power factor.

INSULATION DEVELOPMENTS AFFECTING MEASUREMENTS

Improvements in insulation systems have taken place concurrently with improvements in test equipment, with one field of endeavor often influencing the other. The early tests on terminal bushings disclosed the unsatisfactory life of cork gaskets used to seal bushing caps against entrance of moisture. The cork gasket was soon supplemented or replaced by synthetic rubber, and later improvements led to sealing by a soldering technique.

The use of rolled, resin-bonded paper for the main insulation of bushings has declined in this country during late years for high-voltage application. Unless great care is taken in the winding of the paper, voids are included in the insulation which ionize under high electric stresses and lead to eventual failure. The trend has been to a more porous paper structure oil impregnated and immersed in oil. The oil fills in any voids which might have resulted from the winding process. The use of varnishes in transformer assembly has been restricted, and the use of porous paper has been increased. Drying procedures used on paper and oil before impregnation have been improved, in the case of both bushings and transformers. Paper impregnated with dry oil has a very low power factor. Its increasing use has reduced the magnitude of power factors usually encountered in insulation testing from a range of 1% to 5% to a range of 0.3% to 2% for high voltage insulation.

The growing use of oil as an integral part of insulation has prompted an intense study of the material. Development of reclamation methods, additives, oxidation and moisture content tests for oil, while a direct consequence of insulation testing, is outside the scope of this paper.[4]

SPECIAL BUSHING TEST TECHNIQUES

Bushing design and test techniques have been combined to solve one important testing problem: the testing of a bushing which is an integral part of a transformer or circuit breaker.[5] The first successful tests of this type were on transformer bushings of the draw-lead type. In small transformers the draw lead

could be dropped entirely clear of the bushing, and the bushing could then be tested independently of the transformer winding. In larger transformers the draw lead could not be dropped, but in most cases could be disconnected and cleared from the bushing cap to withstand a potential difference of a few volts. A test technique was designed which allowed test potential to be applied to the bushing cap for measuring purposes while an equivalent potential was applied to the draw lead from a guard circuit. The high potential guard circuit gave the name "hot-guard" to this test technique. The circuit requires either that the measuring instruments be at test potential or that an isolating current transformer be used. Both methods of meeting this requirement have been used and the former has been found more accurate.

The "hot-guard" test has now been replaced by the "ungrounded specimen" test which followed the development of the potential device. The potential device requires a bushing with an electrode near ground potential, and a tap from the electrode accessible at the mounting flange. The main insulation of the bushing is located between the center conductor and the electrode. To make an ungrounded-specimen test on a bushing equipped with a potential device tap, the test circuit is so arranged that when test voltage is applied to the center conductor of the bushing, all currents from the conductor and connected parts (contact assemblies, transformer windings, etc.) which flow to ground are not measured. The current which flows through the main insulation of the bushing, however, is carried from the electrode at the tap by a separate test lead to the measuring circuit. Figure 6 shows a simplified cross section of a potential-device bushing in a transformer, and a test circuit for measuring the main insulation of the bushing by the ungrounded-specimen method. The convenience of being able to separate the main insulation of a bushing from a complex insulation structure by means of the capacitance tap arrangement is so great that many bushings which are not designed for use with potential devices are nevertheless equipped with electrodes for test purposes only. It has been found possible to devise a measuring circuit which can easily be switched for testing either by the standard (grounded-specimen) or the ungrounded-specimen test method.

CONCLUSIONS

The important areas of progress relative to the field testing of power system insulation during the last quarter century may be summarized as follows:

An improvement in measuring equipment in respect to accuracy and flexibility, and in particular the development of the component separation method for field testing.

A stimulus to the use of better processing methods as well as better insulation in power apparatus, resulting in a trend to insulations of lower power factors.

The increasing availability of provisions in power apparatus to facilitate testing, and in particular the general availability of a test tap in high-voltage terminal bushings.

REFERENCES

1. Results of a Questionnaire Covering Current Practices in Electrical Tests on Dielectrics in the Field. AIEE Committee Report. AIEE Transactions, Volume 70, 1951, pages 986-989.

2. The A-C Dielectric-Loss and Power-Factor Method for Field Investigation of Electrical Insulation. Frank C. Doble AIEE Transactions, Volume 60, 1941, Pages 934-939

3. ASTM Method D-150 54-T Section 22a

4. The Reclamation of Insulating Oils. Frank C. Doble Symposium on Insulating Oils, ASTM Special Technical Publication No. 152, June 23, 1952, pages 3-32.

5. Proposed Recommended Guide for Making Dielectric Measurements in the Field AIEE No. 62, Nov. 1956, Section 4.022 (2).

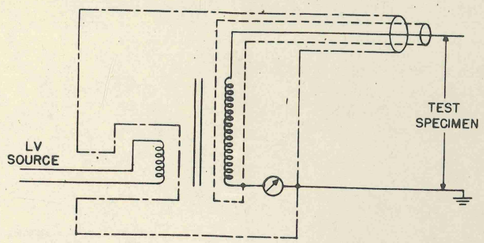

Figure 1. Double Shielded Measurement System

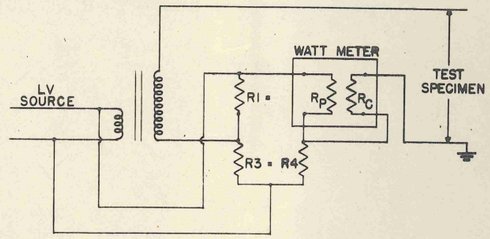

Figure 2. Compensated Wattmeter Circuit

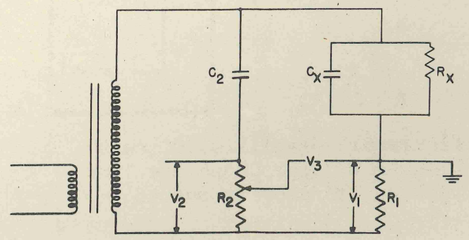

Figure 3. Simplified Circuit Diagram - Component Separation Method

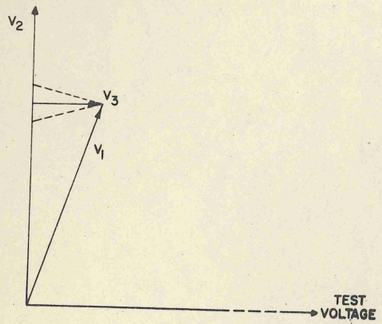

Figure 4. Phasor Diagram - Component Separation Method

G. Raymond Hoffman
Texas Power & Light Co.

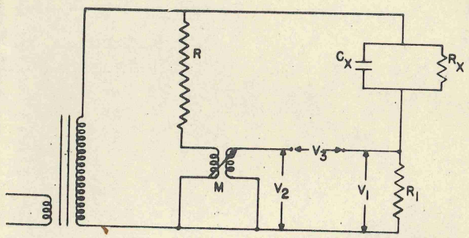

Figure 5. Component Separation Circuit with Mutual Inductor

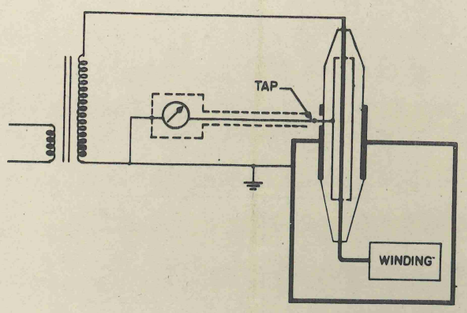

Figure 6. Simplified Circuit Diagram of Ungrounded Specimen Test on Transformer Bushing

Conference Paper

THE DEVELOPMENT OF POWER FACTOR MEASUREMENT OF INSULATION IN THE FIELD

E. H. Povey
Member AIEE
Doble Engineering Co.
Belmont, Mass.

A paper recommended by the AIEE Special Instruments and Auxiliary Apparatus Committee for the AIEE Winter General Meeting, New York, N. Y., February 2-7, 1958. Manuscript submitted October 14, 1957; made available for printing November 19, 1957.

Price: 40¢ To Members
80¢ To Nonmembers

(5¢ per copy additional if first class mailing desired)

All Rights Reserved by the
American Institute of Electrical Engineers
33 West 39th Street, New York 18, N. Y.
Litho in USA

Paper No. CP
58-49

GENERAL ELECTRIC
Research Laboratory
Room 1A66
P. O. Box 1088
Schenectady 5, N. Y.

B E Kingsbury
Insulator Dept.
General Electric Co. Box 57
Baltimore 3, Md.

GENERAL ELECTRIC
Research Laboratory
SCHENECTADY, N. Y.

APJ-5A
9-56 (50M)

Mechanics - Fracture

GENERAL ELECTRIC
Research Laboratory

PHYSICAL NATURE OF PLASTIC FLOW AND FRACTURE

by

J.J. Gilman

Report No. 60-RL-2410 M April 1960

CLASS 1

SCHENECTADY, NEW YORK

Reader Please Note

RESEARCH LABORATORY PRACTICE REGARDING CLASSES OF GENERAL ELECTRIC TECHNICAL REPORTS

CLASS 1: Available to anyone within the limits imposed by Government export regulations. COMPANY BUSINESS INTERESTS ARE NOT INVOLVED. Class 1 reports are listed and abstracted in TIS Briefs.

CLASS 2: Generally available to General Electric personnel for use within the Company. COMPANY BUSINESS INTERESTS ARE INVOLVED. Class 2 reports contain information in which the Company has a proprietary interest; hence, the information they contain should not be disseminated outside the Company. In order to make the information generally available *within the Company*, Class 2 reports are listed and abstracted in TIS Briefs (except in TIS Briefs sent abroad). Additional copies will be supplied to Company personnel on request of Research Information Section.

CLASS 3: Not generally available within General Electric. Class 3 reports contain information of a *highly proprietary nature*. SPECIFIC BUSINESS INTERESTS ARE INVOLVED. The distribution is limited to individuals within the Company specifically selected with reference to the subject. Requests for Class 3 reports are cleared with the management of the originating Research Department before being filled. Not listed in TIS Briefs.

CLASS 4: Available only to employees personally responsible for the Company's interests in the subject. *Highly proprietary*. SPECIAL BUSINESS INTERESTS ARE INVOLVED. Hence, the distribution is *rigidly* limited within the Company. Class 4 reports are issued in individually numbered copies, which should be returned to Research Information Section when they are not needed. Requests for Class 4 reports are cleared with the management of the originating department before being filled. Not listed in TIS Briefs.

GENERAL ELECTRIC

Research Laboratory

REPORT NO. 60-RL-2410 M

PHYSICAL NATURE OF PLASTIC FLOW AND FRACTURE

J.J. Gilman

April 1960

Published by
Research Information Section
The Knolls
Schenectady, New York

ABSTRACT

A review of current knowledge concerning the mechanisms of plastic flow and fracture written for nonspecialists. This report was prepared for the Symposium on Plasticity that will take place at Brown University in April 1960. It is one of a series being prepared by members of the Metallurgy and Ceramics Research Department that will review the "state of the art" in different technical fields. It discusses such topics as:

A. Plastic Flow

1. The Crystallography of Dislocation Motion
2. Kinetics of Dislocation Motion
3. Dislocation Nucleation and Multiplication
4. Dislocations and Macro-flow

B. Fracture

1. Nucleation of Cracks
   (a) In perfect crystals
   (b) By plastic flow

2. Propagation of Cracks
   (a) In elastic bodies
   (b) Effects of plasticity

Manuscript received April 4, 1960.

Physical Nature of Plastic Flow and Fracture

I) General Introduction

II) Plastic Flow - introduction to the unit process

A) The Crystallography of Dislocation Motion

1) Burgers vector
2) Line direction
3) Line energy
4) Glide planes
5) Motions of screw vs. edge dislocations

B) Kinetics of Dislocation Motion

1) The driving force
2) Observations of moving dislocations
3) Relation of dislocation velocities to yield stresses

C) Dislocation Nucleation and Multiplication

1) Nucleation
2) Regeneration
3) The density and distribution of dislocations in strained crystals

D) Dislocations and Macro-flow

1) Yield stress
2) Plastic instability during yielding
3) Strain-hardening

III) Fracture - introduction to the unit process

A) Nucleation of Cracks

1) Nucleation in perfect crystals
2) Role of surfaces in crack nucleation
3) Plastic flow as a crack former

B) Propagation of cracks

1) Griffith condition for propagation
2) Propagation in elastic bodies
   a) low speed
   b) high speed
   c) crystal imperfection
3) Effects of plasticity
   a) shape changes
   b) rate effects
   c) reduction of cohesive strength

PHYSICAL NATURE OF PLASTIC FLOW AND FRACTURE

by

J. J. Gilman

General Electric Research Laboratory
Schenectady, New York

INTRODUCTION

Although the processes of plastic flow and fracture have been studied for several decades by a host of able men, progress has been slow towards interpreting them in terms of molecular structure until recent years. The reason for the slow progress is that both processes are fundamentally heterogeneous in nature. Because of this, it is not possible to describe them adequately in terms of homogeneous quantities like stress, strain and strain-rate. In addition to these homogeneous parameters, it is necessary to have a knowledge of the numbers, distributions and rates of motion of the heterogeneities that are involved. The pertinent heterogeneities are called dislocations and cracks, and this paper will be a review of the state of our knowledge about them. The discussion will be aimed at getting as close to molecular phenomena as possible. However, some parts of the subject cannot be discussed in molecular terms without indulging in undue speculation. These parts will be considered in more macroscopic terms.

The idea that plastic flow and fracture are heterogeneous processes is quite old; what is new is the discovery and development of experimental techniques for observing dislocations and cracks. Early workers concluded that plastic flow and fracture could not be homogeneous processes for the following reasons: (a) they occur at stresses that are far too small (in the case of plastic flow of zinc, by a factor of 50,000 too small);

(b) they are very sensitive to the microstructure of a material; and (c) the observed values of the yield stress and fracture stress have large amounts of random scatter. Many workers had more or less vague ideas about these matters, but the first really clear conceptions of the heterogeneous natures of the processes were formed by A. A. Griffiths (1920) for the case of fracture,(1) and G. I. Taylor, E. Orowan, and M. Polanyi (1934) for the case of plastic flow.(2)

Griffith's idea, now known as his crack theory, is that fracture does not occur in one step, but rather, in two steps. First a crack grows to some critical size (now called the Griffith size) and then it quickly grows further until complete fracture has occurred. Griffith showed how the critical crack size could be calculated in a simple way, and then proceeded to confirm the calculation by experiments on glass.

Similarly, the idea of Taylor, Orowan, and Polanyi, now known as dislocation theory, was that plastic flow occurs in two stages; small regions of plastic shear appear and then grow through the crystals of a material. This process is illustrated by Figure 1. When a block of crystal is subjected to a shearing stress, it undergoes elastic distortion until somewhere within it some sliding starts. The geometric arrangement of the crystal requires that the amount of gliding be a definite amount equal to a translation distance of the crystal structure. This is necessary in order that the crystal structure be restored after the gliding process is complete. Thus, as in Figure 1, part of the material glides with respect to the rest by one unit of the crystal structure. This occurs uniformly over the cross-hatched portion of the glide plane, but not over the entire glide plane. The line which bounds the area over which glide has occurred, separating it from the un-glided area, is called a dislocation line. It has

this name because the displacement across the glide plane changes discontinuously at this line from a unit amount to zero.

Although the Griffith crack theory received early confirmation in the hands of Griffith himself, dislocation theory had a relatively long wait, and had to overcome much hostility before it was sufficiently well confirmed to be accepted. However, in the past few years several methods have been developed for making direct observations of dislocation lines. This has allowed measurements to be made of their properties as well as providing convincing evidence of their existence.

PLASTIC FLOW

When one speaks of plastic flow in the sense of materials mechanics, it is implied that crystalline materials are being considered because other types of materials do not usually exhibit the abrupt yielding at a critical stress, and the strain-rate insensitivity that normally characterize plastic flow. This macroscopic mechanical behavior of crystals is a direct reflection of the way in which dislocations behave within them. Thus the special mechanical features of plastic flow are deeply rooted in the atomic mechanism of the process.

A basic principle of plastic deformation in crystals is that the deformation changes the shape of the crystal without destroying the crystallinity of the material. Sometimes many imperfections are driven into a crystal by the process, but nonetheless the crystal preserves its crystalline character to as great an extent as possible. The experimental proof of this principle has been obtained by many workers by means of x-ray diffraction.

The fact that a crystal remains a crystal during plastic

deformation imposes severe limits on the number of ways that it is possible for a crystal to deform. Only two possibilities called translation-gliding and twin gliding exist, and only the first of these will be discussed in this paper. Translation-gliding occurs as shown in Figure 1. Layers of a crystal glide over one another by distinct amounts that are equal to, or multiples of, the unit crystal structure. In this way the geometric pattern of the crystal always comes back into registry after a gliding motion has taken place. Gliding does not usually occur on every plane of the crystal, but only on a few planes that are widely separated from each other. Therefore, the deformation that results is highly heterogeneous.

The layers of a crystal do not glide over one another rigidly like two blocks of wood. Instead, the gliding starts at some small local region: perhaps at a corner as in Figure 1. This makes the force that is needed to cause the gliding much smaller than it would be for rigid gliding. When the glided region has grown until it spreads completely across the crystal, the shape of the crystal becomes permanently changed as shown at the bottom of the figure. Before this happens, when the gliding has only spread over part of the crystal, there exists a boundary line (dislocation line) between the part that has glided and the part that has not. It represents the place where the glide displacement changes discontinuously from one crystal spacing to zero. As glide proceeds the dislocation-line moves forward with the edge of the glided region; if the glide process reverses, then the dislocation-line retreats.

Since glide occurs in jumps that are exactly equal to the size of the atomic pattern in a crystal, the part of the crystal that is above the glide plane and behind the dislocation-line in Figure 1 has been displaced forward by one pattern spacing. The displacement is constant over the glided area except where it

suddenly drops to zero at the dislocation-line. Although the entire crystal has elastic strains in it while glide proceeds, the normal crystal structure exists everywhere except in the immediate vicinity of the dislocation-line.

A single dislocation passing across a one centimeter cube of crystal would produce an offset of atomic size: $b \simeq 3\times10^{-8}$ cm. Since the height of the block is one centimeter, this represents a shear strain of only 3×10^{-8}. Thus if large amounts of plastic strain are to be obtained, the motions of a large number of dislocations will be involved. The total macroscopic plastic strain is given by the sum of all the small strains due to individual dislocations. Figure 2 is helpful in seeing how this is done. The figure shows some edge dislocations that have moved various distances through a unit cube of crystal. The total displacement of the top of the cube with respect to the bottom is Δ. This is made up of small displacements δ_i due to the individual dislocation motions. When a dislocation moves completely across the crystal it causes a displacement b, but before it starts the displacement is zero. Since b is very small compared with L or h, the displacement, δ_i, for positions of the dislocation, x_i, that are intermediate between $x_i = 0$ and $x_i = L$ will be proportional to the fractional distance, x_i/L, that the dislocation has moved. Therefore:

$$\delta_i = \frac{x_i}{L} b$$

summing up the small displacements:

$$\Delta = \Sigma\delta_i = \frac{b}{L} \sum_{1}^{N} x_i$$

where N is the total number of dislocations that have moved. Thus

the macroscopic shear strain, γ, is given by:

$$\gamma = \frac{\Delta}{h} = \frac{b}{hL} \sum_{1}^{N} x_i$$

Replacing the sum by the average, $\bar{x}$, times the number, and remembering that h and L are unity, we have:

$$\gamma = bN\bar{x}$$

where N is called the dislocation density and equals the number of moving dislocation lines that cut through a unit cross-section.

Often, it is more useful to consider the strain-rate rather than the total strain. It can be seen from the above equation that this is given by:

$$\frac{d\gamma}{dt} = bN\bar{v} \qquad (1)$$

where $\bar{v}$ is the average dislocation velocity.

A little reflection will convince the reader that the same expressions hold for a dislocation line that moves perpendicular to the plane of Figure 2. Hence, for a complete loop of dislocation line the macroscopic strain is proportional to the area swept out by the moving loop.

We can now see what information is required to describe plastic flow in terms of dislocations. We must know the crystal structure in order to have a knowledge of the displacement distance, b; we must know how many mobile dislocations are present so as to have a value for N; and we must know how fast the dislocations are moving on the average, $\bar{v}$. The quantities N and $\bar{v}$ will generally depend on stress, time, and temperature so these variations must also be known in order to have a complete description. The three basic parameters will be discussed in detail in succeeding sections and then their application to macro-scopic flow will be considered.

(A) The Crystallography of Dislocation Motion

(1) Burgers vector The direction in which a crystal prefers to glide is selected by a very simple rule. Of all the possible translation directions in a crystal, the one that is preferred to accomplish a deformation is the shortest one. An example of the application of this law to a real crystal is the case of iron shown in Figure 3. In iron, the direction of easiest translation-gliding is the direction that passes through two atoms along the diagonal of the cube. This is the shortest translation-distance that will restore the original pattern of the crystal after a unit of glide has taken place. The rationale of this law is simply that a crystal would rather make small jumps than large ones because less straining of the crystal results from small ones. In other words, the energy of a dislocation increases with increasing size of the unit of translation. This will be considered in more detail shortly.

The vector that describes the direction of translation-gliding and its magnitude is called the Burgers vector after J. M. Burgers who made important contributions to our understanding of the geometry of dislocation lines.[3] The Burgers vector, b, is usually the shortest translation vector of the unit cell of the crystal structure; it is about 3A. long for many crystals. In a continuous body, more general dislocation lines can exist with displacement vectors that vary continuously from one point to another, but this discussion is restricted to the case of dislocations in crystals.

(2) Line direction In addition to its Burgers vector, a dislocation line has a direction (its line tangent). In general, this direction makes an angle somewhere between 0 and 90° with the Burgers vector. However, the two extreme cases, 0 and 90°,

have been given special names because they represent quite distinct and characteristic distortions of the crystal structure. When a dislocation line lies parallel to its Burgers vector, it is called a screw dislocation. When it lies perpendicular to its Burgers vector it is called an edge dislocation.

The reasons for the names "screw" and "edge" may be seen in Figure 4. Around the screw orientation of a dislocation line the planes of atoms are warped so as to form a helical or screw-like ramp. Looking along the dislocation line, if the helix advances one plane when a clockwise circuit is made around it, it is said to be right-handed; if the reverse is true, it is left-handed.

At the edge orientation of a dislocation-line, an extra half-plane of atoms is present. In effect this half-plane was initially on the outside surface but has been pushed into the center of the crystal. Most of the distortion in the crystal is near the edge of the extra half-plane; hence the name. If the extra half-plane is above the glide plane, an edge dislocation is said to be positive; if the half-plane is below the glide plane an edge dislocation is negative.

(3) Line energy It was mentioned previously that dislocations with short Burgers vectors are preferred in crystals because they have low energies. Now we shall consider the factors that determine the energies of dislocation lines. The edge and screw orientations will be considered separately. Furthermore, it is conventional to divide the line energy into two parts for convenience in calculation. At the very center of a dislocation the positions of the atoms are so severely strained that elasticity theory does not apply. This region is called the core and atomic cohesion theory must be used to

calculate its energy. Outside the core region, of radius r_o in Figure 5, the strains are small enough to be treated by elasticity theory. This region is called the elastic field of a dislocation line. It usually contains most of the total energy.

For a screw dislocation, the energy of the elastic field can be calculated quite simply as follows. Consider the cross-hatched shell in Figure 5. Since the displacement of the two ends of the shell is b and its circumference is $2\pi r$, the elastic shear strain in it is $\gamma = b/2\pi r$. The shear strains in other directions and the dilatations are all zero. In a body of shear modulus, G, the shear strain energy per unit volume is $\frac{G\gamma^2}{2}$ so the energy of the shell is:

$$dH = \frac{Gb^2}{4\pi}\left(\frac{dr}{r}\right)$$

Integrating from the core radius, r_o, to the external radius of the body, R, we have:

$$H_s = \frac{Gb^2}{4\pi} \ln R/r_o \qquad (2)$$

For an edge dislocation the result is quite similar, but the analysis is more difficult, so we simply state the result:

$$H_e = \frac{Gb^2}{4\pi(1-\gamma)} \ln R/r_o \qquad (3)$$

where γ is Poisson's ratio. These energies are per unit length of dislocation line, and since, for many crystals, $G \simeq 5\times10^{11}$ d/cm^2, $b \simeq 3\times10^{-8}$ cm, $r_o \simeq 5\times10^{-8}$ cm, and $R \simeq 1$ cm, their magnitudes are about 2×10^{-4} ergs/cm or 6×10^{-12} ergs/atom length.

The core energies of dislocation lines are not so easily calculated. The calculation requires a detailed knowledge of interatomic forces which is not available for most crystals. A

favorable case is that of ionic crystals where a very good, and yet simple theoretical model is available. Ionic crystals can be considered to consist of hard, rather rigid spheres which carry positive and negative charges. The spheres of opposite charge are attracted to one another by electrostatic forces, and the minimum distance between them is determined by their size. This simple model of an ionic crystal is quite successful in predicting the cohesive energies and elastic constants of several crystals and it has been applied by Huntington, Dickey and Thomson[4] to dislocation cores. These authors considered the case of NaCl crystals and they conclude that for a screw dislocation the core energy is $\sim 0.24 \times 10^{-12}$ ergs/atom length, and for an edge dislocation it is $\sim 0.62 \times 10^{-12}$ ergs/atom length. Thus the core energy is only 5-10% of the total energy for a single dislocation in a crystal of 1 cm. radius. In a crystal of sufficiently small size the core energy becomes comparable with the energy of the elastic field, but this requires a crystal size of only several atomic diameters.

Equations (2) and (3) show that the elastic energy (and hence substantially the total energy) of a dislocation line is proportional to the square of the Burgers vector. This accounts for the preference of crystals towards glide in the shortest possible translation direction. In this way they can employ dislocations of lowest energy per unit length.

(4) Glide planes The elastic strain field of a dislocation line does not vary significantly as the dislocation moves from one position to another in a crystal. The core energy does vary with position, but, since it is a small fraction of the total energy, its variation causes only a small variation of the total energy. This is the reason why dislocations are so extremely mobile in most crystals. Variations in the core energy cause a small, but

finite, resistance to the motion which is very sensitive to the structure of the core. Since the core structure depends on the plane of an edge dislocation, this means that the force that is needed to move an edge dislocation through a crystal is very sensitive to the glide plane of the dislocation. Hence, in most crystals there are preferred planes for glide.

In some crystals a particular crystallographic plane is strongly preferred for glide (for example in zinc), and in others there is very little preference (for example in silver chloride). Experimental data illustrating the preference of glide on (0001) basal planes over $\{10\bar{1}0\}$ prismatic planes in zinc are given in Figure 6. For both glide planes, the close-packed direction, $\langle 11\bar{2}0\rangle$ is the glide direction, so only the change of the glide plane causes the effect in the figure. It is not surprising that zinc prefers to glide on the basal planes because these are the most widely separated planes in its structure so the chemical bonds perpendicular to them are the weakest ones. The bonds perpendicular to the prismatic planes are the strongest ones in zinc, so it is difficult for glide to occur on them.

From the case of zinc one might think that the most widely spaced planes in a crystal would always be the glide planes. Martius and Chalmers[5] have pointed out that this is true for most metals, but it is not true in general. A notable exception is rock salt (NaCl). It prefers to glide on $\{110\}$ planes even though the $\{100\}$ planes in its structure are more widely spaced. On the other hand, some compounds with the same crystal structure as rock salt prefer to glide on the expected $\{100\}$ planes; galena (PbS) is one of these as indicated in Figure 7. Thus the plane of a crystal on which dislocations prefer to glide is sometimes determined by rather subtle details of the atomic structure and binding.

(5) Motions of screw vs. edge dislocations An important distinction between the behaviors of edge and screw dislocations is that screw dislocations can glide on any plane, whereas edge dislocations cannot (Figure 8). An edge dislocation cannot move upwards or downwards from its initial glide plane because such movements would require the extra half-plane of atoms that is associated with it (Figure 4) to get longer or shorter. Since the half-plane contains a definite number of atoms, addition of atoms to it or subtraction from it would be required in order to change its length. This can and does happen at high temperatures when diffusion is rapid in a crystal, but it occurs to a negligible extent at low temperatures.

In contrast to the edge type of dislocation, the screw-type is cylindrically symmetric about its axis. Therefore, all directions around a screw dislocation look essentially the same, so it is not restricted to gliding on a single plane. This gives screw dislocations comparative freedom of motion and has an important bearing on the overall plastic behavior of crystals. Of course, in crystals that are highly anisotropic, screw dislocations will prefer to move on the more weakly bonded planes, but they can move to other planes if circumstances favor it.

(B) Kinetics of Dislocation Motion

From the point of view of plastic flow, the outstanding property of a dislocation is its mobility. Crystals, such as copper and zinc, in which dislocations are very mobile are easily deformed, whereas crystals like silicon and aluminum oxide are difficult to deform because large stresses are required to move the dislocations in them. In other words, the yield stress of a crystalline material depends intimately on the

mobility of dislocations in it.

Dislocations tend to be very mobile for the reason that is illustrated schematically in Figure 9. When no dislocation is present, as in Figure 9a, it is necessary to stretch and then break all of the bonds across the glide plane AB in order to translate the top half of the crystal over the bottom half. The resistive stress of the stretched bonds increases elastically at first (following Hooke's law), passes through a maximum, and then drops to zero when the top half of the crystal has been translated by one-half of the crystal spacing, b/2. Then the stress becomes attractive until it drops to zero when translation is complete. This variation of stress can be approximated by a sine function:

$$\tau = \tau_m \sin \frac{2\pi x}{b}$$

where τ_m is the maximum stress occurring when the displacement is $x = b/4$. For small x, the elastic strain is $\gamma = \frac{x}{b} = \tau/G$ (G = shear modulus) and $\tau \simeq 2\pi\tau_m(\frac{x}{b})$. Hence, $\tau_m \simeq G/2\pi$. This is a very large stress, especially when it is compared with the measured yield stresses of crystals which may be 1000 times smaller.

In contrast to the case above, when a dislocation is present, resistive and attractive forces act at the same time and approximately cancel each other. Figure 9b shows an edge dislocation that is in a symmetric position in a crystal so that the resistive forces on the left side of it are balanced by attractive forces on the right. If it moves halfway to the next position it takes on another symmetric configuration (Figure 13c) and once more all the forces are balanced. Thus a dislocation almost always has a system of balanced forces acting on it, and only a small biasing stress needs to be applied in order to cause a dislocation to move forward or backward.

The forces on a dislocation are not precisely balanced in

every position that it can have, but detailed calculations are necessary to estimate the small unbalanced forces. The calculation is carried out by determining the potential energy of a dislocation as a function of position in its direction of motion. Then the derivative of the potential energy with respect to the distance gives the force that is necessary to make the dislocation move. The simplest of this type of calculation, called the Peierls-Nabarro theory,[6] gives the result:

$$\tau_g \simeq 4\pi\tau_m\left(\frac{b}{w}\right) e^{-2\pi\left(\frac{w}{b}\right)} \qquad (4)$$

where w = width of the dislocation; defined as the distance along the glide plane where the displacements are greater than 50%. The dislocation width is estimated to be a few times b so τ_g is very sensitive to the value of w and is always much smaller than τ_m, the stress for simultaneous gliding of the whole crystal.

(1) The driving force Shear stress supplies the force that tends to make dislocations glide independently of other components of the applied stresses. This has been discussed theoretically by Nabarro,[7] and it is demonstrated by the experimental law known as Schmid's Law of the Critical-resolved-shear-stress.[8] Two types of experiments have shown that plastic flow begins in crystals when the shear stress on the glide planes reaches a critical value that is independent of the other stress components. One test has been to measure the yield stresses of identical crystals with and without superposed hydrostatic pressures. It has been found by Haasen and Lawson[9] that pressures up to about 5000 atmospheres have very little effect on the yield stresses of Al, Cu, and Ni although such pressures do affect strain-hardening.

The critical shear-stress criterion has also been tested by performing tensile tests on crystals that had various orientations

with respect to the tension axis. The important shear stress is the one on the preferred crystallographic glide-plane that acts in the preferred crystallographic glide-direction. This is readily calculated if the orientation of the crystal with respect to the axis of tension is known. If the angle between the glide plane and tension axis is α, and the angle between the glide direction and the tension axis is β, then the shear stress on the glide plane in the glide direction caused by a tensile stress, σ, is given by $\tau = \sigma \sin\alpha \cos\beta$. Therefore, if plastic flow starts when τ reaches a critical value equal to τ^*, the tensile stress at which flow begins should be $\sigma^* = \tau^*/\sin\alpha\cos\beta$. Measurements of cadmium by Andrade and Roscoe[10] and of zinc by Jillson[11] are compared with this relation in Figure 10. The data follow the relation very well, meaning that normal stresses have little or no effect on plastic flow in crystals. The normal stresses on the glide planes in the tests of Figure 10 varied by a factor of 120.

The force that a shear stress exerts on a dislocation line can be obtained by considering an isolated dislocation in a unit cube of crystal.[7] Let a shearing force F act on the crystal. Now let the dislocation line move a distance dx. Work is done on the dislocation in the amount fdx, where f is the force on the dislocation. At the same time, when the dislocation moves by dx it causes an external displacement bdx as was shown in the foregoing section. Thus the work done by the dislocation is Fbdx. Equating the two amounts of work and remembering that F is a shear stress, τ, because it acts on a unit area, we have:

$$f = \tau b \qquad (5)$$

This force is the same for both edge and screw dislocations and acts in a direction normal to a dislocation line. Since it is a force per unit length, it is analogous to the pressure on a

membrane although it is one-dimensional in character.

(2) Observations of Moving Dislocations Several techniques have been developed in recent years for observing dislocations in crystals. They include x-ray microscopy, transmission electron microscopy, decoration with precipitates, and etch-pitting. The last method has been used to make quantitative measurements of dislocation motions by Johnston and Gilman,[12] and by Stein and Low.[13] Isolated individual dislocations have been put into LiF crystals by special methods.[12] These dislocations can then be etched to locate their initial positions. Next they can be moved by shear stresses of known magnitudes that last for known lengths of time. Afterwards, their final positions can be revealed by further etching treatments (Figure 11). From the distances between the initial and final positions of the dislocation lines and the time durations of the applied stresses, average velocities for the dislocation motions are obtained. By applying stress pulses that varied in length from 10^{-6} to 10^{+5} seconds, and in magnitude from 0.2 to 20.0 kg/mm^2, Johnston and Gilman[12] observed dislocation motions over a very wide range of velocities from about 10 atom distances per second to more than 10^{12} atom distances per second. Results of their measurements of velocities as a function of stress are shown in Figure 12.

Figure 12 demonstrates the high mobilities of dislocations. They move at velocities at least as high as 5×10^4 cm/sec., but probably do not move faster than the velocity of sound, because they are elastic disturbances similar to elastic waves. They can also move very slowly; as little as a few atom distances per second. An important feature of their behavior is that a certain critical stress is required to put them in motion. Once the critical stress is exceeded the velocity increases very

rapidly with small stress increases. The data also show that edge dislocations move about 50 times faster than screw dislocations over most of the velocity range, but the two velocities are not independent because the dislocations have the form of half-loops. Thus each edge dislocation is connected to a screw dislocation and the edge component of a loop can move only a limited amount faster than the screw component. Otherwise the radius of curvature near the edge component would become so small that a large back stress would act on it, tending to retard its motion.

A quite significant feature of the data of Figure 12 is the quasi-viscous nature of the dislocation motion. The velocities that are shown in the figure are steady-state ones so all of the work that is done on the dislocations as they move is being dissipated during the motion. This work is the force per distance moved or τb^3 per atomic distance moved per atom length of dislocation line. Since dislocation motion is so strongly damped by a crystal, it may be said that a crystal possesses a plastic resistance to dislocation motion. This plastic resistance appears to be finite in perfectly pure crystals, but it is extremely sensitive to impurities, temperature, radiation damage, strain-hardening, etc. It has been discussed in some detail by Gilman.[14]

Figure 13 shows the effects of temperature and radiation damage on dislocation velocities in LiF crystals. The primary effect of decreasing the temperature or introducing radiation damage is to shift the dislocation velocity vs. stress curves to higher stresses. The slopes of the curves change very little. Strain-hardening (Figure 14) has a similar effect.[15] In all these cases it may be seen that the effect of a treatment that changes the "hardness" of a crystal is to increase the stress

that is needed to make dislocations move at a certain velocity. This is not only true for lithium fluoride crystals but has also been observed by Stein and Low[13] in steel. Their data for dislocation velocities at various temperatures in silicon steel (Fe + 3% Si) is given in Figure 15. Just as in LiF the primary effect of decreasing the temperature is to shift the velocity vs. stress curve to higher stresses.

(3) Relation of dislocation velocities to yield stresses

The dislocation velocity data strongly suggest that the macroscopic yield stress of a crystal is simply the stress at which dislocations begin to move at some moderate velocity. This is further substantiated by the fact that one can correlate yield stresses with stresses needed to obtain moderate dislocation velocities. Such a correlation is shown in Figure 15, where the stress to move dislocations in LiF and Fe-Si at a velocity of 10^{-6} cm/sec. is plotted against the macroscopic yield stresses of the crystals under the same test conditions. A good linear correlation is observed.

We have seen above that many factors determine how much stress is needed to make dislocations move at a certain speed in a particular crystal. This tends to make plastic behavior unpredictable in terms of the underlying atomic structure of crystals. However, some correlations between atomic binding and dislocation behavior can be found and more will no doubt emerge as more experimental data on dislocation motions are obtained. An example is the role of the elastic modulus or bond stiffness. Equation (4) predicts that the stress needed to move a dislocation through a crystal should be proportional to the elastic modulus of the crystal. For most crystals this proportionality is obscured by the effects of impurities and temperature, but data for face-centered-cubic metals indicate

that it exists. The f.c.c. metals are a particularly favorable case because they are mostly noble metals and hence can be prepared in quite pure form. Furthermore, low temperature data are available for both their elastic moduli and their yield stresses (or hardnesses). Koster[16] has measured many of the elastic moduli, and various authors have measured low temperature hardnesses; especially Druyvesteyn.[17] Figure 17 shows how well the yield stresses of pure f.c.c. metals correlate with their elastic moduli. Both sets of data are for -200°C in order to minimize the effect of temperature (data for 0°K are not available).

(C) Dislocation Nucleation and Multiplication

When a crystal undergoes a moderately large amount of plastic flow the number of dislocations that must move inside the crystal is quite large. For example, consider a one centimeter cube of crystal. Then the maximum average distance for dislocation motion is one centimeter. According to Equation (1), if the crystal is strained one per cent, at least $\gamma/b\bar{x} = 10^{-2}/3\times10^{-8} \simeq 3\times10^{5}$ dislocations must pass completely through it. Usually the average distance that a dislocation moves is far smaller than one centimeter, so still larger numbers of dislocations are needed. The question thus arises: how do so many dislocations get into a crystal?

There are several means by which dislocations can enter crystals:

(a) introduction during crystal growth

(b) nucleation by applied stresses

(c) regenerative multiplication during their motion.

Dislocations are almost always put into crystals when they are grown (possible exceptions are crystal whiskers, and recently,

silicon and germanium crystals). If these dislocations move when a stress is placed on the crystal they cause plastic flow. However, many of them may not move readily because they do not lie parallel to glide planes; or do not have the right Burgers vectors for glide; or have impurity particles precipitated along them. For these reasons Gilman and Johnston[18] observed that "grown-in" dislocations usually do not lead directly to large amounts of plastic flow, although they may help indirectly in a way that will be discussed shortly. Furthermore, crystals that have only 10^4 disl/cm^2 in them after growth can readily be strained in excess of 10%. Their supply of grown-in dislocations would be exhausted long before such large strains were reached. Since the initial dislocation contents of crystals are inadequate to account for large plastic strains, other sources of dislocations must be considered.

(1) Nucleation - If sufficient shear stress is applied to a crystal it may cause spontaneous nucleation of dislocations within the crystal. Such nucleation is said to be homogeneous if it occurs in a region of the crystal that is essentially perfect. When the region where the nucleation occurs contains a defect or some foreign material, the process is said to be heterogeneous nucleation.

Homogeneous nucleation of dislocations occurs only under extreme conditions because it requires a very large stress.[19] This stress may be estimated by a method due to Frank[20] as follows. Imagine that two parallel screw dislocations are nucleated in a crystal by an applied stress, τ, and begin to move apart. The force on each of them is τb and if they move a distance, S, apart they do an amount of work equal to τbS per

unit length. As was shown in a previous section, the energy of each dislocation is: $H_s = + \frac{Gb^2}{4\pi} \ln S/r_o$ where S is now the limit of integration because the strain due to each dislocation is cancelled by the other one at distances large compared with S. Thus the total energy of the process is:

$$H_t = \frac{Gb^2}{2\pi} \ln S/r_o - \tau bS$$

This energy is zero for S = 0, rises to a maximum at a certain value of S = S* and then drops to zero and becomes negative. At the energy maximum:

$$\frac{dH_t}{dS} = 0 = \left(\frac{Gb^2}{2\pi}\right) \frac{1}{S^*} - \tau b$$

so the value of S* is:

$$S^* = \frac{Gb}{2\pi\tau}$$

and, letting $r_o \simeq b$, the energy maximum, H_t^*, is:

$$H_t^* = \frac{Gb^2}{2\pi} \left(\ln \frac{G}{4\pi\tau} - 1\right)$$

For spontaneous nucleation to occur this energy must be reduced to zero by the applied stress; so the term in parentheses must equal zero. This requires a stress, τ_N, which is given by:

$$\tau_N = \frac{G}{2\pi e} \simeq \frac{G}{15}$$

Thus the stress for homogeneous nucleation is not much smaller than the stress for gliding without dislocations.

Homogeneous nucleation should be aided somewhat by thermal vibrations but this does not cause an appreciable reduction in τ_N at ordinary temperatures. Therefore, it must be concluded that very high stresses are required to cause homogeneous dislocation nucleation. This means that other processes will occur in all

but the most perfect crystals before large enough stresses to cause homogeneous nucleation can be applied to them. Experimental verification of this has been provided by testing crystal "whiskers" and by locally stressing dislocation free regions of large crystals. Gyulai[21] has observed NaCl whiskers that were stressed to 165,000 psi without plastic flow, and Brenner[22] applied stresses as high as 1.9×10^6 psi to iron whiskers without getting plastic flow. These stresses are $\sim$ G/11 and $\sim$ G/15 respectively. Gilman[23] found that stresses at least as high as $\sim$ G/85 could be applied locally to LiF crystals by means of a spherical indenter without causing homogeneous dislocation nucleation.

Because of the large stresses that are required to cause it, homogeneous dislocation nucleation is rarely observed in ordinary crystals, but heterogeneous dislocation nucleation is a common occurrence. It is caused by the concentrated stresses found near such heterogeneities as cracks, precipitates, and other defects in crystals.[23] In present day engineering materials, it is probably responsible for initiation of the majority of the dislocations that cause plastic flow.

(2) Regeneration - Once they are present in a crystal, dislocations can increase their numbers through regenerative multiplication. This can occur via at least two modes. One is called a Frank-Read source,[24] and the other will be called multiple cross-glide.

A Frank-Read source is illustrated in Figure 18. It consists of a segment of dislocation line AB (Figure 18-1) that is held at both ends by nodes in a dislocation network or other means. The segment AB lies on the glide plane and has a proper

Burgers vector for glide, whereas the segments BC, BD, AE and AF lie on other planes and may not have suitable Burgers vectors for glide. The plane of the paper represents the glide plane. When a shear stress is applied, the segment AB bows out as at Figure 18-2 because of the force τb, acting on it. Since the energy of a dislocation line is proportional to its length, the line acts like an elastic string and resists the applied force. The tension in the dislocation line is in static equilibrium with the applied force until the stress reaches a value $\tau_{FR} \simeq \frac{GB}{L}$ where L is the length of the segment AB. Further expansion of the loop occurs freely because the applied force dominates the tension of the dislocation line. At the critical stage the radius of the dislocation half-loop equals L/2 as in Figure 18-3. Continued expansion of the dislocation loop causes it to move backward, as well as forward, so that it reaches the configuration of Figure 18-5. Then the dislocations at point G annihilate each other, leaving the original segment AB surrounded by a new loop as at Figure 18-6. Finally, the process starts over again as at Figure 18-7.

Since the segment AB of a Frank-Read source is regenerated each time a new loop is formed, the source can form an indefinite number of dislocation loops, provided that the nodes remain fixed in place, and the local stress on the source exceeds the critical value, τ_{FR}.

The existence of Frank-Read sources has been verified in experiments by Dash[25] on silicon crystals. In these crystals dislocations can be observed by precipitating copper along them and looking at the precipitates with a microscope that is adapted to operate with infrared light (silicon is opaque to visible light but transparent to infrared). Dislocation sources of classic beauty have been found (Figure 19).

The second mode of regenerative multiplication, called multiple cross-glide, was first discussed by Koehler, and Orowan.[26] It operates in a manner that is similar to the operation of a Frank-Read source, but it does not require a dislocation segment that is anchored at its two ends. It does require glide on more than one plane, however, so only screw dislocations can multiply in this way. In order to start the process, a screw dislocation, such as the one moving from right to left in Figure 20-1, must cross-glide onto another plane as in Figure 20-2. This forms segments AB and CD which cannot move in the direction of motion of the original dislocation. AB and CD lie perpendicular to b and therefore are edge dislocations. They can glide parallel to b but not perpendicular to it. On the other hand, the screw dislocation segments OA, BC and DP can glide perpendicular to b in any direction.

With AB and CD to anchor its ends, segment BC can operate like a Frank-Read source if it is long enough (see Figures 20-3, 4, 5, 6). Also OP can become a single dislocation again as in Figure 20-3 and 4. Finally, the loop generated by segment BC can cross-glide as at EFGH in Figure 20-6 and thereby start the whole process over again. At the same time, the segment AD left behind by OP can operate as a Frank-Read source in the opposite direction because it has opposite handedness to segment BC. Segment BC has returned to its starting position and is ready to expand to form another loop.

It may be seen that multiple cross-glide not only causes an increase in the number of dislocations on the original glide plane, but also causes glide to spread to other nearby planes. In fact, this is one of its distinguishing features; the lack of a need for an anchored dislocation segment is another feature. Both of these features have been studied in detail in LiF crystals

by Johnston and Gilman.[27] One type of observation is illustrated here by Figure 21. The top photograph in the figure shows some isolated dislocation half-loops that were deliberately put into the surface of the crystal. Each half-loop is revealed by a pair of etch-pits which locate its two ends. The middle photograph shows what happened when a stress was applied to the crystal that was slightly greater than the yield stress. The shadow of a surface step may now be seen to be running through each pair of pits. These steps are due to local plastic shear. The bottom photograph is the same field after the crystal had been etched and it shows that the plastically sheared regions contain hundreds of dislocation lines. Thus, from original unanchored half-loops of dislocations, hundreds of dislocations have formed and then moved to cause large plastic strains. Since the ends of the loops were not tied in place initially they could not have acted as simple Frank-Read sources. Also, it is clear that the newly formed dislocations are mostly not on the same plane as the initial half-loops, and as time went on the bands of pits became increasingly broad. Because of these and other facts Johnston and Gilman[27] have concluded that multiple cross-glide is the most important mode of dislocation regeneration in LiF crystals. Guard and Low[28] have made a similar conclusion regarding Fe-Si crystals.

(3) <u>The density and distribution of dislocations in strained crystals</u> - Now that we have discussed the various ways by which dislocations find their way into crystals, it is important to consider how the dislocation structure of a crystal changes as the plastic flow process takes place.

The distribution of dislocations in a strained crystal that results from a collection of Frank-Read sources on the one

hand, and from the multiple cross-glide process on the other, are quite different. A Frank-Read source forms a set of concentric and coplanar loops. Hence, its operation should result in atomically sharp glide lines on the surface because gliding occurs on only single planes. In the case of multiple cross-glide, if profuse cross-glide occurs, the process can result in only one dislocation loop being formed each time a critical amount of cross-glide takes place. Then there are no concentric dislocation loops and therefore only monatomic glide lines are produced that will be clustered together into broad, diffuse bands on the surface. However, the multiple cross-glide process can produce concentric sets of loops if critical amounts of cross-glide occur only infrequently, and many loops form at each place that critical cross-glide occurs. In this latter case, the surface structure will be almost indistinguishable from the structure that would result from the operation of a collection of Frank-Read sources.

It should be clear from the above remarks that a whole spectrum of behaviors, and resulting dislocation distributions, exists for strained crystals. The behavior cannot be predicted in advance at present, so each crystal must be investigated separately. There is not space here for a thorough discussion of all the possibilities so only the case of LiF will be considered. This will not seriously restrict the generality of the discussion because the behavior of other ionic crystals is quite similar to that of LiF if one takes into consideration the stress level at which flow occurs. That is, ionic crystals that are softer than average LiF behave more like the softest LiF crystals than the hardest ones; whereas, a crystal like MgO that is harder than the average LiF resembles the hardest LiF crystals more than the softest ones. Also, the behavior that will be discussed is

not restricted to ionic crystals because at least one type of metal (Fe-Si) behaves in a similar fashion.

It is convenient to consider the formation of glide bands as though it occurs in two stages. First, a dislocation loop that has somehow been nucleated, cross-glides as it moves through a crystal and multiplies whenever the amount of cross-glide is sufficient. This continues to happen until the dislocation passes completely through the crystal, and leaves behind it numerous dislocation loops near the initial glide plane of the first dislocation. Then the second stage begins. The loops left behind by the first dislocation grow and cross-glide and thereby multiply. Soon appreciable numbers of the new loops begin to collide with each other and they either annihilate one another, or they become stalemated. Thus the loops near the initial glide plane become immobilized so that further motion of them is slow. Further away from the initial glide plane the dislocations remain free to move and multiply. After a while, a narrow band of dislocations is present which proceeds to widen. The motion of dislocations within the band is relatively slow, but along its edges dislocations can move and multiply freely.

During the first stage of glide band formation the rate of multiplication is proportional to the number of dislocations that are moving. That is, the rate of increase of the number of dislocations, dN/dt, is proportional to the number of dislocations that are already present, N:

$$\frac{dN}{dt} = \alpha N$$

where α is the multiplication coefficient. Hence after a time, t, the number of dislocations becomes:

$$N = N_o e^{\alpha t} \qquad (7)$$

or, in words, the number of dislocations increase exponentially in time. This has been verified experimentally[12].

At the beginning of the second stage of glide band formation, the probability that two dislocations will collide with each other is proportional to the square of the number that is present. Therefore, the rate of change becomes:

$$\frac{dN}{dt} = \alpha N - \beta N^2$$

where β is the rate of attrition. At some value of N the rate of change becomes zero; namely when $N = \alpha/\beta$. At this stage the density of dislocations within the band stops changing, but it is observed that the band grows wider in proportion to the strain.[12] Thus the overall dislocation density in the crystal must increase in proportion to the strain. Finally the widening glide bands encroach upon each other, and the crystal has a uniform density of dislocations in it. The rate at which the bands widen depends upon the stress level so the strain at which the crystal becomes covered also depends on the stress level. For most LiF crystals this "saturation" strain is 1-2 per cent.[12]

When a crystal is completely covered with glide bands so that it is "saturated" with dislocations, the stress that is required to maintain plastic flow in it at the same rate begins to rise because of strain-hardening. The stress increases in proportion to the strain, and the saturation densities of glide bands increase in proportion to the stress, so the overall dislocation density of the crystal increases in proportion to the strain.

The net result of the above somewhat complex behavior is summarized in Figure 22 by plotting the average dislocation density*

*A grand average that includes local areas of zero dislocation density.

in a LiF crystal as a function of the strain. Over the range of strains from 10^{-3} to 10^{-1} the data may be approximated by the linear equation $N(\text{disl/cm}^2) = 10^9 \epsilon$ where ϵ is the compressive strain.

The dislocation multiplication rate, α, depends very sensitively on the applied stress.[12] This plus other factors acts to make the glide bands in a deformed crystal more densely populated with dislocations if the band forms at a high stress level than at a low stress level. Therefore the dislocation density is not a function of a single variable like strain, stress, or time; and the future behavior of a crystal depends on its past history. It is believed that this is the reason why plastic flow generally does not obey a mechanical equation of state.

The behavior of MgO crystals that has been observed by Stokes, Johnston, and Li[29] is quite similar to what has been described here for LiF crystals. In the MgO case the glide bands are more narrow than in LiF, but this appears to result simply from the fact that the stress level is higher. In NaCl, again the behavior is also similar, with the glide bands being broader,[30] and the stress level lower. In Fe-Si the deformation geometry is different from the ionic crystals, but the overall behavior is similar.[27]

(D) Dislocations and Macro-flow

In the three previous sections the three quantities that determine the macroscopic strain-rate of a crystal in terms of dislocations have been discussed, namely, the Burgers vector, the average dislocation velocity, and the number of dislocations in the crystal. We shall now apply our knowledge of these

quantities to discuss macroscopic plastic flow in terms of dislocations. The most common means that is used to describe the macroscopic behavior is the stress-strain curve which typically has the form shown in Figure 23. The curves for different substances all have the same general form, but the various stress levels and slopes take on values that depend on the substance. Each curve has three main features: (1) an initial elastic portion whose slope is the elastic modulus; (2) a sharp change of slope at a stress level called the yield stress; and (3) an extended plastic region of relatively slowly increasing stress whose slope is the plastic modulus or strain-hardening coefficient.

These features are more or less characteristic of the chemical structure of the crystal that is being tested and relatively independent of its initial dislocation content. An additional feature of stress-strain curves is their shape near the yield stress, but this feature is very sensitive to the initial dislocation content of a crystal and hence is not an intrinsic property of crystals.

Since the stress that a crystal will support depends on time as well as the strain in the crystal, stress-strain curves cannot be discussed independently of the dynamic conditions under which they are made. In other words, the characteristics of the machine that is used in making a stress-strain curve are important in interpreting the curve. One of the best ways of testing crystals under controlled conditions is to use a machine that pushes or pulls one end of a specimen rigidly with the other end connected to a stiff spring. The deflection of the spring is then a measure of the applied load, or stress. During plastic flow the applied stress does not change rapidly with increasing strain (Figure 23) so the spring of the machine will have a

nearly fixed deflection, and an almost constant strain-rate in the specimen can be obtained by moving the other end of the specimen at a constant speed. The strain-rate in the specimen is then simply the speed of the machine's motion divided by the length of the specimen. This technique was used by Johnston and Gilman[12] to check the connection between dislocation movements and macroscopic plastic flow.

In terms of dislocation motions, the macroscopic strain-rate of a crystal is given by Equation (1). Using a LiF crystal for which $\bar{v}$ had been measured as a function of stress, Johnston and Gilman calculated $\bar{v}$ from Equation (1) for conditions when the applied strain-rate, stress, and dislocation density were known. The calculated value of $\bar{v}$ was equal to the directly measured value at the same stress within experimental error. Therefore, a distinct connection between dislocation theory and macroscopic plasticity was established.

(1) Yield stress - The yield stresses of crystals are determined primarily by the stress required to move dislocations in them; that is, by the plastic limit of Figure 12. This was demonstrated above by showing that the macroscopic yield stresses of crystals are linearly proportional to the stresses required to cause sensible motions of fresh dislocations in the same crystals. Thus, yield stresses are not ordinarily determined by: (a) the stress to pull dislocations away from impurity atmospheres; (b) the stress to push dislocations through a forest of other dislocations; (c) the stress to operate Frank-Read sources. Rather they are determined by the frictional resistance of a crystal to dislocation motion.

Since $\bar{v}$ is very sensitive to the applied shear stress (Figure 12), and the plastic strain-rate is proportional to $\bar{v}$

(Equation 1), the strain-rate is very sensitive to the applied stress, and the yield stress should be very insensitive to the applied strain-rate. This has been experimentally verified.[18]

(2) Plastic instability during yielding A stress-strain curve may have various shapes at the beginning of the yielding process. Some typical ones are shown schematically by curves A, B and C in Figure 24, where strain-hardening is assumed to be zero. Consider curve C first. In this case, the initial number of dislocations that is present is large as in curve c below the stress-strain curves. Therefore at a stress slightly higher than the stress at which dislocation motion starts, τ_y, the product $\rho\bar{v}$ in Equation (1) is sufficient to deform the crystal at the applied strain-rate. A schematic curve showing the relation between dislocation velocity and stress is drawn at the right in Figure 24. Next, consider curve A, the case when the initial number of mobile dislocations is zero at the stress τ_y. At some higher stress, τ_o a dislocation either nucleates or pulls away from impurities that had locked it in place. It then multiplies rapidly because of the high stress as shown in curve a of the figure. Therefore, although the curve A initially rises above the stress, τ_y, it soon begins to fall when the product $\rho\bar{v}$ at the high stress level becomes larger than what is needed to deform the specimen at the applied strain-rate. Curve B is an intermediate case in which a few dislocations are initially present. These initial dislocations multiply in number and move increasingly faster as the stress rises until $\rho\bar{v}$ is adequate to give the applied strain-rate. Then the stress drops to τ_y; it cannot drop lower because all dislocation motion would then stop.

Strain hardening is not considered in Figure 24, but it is

an added complication that raises the right-hand parts of the stress-strain curves. Hence it tends to eliminate small maxima like the one in curve B.

Confirmation of the above picture of the plastic instability is provided by the fact that the shapes of stress-strain curves of LiF crystals can be controlled by variations in surface preparation in accordance with the above discussion.[18] No predictions can be made for crystals in general because the shapes of the curves depend on: (a) the initial number of mobile dislocations; (b) tthe dislocation velocity vs. stress function; (c) the dislocation multiplication rate as a function of stress; and (d) the strain-hardening coefficient. These quantities are not yet known for crystals other than particular specimens of LiF.

(3) Strain-hardening We have already seen in Figure 14 that straining a crystal slows down dislocation motion in it at a given value of stress. Conversely, to obtain a given dislocation velocity more stress is needed in a strained crystal than in an unstrained one. Gilman and Johnston[15] have shown that this increase in stress is just equal to the difference in flow stress between a strained and unstrained crystal. They have also shown that strain-hardening is a linear function of dislocation density in LiF. The hardening coefficient is about 4 dynes/dislocation. Strain-hardening has not been studied in metals as yet in terms of individual dislocations. It is not clear at present whether strain-hardening is caused primarily by dislocation interactions or by "debris" that is left on glide planes in the wakes of moving dislocations.

FRACTURE

Ample evidence has been assembled in recent years to show that crystals that have no defects in them are extremely strong. In order to break them one must tear their atomic bonds apart by brute force. However, if a crack is present in a crystal, it acts like a lever of very high mechanical advantage. It allows atomic bonds to be broken at its tip even though quite small forces are applied to the crystal at large distances from the tip. Thus fracture occurs far more easily in cracked bodies than in sound ones, just as plastic flow occurs far more easily in crystals that contain dislocations than in crystals with none. Cracks allow gradual fracture to occur much as dislocations allow gradual plastic flow. One difference, of course, is that only one crack is needed for fracture in contrast to the millions of dislocations that are needed for plastic flow.

Fracture begins when a stable crack appears in a crystal, but it does not end until the crack has propagated all of the way through the crystal. Therefore, the problem divides naturally into two parts: (1) the nucleation of cracks, and (2) crack propagation. These two parts will be considered in turn in the following discussion.

(A) Nucleation of Cracks

As in the case of dislocation nucleation we consider two types of crack nucleation. The first is homogeneous nucleation which means nucleation in an essentially perfect crystal. Second, heterogeneous nucleation refers to cracks that form at inclusions or other defects in crystals, or that is a result of plastic flow, or chemical reactions.

(1) Nucleation in Perfect Crystals - Since the nucleation of a crack in a perfect crystal consists essentially of tearing the atoms apart, the first step in calculating the required stress is to decide upon a suitable expression of the interatomic forces. In order to be able to discuss as many crystals as possible a very simple and approximate interatomic potential will be used here. The main justification for this is that the results that are obtained in this way agree reasonably well with much more sophisticated calculations. The approximation used here is quite similar to the one used long ago by Frenkel.[31]

Consider two planes of a crystal that are spaced a distance d_o apart in the absence of applied stresses. The potential energy of these planes as a function of their separation distance is shown in Figure 25 together with the resulting variation of the stress between the planes. For $y = d_o$ the stress between the planes is zero, and as y becomes greater than d_o, it increases to a maximum value, σ_m, and then decreases. For values of y less than d_o the stress becomes compressive. The stress vs. distance curve is actually bell-shaped, but it can be approximated by one-half of a sine curve as shown in the figure. This curve has a maximum value, σ_m, and its half-wave length is a. The value of a is the "range" of the interatomic forces and it seems reasonable to take it to be equal to the interatomic distance in the crystal. The solid line in the figure represents the stress if all the distances in the crystal are changed uniformly. When two blocks of intact crystal are separated across one plane, however, the attractive stress will drop to zero much more steeply after the maximum has been reached than the solid line. Hence the sine curve will

approximate the behavior. According to Hooke's law, for small strains, the stress between the planes is:

$$\sigma = E\epsilon = E(y/d_o)$$

where E = Young's modulus, and ϵ = strain.
But, according to Figure 25, the stress is also given by:

$$\sigma = \sigma_m \sin \frac{\pi y}{a} \qquad 0 \leq y \leq a$$

$$\simeq \frac{\pi \sigma_m y}{a} \quad \text{for } y \ll 1$$

Equating the stress values and solving for σ_m:

$$\sigma_m = \frac{Ea}{\pi d_o} \tag{8}$$

or:

$$\sigma(y) = \frac{Ea}{\pi d_o} \sin \frac{\pi y}{a}$$

The surface energy, γ, can readily be obtained from this since it is equal to the work that is required to make the surfaces:

$$\gamma = \frac{1}{2} \int_o^a \sigma(y)\,dy$$

where the fact 1/2 accounts for the fact that two surfaces are created. The result of inserting the value of $\sigma(y)$ and integrating is:

$$\gamma = \frac{E}{d_o} \left(\frac{a}{\pi}\right)^2 \tag{9}$$

On the above basis, the theoretical cohesive strength of a crystal is about E/5. Zwicky[32] made a detailed calculation that yielded E/22 for rocksalt; and a calculation by deBoer[33] yields E/17, as well as an estimate of E/11. These calculations

are based on tensile cleavage, but failure could occur by yielding followed by shearing off. A calculation due to Mackenzie[34] of the theoretical shear strength of a crystal yields the value: G/30. This can be expressed in terms of tensile stress and E, if it is remembered that the tensile stress equals twice the shear stress in a rod, and that $G \simeq 3/8E$. The shear strength criterion is then equivalent to ~E/40.

The strengths of various materials that have been reported in the literature are listed in Table I, together with the elastic moduli of the materials and the modulus/strength ratios. Strengths that approach the theoretical values have been obtained in a variety of substances, and exceptionally high strength has been obtained for silica fibers. This indicates that the atomic theory of strength is essentially correct although it will require refinement as additional experimental strength-values become available. Also, it may be seen that strengths as high as 5% of the elastic modulus can certainly be attained in crystals, and perhaps as high as 10%.

Ordinary materials break at far smaller stresses than those discussed above: as small as E/100,000. Many of these low stress fractures are caused by surface defects in the crystals, but others occur even when the surfaces are carefully prepared. These latter fractures can often by attributed to plastic flow that precedes fracture and creates very high stresses in localized regions causing cracks to form. When both plastic flow and surface defects are eliminated from crystals (as in "whiskers") the very high stresses discussed above are required to make them fracture.

(2) Role of surfaces in crack nucleation - Crystals whose surfaces have been carefully polished by chemical or mechanical

means are often very strong initially, and then degenerate with time. One of the best known cases is that of rocksalt for which the phenomenon is known as the Joffe effect.[35] Rocksalt crystals that are immersed in under-saturated water have quite high fracture stresses. However, if they are dried and then aged in room atmosphere they soon become quite brittle. Also, freshly cleaved crystals are often quite strong, but upon aging they lose their strength. In the past, some authors have thought that these effects arise because crystal surfaces were inherently unstable so they would tend to acquire microscopic cracks spontaneously, but this is not supported by theory, and recent experiments have clarified the true nature of the Joffe effect.

A fact that should be recognized at the outset is that not all crystals exhibit surface effects. For example, Dash[36] has shown that polished silicon retains its high strength indefinitely in a room atmosphere. Also, Gorum, Parker and Pask[37] showed that the strength of freshly cleaved LiF crystals does not decrease with age, and the present author's experience agrees with this. Thus the Joffe effect is not a universal one, but depends somehow on the particular reaction of NaCl with a room atmosphere.

Some of the specific reactions of crystals with the atmosphere have been determined in recent experiments. In the case of NaCl, Class, Machlin and Murray[38] have found that the surface of NaCl reacts with oxygen (especially ozone) in the atmosphere to form $NaClO_3$. This compound probably forms a brittle surface film (as well as local stresses) that causes surface cracking. Another specific reaction that promotes crack formation is that of water vapor with Al_2O_3 or SiO_2 crystals. Charles[39] has shown that water vapor promotes static fatigue of these crystals. The fact that the fracture strengths of crystals do not change rapidly if the crystals are contained in a vacuum is further evidence of the importance of chemical reactions in nucleating

cracks at surfaces.

The detailed mechanism by which chemical reactions cause crack formation remains obscure. There is no reason to believe that uniform chemical reaction with a surface should make it significantly easier for cracks to form there. Thus it seems that, in order for a reaction to cause cracking, the reaction products must either form a brittle surface film, or must somehow penetrate into a crystal and exert a wedging action that eventually produces cracks. Some support for the former of these two mechanisms has already been mentioned, and Nielson[40] has reported experiments that support the second one.

(3) Plastic flow as a crack former One of the most important means by which cracks form in solids is localized plastic flow. The process depends on the fact that plastic flow is heterogeneous, occurring in local regions of a material while the remainder of the material is either elastic or contains a different amount of plastic strain. At the boundaries of these localized regions, high concentrations of stress are formed and sometimes the concentrated stress becomes equal to the cohesive strength of the material, thereby causing cracking. The conception of this mechanism of crack formation originated at least as far back as Taylor[41] and Starr.[42] It was also discussed by Stepanov,[43] and Zener,[44] and in recent times Stroh[45] has treated it in considerable detail.

There are at least three essentially different modes by which plastic flow can lead to fracture: (a) shear disks, (b) plastic strain interfaces, (c) crossed glide bands. These are illustrated schematically in Figure 26. There are many variations of these modes, of course, but most possibilities can be reduced to one or another of them.

A shear disk is a thin lamellar region in which plastic flow has occurred. The shear direction is parallel to the plane of the disk, and the largest dimension of the disk is large compared with the thickness. The most extreme possibility is for the disk to lie on a single glide plane. Then its thickness is just one crystal lattice spacing. However, a shear disk may also consist of a set of planes on which glide occurs, or it may be a twin lamella. In all these cases, what happens is that the strain energy that is in the material because of the applied stress, τ, is relaxed near the shear disk in a region of area $4\pi cL$; where 2L is the length of the disk (we consider the two-dimensional case here). This strain energy becomes concentrated near the ends of the shear disk in regions of radius, 2c, where c is the radius of curvature of the edge of the disk. For a thin disk, 2c is approximately the thickness. If we consider unit thickness of material, the strain energy that is relaxed will be $(4\pi cL)\tau^2/2G$ and, if τ^* is the concentrated stress, the concentrated strain energy will be $(2\pi c^2)\tau^{*2}/2G$. These energies must equal each other, so:

$$\tau^* \alpha \tau\sqrt{L/c}$$

This concentrated shear stress is accompanied by high tensile stresses which tend to form cracks as shown in Figure 26.

If the shear disk consists of a single glide plane then the problem can be treated in terms of dislocations. The dislocations will be distributed as in Figure 27 and Cottrell[46] has shown that the concentrated shear stress that is needed to hold the first dislocation in place is $\tau^* = n\tau$ if there are n dislocations in the array. In terms of L, the length of the glide plane, the concentrated stress is $\tau^* = \tau\sqrt{L/x}$ for large n;

here x is the distance along the glide plane in front of the leading dislocation. This was shown by Eshelby, Frank and Nabarro.[47]

Large tensile stresses can also be developed at an interface where the plastic strain in a body suddenly changes to some smaller value.[48] The situation is shown at (b) in Figure 26 where the shear strain across the interface AB changes by the shear angle, θ. If the shearing occurred on glide planes lying parallel to AB, then no incompatible strains would develop and hence no tensile stresses. However, if the shearing must occur along glide planes such as CD, then the height of the body, h, after shearing will be different than the height, h_o, before shearing. The height difference $h_o - h$ produces a tensile strain in the sheared portion of about $(h_o - h)/h_o$, and a tensile stress of $\sim E(1 - h/h_o)$. Since $h = h_o \cos\theta$, the tensile stress is $\sim E(1 - \cos\theta)$, and quite small shear angles can produce very high tensile stresses.

Another way in which plastic flow can produce high concentrations of stress is shown at (c) in Figure 26. It is common for two rather sharp glide bands to cross in a crystal, and this relaxes the elastic stresses in a large volume of material. Suppose that, as in Figure 26c, two glide bands cross at the center of a body that has a width, D, and unit thickness (D might also describe a small region in a much larger body). The relation between stress and strain within the bands can be described by a plastic modulus, P, while the material outside them is described by E, the elastic modulus. P will generally be quite small compared with E. Since the regions F and G are surrounded by material of low modulus they cannot carry much of the load, $F = \sigma D$, so almost all of it will be carried at the glide band intersection which has the width,

d. Thus the concentrated stress, σ^*, at the intersection will be: $\sigma^* = \sigma(D/d)$. If the glide bands are narrow, this concentrated stress can reach very high values.

Most current experimental work on crack nucleation is discussed in terms of dislocation pile-ups like those in Figure 27. However, pile-ups sufficiently large to cause fracture have never been observed. On the other hand, the more macroscopic situations shown in Figure 26 have often been observed. Therefore, although dislocation pile-ups produce more intense stress concentrations than the other mechanisms, it seems prudent at the present time to attempt to explain crack nucleation events in terms of the mechanisms of Figure 26, rather than in terms of individual dislocation pile-ups. If and when experiments reveal large isolated pile-ups, they can be discussed more realistically as a mechanism for crack nucleation. In what follows, the general evidence that plastic flow causes crack nucleation will be presented and then the evidence for the specific mechanisms.

It was established by Low[49] that the fracture stress of polycrystalline iron is equal to the yield stress for a wide range of grain sizes. Figure 28 shows the data. The yield stresses were measured in compression, while the fracture stresses were measured in tension. The close correlation between fracturing and yielding indicates that a small amount of plastic flow is sufficient to cause fracture at a low average stress level.

Zinc crystals normally fracture at low stresses, but if plastic flow is suppressed in them, very high stresses are required for fracture as shown by Gilman.[50] Zinc crystals have only one glide plane so plastic flow can be suppressed in them

by orienting the glide planes normal to the tension axis. Then there is no shear stress on the glide planes and hence no driving force for plastic flow. Figure 29 shows how the fracture stress increases precipitously as the orientation angle approaches perpendicularity.

Several authors, including: Stepanov,[43] Stokes, Johnston, and Li,[51] and Parker[52] have observed that small cracks often form at the intersections of glide bands. This not only confirms that there is a connection between plastic flow and fracture, but also provides evidence of the mechanism in Figure 26c. An example of this type of observation is shown in Figure 30a.

A case in which the mechanism of Figure 26b has operated is shown in Figure 30b. The photograph shows a zinc crystal that was plastically deformed at a low temperature (-196°C) such that more plastic straining occurred at the left of the kink boundary than to the right. This produced tensile stresses parallel to the boundary and thence fracture. The shear strain discontinuities that form at the intersection of two twins can also cause cracking as Bell and Cahn have discussed.[53]

(B) Propagation of Cracks

The fact that a crack nucleates in a body does not necessarily mean that it will propagate. In polycrystalline iron, Low[54] has found that fine-grained specimens form micro-cracks within the grains as soon as they plastically yield, but these micro-cracks do not propagate until the applied stress increases considerably. Even in mono-crystals, cracks can nucleate without propagating as many authors, for example, Stokes, et al.,[51] have shown. In these cases the

cracks have nucleated in regions of intense stress concentration and then expanded into material that had only the average stress on it, or they have collided with crystal boundaries that they could not penetrate.

In order for a crack to propagate it is apparent that the stress at its tip must exceed the cohesive strength of the material. This is the fundamental criterion for crack propagation. It is not a very useful criterion, however, because no one has yet devised a method for measuring the stress at the very tip of a crack. Therefore, an equivalent criterion is commonly used which states how much force must be applied to a body that contains a crack in order to make the crack propagate. This is known as the Griffith crack-propagation criterion and it is obtained by forming an energy balance.(1) The Griffith criterion depends, of course, on the shape of the body and how the crack is disposed in it. A few simple cases are shown schematically in Figure 31, and they will be considered in turn.

(1) Griffith condition for crack propagation - In Figure 31a, a narrow plate is shown that is held rigidly along its top and bottom edges. Initially the plate contains a stress σ and its height is L_1. A crack moves from left to right through the plate. Each time the crack advances a distance Δx, two things happen. First, some new surface is created on either side of the crack, and if the plate thickness is t, this new surface area is $2t\Delta x$. Second, the stress drops to zero behind the crack in a volume that is approximately equal to $L_1 t\Delta x$. The energy of the plate is increased by the first change by an amount, $2\gamma t\Delta x$, where γ is the surface energy per unit area; and it is decreased by the second change. The

initial strain energy density is $\sigma^2/2E$, where E is Young's Modulus, so the second change is approximately equal to $-\frac{\sigma^2}{2E} L_1 t\Delta x$. We see then that the total energy change is:

$$\Delta U = 2\gamma t\Delta x - \frac{\sigma^2}{2E} L_1 t\Delta x$$

If L_1 is very small, the second term in the above expression is negligible so the energy change is positive for an increase, Δx, in the length of the crack. Therefore, if the other quantities are held constant, and L_1 is made small, we do not expect the crack to get larger. On the other hand, if L_1 is increased to such a value that the second term dominates and ΔU becomes negative, we expect the crack to grow because this will cause an overall decrease in the energy of the system. The situation is critical at the transition between small and large L_1 when $\Delta U/\Delta x = 0$. The critical stress can be obtained from this condition. It is:

$$\sigma = \sqrt{\frac{4E\gamma}{L_1}} \qquad (10)$$

This Griffith condition is equivalent to the condition that the local stress reach the cohesive strength because γ is a measure of the cohesive strength. It can be defined as the work per unit area that is required to separate a body at a surface, and this depends on the cohesive attraction between the surfaces. This point has been discussed further by Orowan.(55)

A practical situation that corresponds to the loading condition of Figure 30a is the case of glue in a joint between two rigid pieces of material. This is one of the reasons why it is desirable to make glue layers as thin as possible. The thinner the glue, the larger the stress needed for crack

growth, according to equation (10).

For a moving crack, equation (10) does not provide a complete description of the behavior because it neglects the kinetic energy possessed by a moving crack. This was first pointed out by Mott.[56] The kinetic energy is associated with the sideward motion that occurs in the material on either side of the crack when the crack advances. The sideward displacements in the elementary volumes $\frac{L_1 t\Delta s}{2}$ are given approximately by $\frac{\epsilon L_1}{2}$ where ϵ is the initial elastic strain, equal to σ/E. If the crack has a velocity, V_c, the time for it to advance a distance $L_1/2$ is $L_1/2V_c$. Thus the sideward velocities are $\sim \frac{\sigma V_c}{E}$. If g is the density, the masses that are moved are approximately $\frac{gL_1 t\Delta x}{2}$; so the kinetic energy is $1/2mV^2 = \frac{g}{2}\left(\frac{\sigma V_c}{E}\right)^2 L_1 t\Delta x$. Since the velocity of sound, V_s, is equal to $\sqrt{E/g}$; the kinetic energy can be written: $\left(\frac{V_c}{V_s}\right)^2 \frac{\sigma^2 L_1 t\Delta x}{2E}$.

This is a positive energy so the balance becomes:

$$\Delta U = 2\gamma t\Delta x - \frac{\sigma^2}{2E} L_1 t\Delta x + \left(\frac{\sigma^2}{2E}\right)\left(\frac{V_c}{V_s}\right)^2 L_1 t\Delta x$$

For steady motion $\Delta U/\Delta x = 0$ and the crack velocity is:

$$V_c = V_s \sqrt{1 - \frac{\Delta E\gamma}{\sigma^2 L_1}} \qquad (11)$$

From this equation we can see that large L_1 or large stress leads to fast crack motion that approaches sound velocity as an upper limit.

The case that was treated by Griffith himself is shown at (b) in Figure 31. In this case a small crack of length, $2L_2$, exists in an infinite sheet of solid that is subjected to a

uniform tensile stress, σ. If the crack extends a small amount, surface area is created, and elastic strain energy is relaxed just as in the previous case. The condition for propagation of the crack that Griffith derived is:

$$\sigma = \sqrt{\frac{2E\gamma}{\pi L_2}} \qquad (12)$$

which is analogous to equation (10) above.

The final case that will be considered here is shown at (c) in Figure 31. Here a solid body is being split by a crack of length, L_3. The forces, F, applied to the ends of the two cantilevered bars produce bending moments, FL_3, at the tip of the crack. The elastic energy associated with the bending of each beam is $U = F^2 L_3^3/6EI$, where I = the moment of inertia of the cross-section = $wt^3/12$. The surface energy of one side of the crack is $S = \gamma L_3 w$. The work, W, that is done by the applied force on each beam is $F\delta_o$ where δ_o is the beam deflection at the point of application of the force, and $\delta_o = 2U/F$ so $W = 2U$. In order for the crack to advance a distance dL_3, the work that is done on the body must provide whatever surface energy is required and the additional elastic energy that each beam acquires when the crack moves forward. Thus the Griffith condition for crack motion is:

$$\frac{dW}{dL} - \frac{dU}{dL} - \frac{dS}{dL} = 0$$

or

$$S = 3U$$

The bending moment that is needed to satisfy this condition is:

$$M^* = FL_3 = \sqrt{2EIw\gamma} \qquad (13)$$

It is independent of the crack length so this type of configuration is especially useful in studying the propagation of cracks.

Equations 10, 12 and 13 emphasize a very important principle: namely, that fracture depends not only on the material properties of a body, but also on the dimensions of the body. In other words, there is a "size effect" associated with fracture. This effect appears because the Griffith energy balance always requires the specification of a length; otherwise the dimensions in the crack propagation conditions (equations 10, 12 and 13) cannot be balanced. It is not always clear what length in a system is the important one, but the length is always related to the size of the region in which the crack relieves the stresses. This can, of course, vary quite a bit from one situation to another. In Figure 31a the important length is the height of the plate because this defines the volume in which the crack relaxes the stress. On the other hand, in the case of a crack in an infinite plate (Figure 31b) it is the crack length that is the important dimension because the region in which the stresses are relieved is a pillbox-shaped volume of approximate diameter L_2. In the third case (Figure 31c) the thickness, t, is most important because it defines the size of the region in which the stresses are concentrated.

In engineering structures, the important length is not always obvious. In the case of the bursting of a pipe it is clear that the pipe circumference is most important because a crack in the pipe wall relieves stresses in the whole circumference. However, in more complex structures like ships, large rotors, etc., the important length may be somewhat obscure. Further confusion can result if plastic deformation precedes cracking. Then a length of the plastic zone may be the most important dimension. For example, it might be the radius of the notch in a notched bar, or for a crack running

through a semi-ductile plate, it might be the thickness of the plate.

It should also be noted that it is not the relative dimensions of a structure that are important; it is an absolute dimension. This is the reason for speaking of a "size effect." Of course, in a large structure the crack's own length may be important at first, and only after the crack has grown will a length of the structure become important. Nonetheless, because of the size effect, large structures are more susceptible to catastrophic fracture than small ones.

(2) Crack propagation in elastic bodies - A crack passes through a completely elastic solid by rupturing its atomic bonds successively. Therefore, if the atoms of the body are arrayed geometrically (a crystal) or randomly (a glass) all that the crack does is to create two new surfaces. If the crack moves slowly (reversibly), the energy that must be supplied to it is the surface energy. If it moves more rapidly, kinetic energy is also required. Finally, if the crack moves through a crystal that is not perfect, but contains crystal defects (especially screw dislocations), additional energy will be needed to make it move. These three cases will now be discussed in more detail.

(a) Low speed elastic cracks Griffith himself was first to show that the energy needed to propagate a crack in an elastic solid is the surface energy. He put small cracks in

thin walled glass bulbs and tubes and then put gas under pressure into them and measured the bursting pressure. This experimental arrangement is a close approximation to the ideal case of Figure 31b, so the bursting pressure should be related to the crack length by equation (12). Figure 32 shows that indeed the theoretical form of the equation is obeyed. Furthermore, the slope of the line in Figure 32 equals $(2E\gamma/\pi)^{1/2}$, so a value of the surface energy can be calculated (Griffith measured E independently). The resulting value is 510 ergs/cm^2. This may be compared with the 550 ergs/cm^2 that Griffith measured in a different way by determining the surface tension of his glass at high temperatures, and then extrapolating to room temperature. The agreement between the two values seems remarkably good considering the many difficulties involved, and may be taken as evidence that the theory is essentially correct.

Since the time of Griffith, Berdennikov[57] and Shand[58] have done experiments similar to his. They scratched glass plates and then measured the stress required to break them. Their results are generally consistent with those of Griffith, but Berdennikov found that the fracture surface energy of glass depends on the environment. It varies from about 1200 ergs/cm^2 for a soda-lime glass tested in vacuum, to about 290 ergs/cm^2 for the same glass immersed in water. Thus, the intermediate value that Griffith measured may have been influenced by atmospheric water vapor.

An experiment that is closely related to that of Griffith was first performed by Obreimov[59] who used the experimental configuration of Figure 31c to measure the surface energy that is required to split mica. He was not able to measure the true surface energy of mica, because freshly cleaved mica surfaces are not electrically neutral; there are residual patches

of charged ions on them. However, Obreimov was able to show that the method is capable of yielding reproducible results, and that the cleavage surface energy is sensitive to the environment. Furthermore, the values of surface energy that he obtained are approximately what is to be expected from atomic theory.

It may be concluded from these measurements of crack propagation in elastic bodies that there is a sound experimental basis for the idea that, in order for a crack to propagate, the stress at its tip must be sufficient to break the bonds between atoms. In a crystal, in contrast to glass, the atomic bonds have different strengths in various directions, and a crack will normally seek out the plane of the crystal across which the atomic binding is weakest.

Among the many planes of a crystal, the one that is the first preference for crack propagation is called the primary cleavage plane. In some crystals cracks will propagate along secondary or tertiary cleavage planes if the applied normal stress on the primary plane is small, but the preference for the primary plane is usually strong. In many cases, the primary cleavage plane can be predicted in a simple way from the elastic constants and the atomic radii.[60] The work needed to separate the crystal across various planes can be estimated by calculating the pertinent Young's modulus perpendicular to the planes and substituting these into equation (9) together with the appropriate atomic radii. Some results of this procedure are given in Table II as well as the primary cleavage planes of the crystals. The method fails for crystals that are only slightly anisotropic, but it illustrates the principles that seem to be involved.

(b) High speed elastic cracks It might be thought that a crack could travel at an arbitrary speed because the speed with which an atomic bond can be broken is limited only by the rate at which forces can be applied to it. However, the stresses that act at the tip of a crack must be transmitted elastically to the crack tip through solid material. The rate at which this can occur is limited by the velocity of elastic waves in the solid[56] and the shape of the body. The shape factors can be eliminated by considering a crack in an infinite plate. Then the limiting velocity is the Rayleigh surface-wave velocity. Stroh[61] has given a simple argument to support this, and Craggs[62] has proved it rigorously. Stroh's argument is that if the limiting velocity is determined by inertial effects and not by the time that it takes to break atomic bonds, then the forces exerted by the atomic bonds are negligible across a crack that is moving at the terminal speed. Therefore, each half of the crack may be thought of as an elastic disturbance that is moving along a stress-free surface. The velocity with which such a disturbance moves is the Rayleigh surface-wave velocity.

For crystals, only one measurement of terminal crack velocities has been made, but several measured values are available for polycrystalline or glassy materials. Gilman, Knudsen, and Walsh[63] measured crack velocities in LiF crystals by evaporating thin metallic stripes onto the crystals and then observing electrically the rate at which the stripes were broken by moving cracks. They found that the fastest cracks they could produce traveled at 2×10^5 cm/sec along $\{100\}$ planes. A theory of surface-wave propagation in cubic crystals has been worked out by Stoneley.[64] This theory, together with the measured values of the elastic constants for LiF crystals, yields a

velocity of 2.95×10^5 cm/sec for surface waves on the $\{100\}$ faces of LiF crystals. Comparison with the value above indicates reasonable agreement between theory and experiment.

Data for terminal crack velocities in a variety of types of materials are presented in Figure 33 as a function of the best estimate that can be made of the Rayleigh wave velocity for each material. There is a generally good correlation between the two velocities, but the experimental crack velocities tend to be somewhat smaller than the wave velocities. Sources of the data are given in reference (65).

(c) Effect of crystal imperfections As a crack passes through a crystal it often encounters crystal defects along its path. Some of these defects, such as lattice vacancies and impurity atoms, seem to have little effect on the ease of crack motion; but screw dislocations have a large effect. This results from the fact that a screw dislocation converts the crystallographic planes that lie normal to it into a helical ramp centered on the dislocation line (Figure 4 and 34). Therefore, a crack that runs parallel to these planes does not lie on a single plane after it has intersected the dislocation line. The two parts of the crack lie on planes separated by the magnitude of the Burgers vector of the screw dislocation, and they usually rejoin by forming a step between the two levels as shown in Figure 34. Direct experimental evidence for this interaction between cracks and screw dislocations to form cleavage steps has been presented by Gilman.[66] He correlated etchpit and leavage step patterns on the surfaces of cleaved LiF crystals. The screw dislocations may be present in a variety of forms:

(a) Twist-type sub-boundaries

(b) Glide bands introduced by prior plastic deformation

(c) The dislocation loops that are nucleated just ahead of a moving crack.

Cleavage steps can influence the ease of crack propagation because they increase the area of a cleavage surface and thereby make its energy greater than the energy of a smooth surface. Also, considerable tearing may accompany the production of the steps and this absorbs energy. If a step forms by cleavage perpendicular to the plane of the main crack, the energy absorption is simply proportional to the step height and is generally rather small. If, however, step formation involves plastic tearing or shearing, then the energy absorption is proportional to the square of the step height[67] and considerable energy may be absorbed for steps that are greater than ~ 100A in height.

The increases in cleavage surface energy that accompany step formation may cause cracks to move more slowly than they normally would under the same driving force.[63] They may also cause them to stop temporarily at regions of high screw dislocation density as Melankholin and Regel[68] have observed.

Although isolated point defects (vacancies, impurities, etc.) appear to have little direct effect on crack propagation, it is evident that if they become aggregated they can have large effects. Mono-layers of them parallel to cleavage planes can be disastrous if the bonds between the point defects and the crystal are weaker than the normal crystal bonds. The effective surface energy at such a region is lowered so crack propagation through the region is facilitated. Examples of this effect are: potassium sulfate which cannot be cleaved when it is pure, but cleaves readily if it contains internally adsorped dye molecules;[69] the effect of hydrogen on cleavage in vanadium;[70] the effect of oxygen on cleavage in tantalum;[71] and the effect of radiation

damage on LiF crystals which causes mono-layers of lithium to form along the cube planes thereby making the crystals very weak.[72]

(3) Effects of plasticity Many complications are introduced when the material in which a crack moves is plastic as well as elastic. Perhaps the most important effect is that the shape of the crack tip becomes changed by plastic deformation. It becomes blunted, and usually it also becomes jagged because plastic deformation puts screw dislocations or twins in its path. These cause local deflections of the plane of cracking. Another factor which becomes important is time. Plastic flow requires time to occur, so the amount that can take place at a crack tip depends on how fast the crack is moving. Finally, because it puts defects into a crystal, plastic flow may reduce the cohesive strength of a crystal, and thereby weaken the material just in front of a crack. An extreme case of this occurs during the propagation of fatigue cracks.

If plastic flow occurs, it can be expected to occur in front of a moving crack, rather than behind it, because the concentrated stresses at a crack tip become negligible very quickly behind the point at which the atomic bonds are broken.[73] The concentrated stresses in front of a crack tip can cause plastic flow not only by moving existing dislocations that happen to lie near the plane of the crack, but also through the motion of dislocations that are created at the crack tip itself.[74] Dislocation creation occurs at crack tips in a variety of crystals.[66] Twinning may also occur just in front of a moving crack and this has been discussed by Bilby and Bullough.[75]

(a) Crack shape changes The various features of materials that make cracks jagged have recently been reviewed by Low[76] so they will be considered only briefly here. The main defects which deflect cracks are screw dislocations and twins. The screw dislocations may be present initially in twist-type grain boundaries and in glide bands, or they may be created just ahead of the crack and then cut through. Twins are sometimes weak along the plane of twinning, so if a twin forms ahead of a crack, the crack may be deflected from the primary cleavage plane to the twin plane as Berry[77] has shown in the case of iron. Both Gilman[60] and Friedel[78] have concluded that these various roughening effects in themselves have only a small effect on the energy required to propagate a crack. However, the appearance of fracture surfaces that have been roughened by the above mechanisms are valuable diagnostic tools. They give an indication of the initial structure of the material that has been cracked; of the type of deformation that preceded a crack; and some measure of the amount of deformation that occurred.

The major effect of plastic deformation on crack propagation is that it blunts the profile of a crack. Orowan[55] has pointed out that this reduces the stress concentration factor at the crack tip which greatly increases the amount of applied stress that is needed to make the concentrated stress exceed the cohesive strength of the material. If it is assumed that the material is ideally plastic, then a quantitative estimate can be made of the magnitude of this effect along lines suggested by Gilman[60] and Friedel.[78] The thing that is to be estimated is the effective fracture-surface energy in the presence of plastic flow in terms of the yield stress and the ideal cleavage surface energy.

Consider Figure 35. On the left is shown a crack of length 2L and thickness 2h. The latter depends on the applied stress and for plane stress, is given by (73):

$$h = \left(\frac{\sigma}{E}\right) L \qquad (14)$$

In order for the crack to propagate, the concentrated stress, σ_m, at its tip must exceed the cohesive strength, σ_c, of the material. The stress concentration factor is $2\sqrt{L/c}$ where c is the radius of curvature at the tip of the crack (1), so the concentrated stress is:

$$\sigma_m = 2\sigma\sqrt{L/c}$$

If L is eliminated from this equation by using equation (12) a fracture criterion is obtained in terms of c:

$$\text{(at fracture)} \quad \frac{\gamma}{c} = \frac{\pi\sigma^2 c}{8E}$$

In other words the ratio of the fracture surface energy, γ, to the radius of curvature is constant for a given material. For elastic behavior, γ is the intrinsic surface energy, γ_s, and c is approximately an atomic radius, a. For plastic behavior, γ will be increased to an effective value, γ_p, by the plastic work that will accompany crack propagation. The cohesive strength and elastic modulus are unaffected by plasticity so:

$$\gamma_p/c = \gamma_{s/a} \qquad (15)$$

Now an estimate will be made of the maximum value of γ_p that can be expected. The greatest value that the applied stress can take is σ_y because this will cause general yielding. This stress is sufficient to cause an elastic crack to open up to a

thickness, $h = (\sigma_y/E)L$. As may be seen at the right in Figure 35, plastic relaxation of the concentrated stresses could then increase the radius of curvature at the crack tip to $c = h$ as a maximum. The maximum value that L could have without having a high probability that the crack will convert to the elastic mode of crack propagation is given by the Griffith condition; $L = 2E\gamma_s/\pi\gamma\sigma_y^2$, so:

$$c = h = \left(\frac{\sigma_y}{E}\right) L = \frac{2\gamma_s}{\pi\sigma_y}$$

But, according to equation (9), $\gamma_s \simeq \frac{Ea}{2}$, making $c \simeq 2Ea/\pi^3\sigma_y$. Substituting into equation (15) above:

$$\gamma_p \simeq \frac{1}{15}\left(\frac{E}{\sigma_y}\right)\gamma_s \simeq \left(\frac{\sigma_c}{\sigma_y}\right)\gamma_s \qquad (16)$$

where σ_c is the cohesive strength of the crystal. This equation shows that if the ratio of the cohesive strength to the yield stress is large, very large values of the effective fracture-surface energy can be obtained. Conversely, if the yield stress of a material approaches its cohesive strength, γ_p will equal γ_s so only the intrinsic surface energy will provide resistance to crack propagation. It must be kept in mind, of course, that equation (16) is an upper limit; there are several factors that might make γ_p smaller than the value it indicates. However, the equation is in approximate agreement with the experimental results of Low[54] who obtained a value of γ_p equal to 100,000 ergs/cm^2 for steel with $\gamma_s \simeq 1000$ ergs/cm^2 and $\sigma_c/\sigma_y \simeq 100$.

(b) Rate effects In a previous section it was shown that dislocations move through crystals in a viscous manner with a speed that depends on the magnitude of the applied stress (see Figure 12 especially). Therefore, the rate at which plastic flow can occur at a given level of stress is limited. Near the tip of a fast moving crack there may be insufficient time for plastic relaxation to occur even though the local stresses exceed the static yield stress. Then the dynamic yield stress must be used in equation (16) and this will reduce the value of γ_p and hence the resistance to crack motion.

The differences between dynamic and static yield stresses of crystals depends strongly on the type of crystal. For pure metals the difference is generally small so that many metal crystals are very resistant to crack propagation and insensitive to the rate of loading. For alloyed metal crystals, ionic crystals, and especially for covalent crystals the difference between the dynamic and static yield stress increases rapidly with increasing rate of loading. In extreme cases like germanium or silicon crystals, the dynamic yield stress equals or exceeds the cohesive strength at low temperatures so the only resistance to crack motion that is presented is that of their intrinsic surface energy.

(c) Reduction of cohesive strength associated with plastic flow - Although the plastic flow that occurs near a crack tip tends to provide resistance to crack motion, it also introduces defects into the material which may reduce its cohesive strength. It is fortunate that this latter effect is usually relatively small, but there is growing experimental evidence that it can have a dominating effect in certain types

of crystals.

Some defects that are introduced by plastic flow are vacancies, twin interfaces, and dislocations. Isolated vancancies probably have little effect on strength, but when they become aggregated into voids after cyclic straining, or large monotonic strains, they can cause weakening of crystals. Twin interfaces appear to be weak in some crystals, especially those with directed chemical bonds. This happens because atomic neighbors across a twin interface are arranged in such a way that bonds between them cannot be made at normal bond angles. Hence the bonds are weaker than normal. Dislocations cause weakening because the cohesion across their glide planes is less than across a perfect plane in a crystal.

The decreased cohesion across the glide plane of an edge dislocation can be strikingly demonstrated with the aid of the bubble model of a crystal. If a bubble raft is stressed in tension perpendicular to the glide plane of an edge dislocation in it, a crack readily opens up along the glide plane as shown in Figure 36.

The glide planes of dislocations are weak for two reasons. One is that at least the equivalent of one atomic bond is missing at the center of an edge dislocation. A second is that, since the atoms of the crystal are sheared from their normal positions at the center of the dislocation, they do not fit together with their normal interplanar spacing in the direction penpendicular to the glide plane. Therefore, a dilatation is produced in the perpendicular direction. The amount of the dilatation depends on the crystal structure, and it acts like a small wedge tending to split the crystal open along the glide plane.[79] The strain energy associated with a dilatational displacement, y, is $\sim Gy^2/\pi$ which is typically equal to the energy of one atomic bond.

TABLE I

Highest Strengths Attained by Various Forms of Solids

Material	σ_f = Maximum Observed Strength	E (#/in^2)	E/σ_f	Reference
Music Wire	0.4 x 10^6 #/in^2	20x10^6	72	NBS Circular C447
Silica Fibers	3.5	14	4	Anderegg
Iron Whisker	1.9	43	23	Brenner
Al_2O_3 Whisker	2.2	72	33	Brenner
NaCl	0.16	6.3	40	Gyulai
Silicon Whisker	0.94	24	26	Evans
Mica	0.43			Orowan
Silicon (bulk)	0.75	24	32	Pearson, Read, Feldman
Boron	0.35	51	145	Talley
Austformed Steel	.45	29	64	Shine, Zackay Schmatz

References

F. O. Anderegg - Ind. Eng. Chem. 31, 290 (1939).

S. S. Brenner - Growth and Perfection of Crystals, J. Wiley and Sons, New York, p. 157 (1958).

C. C. Evans - Reported by J. E. Gordon, ibid, p. 219.

Z. Gyulai - Zeit. F. Phys. 138, 317 (1954).

NBS Circular C447 - U. S. Gov. Print Off. (1943).

E. Orowan - Zeit. F. Phys. 82, 235 (1933).

G. L. Pearson, W. T. Read, W. L. Feldman - Acta Met 5, 181 (1957).

C. P. Talley - Jour. App. Phys. 30, 1144 (1959).

J. C. Shine, V. F. Zackay, D. J. Schmatz - ASM Preprint #163 (1959).

TABLE II

Work of Cleavage for Various Crystal Planes
According to Equation (9)

Crystal	Work of Cleavage $\left(\frac{ergs}{cm^2}\right)$ {100}	{110}	{111}	Observed Primary Cleavage Plane
MgO	1310	2330	*	100
LiF	374	780	*	100
NaCl	310	345	*	100
Si	1350	1270	887	111
Diamond	7050	5500	3500	111
α-iron	1440	1710	5340	100

*Non-neutral planes

REFERENCES

1. A. A. Griffith, "The Phenomena of Rupture and Flow in Solids," Phil. Trans. Roy. Soc., 221, 163 (1920).

2. G. I. Taylor, Proc. Roy. Soc. (London) 145A, 362 (1934).
E. Orowan, Z. Phys. 89, 606 (1934).
M. Polanyi, Z. Phys. 89, 660 (1934).

3. J. M. Burgers, Proc. Roy. Ned. Acad. Sci. (Amsterdam) 42, 293 (1939).

4. H. B. Huntington, J. E. Dickey, R. Thomson, "Dislocation Energies in NaCl," Phys. Rev. 100, 1117 (1955).

5. U. Martius, B. Chalmers, "Slip Planes and Energy of Dislocations," Proc. Phys. Soc. 213A, 175 (1952).

6. F. R. N. Nabarro, "Dislocations in Simple Cubic Lattices," Proc. Phys. Soc. (London) 59, 256 (1947).

7. F. R. N. Nabarro, "The Mathematical Theory of Stationary Dislocations," Adv. Phys. 1, 299 (1952).

8. E. Schmid, W. Boas, "Plasticity of Crystals," F. A. Hughes Co., London (1950).

9. P. Haasen, A. W. Lawson, "Der Einfluss Hydostatischen Druckes Auf Die Zugverforming von Einkristatten," Z. Metallk. 49, 280 (1950).

10. E. N. da C. Andrade, R. Roscoe, "Glide in Metal Single Crystals," Proc. Phys. Soc. 49, 166 (1937).

11. D. C. Jillson, "Quantitative Stress-strain Studies on Zinc Single Crystals in Tension," Trans. AIME 188, 1117 (1955).

12. W. G. Johnston, J. J. Gilman, "Dislocation Velocities, Dislocation Densities, and Plastic Flow in Lithium Fluoride Crystals," J. App. Phys. 30, 129 (1959).

13. D. L. Stein, J. R. Low, Jour. App. Phys. (Feb. 1960).

14. J. J. Gilman, "The Plastic Resistance of Crystals," Jour. Australian Inst. Phys. (1960).

15. J. J. Gilman, W. G. Johnston, "Behaviour of Individual Dislocations in Strain-hardened LiF Crystals," to be published in J. App. Phys.

16. W. Koster, "The Temperature Dependence of the Elastic Modulus of Pure Metals," Z. Metallk. 39, 1 (1949).

17. M. J. Druyvesteyn, "Experiments on the Effect of Low Temperature on Some Plastic Properties of Metals," App. Sci. Res. A1, 66 (1947).

18. J. J. Gilman, W. G. Johnston, "Dislocations and Mechanical Properties of Crystals," J. Wiley and Sons, Inc., New York, p. 69 (1957).

19. F. Seitz, T. A. Read, "Theory of the Plastic Properties of Solids," J. App. Phys. 12, 100 (1941).

20. F. C. Frank, "The Origin of Dislocations," ONR Symposium NAVEXOS-P-834, Pittsburgh (1950).

21. Z. Z. Gyulai, "Strength and Plastic Properties of NaCl Needle Crystals," Z. f. Physik, 138, 317 (1954).

22. S. S. Brenner, "Growth and Perfection of Crystals," p. 157 J. Wiley and Sons, New York (1958).

23. J. J. Gilman, "Dislocation Sources in Crystals," J. App. Phys. 33, 1587 (1959).

24. F. C. Frank, W. T. Read, "Multiplication Processes for Slow-moving Dislocations," Phys. Rev. 79, 722 (1950).

25. W. C. Dash, "Dislocations and Mechanical Properties of Crystals," p. 57, J. Wiley and Sons, New York (1957).

26. J. S. Koehler, Phys. Rev. 86, 52 (1952); E. Orowan, "Dislocations in Metals," p. 103 AIME, New York (1954).

27. W. G. Johnston, J. J. Gilman, "Dislocation Multiplication in Lithium Fluoride Crystals," to be published Jour. App. Phys. (1960).

28. R. W. Guard, J. R. Low, "The Dislocation Structure of Slip Bands in Iron," Acta Met. 7, 171 (1959).

29. R. J. Stokes, T. L. Johnston, C. H. Li, "Effect of Surface Condition on the Initiation of Plastic Flow in Magnesium Oxide," Trans. AIME 215, 431 (1950).

30. W. G. Johnston - unpublished results.

31. J. Frenkel, Zeit. Phys. 37, 572 (1926).

32. F. Zwicky, "The Strength of Rocksalt," Phys. Zeit. 24, 131 (1923).

33. J. H. deBoer, "The Influence of van der Waal's Forces and Primary Bonds on Binding Energy, Strength, etc." Trans. Far. Soc. 32, 10 (1936).

34. J. K. Mackenzie, reported by A. Seeger, Hand. d. Phys. 7(2), 9 (1958).

35. A. F. Joffe, "The Physics of Crystals," McGraw-Hill Book Co., Inc., New York (1928).

36. W. C. Dash, "Growth and Perfection of Crystals," J. Wiley and Sons, New York, p. 189 (1958).

37. A. E. Gorum, E. R. Parker, J. A. Pask, "Effect of Surface Conditions on Room Temperature Ductility of Ionic Crystals," Jour. Am. Cer. Soc. 41, 161 (1958).

38. W. Class, E. S. Machlin, G. T. Murray, "NaCl Embrittlement by Surface Compound Formation," Jour. Met. p. 583, Sept. (1959).

39. R. J. Charles, "The Strength of Silicate Glasses and Some Crystalline Oxides," Fracture p. 225, M.I.T. Technology Press, Cambridge, Mass. (1959).

40. N. A. Nielson, "The Role of Corrosion Products in Crack Propagation in Austenitic Stainless Steel," Phys. Met. of Stress Cor. Frac. ed. Rhodin, p. 121 Interscience Pub., New York (1959).

41. G. I. Taylor, "Resistance to Shear in Metal Crystals," Trans. Far. Soc. 25, 121 (1928).

42. A. T. Starr, "Slip in a Crystal and Rupture in a Solid Due to Shear," Proc. Camb. Phil. Soc. 24, 489 (1928).

43. A. V. Stepanov, "Artificial Slip Formation in Crystals," Nature 140, 64 (1937).

44. C. Zener, "The Micro-mechanism of Fracture," Fracturing of Metals, p. 8 ASM, Cleveland, Ohio (1952).

45. A. N. Stroh, "The Formation of Cracks as a Result of Plastic Flow," Proc. Roy. Soc. 223A, 404 (1954).

46. A. H. Cottrell, "Dislocations and Plastic Flow in Crystals," p. 104 Oxford Univ. Press, London (1953).

47. J. D. Eshelby, F. C. Frank, F. R. N. Nabarro, "The Equilibrium of Linear Arrays of Dislocations," Phil. Mag. 42, 351 (1951).

48. J. J. Gilman - Discussion p. 51, Fracture, M.I.T. Technology Press, Cambridge, Mass. (1959).

49. J. R. Low, Deformation and Flow of Solids, p. 60, I.U.T.A.M. Madrid Colloquium, Springer, Berlin (1956).

50. J. J. Gilman, "Fracture of Zinc Monocrystals and Bicrystals," Trans. AIME, 212, 783 (1958).

51. R. J. Stokes, T. L. Johnston, C. H. Li - Phil. Mag. 3, 718 (1958).

52. E. R. Parker, "Fracture of Ceramic Materials," Fracture, p. 181 M.I.T. Technology Press, Cambridge, Mass. (1959).

53. R. L. Bell, R. W. Cahn, "The Initiation of Cleavage Fracture at the Intersection of Deformation Twins in Zinc Single Crystals," J. Inst. Met. 86, 433 (1957).

54. J. R. Low, "The Relation of Microstructure to Brittle Fracture," Trans. ASM, 46A, 163 (1954).

55. E. Orowan, "Energy Criteria of Fracture," Welding Journal 34, 1575 (1955).

56. N. F. Mott, "Fracture of Metals - Theoretical Considerations," Engineering Jan. 2, 1948, p. 16.

57. W. P. Berdennikov, "Measurement of the Surface Energy of Solids," Phys. Zeit. d. Sowjet. 4, 397 (1933).

58. E. B. Shand, "Experimental Study of the Fracture of Glass," Jour. Am. Cer. Soc. 37, 559 (1954).

59. J. W. Obreimov, "The Splitting Strength of Mica," Proc. Roy. Soc. 127A, 290 (1930).

60. J. J. Gilman, "Cleavage, Ductility, and Tenacity in Crystals," Fracture, p. 193, M.I.T. Technology Press, Cambridge, Mass. (1959).

61. A. N. Stroh, "A Theory of the Fracture of Metals," Adv. in Phys. 6, 418 (1957).

62. J. W. Craggs, "On the Propagation of a Crack in an Elastic-Brittle Material," ONR Report NR-064-406 May (1959).

63. J. J. Gilman, C. Knudsen, W. Walsh, "Cleavage Cracks and Dislocations in LiF Crystals," J. App. Phys. 29, 601 (1958).

64. R. Stoneley, "The Propagation of Surface Elastic Waves in a Cubic Crystal," Proc. Roy. Soc. 232, 447 (1955).

65. Data sources for Figure 33: Columbia resin-G. R. Irwin, Hand. d. Physik 6, 551 (1958); Steel - D. K. Roberts and A. A. Wells, Engineering 178, 820 (1954); High Polymers, A. M. Bueche and A. V. White, J. App. Phys. 27, 980 (1956); Glass, H. Schardin, Fracture p. 297, M.I.T. Tech. Press, Cambridge, Mass. (1959).

66. J. J. Gilman, "Creation of Cleavage Steps by Dislocations," Trans. AIME 212, 310 (1958).

67. J. J. Gilman, "Propagation of Cleavage Cracks in Crystals," Jour. App. Phys. 27, 1262 (1956).

68. N. M. Melankholin, V. R. Regel, "Investigation of the Fracture Process in Sodium Chloride Crystals," Zhur. Eksptl. Teoret. Fiz. 29, 817 (1955); Soviet Phys. JETP 2, 696 (1956).

69. H. E. Buckley, "On Cleavage Induced by Impurity," Z. Krist. 88, 122 (1934).

70. B. W. Roberts, H. C. Rogers, "Observations on the Mechanical Properties of Hydrogenated Vanadium," Trans. AIME 206, 1213 (1956).

71. C. S. Barrett, R. Bakish, "Twinning and Cleavage in Tantalum," Trans. AIME 212, 122 (1958).

72. M. Lambert, A. Guinier, "Imperfections de structure du fluorure de lithium irradie aux neutrons: rassemblements d'atomes interstitiels," Comptes Reudus 245, 526 (1957).

73. H. A. Elliott, "An Analysis of the Conditions for Rupture Due to Griffith Cracks," Proc. Phys. Soc. 59, 208 (1947).

74. J. J. Gilman, "Nucleation of Dislocation Loops by Cracks in Crystals," Trans. AIME 209, 449 (1957).

75. B. A. Bilby, R. Bullough, "The Formation of Twins by a Moving Crack," Phil. Mag. 45, 631 (1954).

76. J. R. Low, "A Review of the Microstructural Aspects of Cleavage Fracture," Fracture, p. 68, M.I.T. Technology Press, Cambridge Mass. (1959).

77. J. M. Berry, "Cleavage Step Formation in Brittle Fracture Propagation," Trans. ASM 51, 556 (1959).

78. J. Friedel, "Propagation of Cracks and Work Hardening," Fracture, p. 498, M.I.T. Technology Press, Cambridge, Mass. (1959).

79. E. H. Yoffe, "The Centre of a Dislocation: II - The Dilated Slit" Phil. Mag. 3, 8 (1958).

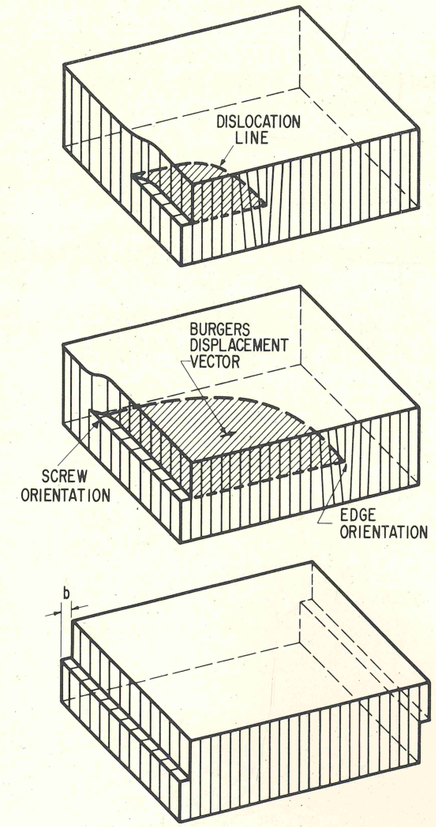

Fig. 1 Spread of translation gliding across a crystal.

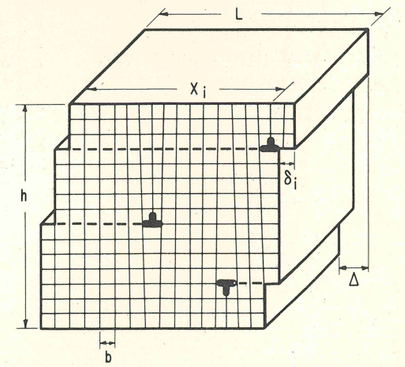

Fig. 2 The strain caused by dislocations.

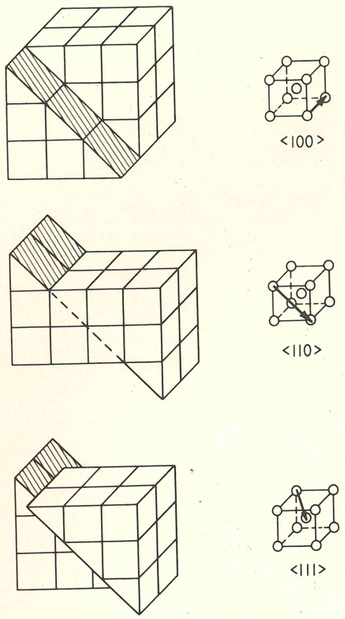

Fig. 3 Three possible glide directions in iron--the shortest one, <111>, is preferred.

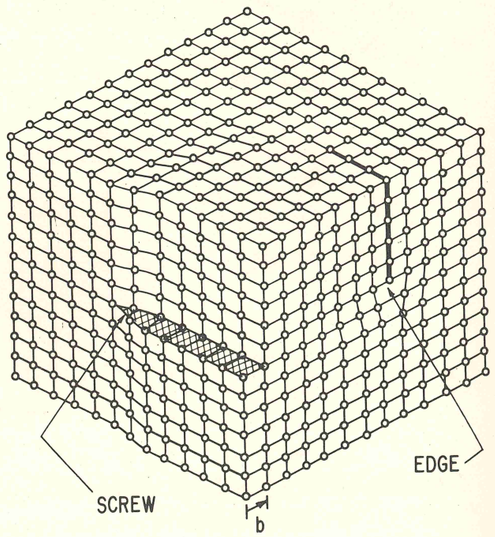

Fig. 4 Distortions of a crystal near the screw and edge orientations of a dislocation line.

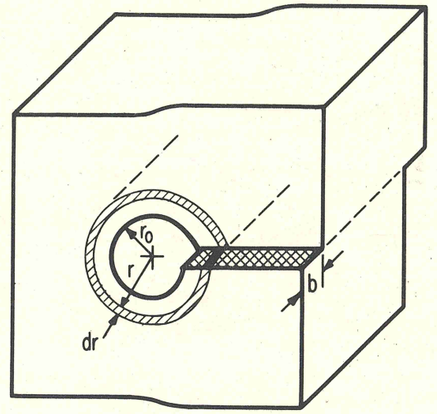

Fig. 5 Strained elastic shell around a screw dislocation.

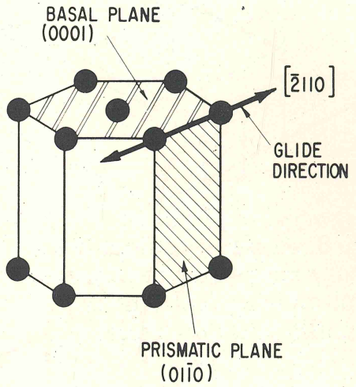

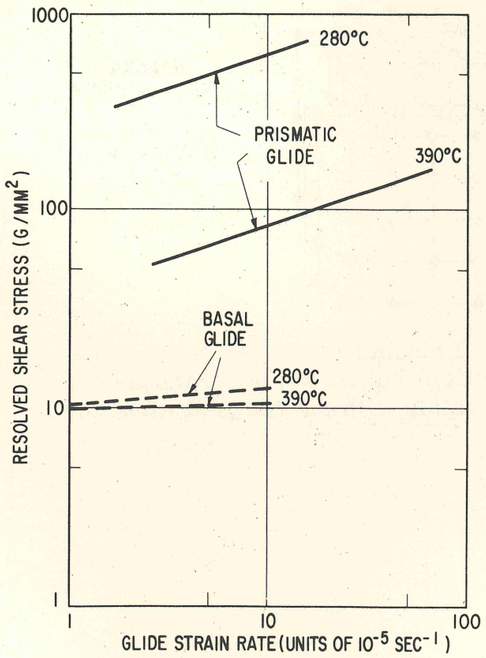

Fig. 6 Translation gliding in the close-packed direction is more difficult on the prism planes of zinc crystals than on their basal plane.

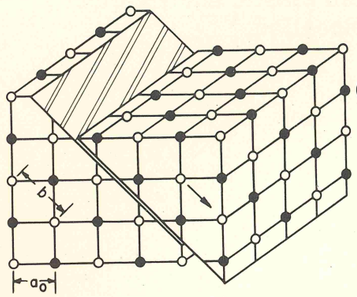

ROCKSALT
(SODIUM CHLORIDE)

{110}<110> GLIDE

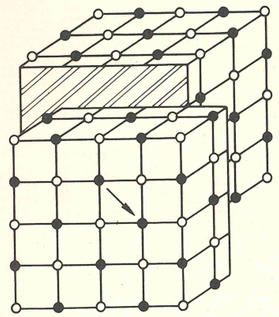

GALENA
(LEAD SULFIDE)

{100} <110> GLIDE

Fig. 7 Translation-gliding in the same direction, but on two different planes in crystals with the rocksalt structure.

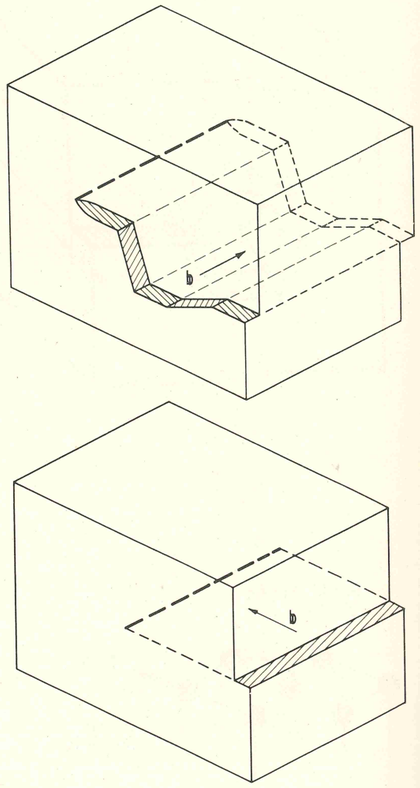

Fig. 8 A screw dislocation (top) may glide on any plane but an edge (bottom) is confined to one plane.

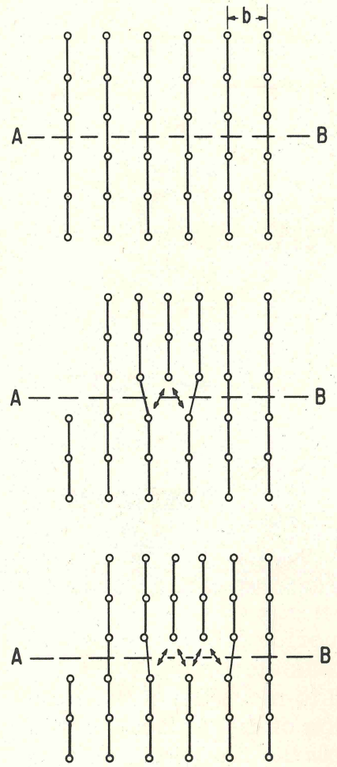

Fig. 9 Balanced forces at a moving dislocation.

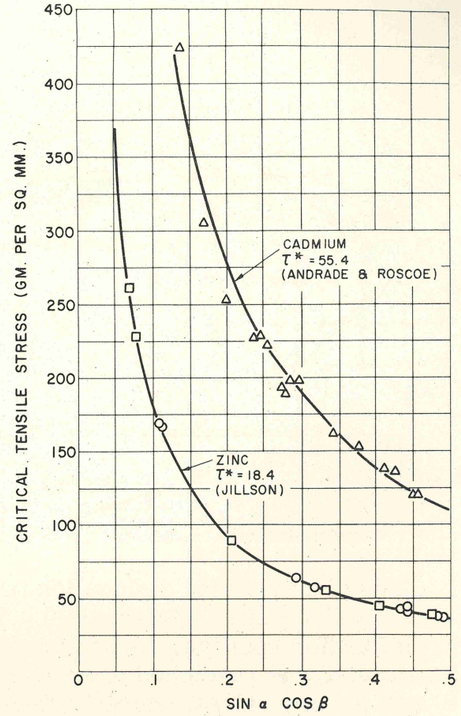

Fig. 10 Tensile stresses required to cause plastic flow in zinc and cadmium crystals as a function of orientation angles (Jillson, Andrade, and Roscoe).

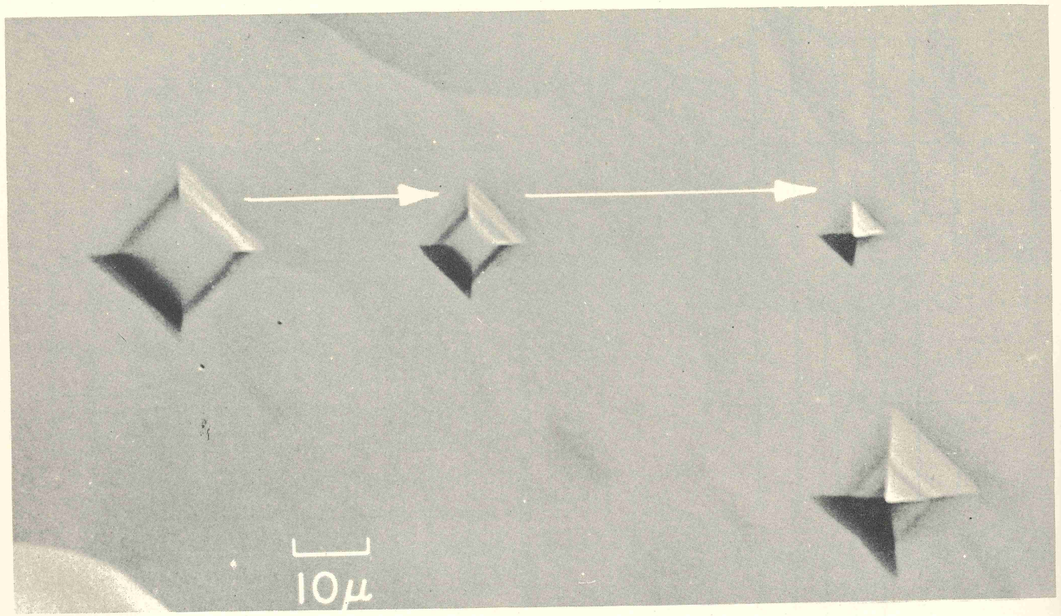

Fig. 11 Glide of an isolated dislocation in a lithium fluoride crystal revealed by etch-pits (after Gilman and Johnston). The crystal was etched to show the initial dislocation position; then a stress was applied to move the dislocation, and the crystal was re-etched to show the new position of the dislocation some more, and the crystal was etched a third time to show the final position of the dislocation. The arrows indicate the direction of motion.

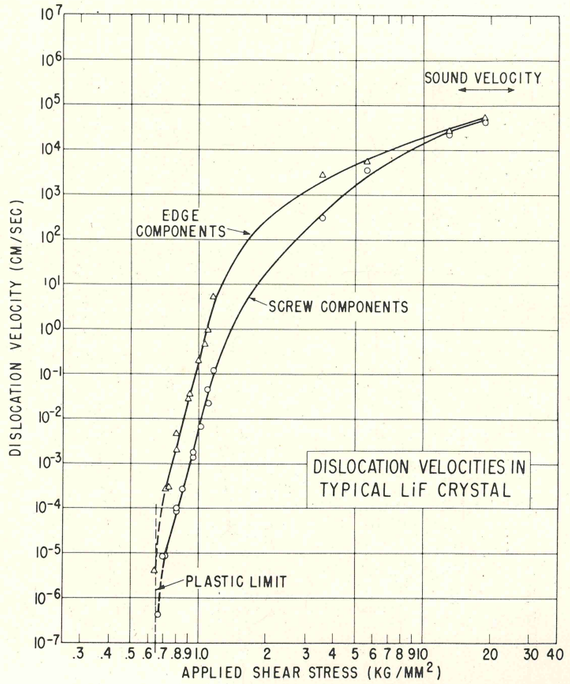

Fig. 12 Dislocation velocities in typical LiF crystal.

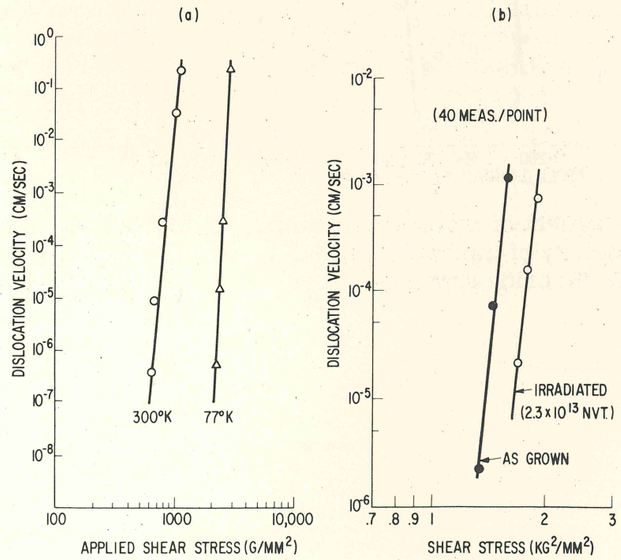

Fig. 13 Dislocation velocity vs stress for crystals that were given various treatments (screw dislocations). (a) Effect of decreasing the temperature. (b) Effect of radiation damage.

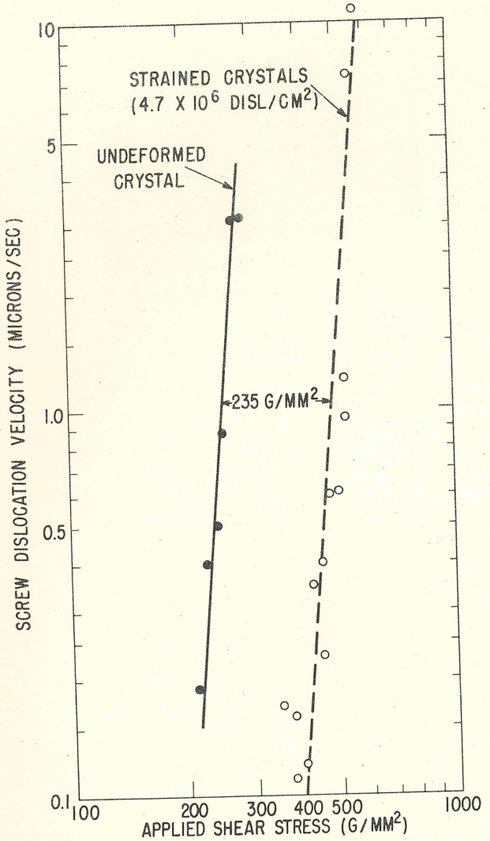

Fig. 14 Effect of strain-hardening on mobility of dislocations in lithium fluoride crystals.

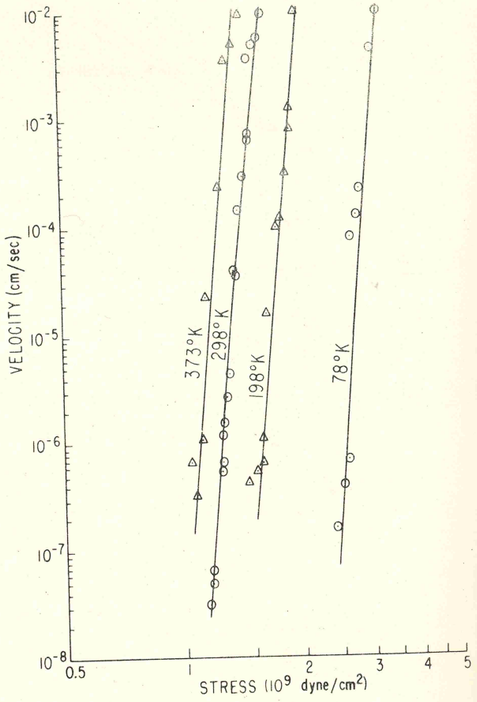

Fig. 15 Edge dislocation motions in Fe - 3 per cent Si crystals (Stein and Low).

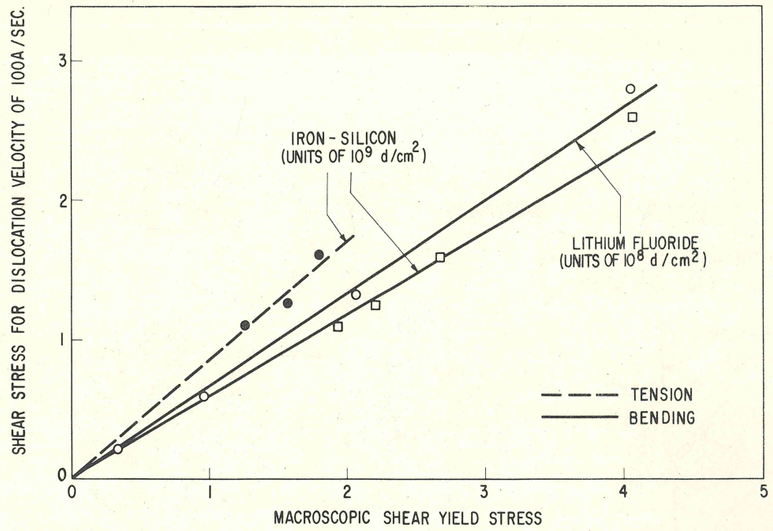

Fig. 16 Correlation between stress to cause dislocation motion and the macro-yield stresses of crystals.

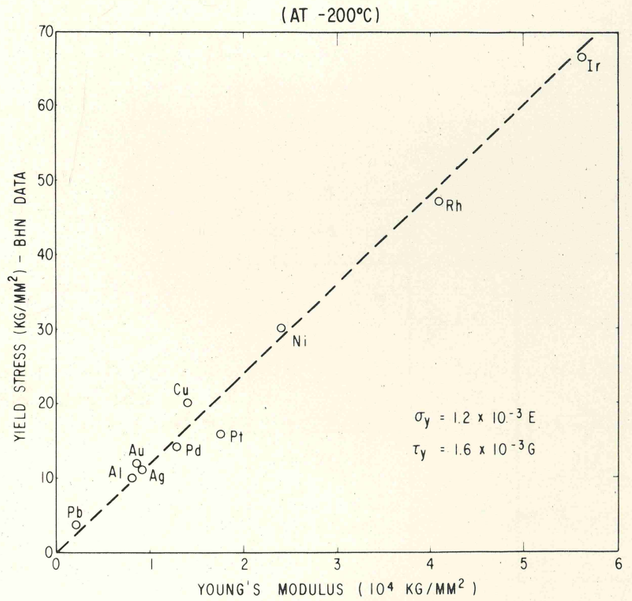

Fig. 17 Relation of yield stress to elastic modulus for face-centered cubic metals.

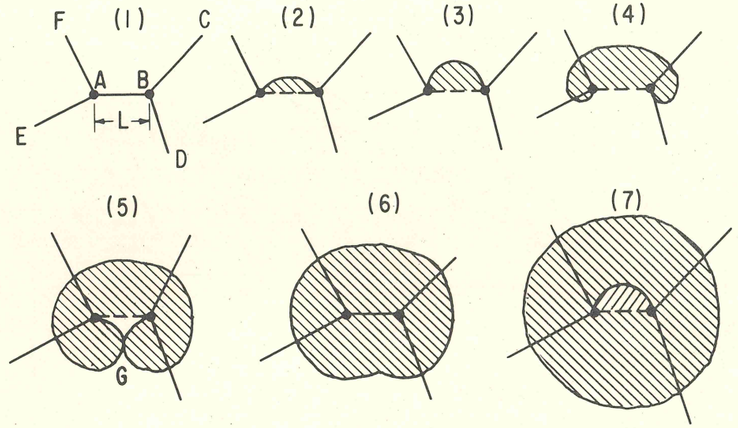

Fig. 18 Multiplication of dislocations via a Frank-Read source.

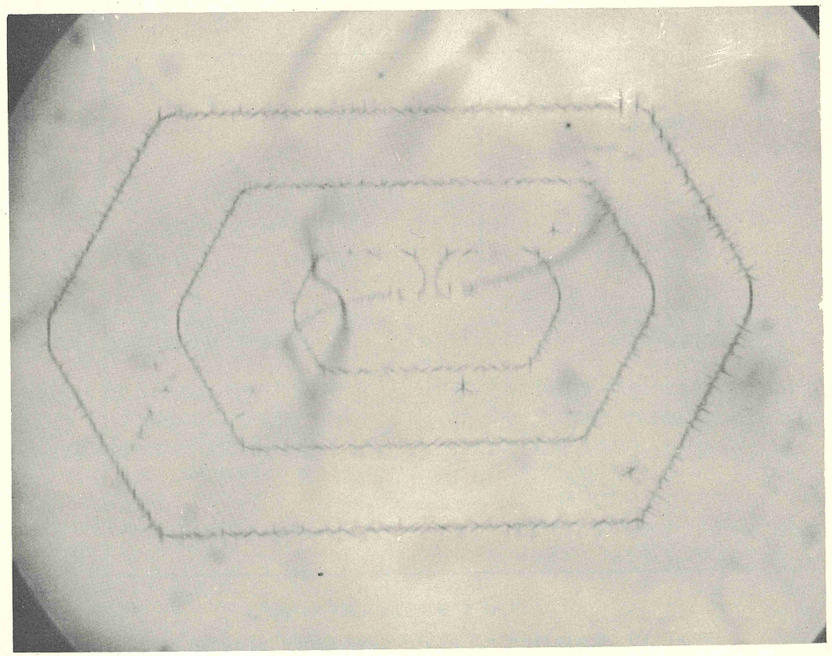

Fig. 19 A Frank-Read source seen in plastically deformed silicon. Copper precipitates reveal the dislocation lines. The dislocations lie on the (111) plane of silicon (Courtesy of W.C. Dash). 400X

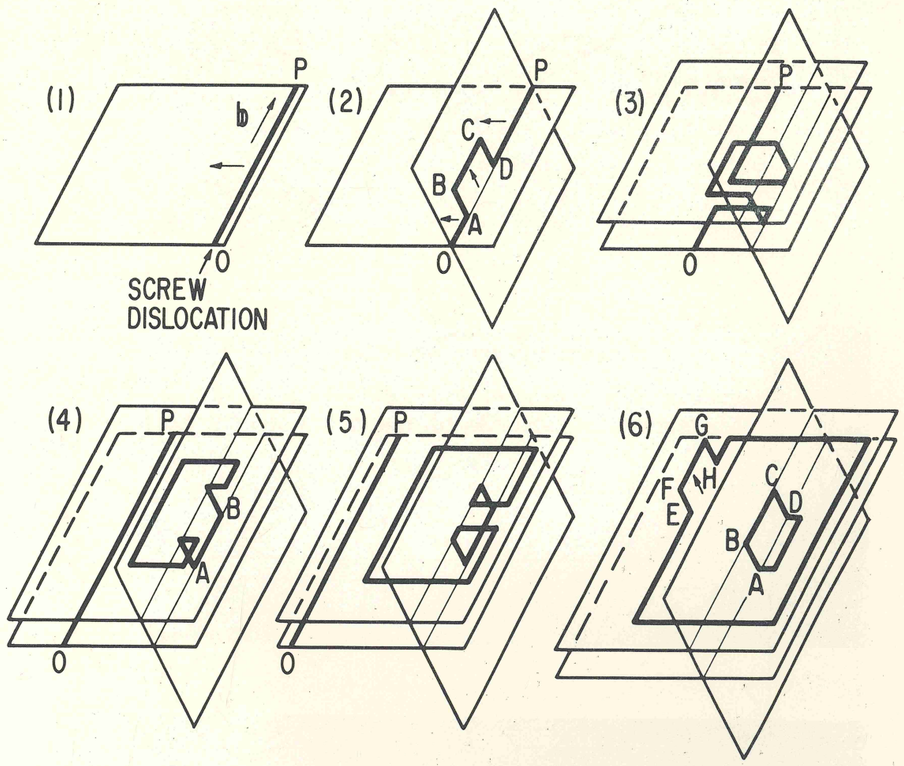

Fig. 20 Multiplication of dislocations via multiple cross-glide.

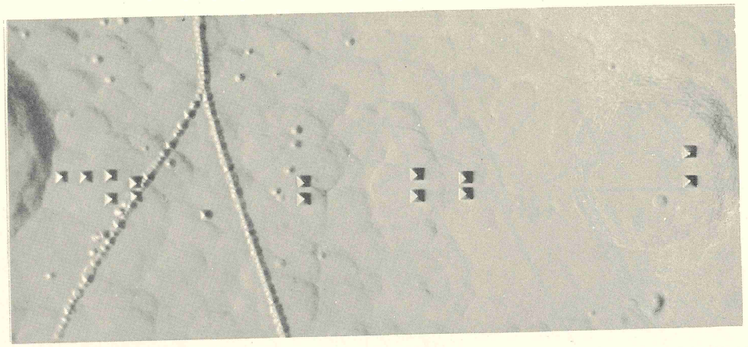

(a)

(b)

(c)

Fig. 21 Dislocation multiplication in a LiF crystal (after Gilman and Johnston): (a) dislocation half-loops at the surface; (b) same area after crystal had been bent; glide steps pass through five of the pairs of pits; (c) same area after light etch; showing many pits at each glide step.

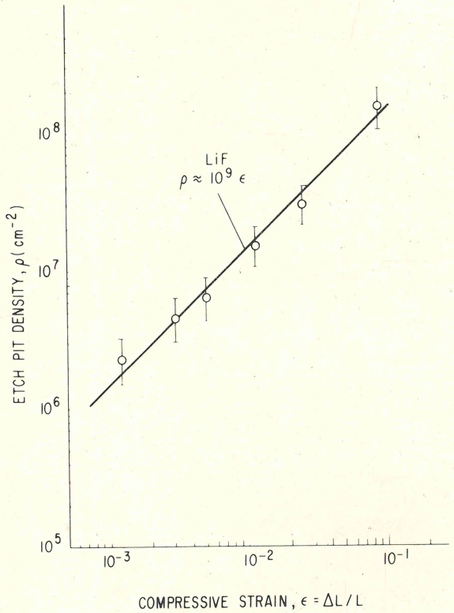

Fig. 22 Average dislocation density vs plastic strain for a typical LiF crystal.

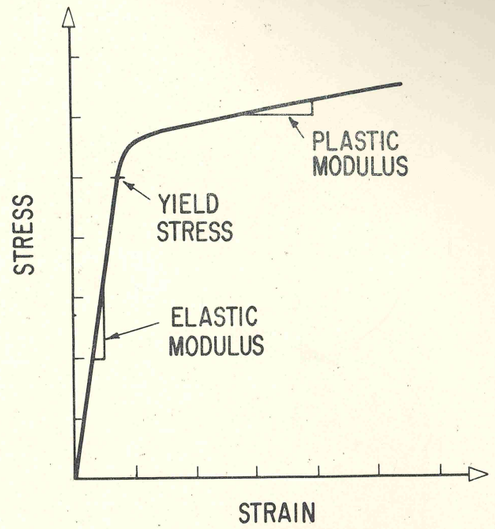

Fig. 23 General form of stress-strain curves.

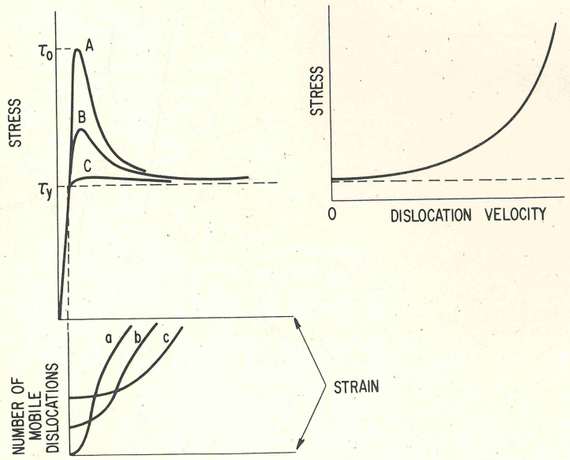

Fig. 24 Interpretation of plastic instability at yield point.

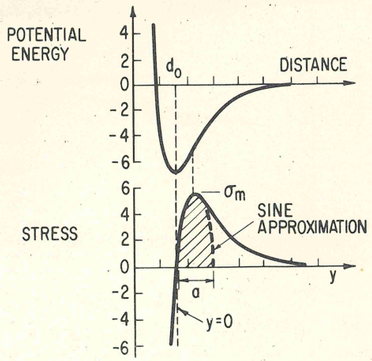

Fig. 25 Schematic energy and stress between two adjacent planes of a crystal.

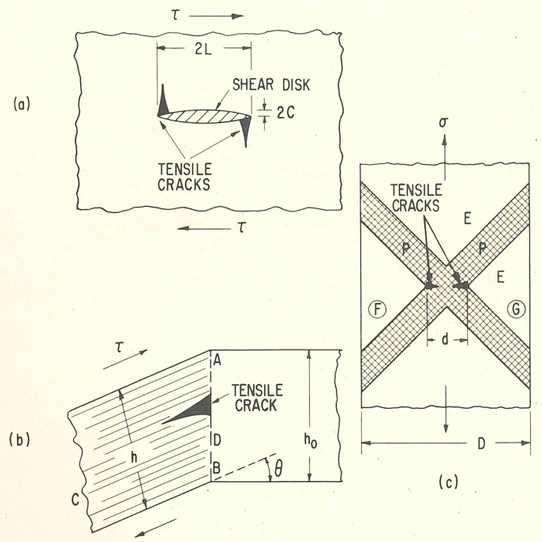

Fig. 26 Formation of cracks at the edges of shear disks (a), at plastic strain interfaces (b), and at glide band intersections (c).

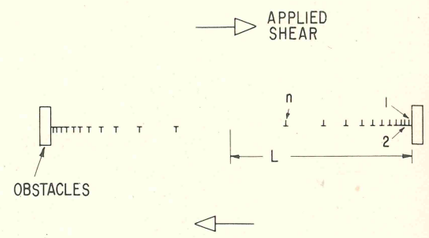

Fig. 27 Edge dislocation distribution in shear disk when shearing occurs on a single glide plane.

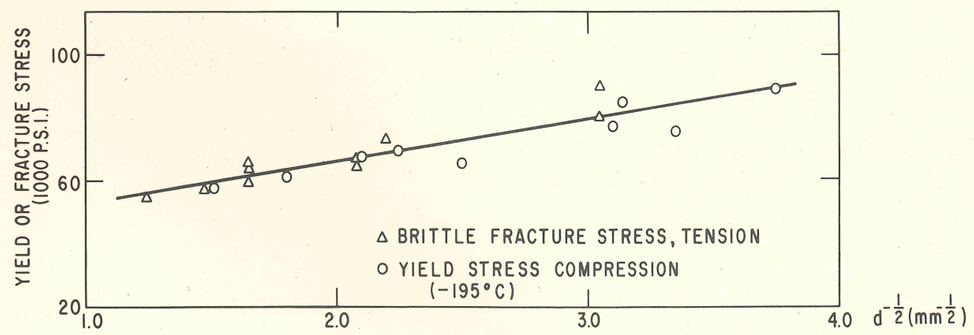

Fig. 28 Equality of fracture stress (tension) and yield stress (compression) for mild steel specimens of various grain sizes (after Low).

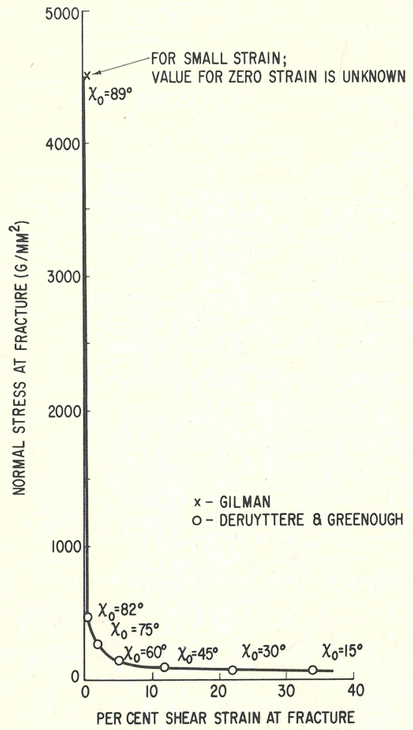

Fig. 29 Effect of glide strain on fracture stress of zinc crystals (at -196°C).

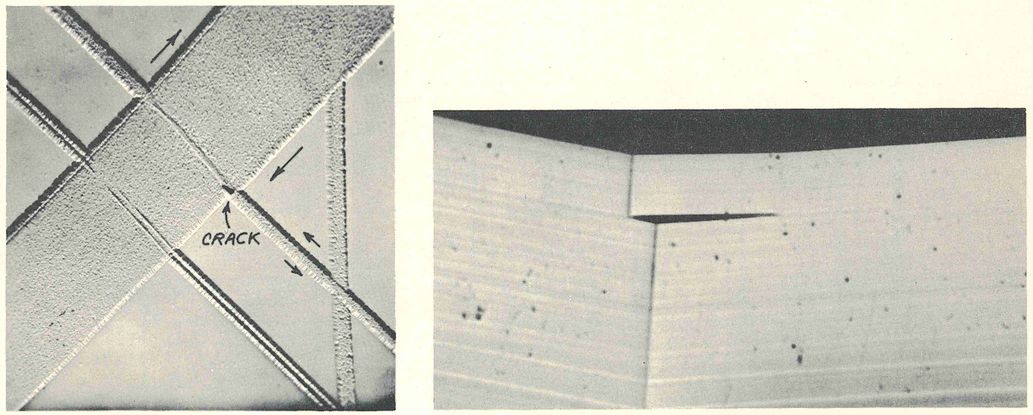

(a) (b)

Fig. 30 Examples of cracks that were produced by plastic deformation: (a) crack in MgO crystal (courtesy W. G. Johnston); example of cracking by mechanism of Fig. 26(c); (b) crack in Zn crystal; example of cracking by mechanism of Fig. 26(b) (after Gilman).

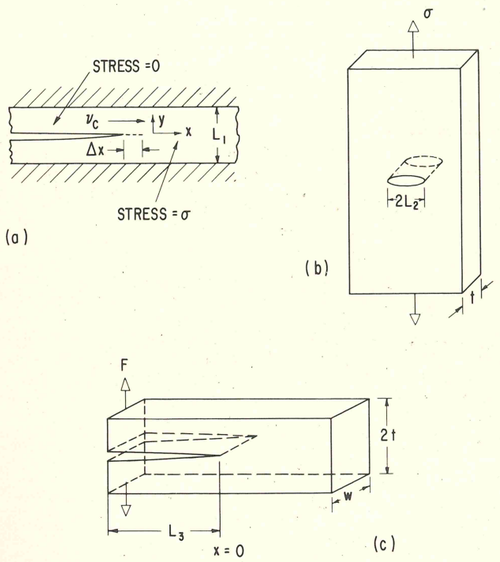

Fig. 31 Some schematic configurations of cracks in solids.

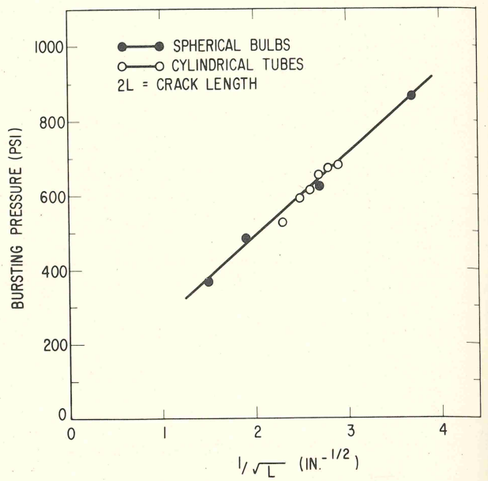

Fig. 32 Griffith's data for stresses required to propagate cracks in glass.

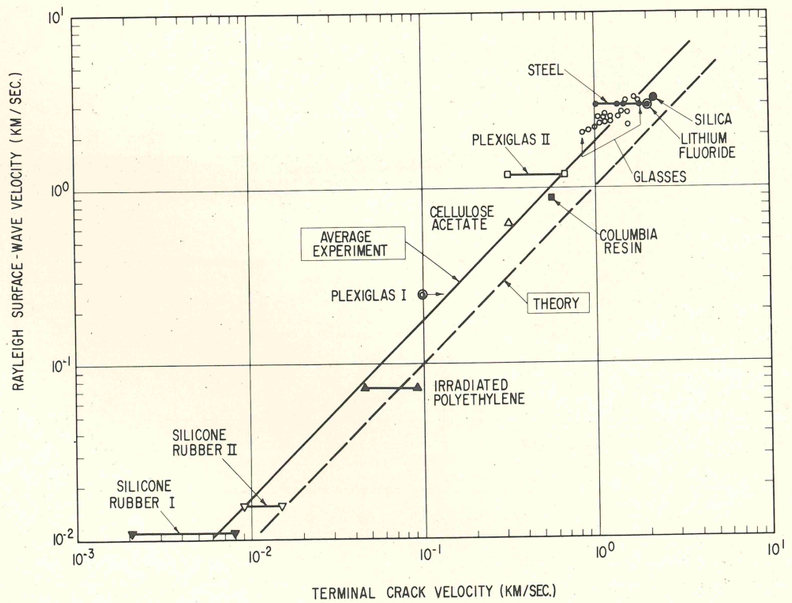

Fig. 33 Approximate equality of terminal crack velocities and sound wave velocities in various solids.

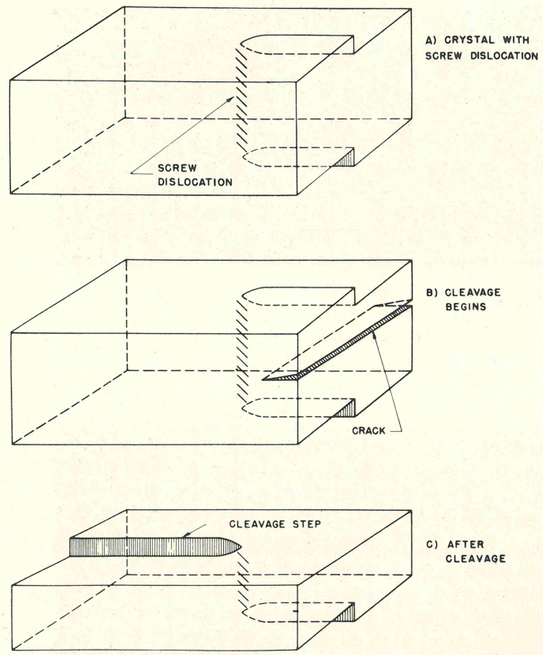

Fig. 34 Cleavage step formation by the intersection of a crack with a screw dislocation.

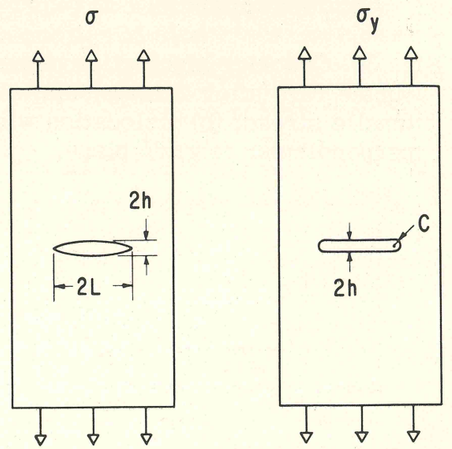

Fig. 35 Effect of plastic relaxation on the shape of a crack.

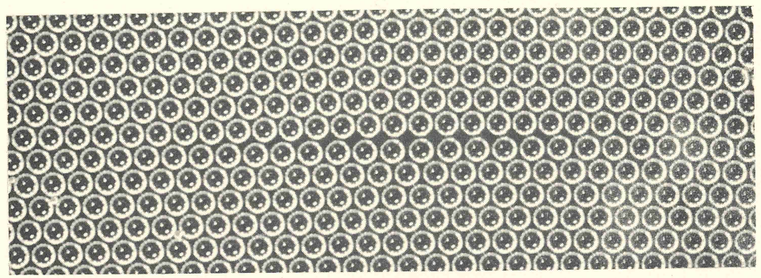

(a)

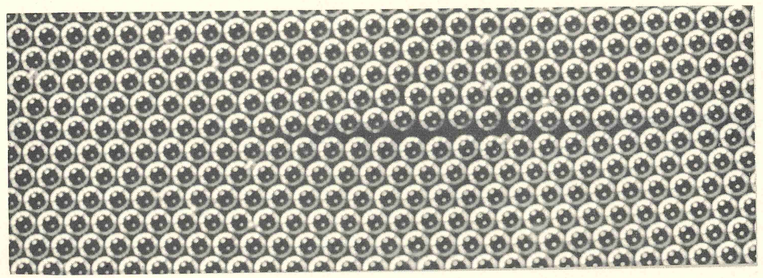

(b)

Fig. 36 Cracking along glide plane of dislocation in bubble raft (after Gilman): (a) dislocation with no tensile stress; (b) dislocation with tensile stress perpendicular to glide plane.

GENERAL ELECTRIC

Research Laboratory

SCHENECTADY, NEW YORK

TECHNICAL INFORMATION SERIES

Title Page

AUTHOR	SUBJECT CLASSIFICATION	NO.
Gilman, J.J.	fracture; plastic flow	60-RL-2410M
		DATE: April 1960

TITLE: Physical Nature of Plastic Flow and Fracture

37-9324

ABSTRACT: A review of current knowledge concerning the mechanisms of plastic flow and fracture written for non-specialists. This report was prepared for the Symposium on Plasticity that will take place at Brown University in April 1960. It is one of a series being prepared by members of the Metallurgy and Ceramics Research Department that will review the "state of the art" in different technical fields. It discusses such topics as:

A. Plastic Flow
   1. The Crystallography of Dislocation Motion
   2. Kinetics of Dislocation Motion
   3. Dislocation Nucleation and Multiplication
   4. Dislocations and Macro-flow

B. Fracture
   1. Nucleation of Cracks
      (a) In perfect crystals
      (b) By plastic flow
   2. Propagation of Cracks
      (a) In elastic bodies
      (b) Effects of plasticity

G.E. CLASS	REPRODUCIBLE COPY FILED AT	NO. PAGES
1	Research Information Section The Knolls Schenectady, New York	86
GOV. CLASS		

By cutting out this rectangle and folding on the center line, the above information can be fitted into a standard card file.

INFORMATION PREPARED FOR:

SECTION: Materials and Processes Studies

DEPARTMENT: Metallurgy and Ceramics Research

GENERAL ELECTRIC
Research Laboratory
Room 1A66
P. O. Box 1088
Schenectady 5, N. Y.

B E Kingsbury

Insulator Dept.
General Electric Co. Box 57
Baltimore 3, Md.

GENERAL ELECTRIC

Research Laboratory

SCHENECTADY, N. Y.

APJ-5A
9-56 (50M)

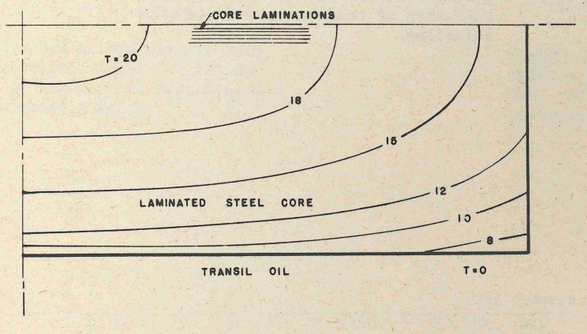

Figure 9. Temperatures in a cross section through one quarter of a transformer core. The contours are isothermal lines representing the temperature rise T in degree C with respect to the surrounding oil. No isothermal lines appear in the oil which is at a uniform temperature (T=0).

AIEE
Technical Paper
51-240

May 1951
Litho in USA

Equipment - Testing

SOME ENGINEERING APPLICATIONS OF THE ELECTROLYTIC FIELD-ANALYZER

H. K. Farr
Member AIEE
General Electric Company,
Pittsfield, Mass.

W. R. Wilson
Member AIEE
General Electric Company,
Philadelphia, Pa.

Advance Copy
Not Released for Publication

All Rights Reserved by the
American Institute of Electrical Engineers
33 West 39th Street, New York 18, N.Y.

A paper recommended by the AIEE Committee on Instruments and Measurements and approved by the AIEE Technical Program Committee for presentation at the AIEE Summer General Meeting, Toronto, Ont., Canada, June 25-29, 1951. Manuscript submitted March 26, 1951; made available for printing May 31, 1951.

PRICE: 30¢ To Members
60¢ To Nonmembers

SOME ENGINEERING APPLICATIONS OF THE ELECTROLYTIC FIELD-ANALYZER

by

H. K. Farr
Member AIEE

and

W. R. Wilson
Member AIEE

Introduction

Many of the problems encountered by the electrical engineer require for their solution the determination of potential fields. He may wish to know the electrical stresses on the insulation in an apparatus, the a-c resistance of a group of conductors or the hot spot temperature on a transformer core. The mathematical solution to such problems is usually very arduous if not impossible. Direct measurements on conducting models, however, often provide answers quite rapidly and conveniently to even rather complex problems.

The electrolytic field-analyzer or electrolytic tank is a device for measuring by analogy the physical quantities representing conditions in materials subjected to electric, magnetic, thermal or other fields. Voltage and current are applied and measured around models consisting of conductors and insulators immersed in an electrolyte. The principle is an old one familiar to many engineers. Special circuits and model techniques have, however, permitted its extension to problems for which this instrument is not usually considered appropriate.

It has been found possible, for example, to represent the flow of heat in a material whose conductivity changes with direction, by distorting the shape of the model. A tank of special shape has been devised for the study of the magnetic field around circular coils. (The tank used for axially symmetric electric fields is of different shape.) Under certain conditions the distribution of high frequency currents in conductors can be determined by setting up similar conductors in an electrolyte. A technique has also been worked out for the more difficult, low frequency condition, when it is necessary to connect capacitors in series with small electrodes to obtain the correct current distribution. A guarded bridge circuit has been used to determine the direct capacitance between any two conductors of a group by measurement of the resistance between electrodes of a model. These techniques have been applied by the authors during the past few years, in two industrial laboratories connected with the design of electrical apparatus. The field plots and other data used to illustrate the discussion were obtained in the course of this work.

Table I summarizes the more important fields that may be studied by means of the electrolytic field-analyzer. The present paper is concerned mainly with field types one through four. All of these fields are governed by similar laws; but field number three, the flow of an electric current in a conducting medium, is that of the electrolytic field-analyzer itself. It is chosen to represent other fields because it is the simplest to control and measure.

Mr. Farr is in the Electrical Research Section, Transformer and Allied Product Divisions Laboratory, Pittsfield, Mass., and Mr. Wilson is Section Head of the Electrical Section, Switchgear Divisions Laboratory, Philadelphia; both are with the General Electric Company. Acknowledgement is due to Mr. T. R. Walters for his interest and encouragement.

Practical considerations may impose limitations on the types of problems that can be solved by this method. Some symmetry may be required for electrostatic fields in composite dielectrics or for magnetic fields due to electric currents. Though usually applied to static fields, the instrument may handle certain dynamic problems if lumped impedance elements are connected externally to the model.

Certain quantitative relations are needed to convert the data supplied by the field-analyzer into quantities which characterize the "initial" field. (It is convenient to refer to the field of interest as the initial field and to its analogue in the field-analyzer as the model.) These relations are derived in the appendix, which discusses the model scale factors and which is intended to supply the necessary theoretical justification for the model techniques presented here.

General Construction and Operation of the Electrolytic Field-Analyzer

Although the general principles have been discussed by others,[1, 2, 3] they will be outlined briefly. The basic equipment, sketched in Fig. 1, comprises: (1) the electrolytic tank and model, (2) the external electric circuit, (3) a pantograph. The probe and bridge circuit measures the voltage at any point of the model with respect to some one fixed electrode. This voltage is conveniently expressed as a percentage of the total applied to the model. With the bridge arms set at any desired ratio the corresponding equipotential line may be traced with the pantograph, by moving the probe from point to point where a balance is shown on the null indicator. Although some workers[4, 5, 6] have constructed servo devices for automatic plotting, the labor of manual plotting with a pantograph may be much less than that of constructing a complicated model.

Figure 2 shows the field analyzer equipment arranged with a vertical plotting board. By substituting different tanks for different problems, one may use either a deep tank, or a shallow tank with a bottom that may be flat, sloping, or of hyperbolic contour.

An alternating voltage of about 1000 cycles per second is supplied to the model. At lower frequencies errors may be caused by electrolytic films at the electrodes, whereas stray capacitances become troublesome at high frequencies. Because of its phase indication and rapid response a cathode ray oscilloscope makes a good null indicator.

It is possible to use tap water (resistivity about 10,000 ohm cm) as the electrolyte. The electrodes, preferably copper, should be clean and the water renewed each day.

If it is desired to measure the resistance between two electrodes of the model, a third calibrated variable resistor may be connected in series with the electrodes so as to form a Wheatstone bridge. When the model requires a number of electrodes carrying specified currents, the electrodes may be connected to the generator circuit through individually variable series resistors. Also, one or more additional voltage dividers may be connected across the generator to maintain various electrodes at specified voltages.

Models for Plotting Equipotential Lines in Electrostatic Fields

The electrolytic field-analyzer is especially well suited to the study of electric fields. In this connection it may be used to help in the design of insulation for high voltage equipment,[7] to predict stresses on dielectric materials under test or to

determine capacitances. For equipotential plots the model is constructed so that: (1) electrodes have the same shape and position as those in the initial structure; (2) the electrolyte in the model has a conductivity which is everywhere proportional to the dielectric constant of the initial medium. Because of the practical difficulty of maintaining liquids with different conductivities, the application of the electrolytic field-analyzer to problems involving several dielectrics is usually restricted to fields with sufficient symmetry to permit the use of a cross sectional model in a shallow tank.

Symmetry Considerations

Geometries of two special types which lead to important simplifications in model construction are those of "translational" and "rotational" symmetry. Translational symmetry is represented by a group of long, straight, parallel conductors like a three-phase cable or a system of bus bars. Rotational symmetry is that of a figure of revolution like a high voltage bushing or a coaxial cable. For translational symmetry one uses a flat, shallow tank which represents a cross section of the initial structure. With rotational symmetry the model represents a wedge shaped segment of the initial structure. This is set up in a tank with a sloping bottom. The axis of symmetry is the "shore line" where the top and bottom surfaces of the water meet.

If additional planes of symmetry are present, other portions of the model may be eliminated and the model enlarged to permit greater accuracy.

Composite Dielectrics

In the shallow tanks used for translational or rotational symmetry, it is possible to separate by special walls the liquids which represent various dielectrics. Fine, closely spaced, vertical, conducting, hair-pin paths carry the current over thin insulating barriers.[8]

The results of this technique are illustrated in Fig. 3, an equipotential plot of the field around a glass bushing used on large capacitors. Askarel, glass and air were represented by electrolytes of different conductivities in a sloping tank.

With models of translational symmetry the conducting medium may be characterized by the "conductance per square". This is the specific conductivity of the electrolyte multiplied by the depth, and is similar to the surface conductivity of a material. It is the conductance measured between two plane vertical electrodes extending across a rectangular tank with vertical insulating sides and of width equal to the separation of the electrodes. Practically, it may be determined by measuring the conductance between two vertical concentric cylinders placed in the tank and multiplying by an appropriate geometrical factor.

For translational symmetry, it is sufficient that the conductance per square be everywhere proportional to the dielectric constant. It is, therefore, possible to represent different dielectrics by variations in the depth of a single electrolyte with a constant specific conductivity. Even a dielectric whose permittivity changes gradually and continuously from point to point may be represented in this way. Where it changes abruptly, however, a line of vertical conducting pins should be placed along the edge of the step. Otherwise the step will distort the current pattern and cause a spurious voltage drop. When this technique is used in the sloping tank, the angle of slope is everywhere proportional to the dielectric constant; the change in depth at a boundary of the dielectric is the same as in a flat tank.

Capacitance Determination

The capacitance between two electrodes of the initial structure may be determined from a measurement of the resistance between corresponding electrodes of the model. For translational symmetry, the capacitance between two parallel conductors, per unit length of one of the conductors, is $\epsilon/\sigma R$ where R is the resistance of the model, σ is the conductance per square of the electrolyte and ϵ is the permittivity (inductive capacity) of the initial medium. This relation is developed in the appendix. If R and σ are in ohms and mhos and ϵ is in rationalized MKS units, the resulting capacitance is expressed in farads per meter of conductor length.

If there are more than two conductors, the direct capacitance between any two (also called "partial" capacitance) may be determined from an electrolytic model using a guarded resistance bridge. This circuit is shown in Fig. 4, connected so as to determine the capacitance between electrodes A and B. Electrode G in this diagram represents all the other conductors in the problem. The resistance R_{AB} is the partial resistance between electrodes A and B. With the null detector connected to B one adjusts R_3 so as to bring B and G to the same potential. The null detector is then switched over to the voltage divider (R_1 and R_2) which is also adjusted for a null reading. Then $R_{AB} = R_1R_3/R_2$ and the corresponding capacitance is $\epsilon/\sigma\ R_{AB}$.

Electrostatic Flux Plotting

By the methods already described, one plots equipotential lines of a model which correspond to equipotential lines of the initial electrostatic problem. For problems of translational symmetry, it is possible to construct a model whose equipotential lines correspond to flux lines of the initial problem. In such a model, insulators are used to represent conductors of the initial problem and the conductance per square of the electrolyte is made inversely proportional to the dielectric constant. Electrodes of the model are constructed to follow certain flux lines of the initial field. This is known as the conjugate or orthogonal method.

Figure 5 is a plot[9] made from electrolytic models showing both equipotential lines and flux lines about a gas inclusion in porcelain near the porcelain surface. Because this problem was set up in the flat tank, the gas inclusion was represented as a cylinder. This approximates an actual inclusion which would be roughly spherical.

Magnetic Fields at High Frequencies

The most convenient method for plotting magnetic fields produced by electric currents is that which represents the initial magnetic flux lines as potential lines of the model: that is, the orthogonal representation[10]. The most tractable fields are those of translational symmetry at frequencies high enough so that currents flow only on the conductor surfaces (skin effect) but not so high that displacement currents are significant. For such fields, each conductor in the initial problem is accurately represented by a solid conductor of the same cross sectional shape in the model. The current supplied by the external circuit to each conductor in the model is adjusted so as to be proportional to the total current flowing along the corresponding conductor of the initial problem. The distribution of current density over each conductor surface is then found to be the same in the model as in the initial structure. (The direction of this current is, of course, normal to the conductor surface in the model but along the surface in the initial problem.) Magnetic fields due to short pulse or transient currents may also be represented in this way. At any frequency it is correct to choose the conductance σ of the electrolyte so as to be everywhere inversely proportional to the magnetic permeability μ of the initial structure. Ferromagnetic materials of very high permeability may often be represented as insulators.

If two long, parallel conductors are connected together at one end, the self inductance of the loop per unit length of one conductor is $\mu\sigma R$ where R is the resistance measured between corresponding conductors of the model. Similar expressions may be obtained for the mutual inductance or the leakage inductance among several conductors.

Figure 6 shows the magnetic flux distribution in a portion of the winding of a pulse transformer, plotted by the orthogonal method. Conductor (1) was in the low voltage winding and all others were in the high voltage winding. The same model with different connections was used to measure leakage inductance, interwinding capacitance and electric field intensities.

Quantitative Relations Between Model and Prototype

Table II exhibits the correspondence between pairs of quantities which characterize electrostatic or magnetic fields of translational symmetry and their electrolytic models. Similar relations hold for fields of rotational symmetry and, in the case of electrostatics, for fields without symmetry. Their derivation is sketched in the appendix. The expressions already given for capacitance and inductance follow from entries 3 and 8 of the table.

Flux Fields of Rotational Symmetry

It is possible to represent magnetic fields of rotational symmetry by the orthogonal method. In regions where the permeability is constant, the depth of the tank is made inversely proportional to the radius (measured from the axis of symmetry). This is in contrast to the direct representation for which one uses a sloping tank of depth proportional to the radius. This allows the convenient representation of circular windings. The method has some practical limitations which do not apply to the sloping tank. The change in depth must be sufficiently gradual so that current flow is everywhere essentially horizontal. The model must be so proportioned that the region of interest is not too close to the deep part of the tank near the axis where the depth changes rapidly. A conducting surface is placed near the axis to replace the portion of the tank where the depth would otherwise become infinite and may be used as the return circuit for the currents supplied to the conductors representing the winding.

A tank of the same shape may be used for flux plotting in electrostatic fields of rotational symmetry.

Magnetic Fields at Low Frequencies

At frequencies below those at which skin effect predominates, the currents in the initial problem are distributed over the cross section of each conductor. It may then be necessary to use special methods to insure that the currents introduced into the model from the external circuit are correctly distributed and have the proper phase at each point.

At very low frequencies the currents are distributed over the cross section of an initial conductor uniformly and in phase. In the model the corresponding conductor, which would be solid in a high frequency problem, is now broken up into an array of uniformly spaced vertical pins or small electrodes distributed over the area representing the cross section of the initial conductor. Equal current is supplied to each small electrode from an individual, variable, series resistor which is adjusted by trial and error. An alternative is the use of fixed series resistors of very high resistance. The number of electrodes which should be used to represent a given conductor (that is, the extent to which the subdivision should be carried) will depend on the size of the initial conductor and on the accuracy required. Karasev[11] uses a block of resistance material which makes contact with the surface of the electrolyte.

At intermediate frequencies the conductor is subdivided in the same way. Instead of a resistor, however, one connects in series with each small electrode a capacitance equal to $f_i \mu \sigma / f_m \tau$ where τ is the d-c resistance per unit length of the conductor or portion of a conductor in the initial problem corresponding to the area of the model apportioned to that particular electrode. The frequencies f_i and f_m are those of the initial problem and model respectively. The drop in the capacitor corresponds to the resistive drop in the initial problem and the drop in the electrolyte to the inductive voltage drop. In principle, the representation may be made exact provided a sufficiently large number of very small electrodes are used.

Figure 7 illustrates a model of this kind which was used in a problem of bus bar design. As the initial structure was symmetrical about two perpendicular planes, the model comprised only one quadrant of the cross section. One symmetry plane divided two groups of buses carrying opposing currents. In the model this plane was replaced by a conducting wall. The other symmetry plane, which bisected each bus bar, was replaced by an insulating wall. In this way, one half of the bus bars were eliminated completely and, of the remaining four bars, one half of each was included in the model. As two electrodes occupied an area corresponding to one half of the cross section of a bus bar, each electrode represented one quarter of a complete bus bar. An external resistor was also connected in series with each electrode to represent approximately the internal inductive effects for that portion of the conductor: that is, the drop that should occur in the electrolyte replaced by the conductor. Current from one generator terminal flows through the capacitors and resistors to the various electrodes, then through the electrolyte to the conducting wall of the tank, and back to the generator.

No equipotential plot is necessary for this test. A measurement of the voltage at each electrode allows a determination of the I^2R loss in the corresponding portion of the bus bar. The total power loss for each bar is shown in Table III, for a power frequency of f_i = 60 cycles per second. The current distribution is evidently very nonuniform.

Resistive Current Flow

For problems involving the flow of electric current through a medium obeying Ohm's law, the correspondence with the electrolytic model is not by an analogy but is direct. Regions in the initial problem which differ in conductivity are represented by electrolytes of proportional conductivity.

Figure 8, for example, shows the potential field throughout one of a pair of contacts in a circuit breaker. Each contact consists of an arc-resistant alloy plate brazed to a copper backing. This plot was made to show the effect of an incomplete braze. The alloy and the copper backing were represented in the model by electrolytes of different conductivities.

Steady State Conductive Heat Flow in an Anisotropic Medium with Distributed Sources

The field analyzer is also well suited to the solution of problems in the conductive, steady-state flow of heat. Voltage in the model corresponds to temperature T and current density to heat flow h in watts/inch^2.

Figure 9 is a temperature plot representing conditions in a transformer core. By taking advantage of the translational symmetry and of the two planes of mirror symmetry in the core, the model may be set up in a flat shallow tank covering an area corresponding to one quarter of the core cross section. The model presents several unusual problems. Corresponding to the fact that heat is generated uniformly throughout the core, current is introduced into the model through an array of vertical pins, uniformly

spaced. One terminal of the generator is connected to these pins through series resistors which apportion equal currents to each pin. The heat conductivity (which corresponds to the electrical conductivity of the electrolyte) is higher along the laminations than across them. This situation is accurately represented by "stretching" the model in the direction perpendicular to the laminations by an amount equal to the square root of the ratio of the heat conductivities in the two directions. In the oil around the outside of the core, there is an abrupt temperature drop from the metal surface temperature to the constant temperature of the main body of oil. To represent this condition, small electrodes are placed along the two sides of the tank corresponding to the metal-oil boundary. Each of these electrodes is connected through a series resistor to the other terminal of the generator. The voltage at this terminal represents the temperature of the ambient oil and the drop in the resistors, the temperature drop at the metal surface. These resistors are adjusted by trial and error in accordance with known laws of heat convection in oil. Thus, current flows from one generator terminal through resistors to pins distributed throughout the tank, through the electrolyte to the electrodes along the tank wall, then through other resistors to the other generator terminal.

Conclusions

The electrolytic field-analyzer can supply answers to a surprising range of problems. It may be used not only to map fields, but to provide numerical values of such quantities as inductance, capacitance and a-c resistance. Although the accuracy may be poor for unfavorable geometries, it can be made quite satisfactory in many practical problems by observing certain precautions. A careful study of the theory of fields and models will often allow the application of the instrument to be extended to unusual problems by using special models or external circuits. Experience with the electrolytic field-analyzer leads to an intuitive grasp of the analogies between fields of different types, which is very helpful in visualizing particular problems even when the instrument is not directly employed. The cost of assembling the basic equipment is low enough to be offset by the successful solution of even one or two important problems.

Appendix: Mathematical Theory

The following analysis is made in terms of the rationalized MKS system of electromagnetic units.

Electrostatic Fields

The potential ϕ in an electrostatic field is determined by the equation

$$\nabla \cdot \epsilon \nabla \phi = -m \tag{1}$$

where m is the charge density and ϵ is the permittivity. In a linear electrolyte, the voltage V satisfies the equation

$$\nabla \cdot \gamma \nabla V = -P \tag{2}$$

where γ is the conductivity and P is the density of the current which is introduced into the electrolyte from an external circuit, measured per unit volume of the electrolyte. It is clear that V and ϕ will be everywhere the same if the source densities P and m and medium constants γ and ϵ are respectively equal at all points. Equation (2) involves four quantities P, V, γ and length, the last entering through the vector operator ∇. Three of these quantities can be scaled up or down at will; the remaining quantity will then bear a fixed ratio to its analogue in equation (1). Suppose scale factors a, b and k_o are chosen for length, potential and medium properties. Then

$$\nabla_m = a \nabla_i \tag{3}$$

$$\phi = bV \tag{4}$$

$$\epsilon = k_o \gamma \tag{5}$$

The subscripts i and m refer respectively to the initial field and to the model. Combining equations (1) through (5) results in the relation

$$P = \frac{a^2}{bk_o} m \tag{6}$$

for the source density scale factor.

Scale factors for other quantities are readily found from those already known. Thus for the field gradients E and F of the initial and model field,

$$E = -\nabla_i \phi = -\frac{b}{a} \nabla_m V = \frac{b}{a} F. \tag{7}$$

Also

$$D = \epsilon E = \frac{k_o b}{a} \gamma F = \frac{k_o b}{a} J \tag{8}$$

where D is the initial electrostatic displacement and J is the current density per unit area in the model. The total charge on a conductor of the initial problem is

$$Q = \iint D \, dA_i = k_o ba \iint J \, dA_m = k_o baI \tag{9}$$

where I is the total current supplied from the external circuit to a conductor of the model. The integrals are taken over the conductor surface areas A_i and A_m which are in the ratio a^2. The capacitance between two electrodes is

$$C = \frac{Q}{\phi} = k_o a \frac{I}{V} = \frac{k_o a}{R} \tag{10}$$

where R is the resistance measured between electrodes of the model. When symmetry allows the elimination of certain portions of the initial structure, quantities like Q or C in the above equations apply only to the portion of the initial structure which is actually included in the model.

In the flat tank the current flows parallel to the surface of the electrolyte. If h is the depth of the electrolyte, one can define a current density

$$i = hJ \tag{11}$$

amperes per unit length of the electrolyte surface. Then $\nabla \cdot i = p$ where p is the current introduced from the external circuit per unit area of the electrolyte surface. It follows that

$$\nabla \cdot \sigma \nabla V = -p \tag{12}$$

where

$$\sigma = h\gamma \tag{13}$$

is the conductance per square of the electrolyte. If a new scale factor $k = k_o/h$ is used for translational symmetry, then

$$\epsilon = k\sigma. \tag{14}$$

The scale factors a and b remain the same. The relations in Table II for electrostatic quantities are derived by using equations (6) through (11) or by modifying their derivation and by the use of the relation $i = \sigma F$.

Magnetic Fields of Translational Symmetry

The magnetic fields considered here are those due to electric currents, not including displacement currents. It will be assumed that the materials are linear. The flux density $\underline{B}$ and the field intensity $\underline{H}$ are then related by $\underline{B} = \mu\underline{H}$ where μ depends on position but not on $\underline{H}$. If $\underline{B}$ is derived from a vector potential $\underline{A}$ then,

$$\nabla \times \frac{1}{\mu} \nabla \times \underline{A} = \underline{u} \tag{15}$$

where $\underline{u}$ is the current density. For translational symmetry, derivatives with respect to $\underline{z}$ are zero, $\underline{u}$ is parallel to the $\underline{z}$-axis and equation (15) reduces to $A_x = A_y = 0$ and $A_z = \psi$ where

$$\nabla \cdot \frac{1}{\mu} \nabla \psi = -u. \tag{16}$$

Here ψ depends only on x and y and ∇ operates only in these coordinates. Comparison of equations (12) and (16) shows that this field may be represented in a flat tank if

$$\frac{1}{\mu} = k\sigma . \tag{17}$$

Then, since

$$\psi = bV, \tag{18}$$

$$u = \frac{kb}{a^2} p. \tag{19}$$

Since $\underline{B} = \nabla \times \underline{A}$, it follows that $B_x = \partial\psi/\partial y$, $B_y = -\partial\psi/\partial x$, and $B_z = 0$. That is, $\nabla\psi$ and $\underline{B}$ are at right angles but are equal in magnitude. Hence, magnetic flux lines coincide with equipotential lines of ψ and V. The value of ψ at any point is equal to the total flux crossing a surface which is parallel to the z axis, is of unit length in the z direction, and intersects the x-y plane along any curve which extends from the point where ψ is measured to the reference point where ψ has the value zero. For an a-c magnetic field of angular frequency ω the voltage per unit length induced along a path parallel to the $\underline{z}$-axis is

$$\beta = j\omega\psi \tag{20}$$

measured with respect to a reference conductor for which $\psi = 0$. (Here, $j = \sqrt{-1}$.) Item four in Table II follows from the fact that $B = |\nabla\psi|$ and $\nabla\psi = (b/a)\underline{E}$. The other relations in that table are found by methods similar to those used for the electrostatic case.

At high frequencies, of course, in the space adjacent to the conductor, $\underline{B}$ is parallel to the conductor surface. This surface is, therefore, an equipotential surface for ψ and for V. It is then correct to represent conductors in the initial problem by conductors in the model. At low frequencies this is not necessarily true.

Electrostatic Flux Plotting

In simply-connected charge-free regions, $\underline{D}$ can be derived from a vector potential. Then for translational symmetry,

$$\nabla \cdot \frac{1}{\epsilon} \nabla \psi = 0 \tag{21}$$

where ψ now represents the electrostatic flux function. The above restriction requires that the model be constructed so that the electrolyte does not completely enclose any region representing a conductor of the initial structure.

Magnetic Fields of Rotational Symmetry

In magnetic fields of rotational symmetry equation (15) may be expanded in cylindrical coordinates. The current $\underline{u}$ has components in only the θ direction and θ derivatives of the $\underline{A}$ components are zero. This leads to $A_r = A_z = 0$ and

$$\frac{\partial}{\partial z}\left[\frac{1}{\mu r}\frac{\partial(rA_\theta)}{\partial z}\right] + \frac{\partial}{\partial r}\left[\frac{1}{\mu r}\frac{\partial(rA_\theta)}{\partial r}\right] = -u, \tag{22}$$

where $\underline{r}$ is the distance from the axis. This time let

$$\psi = rA_\theta . \tag{23}$$

Then equation (22) reduces to

$$\nabla \cdot \frac{1}{\mu r} \nabla \psi = -u \tag{24}$$

where ∇ operates in the variables $\underline{r}$ and $\underline{z}$ as though they were the rectangular coordinates $\underline{x}$ and $\underline{y}$.

Comparison of equations (12) and (24) shows that the field is accurately represented in a shallow tank provided the current densities are represented in the same manner as for translational symmetry and the conductivity per square of the electrolyte varies as

$$\sigma = \frac{1}{k_1 \mu r} \tag{25}$$

where k_1 is a constant. From equation (13) it is seen that the depth varies as

$$h = \frac{1}{k_1 \gamma \mu r} . \tag{26}$$

If a uniform electrolyte is used to represent a region of constant permeability μ then $\underline{h}$ must be made proportional to $1/r$ and the tank cross section will be a hyperbola.

From the foregoing analysis, relations similar to those in Table II may be obtained for rotational symmetry.

Low Frequency Magnetic Fields

At low frequencies one may not know the current density $\underline{u}$. Equation (16) must, then, be replaced by one which relates the magnetic flux function ψ to the applied voltage rather than to the current. Only translational symmetry will be considered. The general equation for the electric gradient $\underline{E}$ in the initial magnetic field,

$$\nabla \times \underline{E} = -j\omega \nabla \times \underline{A} \tag{27}$$

is expanded in rectangular components. This leads to three differential equations that are satisfied by

$$E_z - \alpha + j\omega\psi = 0. \tag{28}$$

Here α is a potential such that $\underline{e} = z\nabla\alpha$ where $\underline{e}$ comprises the $\underline{x}$ and $\underline{y}$ components of $\underline{E}$. All quantities in this equation are independent of $\underline{z}$. Over the cross section of a conductor the potential α is equal to a constant value α_o which represents the applied voltage per unit length in the $\underline{z}$ direction. The induced voltage is, as was already pointed out, $\beta = j\omega\psi$. Finally, E_z inside a conductor is the resistive drop per unit length. If ρ is the resistivity of the conductor, equation (16) leads to

$$E_z = \rho u = -\rho\nabla\cdot\frac{1}{\mu}\nabla\psi. \tag{29}$$

The combination of equations (20), (28), and (29) results in

$$\beta + j\frac{\rho}{\omega_i}\nabla\cdot\frac{1}{\mu}\nabla\beta = \alpha_o \tag{30}$$

inside a conductor. Outside a conductor this reduces to

$$\nabla\cdot\frac{1}{\mu}\nabla\beta = 0. \tag{31}$$

In order to represent equations (30) and (31) by an electrolytic model β will be associated with the voltage $\underline{V}$ of the model. (On account of equation (20) this is similar to the procedure adopted for high frequencies when ψ was associated with $\underline{V}$). The region of the model which is to represent a conductor is broken up into a number of small areas into each of which current is introduced through a separate series capacitor c_n from a common source of voltage V_o. These capacitances are chosen so that $c_n = c_o A_n$ where A_n is the area apportioned to the corresponding electrode and c_o is a constant. Then

$$V_o = V + \frac{p}{jc_o\omega_m} \tag{32}$$

which, when combined with equation (12), becomes

$$V + j\frac{1}{c_o\omega_m}\nabla\cdot\sigma\nabla V = V_o. \tag{33}$$

This is satisfied by V in the region of current sources. In the remainder of the model

$$\nabla\cdot\sigma\nabla V = 0. \tag{34}$$

In order for equations (30) and (33) to be equivalent, the model conductivity must satisfy equation (17) and the capacities and frequencies must satisfy the relation,

$$\frac{a^2}{kc_o\omega_m} = \frac{\rho}{\omega_i}. \tag{35}$$

The last equation is equivalent to

$$c_n = \frac{\omega_i\mu\sigma}{\omega_m\tau} \tag{36}$$

where τ is the d-c resistance per unit length of the conductor or section of a conductor in the initial device which corresponds to c_n in the model.

The relations given in Table II for magnetic quantities remain unchanged. In the case of item eight, however, $\underline{R}$ is to be interpreted as the equivalent series resistance of the model measured at the generator terminals so as to include the series capacitances with the model. The resultant ℓ will then be the equivalent series inductance per unit length. If $\underline{C}$ is the effective series capacitance of the model, the a-c resistance of the corresponding conductor in the initial device is $\omega_i/(k\omega_m C)$ per meter.

Heat Flow in an Anisotropic Medium

If the coordinate axes are chosen to coincide with the principal axes of the material, the heat flow $\underline{h}$ in watts/inch^2 and the temperature $\underline{T}$ are related by the equations,

$$h_x = -g_x\frac{\partial T}{\partial x}, \quad h_y = -g_y\frac{\partial T}{\partial y}, \quad h_z = -g_z\frac{\partial T}{\partial z} \tag{37}$$

where g_x, g_y and g_z are the heat conductivities along the $\underline{x}$, $\underline{y}$ and $\underline{z}$ axes. If heat is being generated at a rate of $\underline{w}$ watts/inch^3 throughout the material, then $\nabla\cdot h = w$. Hence, if the conductivity is the same at all points (medium homogeneous but anisotropic),

$$g_x\frac{\partial^2 T}{\partial x_i^2} + g_y\frac{\partial^2 T}{\partial y_i^2} + g_z\frac{\partial^2 T}{\partial z_i^2} = -w. \tag{38}$$

Suppose the model to be scaled so that

$$x_i = \sqrt{\frac{g_x}{g_o}}\,x_m, \quad y_i = \sqrt{\frac{g_y}{g_o}}\,y_m, \quad z_i = \sqrt{\frac{g_z}{g_o}}\,z_m \tag{39}$$

where g_o is a constant. Then, in terms of the model coordinates, equation (38) becomes simply

$$g_o\,\nabla_m^2 T = -w. \tag{40}$$

For a uniform electrolyte (γ = const.) equation (2) has this same form. The voltage distribution in the model, therefore, represents the temperature distribution provided that currents $\underline{P}$ are introduced into the model proportional to the rate $\underline{w}$ of heat generation.

This principle may, of course, be applied to other fields such as electric or magnetic fields involving anisotropy in the permittivity or the permeability.

REFERENCES

1. Electromagnetic Fields, Theory and Application, Vol. I Mapping of Fields, Ernst Weber, John Wiley & Sons, New York, 1950.

2. Methods of Plotting Electrostatic Fields, P. E. Green, Jr., Engineering School Bulletin, North Carolina State College, Raleigh, North Carolina, Bulletin No. 45, June, 1949, 35-42.

3. Electron Optics and the Electron Microscope, New York, John Wiley and Sons, 1945, pp. 389, 477, 647, V. K. Zworykin, G. A. Morton, E. G. Ramberg, J. Hillier, and A. W. Vance.

4. Automatic Plotting of Electrostatic Fields, Paul E. Green, Jr., Review of Scientific Instruments, N. Y. 19 (1948), pp. 646-653.

5. Automatic Equipment and Techniques for Field Mapping, J. K. Mickelsen, General Electric Review, Schenectady, N. Y., 52 (Nov. 1949) pp. 19-23.

6. Utilization of the Electric Tank in Different Problems concerning High-Voltage Equipment, G. Balachowski and Tirrolloy, Conference Internationale des Grands Réseaux Électrique à Haute Tension, 112 Boulevard Haussmann, Paris, France, Report #132 (1950).

7. Cable Accessory Design Utilizing New Laboratory Techniques, P. N. Bosworth and H. K. Farr, Electrical Engineering, N. Y. 69, (1950) pp. 119-124.

8. H. Schaefer and R. Stachowiak, Zeitschrift für technishe Physik 32 (1940) p. 307.

9. Operation of Bushings in Carbonized Oil, W. R. Wilson and L. Wetherill, Conference Paper, AIEE General Winter Meeting, 1950.

10. Use of the Electrolytic Tank for Magnetic Problems, R. E. Peierls, Nature, London, England 158 (1946) pp. 831-832.

11. V. A. Karasev, Electrichestvo, Russia, (May 1949).

TABLE I

FIELDS WHICH MAY BE STUDIED BY

MEANS OF THE ELECTROLYTIC FIELD-ANALYZER

	FIELD TYPE	FUNDAMENTAL VARIABLES		EXAMPLES
		POTENTIAL	FLUX	
1.	Electrostatic	Voltage	Electrostatic flux	Electrical stresses about a bushing or between windings of a transformer.
2.	Magnetic	Magnetic potential	Magnetic flux	Leakage inductance of transformer windings. Field in the air gap of a motor.
3.	Resistive flow of electric current.	Voltage	Current	End ring of an induction motor. Current flow from point contact.
4.	Conductive heat flow	Temperature	Heat flow	Hot spot temperature of a transformer core.
5.	Fluid flow	Velocity potential	Fluid flow	Flow around streamlined objects.
6.	Gravitational	Gravitational potential	Force of gravity	Mapping of geological formations.
7.	Functions of a complex variable	Real part of the function	Imaginary part	Impedance function of an amplifier. Transient response of a network.
8.	Mechanical stress	Stress functions such as the sum of the principal stresses		Torsion of cylindrical shafts.

TABLE II

ANALOGOUS QUANTITIES FOR
FIELDS OF TRANSLATIONAL SYMMETRY

	Electrostatic Field Direct Representation		Scale Factor	Electrolytic Model		Magnetic Field Orthogonal Representation	
1	Length and coordinates of position	s_i	a	s_m		s_i	
2	Voltage	ϕ	b	V	Voltage	ψ	Flux per unit length
3	Permittivity	ϵ	k	σ	Conductance per square	$1/\mu$	Reciprocal of the permeability
4	Field Intensity	E	b/a	F	Field intensity	B	Flux density
5	Flux density	D	kb/a	i	Current density per unit length	H	Field intensity
6	Charge (or flux) per unit length	q	kb	I	Total current	U	Total current
7	Charge density	m	kb/a^2	p	Density of current sources per unit area	u	Current density per unit area
8	Reciprocal of capacitance per unit length	1/c	1/k	R	Resistance	ℓ	Inductance per unit length
9	Equipotential lines				Equipotential lines		Flux lines

Any magnetic or electrostatic quantity is equal to the scale factor times the corresponding quantity for the model when expressed in rationalized MKS units. F and i are in the same direction as E and D but at right angles to B and H. The scale factors a, b and k are independent and may be chosen arbitrarily.

TABLE III
CURRENT DISTRIBUTION DETERMINED BY THE
FIELD ANALYZER FOR THE BUS SYSTEM OF FIG. 7

Bar No.	Percent of Total I^2R Loss in Each Bar
1	9.6
2	10.2
3	38.2
4	48.0

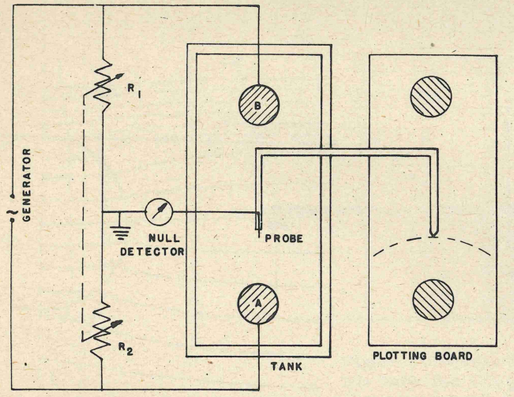

Figure 1. Elements of the Electrolytic Field-Analyzer. The model consists of tank, electrolyte and the electrodes A and B.

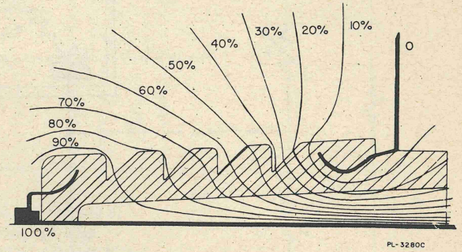

Figure 3. Potential field of a glass bushing obtained with the electrolytic field-analyzer. The contours are equipotential lines with the voltage of each indicated as a percentage of the total applied voltage.

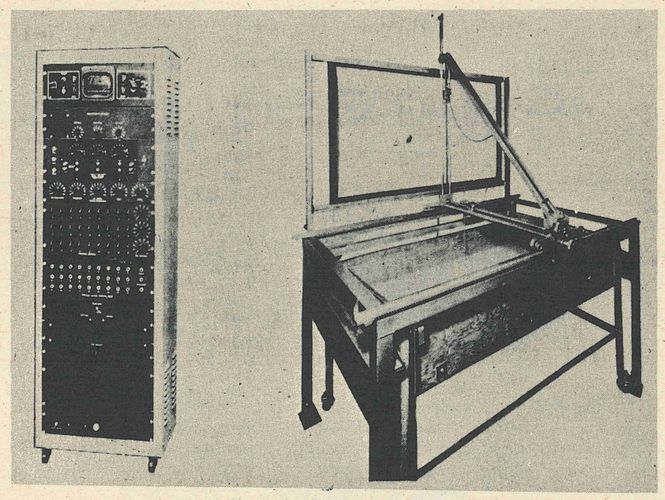

Figure 2. Equipment for field analysis

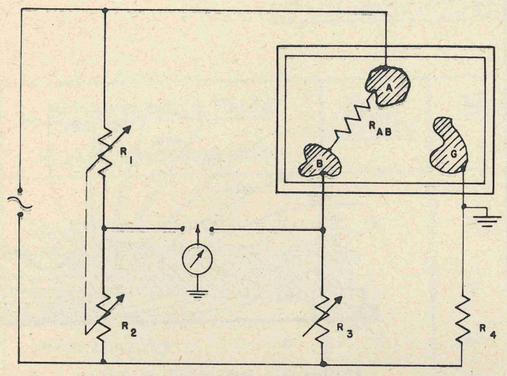

Figure 4. Guarded bridge circuit used with an electrolytic model for the determination of the partial capacitance between electrodes A and B.

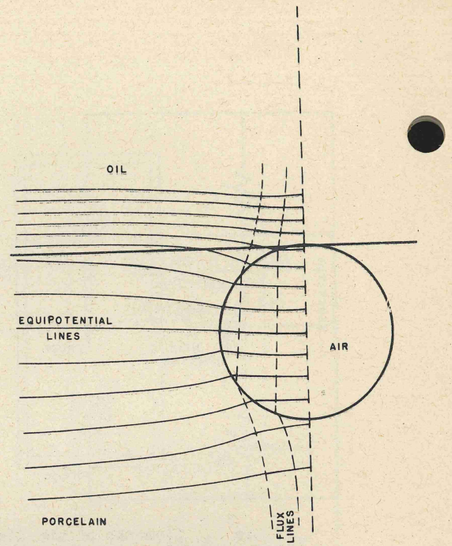

Figure 5. The electrostatic field about a gas inclusion in porcelain near oil. Different models were used for the twotypes of lines.

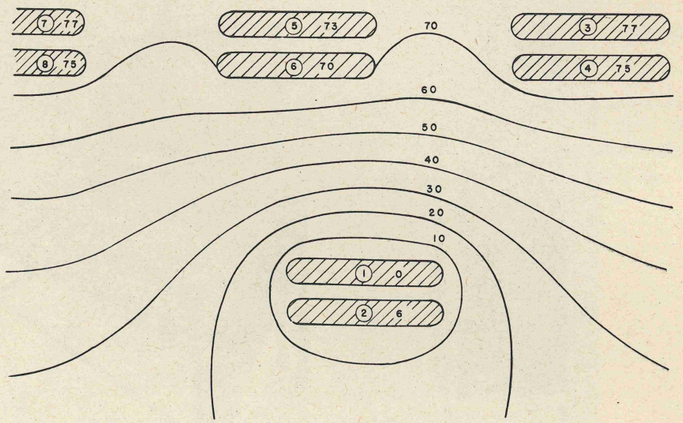

Figure 6. Magnetic flux lines in a portion of a pulse transformer winding. An uncircled number denotes flux linkage with respect to conductor number one. As very little flux penetrates a conductor under pulse conditions, this number is constant for each conductor.

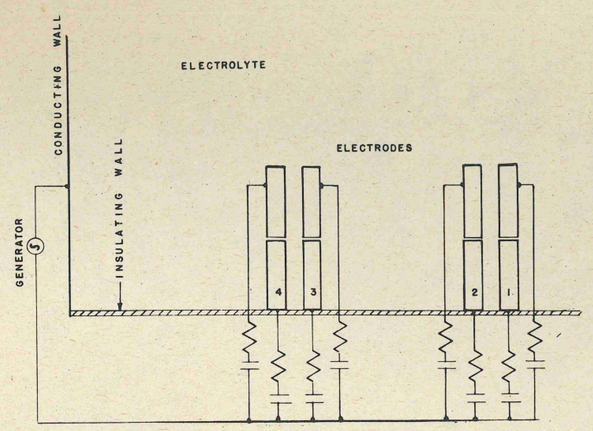

Figure 7. Model of a system of parallel bus bars for the determination of the distribution of current flowing under the influence of resistance and magnetic induction.

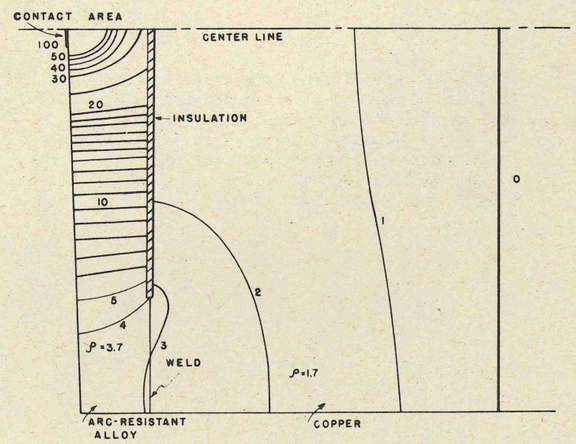

Figure 8. Voltage field produced by current flowing in a circuit-breaker contact assembly. The contours are equipotentials taken at intervals of one or five percent of the total voltage applied to the model. The complete assembly includes two identical contacts of which only one is shown, and which make contact along the 100% equipotential line. The insulating barrier in the model represents an incomplete braze. Values of indicate resistivity. Electrodes in the model were along the 0 and 100% equipotentials.

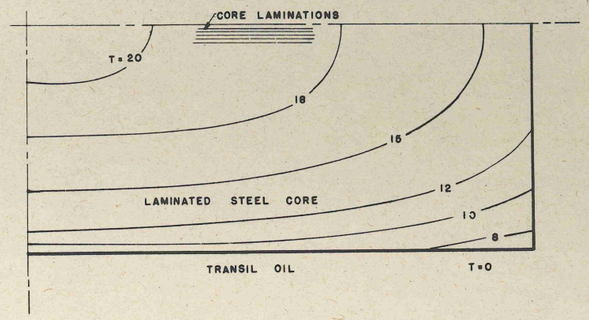

Figure 9. Temperatures in a cross section through one quarter of a transformer core. The contours are isothermal lines representing the temperature rise T in degree C with respect to the surrounding oil. No isothermal lines appear in the oil which is at a uniform temperature (T=0).

AIEE
Technical Paper
51-240

May 1951
Litho in USA

Equipment - Testing

SOME ENGINEERING APPLICATIONS OF THE ELECTROLYTIC FIELD-ANALYZER

H. K. Farr
Member AIEE
General Electric Company,
Pittsfield, Mass.

W. R. Wilson
Member AIEE
General Electric Company,
Philadelphia, Pa.

Advance Copy
Not Released for Publication

All Rights Reserved by the
American Institute of Electrical Engineers
33 West 39th Street, New York 18, N.Y.

A paper recommended by the AIEE Committee on Instruments and Measurements and approved by the AIEE Technical Program Committee for presentation at the AIEE Summer General Meeting, Toronto, Ont., Canada, June 25-29, 1951. Manuscript submitted March 26, 1951; made available for printing May 31, 1951.

PRICE: 30¢ To Members
60¢ To Nonmembers

DMD
BEK
This would be of interest
if it doesn't cost too much
Afm

Equipment
Testing

DF52GL117

RECEIVED
MAY 8 1952
ENG. DEPT.

GENERAL ELECTRIC

General Engineering Laboratory

AN ADJUSTABLE RATE OF RISE CONTROL SYSTEM FOR DIELECTRIC STRENGTH TESTING

By

R. N. Bushman

SCHENECTADY, NEW YORK

FOR USE OF G-E EMPLOYEES ONLY

GENERAL ELECTRIC

GENERAL ENGINEERING LABORATORY

TECHNICAL INFORMATION SERIES

Title Page

AUTHOR	SUBJECT CLASSIFICATION	NO.
R.N.Bushman	Testing - Dielectric Testing - High Potential	DF52GL117
		DATE April 15,1952

TITLE

AN ADJUSTABLE RATE OF RISE CONTROL SYSTEM FOR DIELECTRIC STRENGTH TESTING

ABSTRACT

A control system for dielectric strength testing sets providing adjustable rate of rise over an extremely wide speed range with semi-automatic operation is described.

G.E. CLASS	REPRODUCIBLE COPY FILED AT	NO. PAGES
II	General Engineering Lab. Library, Schenectady, N.Y.	5
GOV. CLASS. None		

CONCLUSIONS

The application of a Thymotrol motor drive to dielectric strength testing equipment provides accurate control of the rate of rise of the testing voltage over an extremely wide range of speeds. This drive combined with properly designed relaying and metering systems becomes an integrated control system which is extremely versatile.

For list of contents—drawings, photos, etc. and for distribution see next page (FN-610-2).

INFORMATION PREPARED FOR General Information

TESTS MADE BY R. N. Bushman

AUTHOR R. N. Bushman R. N. Bushman

COUNTERSIGNED F. M. Clark F.M.Clark April 15, 1952

DIVISION

GENERAL ELECTRIC COMPANY
TECHNICAL INFORMATION SERIES
CONTENTS PAGE

TENTS OF REPORT

NO. PAGES TEXT 6

NO. CHARTS

DRAWING NOS.

PHOTO NOS. #1096046
#1096047

TRIBUTION

M. Fairbanks	-	Construction Materials Laboratory	BRIDGEPORT WORKS
C. Anderson	-	Works Laboratory	" "
W. Staley	-	Laminated Plastics	COSHOCTON WORKS
J. Sherburne	-	Laminated Plastics	" "
A. Kern	-	Works Laboratory	PITTSFIELD WORKS
R. Walters	-	Works Laboratory	" "
R. Meador	-	Power Transformer Engineering	" "
E. Moseley	-	Power Transformer Sales Division	" "
F. Fiedler	-	New Product Development Laboratory	" PLASTICS
W. Pinkham	-	Meter & Instrument Laboratory	WEST LYNN WORKS
K. Drake	-	Works Laboratory	FORT WAYNE WORKS
M. Summers	-	Works Laboratory	" "
Wilcock	-	Thomson Laboratory	RIVER WORKS
O. Straney	-	Thomson Laboratory	" "
A. Ross	-	Thomson Laboratory	" "
H. Catlin	-	Locomotive & Car Equip. Laboratory	ERIE WORKS
A. Coffman	-	Locomotive & Car Equip. Laboratory	" "
R. Wilson	-	Switchgear Laboratory	PHILADELPHIA WORKS
D. Bergh	-	Switchgear Laboratory	" "
T. Burkett	-	Electronics Laboratory	SYRACUSE WORKS
R. Lampman	-	Electronics Laboratory	" "
L. Alger	-	Small & Medium Motors Engineering	SCHENECTADY WORKS
J. Flynn	-	Works Laboratory	" "
Guarnier	-	Construction Materials Laboratory	" "
A. Scott	-	Cable Division Laboratory	" "
A. Loritsch	-	Chemical Department	" "
C. San Jule	-	Testing Division	" "
N. Mathes	-	Works Laboratory	" "
E. Rhoads	-	Control Division Laboratory	" "
A. Schuster	-	Special Products Division	" "

GENERAL ELECTRIC COMPANY
TECHNICAL INFORMATION SERIES
CONTENTS PAGE

NTS OF REPORT

. PAGES TEXT 6

. CHARTS

RAWING NOS.

HOTO NOS. #1096046
#1096047

RIBUTION

A. Edwards	-	General Engineering Laboratory	SCHENECTADY WORKS
M. Clark	-	General Engineering Laboratory	" "
E. Johnson	-	General Engineering Laboratory	" "
A. Lupfer	-	General Engineering Laboratory	" "
A. Palm	-	General Engineering Laboratory	" "
Rudoff	-	General Engineering Laboratory	" "
W. Nordlander	-	Research Laboratory	" "
K. Fraser	-	Materials Laboratory	PETERBOROUGH WORKS
B. Gustafson	-	G. E. X-Ray	MILWAUKEE WORKS
L. Mc Coy	-	Locke Insulator	BALTIMORE WORKS

GENERAL ELECTRIC COMPANY
TECHNICAL INFORMATION SERIES
DF52GL117

Among the many electrical tests used to evaluate the quality of electrical insulating materials, dielectric strength is probably the oldest and still most commonly used. It would be hard to find a producer or user of any quantity of insulating materials who is not equipped with some sort of dielectric strength testing equipment in either laboratory or factory.

Unfortunately, there are many variables which affect the results obtained in dielectric strength tests and unless the test methods are standardized, results obtained on various equipments are not comparable. Among the variables to be considered is the rate at which the test voltage is increased.

Until recently only two dielectric strength test methods were specified by the American Society for Testing Materials. The first, called the Short-Time Test, requires the voltage to be increased at the rate of 500 to 1000 volts per second in the case of solid insulations and 3000 volts per second in the case of liquid insulations. The second method, called the Step-by-Step Test, requires the voltage to be increased in steps with each step to be held for a specified period of time.

While the variation in the specified rates of rise is not large, difficulties were often encountered in meeting the specifications to the required twenty five percent accuracy.

In 1948, A. S. T. M. proposed a third test method designated as the Slow Rate of Rise. This method, designed to replace the rather laborious Step-by-Step test, calls for rates of rise in the order of 13, 25 and 50 volts per second. These additional rates greatly complicate the problem of voltage control.

Prior to 1948, the usual method of speed control had been to adjust the armature and field voltage supplied to a direct current motor. This required a direct current supply, in addition to the alternating current supply required for testing, which was often difficult to obtain. With the advent of the new specifications this method was no longer satisfactory since the speed range required was too great for this type of control.

In reviewing methods of obtaining the necessary speed control the General Electric Thymotrol system stood out as having many advantages for this application. Accordingly, a control system for dielectric strength testing was designed around the Thymotrol. The prototype of this system has been in daily use with an excellent service record.

DESCRIPTION

The heart of the Adjustable Rate of Rise Control System is the General Electric Thymotrol. This electronic motor drive is particularly advantageous for this application for the following reasons:

1. The drive operates from the alternating current lines.

2. The motor operates at a pre-set speed regardless of load as long as the rating is not exceeded.

3. The armature current is automatically limited to a safe value. This allows abrupt changes in speed, load and direction without damage to the motor.

4. Speed is controlled by a single small potentiometer.

Small Thymotrol drives may be obtained with speed ranges of twenty or fifty to one. In some special cases either of these ranges may be sufficient for dielectric strength sets, but in most instances speed ratios of at least two hundred and fifty to one are necessary. To secure this extended range some means of mechanical speed changing is necessary. Since it is desireable to shift speed ranges quickly and automatically, manually operated equipment such as gearshifts are not satisfactory.

The method adopted in the present equipment is to use two motors, each driving one of the input shafts of a differential gear unit through a speed reducer (Fig. 1). The ratio of one speed reducer is made greater than the other by a factor equal to, or less than, the speed range of the Thymotrol drive. The motors are equipped with magnetic brakes to lock the section of the drive not in use. The cage of the differential is belted to the shaft of the voltage regulator. The overall speed range obtainable with this system is as great as twenty-five hundred to one.

While it is more expensive, the induction voltage regulator was chosen as the voltage controller in preference to the variable ratio autotransformer because of its reliability and smooth, stepless output. The surges occuring each time a test sample fails result in pitting of the winding beneath the brush of an autotransformer. Eventually this pitting causes poor contact and erratic voltage output. Since there are no sliding contacts in the induction voltage regulator, these surges do no damage.

The regulator is equipped with limit switches to stop the drive when the maximum or minimum voltage points are reached.

The motor drive and regulator are built as a unit (Fig. 2) and since there are no gears to shift or other manual operations to perform, this portion of the equipment may be installed in any convenient location.

The operating controls, meters and the electronic portion of the drive are contained in a floor mounting cabinet (Fig.3). In the case of equipment having a rating greater than 5 K.V.A. the contactors in the main power circuit and the overload relays are mounted externally.

Above the operating controls are the voltmeters which indicate the test voltage, voltmeter selector switch and the pilot lamps which show the position of the voltage regulator and indicate other operating conditions.

A desk is provided on the front of the control cabinet for the use of the operator in recording test results. Directly above the desk are the main operating controls. These consist of the speed control potentiometer, switches for speed range, transformer selection, manual or automatic rundown, a master control switch and pushbuttons for starting and stopping the test voltage and controlling the motor drive.

Below the desk are switches for turning the control power on and off and selecting the proper overload relay. Also located below the desk are several sets of binding posts for use in connecting recording voltmeters to the voltmeter coils of the testing transformers when the set is operating unattended.

SPECIAL FEATURES

In addition to the variable rate of rise, several other features have been incorporated in the control circuits which simplify the work of the operator and speed up the operation of the equipment.

As mentioned previously, the Thymotrol drive permits quick reversal of the motor without damage. Taking advantage of this feature, the drive is arranged so that when the sample fails the overload relays instantaneously remove the test voltage and at the same time automatically reverse the drive and return the

regulator to the zero voltage position at maximum speed. When the slow speed section of the drive is being used, the relaying system shifts over to the high speed drive automatically on the return. If it is desired to have the drive stop at the point of failure, the automatic rundown may be disconnected by a switch on the operating panel.

Power is supplied to the primary of the testing transformer and to the driving motors through contactors operated by a series of pushbuttons. The contactors are equipped with holding contacts and the pushbuttons may be released after any operation has been started. The operation will continue until a stop button is depressed or the operation is halted by one of the elements in the set such as an overload relay or limit switch. Jog buttons are provided for use when the voltage must be "inched" up or down to some particular value. The use of the job buttons disconnects the holding contacts on the raise and lower contactors and the operation of the drive ceases as soon as the button is released.

The motor drive operates at the preset speed in the forward or raise direction and when jogging in either direction. When the "lower" button is depressed, the drive operates at maximum speed.

The individual pushbuttons are provided for use when step by step or voltage endurance tests are being made. A master operating switch is provided for Short Time and Slow Rate-of-Rise tests. This switch parallels the operation of several push buttons. Turning the switch momentarily to the "start" position closes the power supply contactors and at the same time starts the drive in the "raise" direction at the preset speed. Turning the master switch to "clear" opens the power supply contactors and reverses the drive to "lower" at the maximum speed.

A time meter is included in the set so that the life of test samples may be measured when the set is left running unattended while voltage endurance tests are being run.

SAFETY

The equipment is arranged to meet general safety requirements. Power is supplied to the high voltage testing transformers through two contactors, the main poles of which are connected in series. Should either contactor jam in the closed position the other will

interupt the circuit. Secondary contacts of each contactor are connected in parallel and the power to operate the warning lights fed through the parallel circuit. In the case a contactor should jam closed the warning lights will then remain lighted. Provision is made for connection of an external safety gate circuit which will interupt the power to the operating coils of the contactors in the transformer primary should the gates of the testing enclosure be opened.

The motor drive is arranged so that it will not operate in the "raise" direction unless the power supply contactors are closed. The drive will operate in the "lower" direction regardless of the position of the power supply contactors.

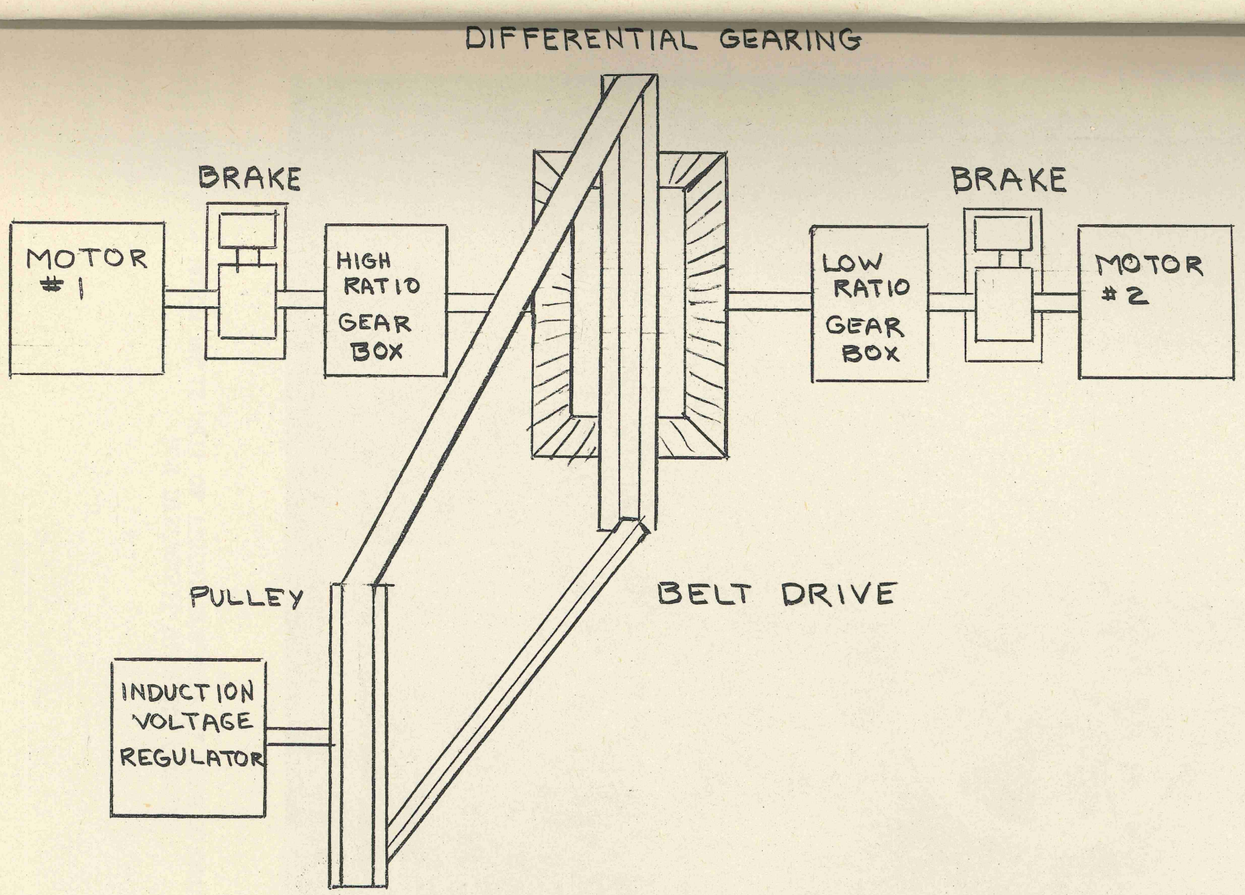

FIG. 1 - DIFFERENTIAL GEAR SYSTEM FOR DRIVING AN INDUCTION VOLTAGE REGULATOR FROM EITHER OF TWO MOTORS.

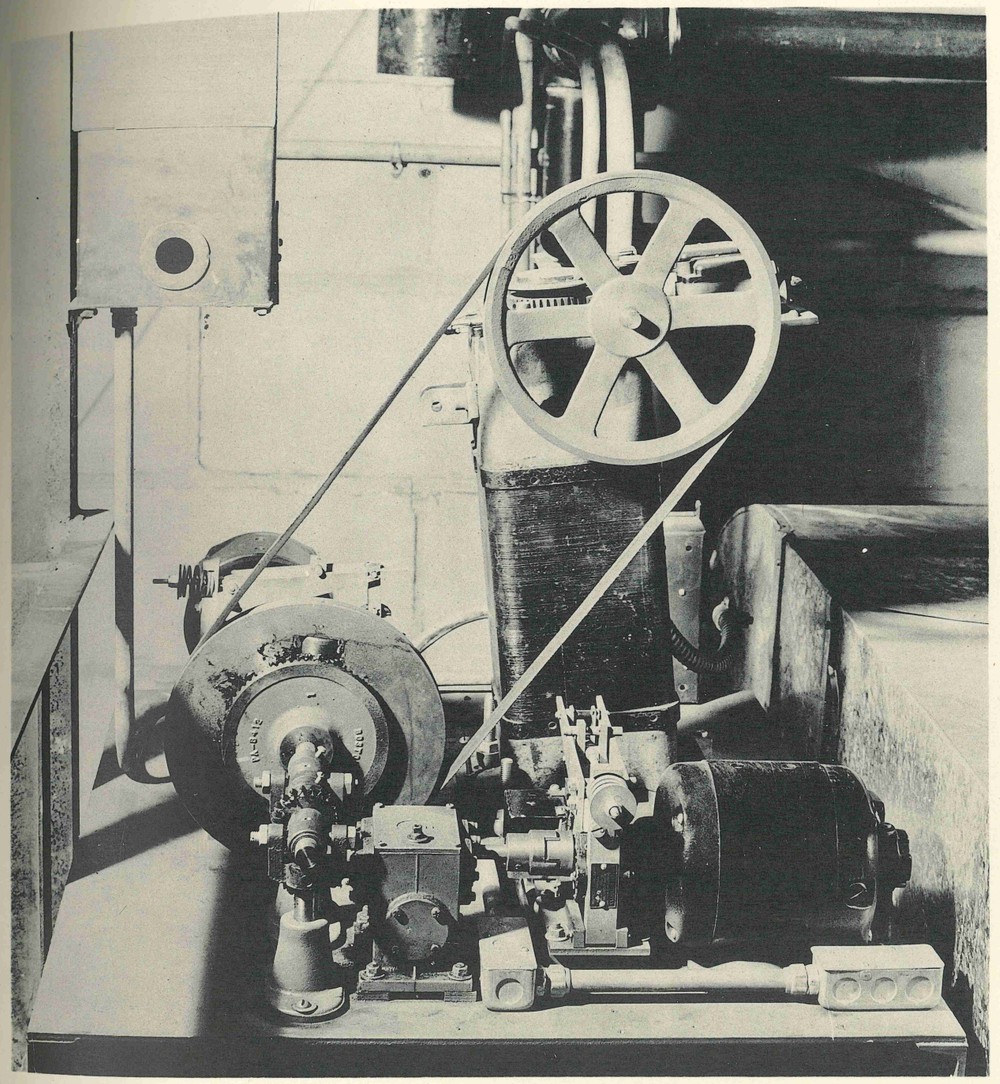

FIG. 2 - MOTOR DRIVE UNIT OF ADJUSTABLE RATE OF RISE CONTROL SYSTEM FOR DIELECTRIC STRENGTH TESTING

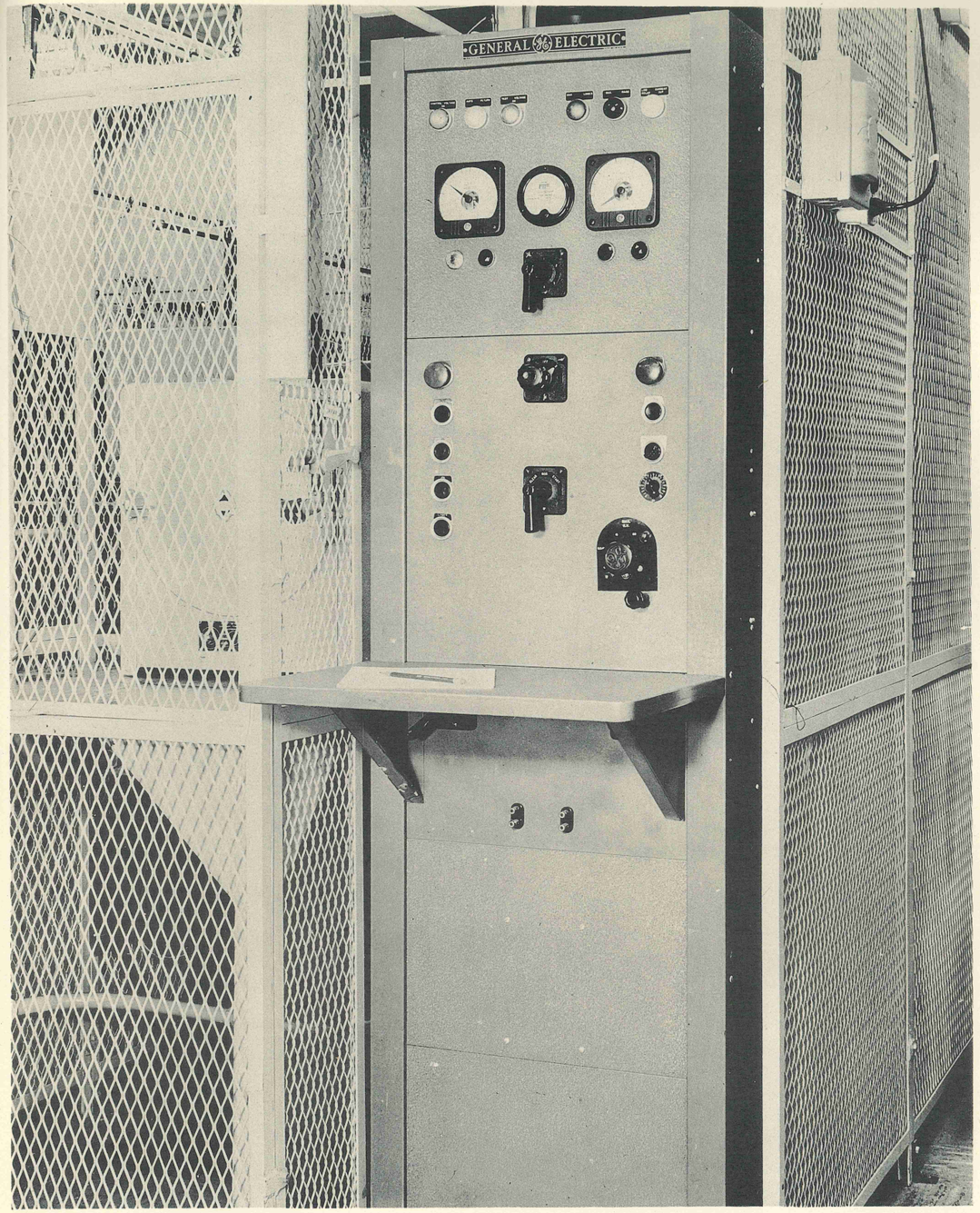
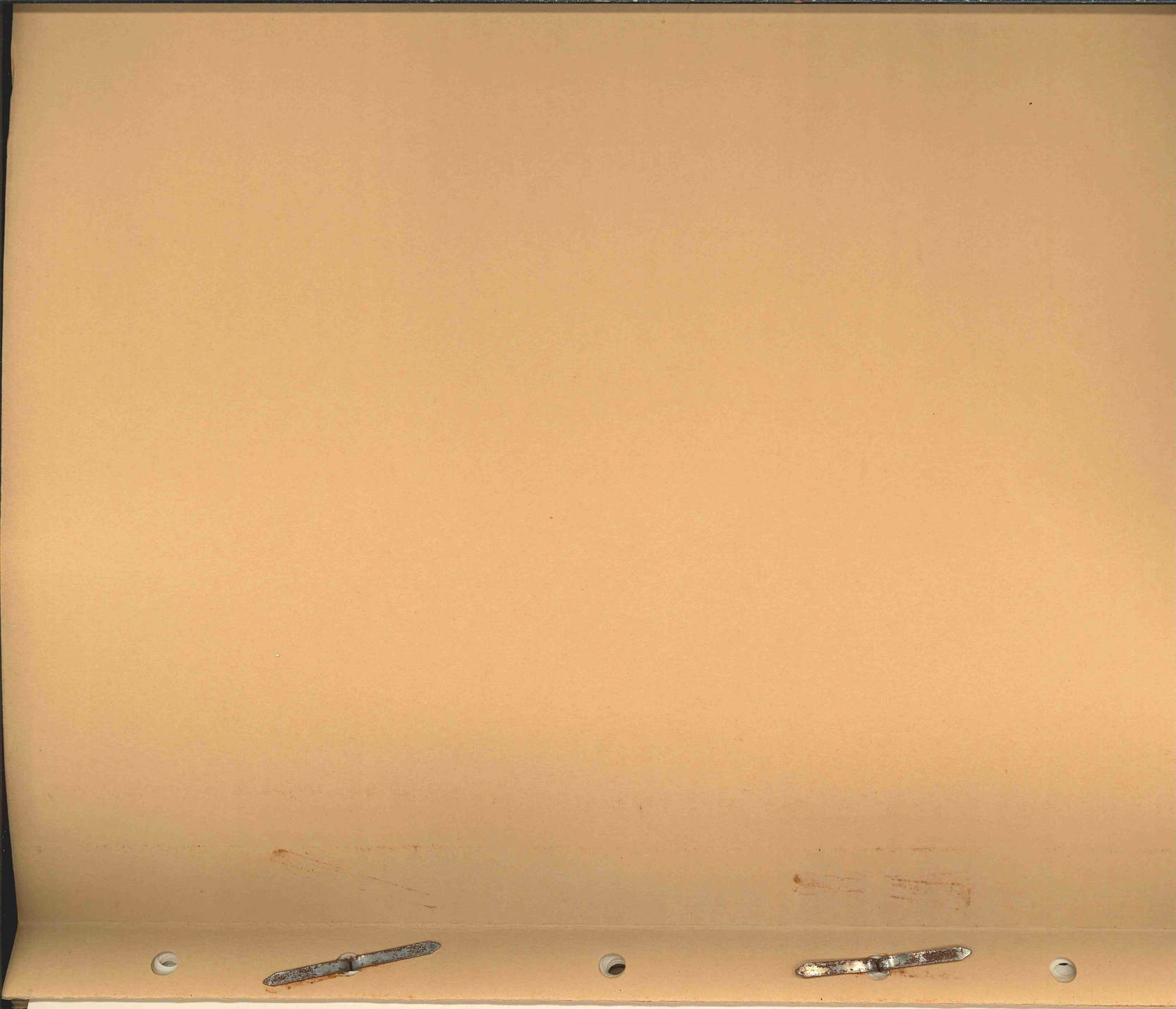
FIG. 3 - CONTROL CABINET OF ADJUSTABLE RATE OF RISE CONTROL SYSTEM FOR DIELECTRIC STRENGTH TESTING